APPLIED COMPUTATIONAL ELECTROMAGNETICS SOCIETY JOURNAL

New Technologies for Electrical Energy Generation and Electric Transportation

Guest Editors:

Antonino Musolino, University of Pisa, Italy
Claudia Simonelli, University of Pisa, Italy
Nicolò Gori, University of Pisa, Italy

June 2026
Vol. 41 No. 06
ISSN 1054-4887

The ACES Journal is abstracted in INSPEC, in Engineering Index, DTIC, Science Citation Index Expanded, the Research Alert, and to Current Contents/Engineering, Computing & Technology.

The illustrations on the front cover have been obtained from the ARC research group at the Department of Electrical Engineering, Colorado School of Mines

Published, sold and distributed by: River Publishers, Broagervej 10, 9260 Gistrup, Denmark

THE APPLIED COMPUTATIONAL ELECTROMAGNETICS SOCIETY
http://aces-society.org

EDITORS-IN-CHIEF

Sami Barmada
University of Pisa, ESE Dept.
56122 Pisa, Italy

Atef Elsherbeni
Colorado School of Mines, EE Dept.
Golden, CO 80401, USA

ASSOCIATE EDITORS

Giulio Antonini
Università degli Studi dell'Aquila
Italy

Marco Arjona
La Laguna Institute of Technology
Coahuila 27266, Mexico

Abd A. Arkadan
Colorado School of Mines, Golden
CO 80401, USA

Alireza Baghai-Wadji
University of Cape Town
Cape Town, 7701, South Africa

Santanu Behera
National Institute of Technology
Rourkela-769008, India

Rui Chen
Nanjing University of Science
and Technology
China

Vinh Dang
Sandia National Laboratories
USA

Sounik Kiran Kumar Dash
SRM Institute of Science and Technology
Chennai, India

Alessandro Formisano
Seconda Universita di Napoli
81031 CE, Italy

Nunzia Fontana
University of Pisa
56122 Pisa, Italy

Fatih Kaburcuk
Sivas Cumhuriyet University
Sivas, Turkey

Piotr Gas
AGH University of Kraków
30-059 Krakow, Poland

Mona El Helbawy
University of Colorado
Boulder, CO 80302, USA

Zhixiang Huang
Anhui University
China

Qiuhua Huang
Colorado School of Mines
USA

Long Li
Xidian University
Shaanxi 710071, China

Yingsong Li
Harbin Engineering University
Harbin 150001, China

Wenxing Li
Harbin Engineering University
Harbin 150001, China

Ibrahim Mahariq
Gulf University for Science and Technology
Kuwait

Riyadh Mansoor
Al-Muthanna University
Samawa, Al-Muthanna, Iraq

Maria Evelina Mognaschi
University of Pavia
Italy

Antonino Musolino
University of Pisa
56123 Pisa, Italy

Sima Noghanian
Wafer LLC
Beverly, MA 01915, USA

Mauro Parise
University Campus Bio-Medico of Rome
00128 Rome, Italy

Luca Di Rienzo
Politecnico di Milano
20133 Milano, Italy

Daniele Romano
Università degli Studi dell'Aquila
Italy

Huseyin Savci
Istanbul Medipol University
Turkey

Stefano Selleri
DINFO – University of Florence
0139 Florence, Italy

Sihua Shao
Colorado School of Mines
USA

Jiming Song
Iowa State University
IA 50011, USA

Sheng Sun
University of Electronic Science
and Technology of China
China

Francesca Venneri
DIMES, Università della Calabria
Italy

Steven Weiss
US Army Research Laboratory
USA

Wei-Chung Weng
National Chi Nan University
Puli, Nantou 54561, Taiwan

Kaikai Xu
University of Electronic Science
and Technology of China
China

Lei Zhao
China University of Mining
and Technology, Jiangsu 221116
China

EDITORIAL ASSISTANTS

Matthew J. Inman
University of Mississippi, EE Dept.
University, MS 38677, USA

Shanell Lopez
Colorado School of Mines, EE Dept.
Golden, CO 80401, USA

EMERITUS EDITORS-IN-CHIEF

Duncan C. Baker
EE Dept. U. of Pretoria
0002 Pretoria, South Africa

Allen Glisson
University of Mississippi, EE Dept.
University, MS 38677, USA

Ahmed Kishk
Concordia University, ECS Dept.
Montreal, QC H3G 1M8, Canada

Robert M. Bevensee
Box 812
Alamo, CA 94507-0516

Ozlem Kilic
Catholic University of America
Washington, DC 20064, USA

David E. Stein
USAF Scientific Advisory Board
Washington, DC 20330, USA

EMERITUS ASSOCIATE EDITORS

Yasushi Kanai
Niigata Inst. of Technology
Kashiwazaki, Japan

Mohamed Abouzahra
MIT Lincoln Laboratory
Lexington, MA, USA

Alexander Yakovlev
University of Mississippi, EE Dept.
University, MS 38677, USA

Levent Gurel
Bilkent University
Ankara, Turkey

Sami Barmada
University of Pisa, ESE Dept.
56122 Pisa, Italy

Ozlem Kilic
Catholic University of America
Washington, DC 20064, USA

Erdem Topsakal
Mississippi State University, EE Dept.
Mississippi State, MS 39762, USA

Alistair Duffy
De Montfort University
Leicester, UK

Fan Yang
Tsinghua University, EE Dept.
Beijing 100084, China

Rocco Rizzo
University of Pisa
56123 Pisa, Italy

Atif Shamim
King Abdullah University of Science and Technology (KAUST)
Thuwal 23955, Saudi Arabia

William O'Keefe Coburn
US Army Research Laboratory
Adelphi, MD 20783, USA

Mohammed Hadi
Kuwait University, EE Dept.
Safat, Kuwait

Amedeo Capozzoli
Univerita di Naoli Federico II, DIETI
I-80125 Napoli, Italy

Maokun Li
Tsinghua University
Beijing 100084, China

Lijun Jiang
University of Hong Kong, EEE Dept.
Hong, Kong

Shinishiro Ohnuki
Nihon University
Tokyo, Japan

Kubilay Sertel
The Ohio State University
Columbus, OH 43210, USA

Salvatore Campione
Sandia National Laboratories
Albuquerque, NM 87185, USA

Toni Bjorninen
Tampere University
Tampere, 33100, Finland

Paolo Mezzanotte
University of Perugia
I-06125 Perugia, Italy

Yu Mao Wu
Fudan University
Shanghai 200433, China

Amin Kargar Behbahani
Florida International University
Miami, FL 33174, USA

Laila Marzall
University of Colorado, Boulder
Boulder, CO 80309, USA

Qiang Ren
Beihang University
Beijing 100191, China

EMERITUS EDITORIAL ASSISTANTS

Khaleb ElMaghoub
Trimble Navigation/MIT
Boston, MA 02125, USA

Kyle Patel
Colorado School of Mines, EE Dept.
Golden, CO 80401, USA

Christina Bonnigton
University of Mississippi, EE Dept.
University, MS 38677, USA

Anne Graham
University of Mississippi, EE Dept.
University, MS 38677, USA

Madison Lee
Colorado School of Mines, EE Dept.
Golen, CO 80401, USA

Allison Tanner
Colorado School of Mines, EE Dept.
Golden, CO 80401, USA

Mohamed Al Sharkawy
Arab Academby for Science and Technology, ECE Dept.
Alexandria, Egypt

JUNE 2026 REVIEWERS

Yusur Jalal Abdulsahib
Chen Hao
Giovanni Landi
Chenxi Li
Maria Evelina Mognaschi
Antonino Musolino
Rui Nie
Fusun Oyman Serteller
Claudia Simonelli
Lorand Szabo
Thanh Nguyen Vu
Peixin Wang

THE APPLIED COMPUTATIONAL ELECTROMAGNETICS SOCIETY JOURNAL

Vol. 41 No. 06 June 2026

TABLE OF CONTENTS

Comparative Analysis of a Novel Linear Rotary Switch Reluctance Machine
Hao Chen, Cheng Liu, Marcin Wardach, Javokhir Toshov, Xing Wang, Ali Asghar Memon, Bodrenkov Evgenii Alexandrovich, Nikolay Korovkin, Sakhno Liudmila, Emmanuel Karapidakis, Aris Dimeas, Sherif Moussa, and Habes Ali Khawaldeh 488

Design and Electromagnetic Analysis of Stator-Modular Tubular Linear Rotary Machine
Hao Chen, Cheng Liu, Marcin Wardach, Javokhir Toshov, Xing Wang, Ali Asghar Memon, Bodrenkov Evgenii Alexandrovich, Popov Stanislav Olegovich, Nikolay Korovkin, Sakhno Liudmila, Emmanuel Karapidakis, Aris Dimeas, Sherif Moussa, and Habes Ali Khawaldeh 500

Electromagnetic Analysis of a Novel Two-Degree-of-Freedom Tubular Linear Rotary Switched Reluctance Machine
Cheng Liu, Hao Chen, Marcin Wardach, Javokhir Toshov, Xing Wang, Bodrenkov Evgenii Alexandrovich, Popov Stanislav Olegovich, Nikolay Korovkin, Sakhno Liudmila, Mohamed Orabi, Mahmoud A. Gaafar, Emmanuel Karapidakis, Aris Dimeas, Sherif Moussa, and Habes Ali Khawaldeh 512

A Lumped Parameter Thermal Network Model for Dual-Stator Mover-PM Linear-Rotary Generators
Chenxi Li, Rui Nie, Shuai Xu, Yanqi Wei, Peixin Wang, and Jikai Si 524

Electromagnetic Analysis of a 12-Pole Single-Phase Switched Reluctance Linear Motor
Hao Chen, Denis Kotin, Aris Dimeas, Emmanuel Karapidakis, Olimjon Toirov, Liu Jingfu, Zhao Wenmin, Xing Wang, and Sherif Moussa 536

Unified 3D Analytical Models of Surface-Inserted Axial Flux Machines With Odd-/Even-Piece Halbach Arrangements
Youyuan Ni, Jinsong Zou, Yong Lin, and Anbang Wang 551

Design and Open-Circuit Fault Analysis of Modular E-Type Stator Switched Reluctance Motor for High-Reliability Applications
Hao Chen, Xin Liu, Sergei Brovanov, Jason Gu, Sherif Moussa, Marcin Wardach, Javokhir Toshov, Ali Asghar Memon, and Xing Wang 566

© 2026, The Applied Computational Electromagnetics Society

Performance Comparison Analysis of Modular Double-Stator Switched Reluctance Motor with Differing Winding Polarities
Fengyuan Yu, Hao Chen, Haidong Yan, Guanjun Wang, and Jun Bao 577

A Dual-Port Integrated Switched Reluctance Motor Power Converter for Electric Vehicles With Flexible Braking and Energy Recovery
Chenhe Zhang, Hao Chen, Olimjon Toirov, Sherif Moussa, Habes Ali Khawaldeh, Marcin Wardach, Sergei Brovanov, Ali Asghar Memon, Emmanuel Karapidakis, and Aris Dimeas 589

© 2026, The Applied Computational Electromagnetics Society

Special Issue

New Technologies for Electrical Energy Generation and Electric Transportation

Guest Editors:

Antonino Musolino, University of Pisa, Italy
Claudia Simonelli, University of Pisa, Italy
Nicolò Gori, University of Pisa, Italy

Electric Energy production, especially from renewable fonts, together with transport electrification is one the key factors in the agenda for sustainable development.

This special issue brings together nine contributions on electrical machines, also considering examples of related power converters, for energy generation and electric transportation. Their shared focus is the relationship between electromagnetic design, operational flexibility, and reliability, addressing the demands of compact renewable energy converters and efficient electric drives.

Three studies investigate tubular linear–rotary switched reluctance machines, with potential applications in integrated actuation and marine energy systems. A comparative investigation combining geometric sensitivity analysis with alternative winding arrangements, identifying improvements in torque, thrust, and output smoothness is carried on in the first study. A second contribution considers H-shaped modular stators that accommodate rotary and linear magnetic circuits with limited electromagnetic coupling. A third examines a two-degree-of-freedom topology through static field analysis and dynamic simulations, clarifying saturation behavior and the interaction between motion modes. Together, these studies support the development of integrated electromechanical systems relevant to combined wind and wave energy conversion.

Thermal management represents an important performance index in renewable generation too. A lumped-parameter thermal network for a Dual-Stator Single-Mover Permanent-Magnet linear–rotary generator accounts for convection under helical motion and partial axial overlap. Comparison with three-dimensional finite element analysis identifies critical winding temperatures and informs cooling design.

The fifth contribution presents a 12-pole single-phase transverse-flux tubular switched reluctance linear motor. Its U-shaped modular stator shortens magnetic paths and improves iron core utilization. Prototype measurements support the modeling approach and the feasibility of the design for high-performance linear electric drives.

A further modeling contribution develops unified three-dimensional analytical models for surface-mounted Permanent Magnet axial flux machines with odd/even piece Halbach arrays. Accounting for air-gap fringing and slotting, the approach supports electromagnetic optimization of compact machines relevant to both generation and transportation.

As for electric drives, modularity is the common feature of two devices. The first is an E-type stator switched reluctance motor, whose performance in terms of manufacturability and continued operation under winding open-circuit faults are considered. The analysis of a modular double-stator motor shows how NSNS and NSSN winding polarities alter magnetic paths, revealing application-dependent trade-offs between torque production and efficiency.

At the converter level, the last contribution considers a dual-port integrated switched reluctance drive which combines flexible power supply arrangements with multilevel excitation and regenerative braking. Simulations investigate motoring and different braking intensities, linking converter reconfiguration to torque capability and energy recovery in electric vehicles.

Collectively, the papers offer analytical and simulation-based foundations for more integrated energy conversion systems. Prototype validation, thermal management, and coordinated machine–converter control remain essential steps toward practical deployment in renewable generation and electric transportation.

© 2026, The Applied Computational Electromagnetics Society

Comparative Analysis of a Novel Linear Rotary Switch Reluctance Machine

Hao Chen[1,2,3,4], Cheng Liu[1], Marcin Wardach[5], Javokhir Toshov[6], Xing Wang[2,3,4], Ali Asghar Memon[7], Bodrenkov Evgenii Alexandrovich[8], Nikolay Korovkin[8], Sakhno Liudmila[8], Emmanuel Karapidakis[9], Aris Dimeas[10], Sherif Moussa[11], and Habes Ali Khawaldeh[12]

[1]School of Electrical Engineering
China University of Mining and Technology, Xuzhou 221116, China
hchen@cumt.edu.cn, Chengliu97@cumt.edu.cn

[2]Shenzhen Research Institute
China University of Mining and Technology, Shenzhen 515100, China
3512@cumt.edu.cn

[3]Jiangsu Province Foreign Expert Workshop on New Energy Power Generation and Electric Transportation
Xuzhou 221008, China

[4]International Joint Research Center of Central and Eastern European Countries on
New Energy Electric Vehicle Technology and Equipment
Xuzhou 221008, China

[5]Department of Electrical Machines and Drives
West Pomeranian University of Technology, Sikorskiego 37, 70-313 Szczecin, Poland

[6]Tashkent State Technical University
University Street No. 2, 100095 Tashkent, Uzbekistan

[7]Mehran University of Engineering and Technology
Department of Electrical Engineering, Jamshoro, Pakistan

[8]The Institute of Energy
Peter the Great Saint Petersburg Polytechnic University, Saint Petersburg, Russia

[9]School of Engineering
Hellenic Mediterranean University, Estavromenos Campus, 71004 Heraklio, Crete, Greece

[10]Athens National University of Technology
Greece

[11]School of Engineering
Canadian University Dubai, 117781, Sheikh Zayed Road, Dubai, United Arab Emirates

[12]The Renewable Energy Engineering Department
Faculty of Engineering, Al al-Bayt University, Mafraq, Jordan
*Corresponding author

Abstract – This paper proposes a novel tubular linear rotary switch reluctance machine (TLRSRM) with modular stator and rotor designs and studies its electromagnetic characteristics. Firstly, the topology and operating mechanism of the two-degree-of-freedom machine are presented. based on the proposed motor design process, the structural dimensions are initially determined, and the 3D finite element model (FEM) with its flux density distribution is provided. Secondly, a sensitivity analysis of critical structural parameters is conducted by using a parameter sweep method to investigate their influence on torque performance. Finally, to evaluate the motor's static characteristics – including flux linkage, inductance, and torque/thrust – comparison analysis is

Submitted On: January 15, 2026
Accepted On: June 15, 2026

1054-4887 © ACES

https://doi.org/10.13052/2026.ACES.J.410601

performed between two TLRSRM variants featuring different winding configurations. Simulation results validate the feasibility of the proposed topology.

Index Terms – 3D finite element model, magnetic field distribution, static electromagnetic characteristics, switched reluctance machine.

I. INTRODUCTION

Against the backdrop of deepening industrial intelligence and rapid development of integrated marine energy systems – such as combined offshore wind and wave power generation – diverse application scenarios demand higher levels of integration and multidimensional motion control capabilities from drive equipment. Traditional single-degree-of-freedom motors increasingly reveal limitations such as restricted functionality, complex system structures, and wasteful space utilization, making them ill-suited for efficient drive demands under complex operating conditions. Against this backdrop, multi-degree-of-freedom motor technology has emerged as a frontier research direction in the field of electric motors, owing to its integrated compact structure, highly consolidated functionality, and flexible motion control methods. Particularly, the switched reluctance motor (SRM) demonstrates broad application prospects in multi-degree-of-freedom drive systems due to its advantages of simple structure, solid robustness, and outstanding adaptability to harsh environments [1–4].

As a novel motor with potential market applications, the dual-degree-of-freedom linear-rotary SRM enables simultaneous coordinated control of rotational and linear motion within a single unit. This capability unlocks significant engineering potential in systems requiring compound motion, such as high-end intelligent manufacturing and marine power generation installations. Currently, academic research and engineering practice remain largely focused on enhancing the performance of traditional single-degree-of-freedom reluctance motors. Research on dual-degree-of-freedom linear-rotary reluctance motors is still in its preliminary exploratory phase. The theoretical and methodological frameworks for aspects such as topological configuration design and electromagnetic coupling mechanism analysis require further establishment and refinement [5–7].

References [8–10] proposed a structurally simple rotary linear switched reluctance motor (RLSRM). The motor can generate motion in two degrees of freedom: the same shaft can undergo both linear rotation and displacement. It can be used in various advanced automotive applications where available space is limited. Reference [11] introduced a novel structure for a RLSRM. It is primarily designed for engaging and disengaging rotary gears. The motor comprises a three-phase 6/4 rotary SRM and a two-phase transverse flux linear SRM. Experimental validation confirms the constructed motor's performance and applicability. Reference [12] proposes a novel direct-drive RLSRM. This motor offers advantages including robust mechanical structure, low manufacturing cost, and capability to operate in harsh environments. Reference [13] presents a linear SRM configuration for wave energy converters (WECs) with a segmented core structure, aiming to achieve higher force and efficiency. Reference [14] discusses an axial flux permanent magnet synchronous generator for buoy-type WECs. To enhance the performance of underwater WEC generators, [15] proposes a linear rotating axial flux modulator generator. To enable efficient, low-cost utilization of offshore renewable energy, [16] proposes a permanent magnet linear-rotary generator (LRG) system with a novel topology for direct-drive wave-wind hybrid energy conversion. The optimization process encompasses initial design, sensitivity analysis of optimization parameters, determination of weight factor for optimization objectives, and final decisionmaking. Results demonstrate that the proposed design and optimization effectively enhance the performance of the LRG.

The aforementioned literature has contributed various types of SRM structures, with corresponding electromagnetic simulations and experimental studies consistently validating the feasibility and effectiveness of these designs in achieving specific motion functions. Despite the clear performance advantages of these multi-degree-of-freedom structures, dual-degree-of-freedom motors capable of simultaneously outputting rotational and linear motion face inherent structural disadvantages compared to traditional single-degree-offreedom motors. The complexity of their motion mechanisms often introduces structural redundancy, leading to higher iron core material consumption and resulting in larger overall weight and volume for the motor's effective moving parts. To leverage the power density enhancement advantages of modularization, this paper innovatively proposes a novel modular linear-rotary switched reluctance machine based on the research foundation of [17].

Compared to conventional integrated cores, adopting a modular stator and rotor topology presents several distinct physical and electromagnetic advantages crucial for multidimensional drive systems. First, the segmented design eliminates redundant iron core materials, thereby substantially reducing the inertial mass of the moving components and enhancing the dynamic response speed. Second, the discrete spatial arrangement of the modules creates an open physical structure, which significantly minimizes air resistance and windage losses during high-speed operations. Ultimately, these structural

benefits synergistically reduce the overall motor weight and optimize the spatial magnetic circuit layout, culminating in a remarkable improvement in both torque density and power density. Its segmented stator-rotor structure significantly reduces motor weight, thereby improving power density. In summary, the lightweight, high-power-density motor solution proposed herein holds promise for industrial applications requiring composite motion, offering dual competitive advantages in both economic cost and overall performance.

Specifically, the research presented in this paper focuses on the conceptual design and theoretical modeling of the novel modular tubular linear rotary switch reluctance machine (TLRSRM) topology. The scope of the current work is limited to the systematic verification of the electromagnetic principles and modeling accuracy through 3D finite element analysis.

II. STRUCTURE AND OPERATING PRINCIPLE OF TLRSRM

The 3D structural model of the proposed TLRSRM is shown in Fig. 1. It can be seen that the proposed TLRSRM consists of segmented stator and rotor components. Its core structural feature lies in the configuration where 12 U-shaped stator modules and eight U-shaped rotor modules, uniformly distributed along the circumference, collectively form the motor's magnetic circuit and moving assembly. Each U-shaped stator module is equipped with a bipolar winding set, where the two coils wound on the same module possess an identical number of turns but are wound in opposite directions to establish contrary magnetic polarities. A key aspect of the winding configuration is that coils from four stator modules, which are spatially separated by 90 degrees mechanically, are connected in series to constitute one phase winding. This specific interconnection pattern is repeated to form a complete and symmetrical three-phase armature winding system, which is essential for generating the requisite rotating or travelling magnetic fields for dual-degree-of-freedom operation. The motor's magnetic circuit core (stator and rotor excitation sections) is laminated from 50DW470 silicon steel sheets to optimize magnetic permeability and control core losses. Collectively, this segmented and modular construction bestows several critical advantages. It substantially reduces the inertial mass of the moving components (primarily the rotor), which is pivotal for improving dynamic response. Furthermore, the open and segmented nature of the structure significantly diminishes air resistance or windage losses during high-speed rotation. These inherent benefits – weight reduction, lower windage loss, and optimized magnetic circuit – synergistically provide the foundational support necessary for achieving superior torque and power density outputs, which are paramount performance metrics for advanced motion control applications.

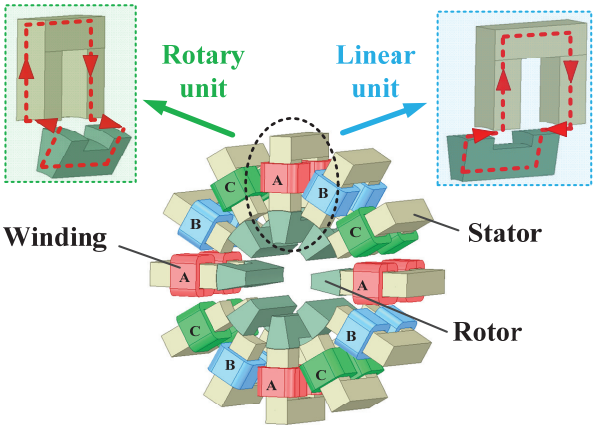


Fig. 1. 3D view of proposed TLRSRM model.

Additionally, as shown in Fig. 1, when the armature winding is energized, a distinct magnetic flux path is established within the motor. This path originates at one end of the energized U-shaped stator pole tooth. After traversing the stator pole tooth, the magnetic flux crosses the air gap radially and enters the corresponding rotor salient pole. Subsequently, the magnetic flux flows along the circumferential closed path of the U-shaped rotor core, reaching the rotor salient pole on the opposite side. It then again traverses the air gap radially, entering the adjacent stator pole. Finally, the magnetic flux forms a closed circuit through the stator back yoke, returning to the initial stator pole.

This magnetic circuit topology forms the core physical foundation for achieving dual-degree-of-freedom motion. To further clarify the dual-degree-of-freedom operating mechanism, the motion of the proposed TLRSRM is determined by the specific excitation patterns applied to the three-phase windings. For rotational motion, the phases are energized sequentially (e.g., A, B, C), generating an asymmetrical magnetic pull force circumferentially that acts on the salient poles to produce torque. Conversely, for pure linear motion, all three phases are excited simultaneously. Under this condition, the symmetrical radial forces cancel each other out entirely. The predominant axial magnetic flux then interacts with the rotor modules, generating purely axial electromagnetic forces that drive the components linearly. A summary of these phase excitation patterns is presented in Table 1.

This modular magnetic circuit and structural design offers significant advantages. First, it optimizes the magnetic path, substantially shortening the effective travel of the main magnetic flux and reducing the total magnetic resistance of the circuit.

Table 1: Phase excitation patterns for different motion types

Motion Type	Excitation Strategy	Phase Excitation Pattern (Example)	Primary Force Generated
Rotational Motion (Forward)	Sequential	A-B-C	Circumferential Torque
Rotational Motion (Reverse)	Sequential	A-C-B	Circumferential Torque
Linear Motion	Simultaneous	A, B, C	Axial Thrust
Coupled (Spiral) Motion	Sequential (while axially offset)	A-B-C	Torque + Axial Thrust

Second, the compact magnetic circuit design allows for the arrangement of more efficient magnetic materials within the same volume, achieving miniaturization and weight reduction. The direct benefits include reduced hysteresis and eddy current losses in the core material and enhanced energy conversion efficiency, ultimately manifested as a comprehensive improvement in both torque density and power density of the motor.

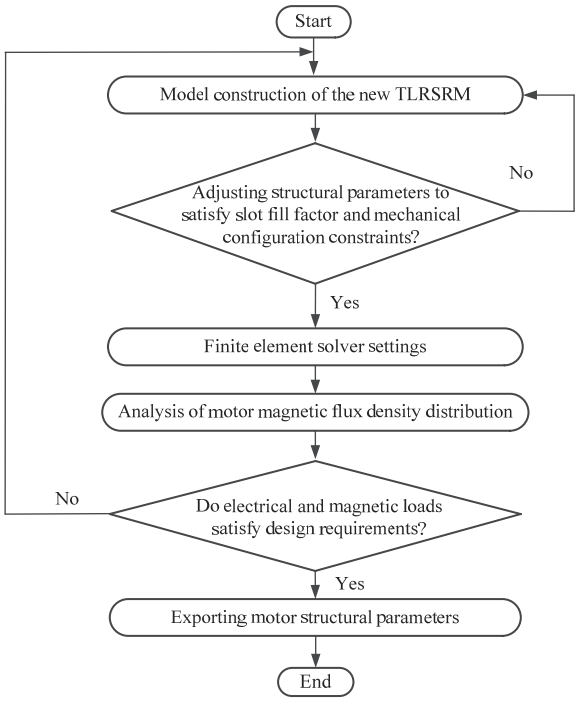


Fig. 2. Design flowchart for the new TLRSRM structure.

The initial design flowchart for the novel TLRSRM structure described in this paper is shown in Fig. 2, where the current density is no greater than 6 A/mm^2, and the slot fill factor is below 50%. Based on conventional design experience and the parameter selection criteria in Fig. 2, the initial dimensional parameters for the TLRSRM are selected and listed in Table 2.

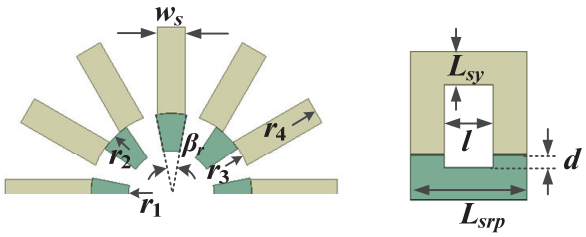


Fig. 3. Structural dimension drawing.

The main structural parameters of the DSSRM are illustrated in Fig. 3.

Table 2: Structure parameters of the TLRSRM

Parameter	Unit	Value
Stator outer diameter/r_4	mm	310
Stator inner diameter/r_3	mm	150.8
Rotor outer diameter/r_2	mm	150
Rotor inner diameter/r_1	mm	80
Rotor pole arc/β_r	deg	9
Stator pole width/w_s	mm	25
Stator yoke thickness/L_{sy}	mm	25
Stator/Rotor axial length/L_{srp}	mm	90
Stator/Rotor slot length/l	mm	38
Rotor slot depth/d	mm	10
Air gap length	mm	0.5
Number of turns per phase	/	160

To preliminarily validate the magnetic pathway and operational principles of the TLRSRM, based on the design parameters provided in Table 1, this study constructed a finite element analysis model of the TLRSRM within the ANSYS simulation environment and conducted a systematic evaluation of its electromagnetic performance. The mesh partitioning of the minimal repeating unit structure of TLRSRM is shown in Fig. 4 (a), and the B-H curve for the silicon steel material used is shown in Fig. 4 (b). Figure 5 provides a comprehensive view of the finite element model (FEM) of this motor and its magnetic field distribution characteristics during a static parameter scan with a constant current applied, specifically when a 15 A excitation current is applied to the stator winding of Phase A. Figures 5 (a) and (b) show magnetic flux density contour plots for rotational and linear motion at the misaligned position. Figure 5 (c) shows magnetic flux density contour plots for both types of motion at the aligned position. The simulations are conducted in ANSYS Maxwell 3D software using the Magnetostatic solver

to evaluate the static electromagnetic characteristics. To balance computational accuracy and speed, the gap size in the air gap is set to 1 mm, while the size of the core section is set to 10 mm.

Observation of the contour distributions indicates relatively uniform magnetic flux density across the tooth and yoke regions of both stator and rotor cores, with no significant localized saturation observed. Notably, peak flux density areas are concentrated at the pole tips near the air gap, consistent with the physical principles governing magnetic field distribution. Simulation data indicates that, throughout the entire operating cycle, the maximum magnetic flux density in the core material remains consistently below 1.8 tesla. This result not only demonstrates the full utilization of the magnetic material but also validates the rationality and feasibility of the proposed motor structure from an electromagnetic design perspective.

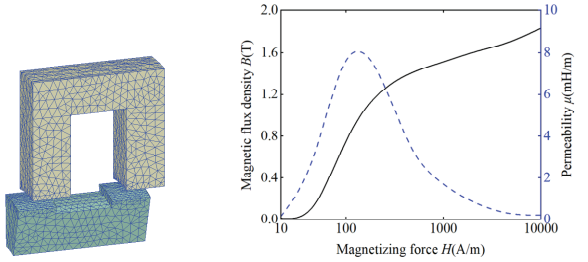


Fig. 4. Finite element mesh diagram: (a) grid division and (b) material B-H curve.

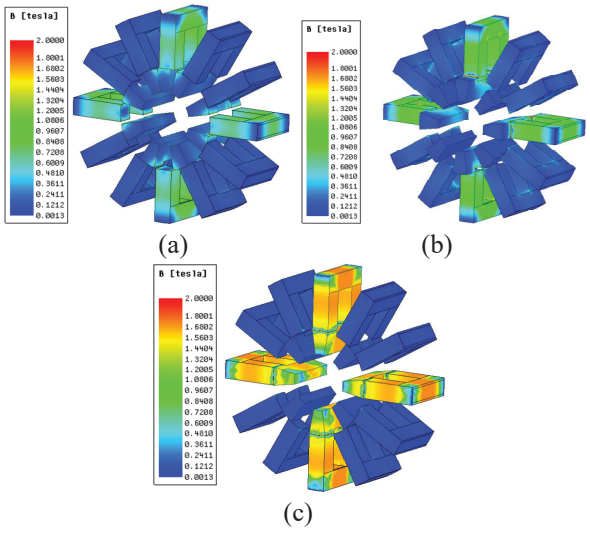


Fig. 5. FE model and magnetic field distribution of TLRSRM: (a) unaligned position in rotary motion, (b) unaligned position in linear motion, and (c) aligned position in rotary/linear motion.

III. SENSITIVITY ANALYSIS OF TLRSRM

In rotary and linear motion, electromagnetic torque and electromagnetic thrust are among the core performance metrics. Here, we present the theoretical formula using rotary motion as an example. Based on the static torque obtained at different angles through the finite element method, the average static torque of the motor can be derived from the following equation:

$$T_{\text{avg}} = \frac{1}{\theta_r} \int_0^{\theta_r} T_{\text{em}} d\theta, \tag{1}$$

where θ_r denotes the rotor pole pitch in radians and T_{em} is the electromagnetic torque. Average static torque is a key indicator for evaluating a motor's static torque output capability.

Considering that the proposed TLRSRM structure must simultaneously satisfy requirements for high average torque and low torque ripple, two objectives average static torque and static torque smoothness coefficient – are selected as optimization targets. Three parameters – rotor pole arc angle β_r, stator/rotor slot length l, and rotor slot depth d – are chosen as design variables for the optimized design of the TLRSRM. During sensitivity analysis of each structural parameter, the values of the remaining parameters under analysis remain constant, and the motor operates under rated conditions. Single-parameter sensitivity analysis for this section is shown in Fig. 6.

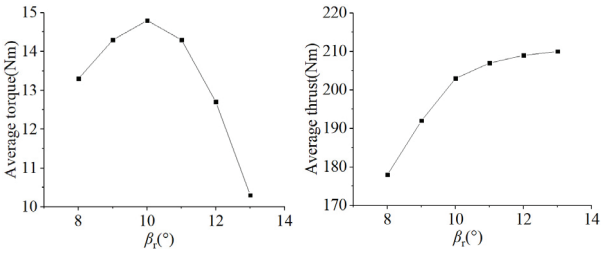


Fig. 6. Sensitivity analysis results under different rotor pole arc β_r : (a) rotary motion and (b) linear motion.

As shown in Fig. 6, the relationship curve between the average torque/thrust of the MLRSRM and the rotor pole arc angle β_r indicates that, in the rotational motion mode, the mean electromagnetic torque exhibits a non-monotonic variation pattern – first increasing and then decreasing – as the β_r angle decreases, reaching its peak at 27° of β_r. For the linear motion mode, the average electromagnetic thrust exhibits a continuously increasing trend with increasing β_r. Beyond a certain critical value, the rate of increase gradually converges. Considering all factors, 10° is ultimately determined as the optimal design parameter for the rotor pole arc.

As shown in Fig. 7, the relationship curve between the average torque/thrust of the MLRSRM and the stator/rotor slot length l indicates that, in rotational motion mode, as l increases, the average electromagnetic torque exhibits a decreasing trend, while the average electromagnetic thrust shows an increasing trend. After comprehensive consideration of all factors, 38 mm is ultimately determined as the optimal design parameter for the stator/rotor slot length.

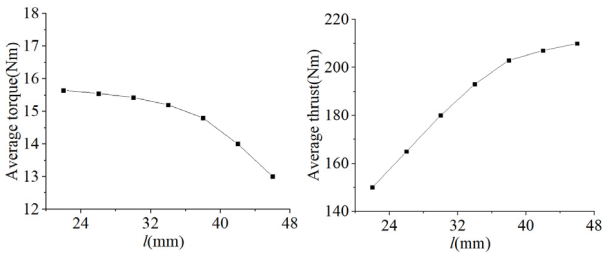


Fig. 7. Sensitivity analysis results under different stator/rotor slot length l : (a) rotary motion and (b) linear motion.

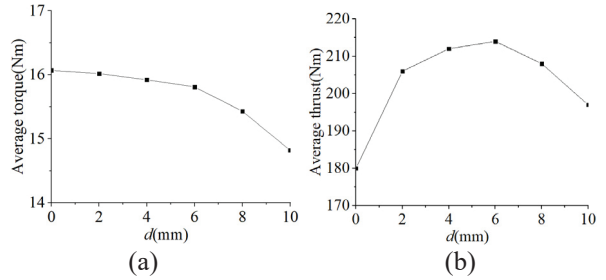


Fig. 8. Sensitivity analysis results under different rotor slot depth d : (a) rotary motion and (b) linear motion.

It can be seen from Fig. 8 that the relationship curve between the average torque/thrust of the MLRSRM and the stator/rotor slot depth d indicates: in the rotational motion mode, as d increases, the average electromagnetic torque shows a decreasing trend, while the average electromagnetic thrust first increases and then decreases. After comprehensively considering all factors, 5 mm was ultimately determined as the optimal design parameter for the stator/rotor slot depth.

It should be emphasized that identifying the final structural parameters entails a critical compromise between the rotary and linear motion capabilities. Because parameters optimal for the rotational torque frequently conflict with those optimal for the linear thrust, optimizing a single metric inevitably leads to the severe degradation of the other. Consequently, the final parameter selection adopts a balanced optimization strategy aimed at maximizing the overall dual degree of freedom performance. Specifically, the chosen values represent the optimal intersection points where the rotary torque is maintained near its peak value while the linear thrust reaches a stable high-performance plateau. This balancing philosophy ensures that the proposed motor delivers robust and symmetrical multidimensional driving forces under complex operational conditions.

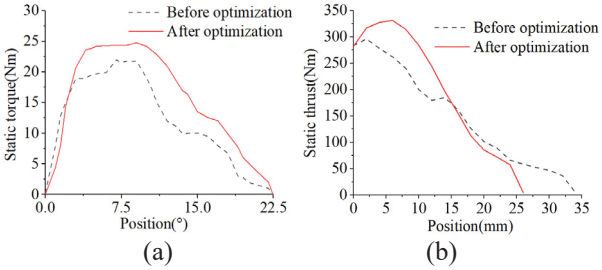


Fig. 9. Performance comparison before and after optimization: (a) static torque waveform and (b) static thrust waveform.

Based on the sensitivity analysis of the aforementioned key design parameters, Fig. 9 illustrates the comparison of the electromagnetic performance of the TLRSRM before and after parameter optimization. This is specifically demonstrated through the static torque and static thrust characteristic curves at different rotor positions. Analysis of the data in Fig. 9 reveals that the optimized motor exhibits significantly enhanced performance: its peak static torque increased by 21.6% compared to the original design, while the peak static thrust improved by 36.6%.

IV. PERFORMANCE COMPARISON OF DIFFERENT TLRSRM STRUCTURES

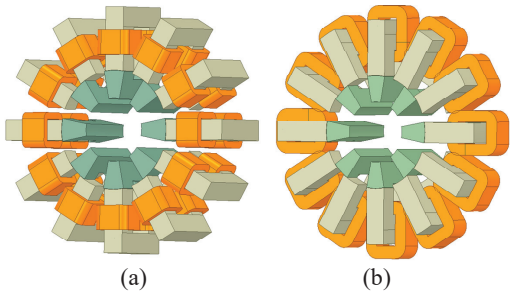


Fig. 10. Comparison of TLRSRM 3D models: (a) T-I type and (b) T-II type.

To fully evaluate the electromagnetic performance of the proposed TLRSRM structure, this section conducts a comparative analysis of two TLRSRM designs with distinct winding configurations. The 3D models of both structures are shown in Fig. 10, namely the baseline T-I type (originally presented in Fig. 1) and the proposed

T-II type. In the T-I type, the winding coils are wound on adjacent teeth of the U-shaped stator, while in the T-II type, the winding coils are wound on the stator yoke. For a fair comparison, both structures have the same number of winding-turns per phase, as well as identical motor volume and rated conditions.

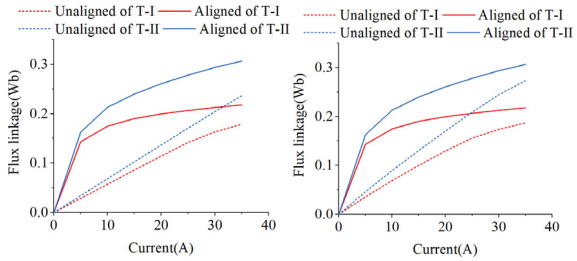


Fig. 11. Flux linkage curve: (a) rotary motion and (b) linear motion.

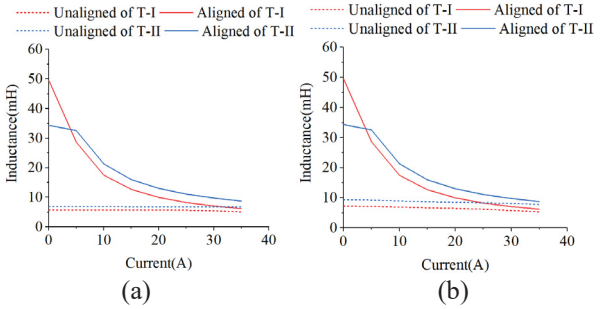


Fig. 12. Inductance curve: (a) rotary motion and (b) linear motion.

The core electromagnetic characteristics of SRMs are primarily reflected in key parameters such as magnetic flux linkage, inductance, and output torque. Figures 11 and 12 illustrate the variation patterns of magnetic flux linkage and inductance with current for a single stator pole in non-aligned and aligned positions under rotational and linear motion modes for two contrasting structures.

During the low-current excitation phase, magnetic flux in both positions increases approximately linearly with excitation current, while corresponding inductance values remain largely constant. This indicates the motor magnetic circuit operates within the linear region of the core material's magnetization curve. However, once the current exceeds a specific saturation threshold, the magnetic flux growth rate at the aligned position noticeably slows, exhibiting nonlinear saturation characteristics, while its inductance value simultaneously decreases significantly. In stark contrast, the magnetic flux and inductance characteristics at the non-aligned position show no significant changes across the entire current range, consistently maintaining a good linear relationship.

The fundamental cause of this difference lies in the varying magnetic resistance within the circuit. At the aligned position, magnetic flux concentrates through the stator and rotor poles, forming a low-resistance path that rapidly increases local magnetic flux density in the core. When current increases to saturate the silicon steel laminations (typically within the 1.8–2.0 T range), the material's permeability decreases and magnetic resistance increases, triggering nonlinear changes in magnetic flux linkage and inductance. In the nonaligned position, however, the air gap magnetic resistance remains dominant, resulting in a lower magnetic flux density level in the core. Consequently, it is difficult for the core to reach saturation.

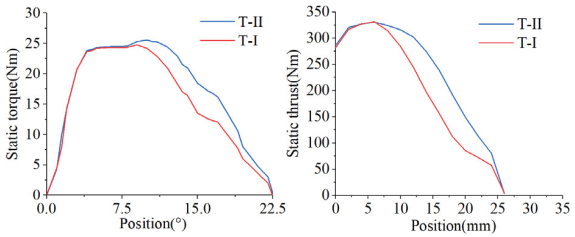


Fig. 13. Static torque/thrust curve: (a) rotary motion and (b) linear motion.

Figure 12 shows the static torque/thrust variation waveforms for the T-I and T-II structural types at a rated current of 15 A. The static torque and thrust for TI are 15.8 Nm and 213 Nm, respectively; T-II exhibits higher static torque and thrust values of 17.6 Nm and 240 Nm. The data indicates that T-II exhibits an 11.52% increase in static torque and a 12.68% increase in static thrust, compared to T-I. These results demonstrate that the structure with windings wrapped around the stator yoke exhibits superior electromagnetic performance compared to the structure with windings wrapped around the stator pole positions. The ripple percentage (K_{ripple}) is defined and calculated as follows:

$$K_{ripple} = \frac{X_{max} - X_{min}}{X_{avg}} \times 100\%, \tag{2}$$

where X_{max}, X_{min}, and X_{avg} represent the maximum, minimum, and average values of the electromagnetic torque (or thrust) over the effective conduction interval.

To address the critical aspect of motion stability, this section further evaluates the static smoothness coefficient for both structural types. Because the proposed analysis focuses on static characteristics, the static torque ripple of the output torque and thrust over the effective conduction zone is adopted as the smoothness

metric. Analyzing the flat-top region spanning from 5° to 17.5° for the rotary mode, the T-II configuration yields a smaller static torque ripple of 42.2% compared to the 64.0% of the T-I configuration. Similarly, within the linear conduction interval from 3 mm to 17.5 mm, the extended high thrust plateau of the T-II structure results in a reduced static thrust ripple of 54.5% contrasting with the 85.7% of the T-I design. The data indicates that winding the coils around the stator yoke effectively diminishes output fluctuations, thereby providing superior motion smoothness for complex multidimensional drive applications.

V. CONCLUSION

This paper proposes a novel TLRSRM employing a modular stator-rotor design. Its electromagnetic characteristics and structural parameter sensitivity were systematically investigated through three-dimensional finite element analysis. Simulation results demonstrate that this topology effectively achieves dual-degree-offreedom rotational and linear motion, with a rational magnetic field distribution and core magnetic flux density consistently maintained within safe limits. Parameter sensitivity analysis identified optimal solutions for critical dimensions such as rotor pole arcs. Post-optimization, static torque and thrust increased by 21.6% and 36.6%, respectively. Further comparison of two winding configurations (T-I and T-II) revealed that the T-II structure with yoke windings outperformed the T-I type with pole windings in both static torque and thrust, achieving improvements of 11.52% and 12.68%, respectively. The proposed TLRSRM structure demonstrates significant advantages in integration, power density, and output performance, offering a viable new solution for high-performance multi-degree-of-freedom drive systems.

ACKNOWLEDGMENT

This work is supported by the National Natural Science Foundation of China International (regional) cooperation and exchange projects NSFC-RSF under Grant W2412064 and the Shenzhen Collaborative Innovation Special Plan International Cooperation Research Project under Grant GJHZ20240218114300002.

REFERENCES

[1] H. Chen, R. Nie, and X. Li, "A transverse-flux single-phase tubular switched reluctance linear machine with 4 poles," *IEEE Transactions on Applied Superconductivity*, vol. 31, no. 8, pp. 1–4, Nov. 2021.

[2] K. Manohar and K. Srichandan, "Analysis of quadrupole magnetic field reluctance-based launcher with different coil switching patterns," *IEEE Transactions on Plasma Science*, vol. 51, no. 5, pp. 1370–1376, May 2023.

[3] L. Zhang, L. Yan, X. Wei, H. Su, Z. Dong, and L. Li, "Stress analysis of a flat linear switched reluctance motor with double excitation windings," in *CSAA/IET International Conference on Aircraft Utility Systems*, Nanchang, China, pp. 1240–1245, 2022.

[4] W. Ding, H. Fu, and Y. Hu, "Characteristics assessment and comparative study of a segmented-stator permanent-magnet hybrid-excitation SRM drive with high-torque capability," *IEEE Transactions on Power Electronics*, vol. 33, no. 1, pp. 482–500, Jan. 2018.

[5] R. Nie, J. Si, Y. Jia, P. Wang, S. Xu, and J. Liang, "Comprehensive comparison of mover-PM and stator-PM linear-rotary generators for wind-wave combined energy conversion system," *IEEE Transactions on Industry Applications*, vol. 60, no. 4, pp. 6170–6185, July-Aug. 2024.

[6] H. Chen, Y. Zhan, and R. Nie, "Multiobjective optimization design of single-phase tubular switched reluctance linear launcher," *IEEE Transactions on Plasma Science*, vol. 47, no. 5, pp. 2431–2437, May 2019.

[7] H. Chen, R. Nie, and H. Wang, "A transverse flux single-phase tubular-switched reluctance linear launcher with eight-pole structure," *IEEE Transactions on Plasma Science*, vol. 47, no. 5, pp. 2331–2338, May 2019.

[8] L. Szabó, I. Benţia, and M. Ruba, "A rotary-linear switched reluctance motor for automotive applications," in *2012 XXth International Conference on Electrical Machines*, Marseille, France, pp. 2615–2621, 2012.

[9] I. Benţia, L. Szabó, and M. Ruba, "On a rotary-linear switched reluctance motor," in *International Symposium on Power Electronics Power Electronics, Electrical Drives, Automation and Motion*, Sorrento, Italy, pp. 507–510, 2012.

[10] I. Benţia, M. Ruba, and L. Szabó, "On the control of a rotary-linear switched reluctance motor," in *2011 5th International Symposium on Computational Intelligence and Intelligent Informatics*, Floriana, Malta, pp. 41–46, 2011.

[11] W. Wu, J. B. Dunlop, S. J. Collocott, and B. A. Kalan, "Design optimization of a switched reluctance motor by electromagnetic and thermal finite-element analysis," *IEEE Transactions on Magnetics*, vol. 39, no. 5, pp. 3334–3336, Sep. 2003.

[12] J. F. Pan, N. C. Cheung, and G.-Z. Cao, "Investigation of a rotary-linear switched reluctance motor," in *The XIX International Conference on Electrical Machines – ICEM 2010*, Rome, Italy, pp. 1–4, 2010.

[13] L. García-Tabarés, M. Lafoz, M. Blanco, J. Torres, D. Obradors, J. Nájera, G. Navarro, F. García,

and A. Sánchez, "New type of linear switched reluctance generator for wave energy applications," *IEEE Transactions on Applied Superconductivity*, vol. 30, no. 4, pp. 1–5, June 2020.

[14] R. R. Sattarov and T. Ziganshin, "Axial-flux permanent magnet synchronous generator for float buoy type wave energy converters," in *2019 Dynamics of Systems, Mechanisms and Machines*, Omsk, Russia, pp. 1–6, 2019.

[15] L. Huang, Y. Li, L. Wei, and M. Chen, "Comparison research on axial flux modulation generators for linear-rotary wave energy conversion," in *2022 IEEE 20th Biennial Conference on Electromagnetic Field Computation*, Denver, CO, USA, pp. 1–2, 2022.

[16] R. Nie, J. Si, P. Wang, Z. Li, J. Liang, and C. Gan, "Optimization design of a novel permanent magnet linear-rotary generator for offshore wind-wave combined energy conversion based on multi-attribute decision making," *IEEE Transactions on Energy Conversion*, vol. 39, no. 3, pp. 1583–1600, Sep. 2024.

[17] H. Chen, X. Wang, C. Liu, M. F. Shamiyev, A. O. Pulatov, and A. Musolino, "Design of a three-phase high torque density modular linear rotary switched reluctance launcher," *IEEE Transactions on Plasma Science*, vol. 53, no. 10, pp. 2653–2661, Oct. 2025.



Hao Chen (SM'08) received the B.S. and Ph.D. degrees from the Department of Automatic Control, Nanjing University of Aeronautics and Astronautics, Nanjing, China, in 1991 and 1996, respectively. In 1998, he became an Associate Professor with the School of Information and Electrical Engineering, China University of Mining and Technology, Xuzhou, where he has been a Professor since 2001. From 2002 to 2003, he was a Visiting Professor at Kyungsung University, Busan, Korea. Since 2008, he has also been an Adjunct Professor at the University of Western Australia, Perth, Australia. He is the author of one book and has also authored more than 190 papers. He is the holder of 15 US Patents, 23 Australian Patents, one Danish Patent, seven Canadian Patents, three South African Patents, 10 Russian Patents, 86 Chinese Invention Patents, and six Chinese Utility Model Patents. His current research interests include motor control, linear launcher, electric vehicles, electric traction, servo drives, and wind power generator control.

Chen was the recipient of both the Prize of Science and Technology of Chinese Youth and the Prize of the Fok Ying Tong Education Foundation for Youth Teachers both in 2004. He was awarded the first prize in the Science and Technology advanced of Province and Ministry once, the second prize in the Science and Technology advanced of Province and Ministry seven times, and the third prize in the Science and Technology advanced of Province and Ministry 14 times. He became the Chinese New Century Hundred-Thousand Ten-Thousand Talents Engineering National Talent in 2007, and won the Government Especial Allowance of People's Republic of China State Department since 2006.



Cheng Liu received the B.S. degree in electrical engineering and automation from Hubei University of Technology, Wuhan, Hubei, China, in 2020, and the M.S. degree in electrical engineering from Hubei University of Technology, Wuhan, Hubei, in 2023. He is currently pursuing a Ph.D. degree in electrical engineering at China University of Mining and Technology, Xuzhou. His research interests include switched reluctance motor design control, ocean wave power generation, and electric vehicles.



Marcin Wardach was born in Poland in 1980. He graduated and received the Ph.D. degree from the Electrical Department, Szczecin University of Technology, Szczecin, Poland, in 2004 and 2009, respectively. From 2020 until now, he has been an Associate Professor with the Faculty of Electrical Engineering, West Pomeranian University of Technology in Szczecin. Since 2024, he has served as Vice-Dean for Organization and Development and Head of the Department of Electrical Machines and Drives at the Faculty of Electrical Engineering, West Pomeranian University of Technology in Szczecin. From 2019 to 2025, he worked as an electrical machine designer at mPower Sp. z o.o. company. His research interests include the design of electrical machines and drives, especially unconventional and hybrid excited. He is the author of over 100 scientific papers and post-conference publications. Since 2022, he has been the President of the Szczecin Branch of the Association of Polish Electrical Engineers (SEP). He is also a member of the Polish Society of Theoretical and Applied Electrical Engineering.



Javokhir Toshov currently works at the Department of Mining Electromechanics, Tashkent State Technical University, Uzbekistan. Toshov does research in Mechanical Engineering and Mining Engineering. Department of Electronic Devices Manufacturing Technologies, Faculty of Electronic and Automation Engineering, Tashkent State Technical University, Tashkent 100095, Department of Theoretical and Experimental Physics, Faculty of Physics, Karshi State University, Karshi 180119.



Xing Wang received the B.S. degree from China University of Mining and Technology, Xuzhou Jiangsu, China, in 1996, and M.S. degree from China University of Mining and Technology, Xuzhou Jiangsu, in 1999. In 2007, she became an Associate Professor with China University of Mining and Technology, Xuzhou. She is a holder of four US Patents, nine Australian Patents, two Canadian Patents, four Russian Patents, 12 Chinese Invention Patents, three Chinese Utility Model Patents, and has authored 15 papers.



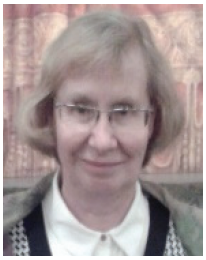
Ali Asghar Memon is professor in Electrical Engineering at Mehran University of Engineering and Technology Jamshoro, Pakistan. He holds B.E and M.E in Electrical Engineering from Mehran University and Ph.D. from University of Leeds, UK. Memon is head of Electrical Machine and Drives group at Mehran University. He has been member of National Curriculum Review Committee in Pakistan. Memon has served as an expert evaluator for National Research Project for Universities (NRPU), post doc fellowship and project(s) under Technology Development Fund (TDF), under Higher Education Commission (HEC), Government of Pakistan. Memon is a keynote speaker and reviewer of prestige international research journals. Memons interests include modeling and simulation of switched reluctance machines and inverters.



Bodrenkov Evgenii Alexandrovich received the B.S. and M.S. degrees from Federal State Budgetary Educational Institution of Higher Education Amur State University, and Ph.D. degree from Federal State Autonomous Educational Institution of Higher Education Peter the Great St. Petersburg Polytechnic University.



Nikolay Korovkin (Member, IEEE) received the M.S., Ph.D., and doctorate degrees in electrical engineering from the State Polytechnic University, Saint Petersburg, Russia, in 1977, 1984, and 1995, respectively. He is currently a Professor with the Institute of Energy, Peter the Great Saint Petersburg Polytechnic University, Saint Petersburg. Since 1996, he has been an Academician with the Academy of Electrotechnical of Russian Federation, Saint Petersburg. He has about 300 published and reviewed works in Russia and abroad. His main research interests include the inverse problems in electromagnetics, systems described by stiff equations, ill conditioned problems, optimization of power networks, optimization of the location FACTS and PMU-devices, SMART grid technologies, methods for the analysis of reliability and ensuring power balance in EPS, methods of multicriteria optimization and their application to steady-state processes in power networks, transients in transmission line systems, impulse processes in linear and nonlinear systems, problems of the electromagnetic prediction of earthquakes, and identification of the behavior of the biological objects under the influence of the electromagnetic fields.



Sakhno Liudmila (Member, IEEE) received the B.S., M.S., and Ph.D. degrees from Russia Polytechnic Institute, Saint Petersburg, Russia, in 1972, 1974, and 1982, respectively, and the doctorate in electromechanics and electrical apparatus from St. Petersburg State Technical University, Saint Petersburg, in 2006. She is currently a Professor of Higher School of High Voltage Power Engineering, Peter the Great Saint Petersburg

Polytechnic University, Saint Petersburg. She has about 200 published and reviewed works in Russia and abroad. Her research interests include electromagnetic problems in power transformers, the skin effect and proximity effect in windings of converter transformers, electromagnetic and thermal characteristics of arc and resistance welding transformers, mechanical strength of structural elements under the action of loads, and field-circuit modeling in high frequency resistance spot welding systems. She obtained eight Russian Federation Patents.



Emmanuel Karapidakis is an Electrical and Computer Engineer. He was Dean at School of Engineering from 2019 to 2025, and Director of Energy, Environment and Climate Change Institute – IEECC (ieecc.hmu.gr) in Hellenic Mediterranean University – HMU (hmu.gr). Since 2022, he is President of the Board in Hellenic Association of Electricity Storage Systems – HAESS (www.haess.gr). His research interests focus on energy systems, power systems operation, diverse & dispersed generation, micro-grids, renewable energy technologies, energy storage, and energy markets. He is/was scientific coordinator (PI) in 12 European financed projects, 15 National programs, and several private funded projects, with more than 8 million euros in total. He has published more than 120 papers (Scopus Author ID 6506872824) in prestigious journals and scientific conferences, and four scientific book chapters. From 2011 to 2015, he was Member of the Board in Regional Council of Innovation, and from 2015 to 2017, Member of Board in Energy Planning Council at Region of Crete.



Aris Dimeas is an Assistant Professor at the School of Electrical and Computer Engineering of the National Technical University of Athens (NTUA), with more than 20 years of experience in power systems operation, smart grids, and energy system digitalization. His expertise spans distribution and transmission system operation, renewable energy integration, microgrids, flexibility markets, artificial intelligence applications, and advanced control and decision-support software. He has played a leading technical and coordination role in more than 30 EU-funded research and innovation projects (H2020 and Horizon Europe), collaborating closely with TSOs, DSOs, regulators, industry, and the European Commission. His work bridges research and real-world deployment, with demonstrated impact on system supervision, resilience, market design, and data-driven grid operation, while his scientific contributions include high-impact publications in leading IEEE and international journals.



Sherif Moussa is Dean of the School of Engineering, Applied Science, and Technology at the Canadian University Dubai (CUD), UAE. He earned his Ph.D. in Electrical and Computer Engineering from the University of Québec at Trois-Rivières, Canada, and his M.Sc. in Electrical and Computer Engineering from the University of Waterloo, Canada. Since joining CUD in 2007, Moussa has led the School's remarkable growth, overseeing the launch and accreditation of several engineering and computing programs, including Mechatronics Engineering, Computer Science, Cybersecurity, Software Design, Power and Renewable Energy Engineering, and the M.Sc. in Artificial Intelligence. His leadership has also advanced international collaborations, notably with Queen's University and the University of Ottawa, and strengthened CUD's engagement with industry partners in emerging technologies. Moussa's research interests span wireless communication, computer networks, machine learning, and digital systems design. He has published widely in international journals and conferences, serves on technical committees, and is the recipient of the 2015 CUD Research Excellence Award. He is also the founder of CUD's Robotics Club and a strong advocate for innovation and experiential learning in engineering education.



Habes Ali Khawaldeh (Member, IEEE) received the B.E. degree in electrical and computer engineering from The Hashemite University, Jordan, in 2009, and the M.S. degree in electrical power engineering from Yarmouk University, in 2013. In 2022, Habes Ali Khawaldeh received his Ph.D. degree in power electronics engineering from the Faculty of Engineering and Information Technology, University of Technology Sydney (UTS), Australia. Since 2018, he has been a Casual Academician with UTS for various power electronics subjects. Since July 2009, he has been working as an electrical engineer with different companies in Jordan. He was a part-time Faculty Member with Yarmouk University for various power electronics subjects. He was

a full-time Faculty Member with Al-Hussein Bin Talal University from 2015 to 2018. His current research interests include renewable energy (RE) systems, power converter design for RE applications, battery systems, multi-port DC/DC converters, and energy conversion systems for the smart grid. He received a Grant from Al al-Bayt University for his Ph.D. degree. He is currently a reviewer for several IEEE, IET, and Elsevier journals. Currently, Habes Ali Khawaldeh is an assistant professor at the University of Al al-Bayt in Jordan.

Design and Electromagnetic Analysis of Stator-Modular Tubular Linear Rotary Machine

Hao Chen[1,2,3,4*], Cheng Liu[1], Marcin Wardach[5], Javokhir Toshov[6], Xing Wang[2,3*], Ali Asghar Memon[7], Bodrenkov Evgenii Alexandrovich[8], Popov Stanislav Olegovich[8], Nikolay Korovkin[8], Sakhno Liudmila[8], Emmanuel Karapidakis[9], Aris Dimeas[10], Sherif Moussa[11], and Habes Ali Khawaldeh[12]

[1]School of Electrical Engineering
China University of Mining and Technology, Xuzhou 221116, China
hchen@cumt.edu.cn, Chengliu97@cumt.edu.cn

[2]Shenzhen Research Institute
China University of Mining and Technology, Shenzhen 515100, China
3512@cumt.edu.cn

[3]Jiangsu Province Foreign Expert Workshop on New Energy Power Generation and Electric Transportation
Xuzhou 221008, China

[4]International Joint Research Center of Central and Eastern European Countries on
New Energy Electric Vehicle Technology and Equipment
Xuzhou 221008, China

[5]Department of Electrical Machines and Drives
West Pomeranian University of Technology, Sikorskiego 37, 70-313 Szczecin, Poland

[6]Tashkent State Technical University
University Street No2, 100095 Tashkent, Uzbekistan

[7]Mehran University of Engineering and Technology
Department of Electrical Engineering, Jamshoro, Pakistan

[8]The Institute of Energy
Peter the Great Saint Petersburg Polytechnic University, Saint Petersburg, Russia

[9]School of Engineering
Hellenic Mediterranean University, Estavromenos Campus,71004 Heraklio, Crete, Greece

[10]Athens National University of Technology
Greece

[11]School of Engineering
Canadian University Dubai, 117781, Sheikh Zayed Road, Dubai, United Arab Emirates

[12]The Renewable Energy Engineering Department
Faculty of Engineering, Al al-Bayt University, Mafraq, Jordan
*Corresponding author

Abstract – This paper proposes a novel modular stator 6-pole tubular linear rotary switch reluctance machine (TLRSRM). The proposed structure employs circumferentially distributed H-shaped stator modules, with each module's four poles wound with concentrated windings. The outer stator pole windings and outer rotor form a three-phase radial magnetic circuit driving rotational motion, while the inner stator pole windings and inner rotor constitute a single-phase transverse magnetic circuit driving linear motion. This paper elucidates

Submitted On: January 16, 2026
Accepted On: June 12, 2026

1054-4887 © ACES

https://doi.org/10.13052/2026.ACES.J.410602

the motor's operating principle and electromagnetic design process. Based on the three-dimensional magnetic field distribution characteristics, finite element analysis (FEA) was employed for three-dimensional magnetic field calculations to obtain flux linkage and torque characteristics. Additionally, the electromagnetic coupling effects between rotational and linear motions were investigated for the conjugate rotary-linear magnetic circuit within the modular stator. Simulation results indicate minimal electromagnetic coupling effects in the proposed TLRSRM structure. This study provides a robust theoretical foundation and empirical data support for further optimization and practical application of this motor topology.

Index Terms – 3D finite element model, magnetic field distribution, static electromagnetic characteristics, switched reluctance machine.

I. INTRODUCTION

With the advancement of industrial automation and the growing utilization of integrated ocean energy systems (e.g., hybrid offshore wind and wave energy conversion), there is an increasing demand for drive systems with enhanced functional integration and multi-axis motion control capabilities. Conventional single-degree-of-freedom electric motors exhibit inherent constraints, including limited operational flexibility, cumbersome mechanical arrangements, and suboptimal spatial efficiency, which restrict their applicability in sophisticated working environments. In response to these challenges, multi-degree-of-freedom motor architectures have gained prominence as a cutting-edge research domain, characterized by their compact modular construction, multifunctional operation, and adaptable kinematic control. Among various machine types, the switched reluctance motor (SRM) has become a potential choice for multi-degree-of-freedom drive applications, owing to its mechanical simplicity, operational ruggedness, and reliable performance under demanding conditions [1–4].

The two-degree-of-freedom linear-rotary SRM represents an emerging motor category with promising practical implications. This configuration achieves synchronized rotational and translational movements within a unified electromagnetic structure, thereby creating new possibilities for advanced applications requiring complex motion patterns, such as precision industrial automation and marine power generation equipment. Nevertheless, current research efforts continue to concentrate predominantly on performance refinement of conventional single-degree-of-freedom reluctance machines. Investigations into two-degree-of-freedom linear-rotary variants remain at an early developmental stage, with fundamental aspects including topological synthesis and electromagnetic interaction mechanisms necessitating further systematic investigation and theoretical consolidation [5–7].

Two-degree-of-freedom motors can be categorized into coaxial and non-coaxial structural types based on the relationship between their rotational and linear motion axes. Regarding coaxial configurations, [8–10] report a structurally simplified rotary-linear SRM. Its distinctive feature lies in simultaneously achieving rotational motion and axial displacement via a single shaft, offering a novel drive solution for advanced automotive applications with stringent spatial constraints. Reference [11] proposes a rotating linear switched reluctance motor (RLSRM) specifically designed for gear engagement/disengagement control. This innovative design integrates a three-phase 6/4 rotary reluctance unit with a two-phase transverse flux linear reluctance unit. Experimental studies validate its operational performance and engineering applicability. Reference [12] further developed a three-phase modular linear-rotary switched reluctance motor (MLRSRM) for electromagnetic launch applications. Its segmented stator-rotor design not only reduces motor mass but also optimizes magnetic circuit efficiency, significantly enhancing torque density through improved material utilization. Finite element simulation systems evaluated the device's static and dynamic characteristics.

Regarding non-coaxial structures, [13] developed a dual-degree-of-freedom SRM with decoupled rotational and linear motion mechanisms. Its innovation lies in employing a disc-type dual-rotor 12-slot 10-pole structure for rotational motion, while an external tubular magnetic ring assembly achieves linear drive. Both winding systems can be independently controlled. Addressing the application requirements of wave-wind combined power generation systems (WWCPGS), [14] proposes a linear-rotary permanent magnet generator (LRPMG). Key electromagnetic parameters, including three-phase counter-EMF, output voltage, air gap magnetic flux density distribution, and external characteristics, are systematically analyzed using finite element methods.

Although existing research has developed various configurations of two-degree-of-freedom motors and validated their feasibility in achieving composite motion functions through electromagnetic simulation and experimentation, such motors face inherent structural limitations despite their performance advantages. Compared to traditional single-degree-of-freedom motors, two-degree-of-freedom structures capable of simultaneously outputting rotational and linear motion often suffer from configuration redundancy due to increased mechanical

complexity. This redundancy leads to higher iron core material consumption, consequently increasing the overall mass and volume of moving components.

Based on the research in [12, 13], this paper innovatively proposes a linear-rotary SRM employing a modular stator design. This structure effectively reduces the overall motor weight through the modular integration of stator units, thereby significantly enhancing the system's power density.

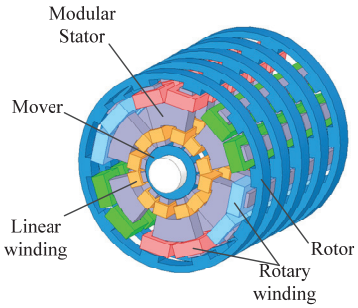
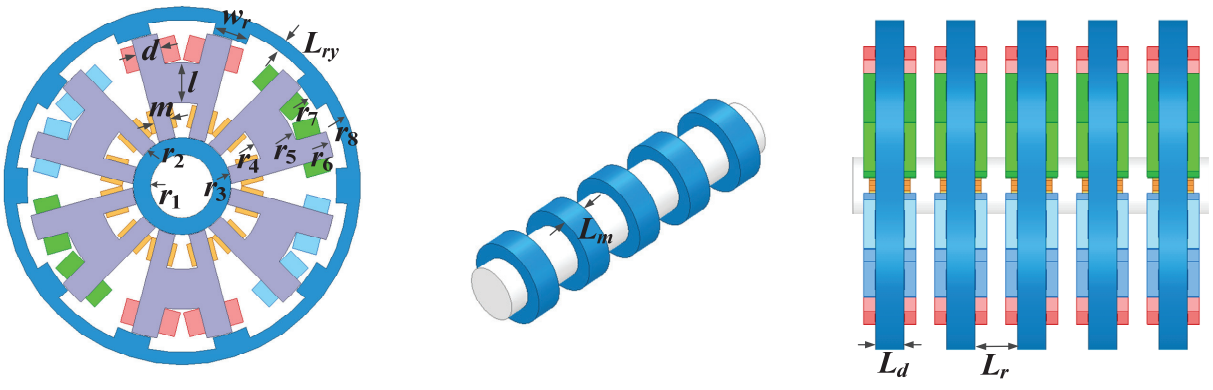


Fig. 1. 3-D views of proposed TLRSRM model.

II. STRUCTURE AND OPERATING PRINCIPLE OF TLRSRM

Building upon existing research and addressing the application requirements of two-degree-of-freedom composite motion motors, this paper proposes a novel modular stator 6-pole cylindrical linear rotary switch reluctance motor (TLRSRM). This TLRSRM inherits the typical characteristics of SRMs, with its cross-sectional structure closely resembling that of traditional rotary SRMs. The rotor is assembled within the space enclosed by stator modules, maintaining an air gap with the stator. Both the stator and rotor magnetic paths are constructed by stacking 50DW470 silicon steel sheets with excellent magnetic permeability. Figure 1 displays the 3D model of the TLRSRM. Figure 2 presents views of the TLRSRM from different angles. Figure 2 (a) shows a cross-sectional view of the TLRSRM, Fig. 2 (b) depicts the rotor structure, and Fig. 2 (c) illustrates the side view of the ferromagnetic ring arrangement. The stator of the TLRSRM comprises six H-shaped modular units. Each H-shaped unit features four magnetic poles, with windings wrapped around each pole. Windings on adjacent poles exhibit opposite polarity. In the symmetrical pair of H-shaped stator modules, windings on the two pole teeth facing away from the axis are connected in series. This configuration forms one phase of the three-phase rotating winding, driving rotational motion. The windings on the two pole teeth facing the axis in all H-type module stators are connected to form one phase for single-phase linear drive. As a single-phase configuration, its feeding mechanism does not involve multi-phase commutation. Instead, it relies on a single-channel pulsed direct current (DC) excitation. This excitation is strictly synchronized with the real-time axial position of the mover rings to maximize the electromagnetic pull towards the alignment position. The rotor of the TLRSRM consists of a non-magnetic central shaft and ferromagnetic rings uniformly mounted at specific intervals around the central shaft. Specifically, the axial spacing distance between adjacent ferromagnetic rings (denoted as L_r) is designed to be 25 mm, as listed in Table 1. This specific interval is a critical structural parameter, as it dictates the periodic variation of the transverse magnetic reluctance and directly governs the generation and magnitude of the axial thrust force. This rotor design features a simple structure, facilitates easy assembly, and is straightforward to manufacture. The non-magnetic central shaft, which provides structural support, can be fabricated from aluminum, contributing to reduced overall weight and lower production costs. This phase-splitting design enables the motor



(a) (b) (c)

Fig. 2. Multi-angle views of TLRSRM: (a) cross-sectional split diagram, (b) movers assembly drawing, and (c) side view of ferromagnetic ring arrangement.

to independently control rotational and linear motion, achieving a dual-axis output structure where the inner rotor handles linear displacement and the outer rotor performs rotational motion. The proposed TLRSRM features quadrant operation capability, functioning both in electric drive mode and power generation mode. It holds broad application prospects in fields requiring composite motion control, such as industrial smart manufacturing equipment and ocean energy power generation systems.

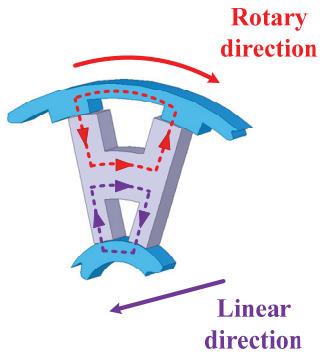


Fig. 3. Schematic diagram of magnetic circuit flow path.

As illustrated in the structural breakdown in Fig. 2, the proposed TLRSRM utilizes an H-shaped stator module where the outer poles govern rotary motion and the inner poles are dedicated to linear motion. Figure 3 further elucidates the three-dimensional magnetic flux flow paths within a single H-type stator unit. In the rotational motion mode, the magnetic flux generated by the outer rotary windings flows radially and forms a closed loop circumferentially through the outer rotor and the stator yoke. This radially configured annular magnetic circuit generates a tangential electromagnetic force in the air gap, driving the outer rotor components to rotate.

Conversely, the generation of axial thrust force relies on a distinctly different transverse flux mechanism. As depicted by the flow paths in the inner section of Fig. 3, when the inner linear windings are excited, the magnetic flux travels radially through the inner H-stator poles and then closes its path axially through the stator yoke and the inner rotor. Crucially, as shown in Figs. 2 (b) and (c), the inner rotor consists of discrete ferromagnetic rings separated by non-magnetic spaces along the axial direction. Driven by the principle of minimum magnetic reluctance, this transverse flux distribution within the inner stator-rotor air gap generates a strong axially acting electromagnetic force. This thrust force pulls the nearest inner rotor ferromagnetic rings into alignment with the excited stator poles, thereby propelling the central shaft in a linear displacement.

The H-shaped stator-modular design employed in the TLRSRM enables the magnetic flux to form a closed circuit along a more compact path during motor operation. This structural feature not only effectively reduces the total magnetic resistance of the magnetic circuit but also significantly enhances the utilization efficiency of the core material. The combined effects of shortened magnetic circuit length and reduced magnetic resistance effectively improve the motor's torque output capability and power density.

Furthermore, to accommodate continuous rotational motion exceeding 360° (such as in wind energy conversion applications), the mechanical connection between the inner and outer moving components, as well as the layout of the stator conductors, requires specific engineering considerations. In practical implementation, the inner central shaft and the outer rotor are mechanically coupled via a rigid connecting flange on one side of the machine. Consequently, the modular stator is supported by a stationary cantilever structure from the opposite side. This single-sided support configuration ensures that the coupled movers can rotate freely without interfering with the stator supports. Crucially, the stationary cantilever support provides a dedicated hollow pathway for safely routing the power conductors to the inner and outer stator windings. To ensure the mechanical robustness of this cantilevered construction under operational vibrations and radial magnetic pulls, high-strength structural materials and heavy-duty precision bearings must be employed at the single-sided support end.

III. DESIGN PROCESS OF TLRSRM

The design process for the novel TLRSRM proposed in this paper is illustrated in Fig. 4. Considering that rotational and linear motion follow similar electromagnetic principles, this study establishes a corresponding mathematical model using rotational motion as an example. Based on the law of conservation of energy and Faraday's law of electromagnetic induction, the terminal voltage across each stator phase winding can be described by the combined effects of resistance voltage drop and the induced electromotive force generated by magnetic flux variation. Accordingly, the terminal voltage equation for the k th phase winding of the motor can be expressed as [12]:

$$U_s = i_k R + \frac{d\psi_k}{dt}, \tag{1}$$

where U_s is winding voltage, i_k and Ψ_k represent the winding current and magnetic flux generated in the kth phase winding of the generator, respectively, and R is the stator resistance.

Due to the double-convex pole structure of the SRM, when a large excitation current is applied, the core saturation causes its electromagnetic characteristics to exhibit nonlinearity. Magnetic flux and inductance are

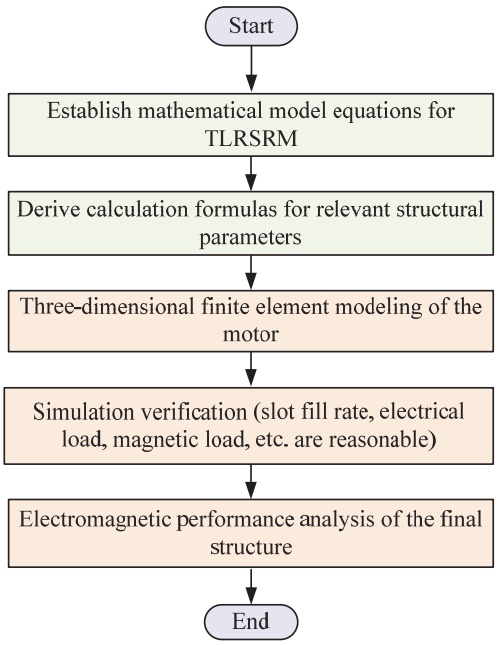


Fig. 4. Design flowchart for the new TLRSRM structure.

functions of both current and rotor position. Magnetic flux can be calculated as the product of the winding inductance and current, as shown in Equation (2)

$$\psi_k(i,\theta) = L_k(i,\theta) i_k, \tag{2}$$

where θ is the position of the rotor and L_{k} is the winding inductance of the kth phase.

When the stator and rotor are aligned, the expression for the single-phase flux linkage is

$$\psi = L_a i = B_{\mathrm{sp}} A_{\mathrm{sp}} N_{\mathrm{ph}}, \tag{3}$$

where L_{a} is inductance at the alignment position, B_{sp} is the average magnetic density of the surface of the stator pole section at the aligned position, initially assumed to be 1.8 T,A_{sp} is the overlapping cross-sectional area of the stator and rotor poles, and N_{ph} is the number of windings turns per phase of the motor.

Integrating equation (2) results in the expression for the magnetic co-energy of the winding

$$W_m(i,\theta) = \int_0^i \psi(i,\theta)\mathrm{d}i. \tag{4}$$

By performing the partial derivative of magnetic co-energy W_{m} at any operating position θ, the electromagnetic torque of the motor can be obtained. Its calculation equation is [13]

$$T(i,\theta) = \left.\frac{\partial W_m(i,\theta)}{\partial \theta}\right|_{i=const}. \tag{5}$$

Similarly, the generation of axial thrust force is governed by the tendency of the single-phase transverse magnetic circuit to minimize its reluctance. When the linear windings are excited, an axially acting electromagnetic force is produced to align the inner rotor ferromagnetic rings with the inner stator poles. The axial thrust force F_{z} can be calculated by taking the partial derivative of the magnetic co-energy with respect to the linear displacement z

$$F_z(i,z) = \left.\frac{\partial W_m(i,z)}{\partial z}\right|_{i=const}. \tag{6}$$

Based on the established mathematical model of the motor system, the next step involves dimensional design of the motor's primary structural parameters. The rotating section adopts an inner stator-outer rotor configuration, while the linear section's structure closely resembles that of a rotary reluctance motor (RSRM) in cross-sectional height. Given the scarcity of literature on structural parameter design for transverse flux switch reluctance linear motors, the proposed motor's structural parameters were determined by drawing upon design experience from RSRMs.

If the linear unit is not considered, according to the design theory of the rotary motor, the main size expression of the rotary unit is [14]

$$(2r_6)^2 L_d = C\frac{P}{\cos\varphi n} \tag{7}$$

where r_6 is the outer radius of the stator, L_{d} is the axial length of the stator, P is the power of the rotary part, $\cos\varphi$ is the power factor, n is the rotational speed, and the output coefficient C represents the combined utilization level of the electric and magnetic loadings per unit stator volume in the main sizing equation. A larger C value indicates higher material utilization and greater power density. Based on design experience from RSRMs, the typical recommended range of C is 0.4 to 2.0 $\mathrm{kW}\cdot\mathrm{min/m^3}$. In this design, C = 1 $\mathrm{kW}\cdot\mathrm{min/m^3}$ is selected according to the rated power and speed requirements.

The inner radius r_3 and outer radius r_6 of the H-type stator pole can be expressed by

$$\begin{cases} \dfrac{r_4+r_5}{2} = k_1 r_6 \\ r_3 = k_2 \dfrac{r_4+r_5}{2} \end{cases}, \tag{8}$$

where r_4 and r_5 represent the inner radius and outer radius of the H-type stator yoke, respectively, k_1 and k_2 denote proportional coefficients, typically ranging from 0.4 to 0.7 based on RSRM's design experience. In this design, $k_1 = 0.5$ is selected to balance the slot fill

factor and magnetic circuit length, $k_2 = 0.5$ is selected to ensure the yoke flux density remains within the saturation limit while maintaining sufficient winding space.

The equation for calculating the thickness l of an H-type stator yoke satisfies

$$l = (1.1 \sim 1.3)(d+m), \tag{9}$$

where d and m represent the widths of the upper and lower pole teeth of the H-type stator, respectively.

Additionally, when determining the values for the stator inner radius r_1 and rotor outer radius r_8, it is important to note that excessively small values may result in insufficient mechanical strength of the motor. This could lead to fractures during operation, thereby reducing the motor's service life. Therefore, mechanical strength must be considered when selecting these values. Simultaneously, while ensuring mechanical strength, the dimensions of the rotor yoke and stator yoke must be maintained to satisfy the requirements for magnetic circuit saturation.

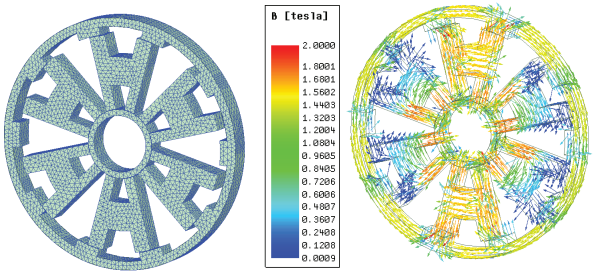
Based on the theoretical derivation from equations (7)–(9) and drawing upon established design practices for conventional RSRMs, the initial values for key structural dimensions of the proposed TLRSRM can be preliminarily determined, as listed in Table 1.

Table 1: Structure parameters of the TLRSRM

Item	Unit	Value
Mover inner radius/r_1	mm	13
Stator pole inner radius/r_3	mm	16
Stator yoke inner radius/r_4	mm	26
Stator yoke thickness/ l	mm	14
Stator pole outer radius/r_6	mm	50
Rotary stator pole width/d	mm	8.2
Linear stator pole width/m	mm	5.3
Rotor outer radius/r_8	mm	58
Rotor pole width/w_r	mm	11
Rotor yoke thickness/ L_{ry}	mm	4
Mover ring length/L_{m}	mm	10
Stator ring length/L_{d}	mm	10
magnetic ring spacing width/L_{r}	mm	25
Stator-rotor air gap length	mm	0.3
Stator-mover air gap length	mm	0.2
Core axial length	mm	110

IV. 3D FINITE ELEMENT CALCULATION OF TLRSRM

This study employed finite element analysis to simulate the electromagnetic performance of the designed TLRSRM. In the simulation calculations, eddy currents within the core causing magnetic field disturbances are not considered at this stage. For clarity, one phase of the rotary winding and the single-phase linear winding within a single ferromagnetic ring structure are selected as representative examples for analysis. By applying independent excitation to each phase winding, the magnetic field distributions of the stator, rotor, and mover are obtained at both aligned and misaligned positions (Figs. 5 and 6). Figure 5 (a) displays the three-dimensional mesh partitioning diagram of the TLRSRM in the finite element software, while Fig. 5 (b) presents the vector diagram of the three-dimensional magnetic flux paths. When the rotating rotor and linearly displacing stator are in misaligned and aligned positions, respectively, the TLRSRM exhibits four distinct positional states. Their magnetic flux density contour plots are displayed in Fig. 6. Simulation results indicate that, when the stator and rotor/mover are aligned, the maximum magnetic flux density within the stator core region occurs at the core edges where components meet the air gap, reaching approximately 1.8 T. The rated current for the rotating winding is 9 A, and the rated current for the straight winding is 6 A. Figures 5 and 6 show the magnetic flux density contour plots under rated operating conditions.



(a) (b)

Fig. 5. 3D finite element model: (a) finite element mesh diagram and (b) magnetic flux density vector diagram.

In the proposed TLRSRM structure, the rotary winding and linear winding are integrated within the same set of stator modules. As shown in Fig. 3, the magnetic paths generated by the two motion modes overlap at the stator yoke, inevitably inducing electromagnetic coupling effects. Therefore, to analyze the impact of this coupling effect, we examined the mutual influence between linear motion and rotary motion under different current directions and levels.

While maintaining the current of one phase of the rotary winding at its rated value, the excitation state and direction of the linear winding's current were varied. Figures 7 and 8 display the magnetic flux density contour plots within the motor when the linear winding operates under zero excitation, rated excitation, and double overload excitation conditions.

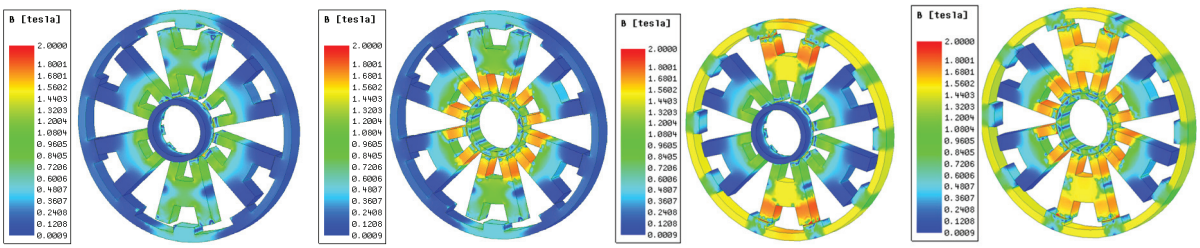


Fig. 6. Magnetic flux density contour map: (a) rotor and mover at unaligned position, (b) rotor at unaligned position, and stator at aligned position, (c) rotor at aligned position, and stator at unaligned position, and (d) rotor and stator at aligned position.

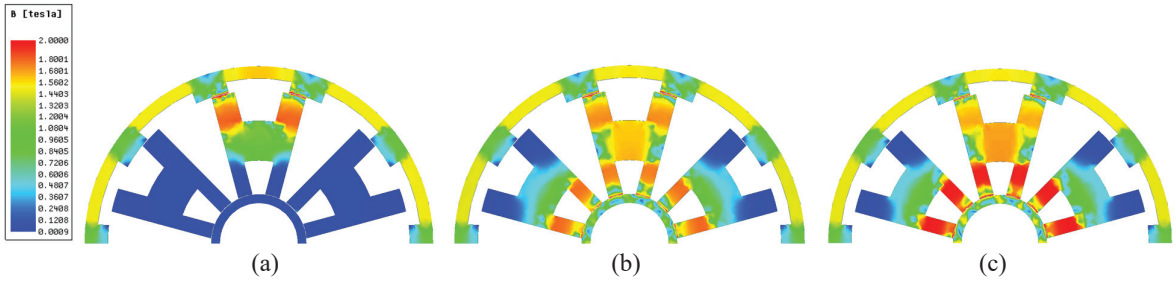


Fig. 7. Magnetic flux density contour map under positive current excitation of different linear windings: (a) zero excitation, (b) rated excitation, and (c) double rated excitation.

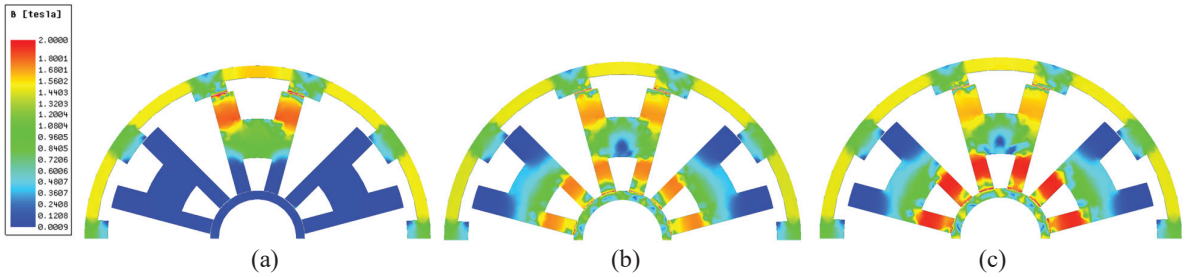


Fig. 8. Magnetic flux density contour map under reverse current excitation of different linear windings: (a) zero excitation, (b) rated excitation, and (c) double rated excitation.

It can be observed that in Fig. 7, the magnetic flux direction generated by the linear winding within the stator yoke is identical to that of the rotary winding. Consequently, the magnetic flux density in the stator yoke approaches saturation. In Fig. 8, the magnetic flux direction generated by the linear winding in the stator yoke is opposite to that of the rotating winding. Thus, the magnetic fluxes in the stator yoke cancel each other out, resulting in a low magnetic flux density.

Corresponding to these three operating states, Fig. 9 (a) presents the static torque waveform generated by rotational motion when the magnetic fluxes of the rotating and linear windings are in the same direction. Figure 9 (b) shows the static torque waveform when the magnetic flux directions of the rotating and linear windings are opposite. It can be observed that regardless of whether the linear winding current direction changes, or when the current magnitude varies from zero excitation to double excitation, the static torque waveform exhibits only minor changes. The variation rate of the static average torque value does not exceed 5%. This data indicates that the electromagnetic coupling effect is relatively small.

Additionally, Fig. 10 displays the dynamic response waveform of the radial force exerted by the linear winding excitation on the rotor during its movement from a misaligned position to an aligned position. Analysis reveals that throughout the entire motion process, the fluctuation amplitude of the radial force remains relatively limited, with its numerical variation consistently within acceptable engineering tolerance ranges. This phenomenon further confirms, from a mechanical

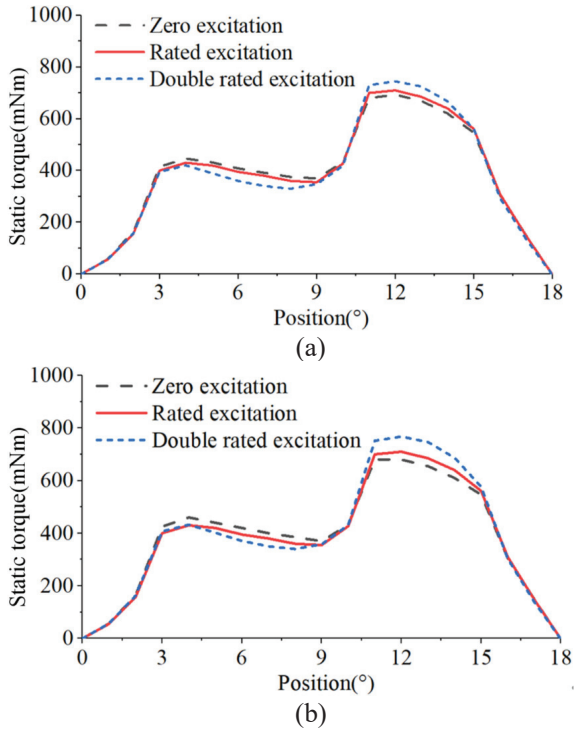


Fig. 9. Static torque waveforms under different linear winding current excitation: (a) positive current and (b) reverse current.

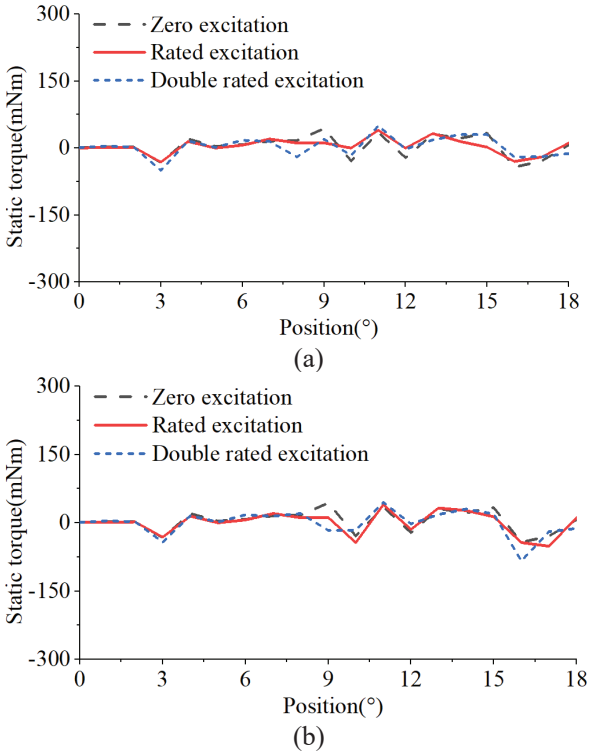


Fig. 10. Radial force waveform under different linear winding current excitation: (a) positive current and (b) reverse current.

characteristics perspective, that the TLRSRM topology proposed in this paper exhibits weak electromagnetic coupling effects between different motion modes and possesses excellent decoupling characteristics.

To further analyze the fundamental magnetic flux and torque characteristics of the proposed TLRSRM structure, the static characteristics as a function of current are presented for both rotational and linear motion modes. It should be noted that these baseline curves are evaluated under independent excitation conditions; that is, when analyzing the static characteristics of one motion mode, the supply current of the other motion mode is strictly held at zero. The magnetic flux curve is shown in Fig. 11, while the static torque and static thrust curves are depicted in Fig. 12.

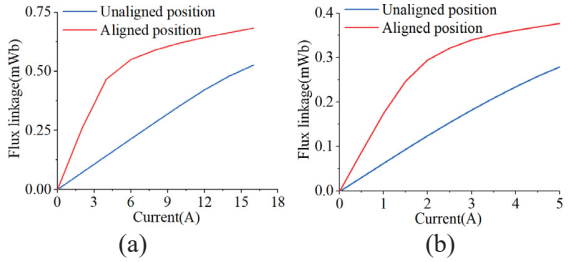


Fig. 11. Flux linkage curve: (a) rotary motion and (b) linear motion.

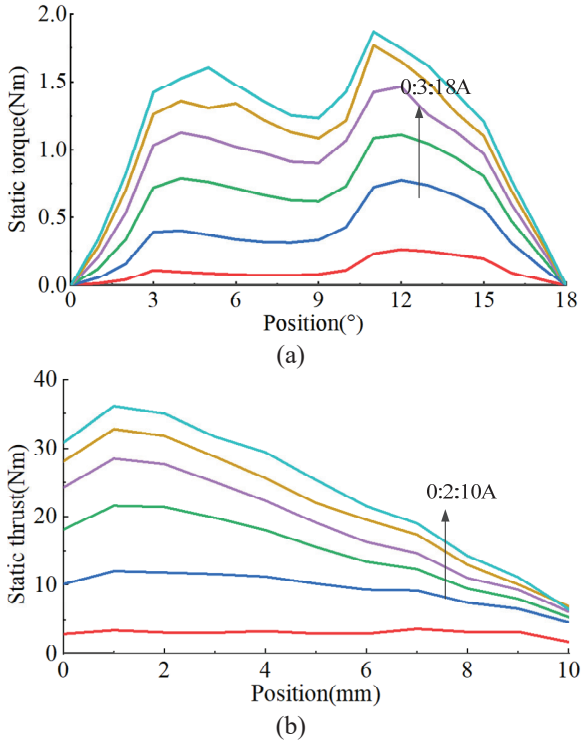


Fig. 12. Static torque and static thrust curves: (a) rotary motion and (b) linear motion.

It can be observed that in the non-aligned state, the magnetic flux and current maintain an approximately linear relationship, reflecting a larger air gap and higher magnetic resistance in the magnetic circuit at this time, with the core material consistently operating in the non-saturated region. At the alignment position, the magnetic flux exhibits linear growth at lower currents; when the current increases significantly, the growth rate slows markedly, demonstrating typical nonlinear saturation characteristics. This phenomenon arises because at alignment, magnetic flux concentrates through the stator and rotor/armature, forming a low-magnetic-resistance path. This causes the local magnetic flux density in the core to rapidly increase into the saturation region, reducing magnetic permeability and thereby diminishing the magnetic flux's ability to increase with current.

V. CONCLUSION

This study designed and validated a tubular linear-rotary switch reluctance motor employing a modular stator configuration. Through three-dimensional electromagnetic field simulation and static characteristic analysis, the magnetic field distribution patterns of this topology and its coupling characteristics under compound motion conditions were systematically evaluated. Simulation data indicates that electromagnetic interference from the linear motion unit to the rotational unit remains at a low level: under rated conditions, torque fluctuations induced by the linear winding excitation exhibit limited amplitude, with static average torque deviation consistently controlled within 5%. Concurrently, radial force fluctuations generated during motion fall within engineering application standards. These characteristics fully demonstrate that the proposed motor structure exhibits excellent electromagnetic decoupling performance when achieving combined rotational and linear motion, providing an effective technical solution for multi-degree-of-freedom drive systems.

Building on these static results, future work will focus on constructing a prototype for experimental validation. Subsequent research will also explore optimizing the stator dimensions to maximize power density, along with developing dynamic control strategies for the linear and rotary motions.

ACKNOWLEDGMENT

This work is supported by the National Natural Science Foundation of China International (regional) cooperation and exchange projects NSFC-RSF under Grant W2412064 and the Shenzhen Collaborative Innovation Special Plan International Cooperation Research Project under Grant GJHZ20240218114300002.

REFERENCES

[1] H. Chen, R. Nie, and X. Li, "A transverse-flux single-phase tubular switched reluctance linear machine with 4 poles," *IEEE Transactions on Applied Superconductivity*, vol. 31, no. 8, pp. 1–4, Nov. 2021.

[2] K. Manohar and K. Srichandan, "Analysis of quadrupole magnetic field reluctance-based launcher with different coil switching patterns," *IEEE Transactions on Plasma Science*, vol. 51, no. 5, pp. 1370–1376, May 2023.

[3] L. Zhang, L. Yan, X. Wei, H. Su, Z. Dong, and L. Li, "Stress analysis of a flat linear switched reluctance motor with double excitation windings," in *CSAA/IET International Conference on Aircraft Utility Systems*, Nanchang, China, pp. 1240–1245, 2022.

[4] L. Szabó, "On the use of rotary-linear generators in floating hybrid wind and wave energy conversion systems," in *2018 IEEE International Conference on Automation, Quality and Testing, Robotics*, Cluj-Napoca, Romania, pp. 1–6, 2018.

[5] R. Nie, J. Si, Y. Jia, P. Wang, S. Xu, and J. Liang, "Comprehensive comparison of mover-PM and stator-PM linear-rotary generators for wind-wave combined energy conversion system," *IEEE Transactions on Industry Applications*, vol. 60, no. 4, pp. 6170–6185, July–Aug. 2024.

[6] J. Zhang, M. Chen, and Y. Liu, "A tubular linear-rotary generator with dual stators for direct drive wind-wave complementary energy generation platform," *IEEE Access*, vol. 13, pp. 132426–132439, 2025.

[7] H. Chen, R. Nie, and H. Wang, "A transverse flux single-phase tubular-switched reluctance linear launcher with 8-pole structure," *IEEE Transactions on Plasma Science*, vol. 47, no. 5, pp. 2331–2338, May 2019.

[8] L. Szabó, I. Benţia, and M. Ruba, "A rotary-linear switched reluctance motor for automotive applications," in *2012 XXth International Conference on Electrical Machines*, Marseille, France, pp. 2615–2621, 2012.

[9] I. Benţia, L. Szabó, and M. Ruba, "On a rotary-linear switched reluctance motor," in *International Symposium on Power Electronics Power Electronics, Electrical Drives, Automation and Motion*, Sorrento, Italy, pp. 507–510, 2012.

[10] I. Benţia, M. Ruba, and L. Szabó, "On the control of a rotary-linear switched reluctance motor," in *2011 5th International Symposium on Computational Intelligence and Intelligent Informatics*, Floriana, Malta, pp. 41–46, 2011.

[11] W. Wu, J. B. Dunlop, S. J. Collocott, and B. A. Kalan, "Design optimization of a switched reluctance motor by electromagnetic and thermal finite-element analysis," *IEEE Transactions on*

Magnetics, vol. 39, no. 5, pp. 3334–3336, Sep. 2003.

[12] H. Chen, X. Wang, C. Liu, M. F. Shamiyev, A. O. Pulatov, and A. Musolino, "Design of a three-phase high torque density modular linear rotary switched reluctance launcher," *IEEE Transactions on Plasma Science*, vol. 53, no. 10, pp. 2653–2661, Oct. 2025.

[13] H. Chen, X. Wang, C. Liu, A. Musolino, P. Rafajdus, and X. Li, "Flux characteristics analysis of a novel two-degree-of-freedom tubular linear rotary switched reluctance machine," *IEEE Transactions on Plasma Science*, vol. 53, no. 10, pp. 2704–2711, Oct. 2025.

[14] F. Xinghe, W. Jianhao, and L. Mingyao, "Design and analysis of linear rotary permanent magnet generator for wind-wave combined power generation system," in *2017 20th International Conference on Electrical Machines and Systems*, Sydney, NSW, Australia, pp. 1–6, 2017.



Hao Chen (SM'08) received the B.S. and Ph.D. degrees from the Department of Automatic Control, Nanjing University of Aeronautics and Astronautics, Nanjing, China, in 1991 and 1996, respectively. In 1998, he became an Associate Professor with the School of Information and Electrical Engineering, China University of Mining and Technology, Xuzhou, where he has been a Professor since 2001. From 2002 to 2003, he was a Visiting Professor at Kyungsung University, Busan, Korea. Since 2008, he has also been an Adjunct Professor at the University of Western Australia, Perth, Australia. He is the author of one book and has also authored more than 190 papers. He is the holder of 15 US Patents, 23 Australian Patents, one Danish Patent, seven Canadian Patents, three South African Patents, 10 Russian Patents, 86 Chinese Invention Patents, and six Chinese Utility Model Patents. His current research interests include motor control, linear launcher, electric vehicles, electric traction, servo drives, and wind power generator control.

Chen was the recipient of both the Prize of Science and Technology of Chinese Youth and the Prize of the Fok Ying Tong Education Foundation for Youth Teachers in both 2004. He was awarded the first prize in the Science and Technology advanced of Province and Ministry once, the second prize in the Science and Technology advanced of Province and Ministry seven times, and the third prize in the Science and Technology advanced of Province and Ministry 14 times. He became the Chinese New Century Hundred-Thousand Ten-Thousand Talents Engineering National Talent in 2007, and won the Government Especial Allowance of People's Republic of China State Department since 2006.



Cheng Liu received the B.S. degree in electrical engineering and automation from Hubei University of Technology, Wuhan, Hubei, China, in 2020, and the M.S. degree in electrical engineering from Hubei University of Technology, Wuhan, Hubei, in 2023. He is currently pursuing a Ph.D. degree in electrical engineering at China University of Mining and Technology, Xuzhou. His research interests include switched reluctance motor design control, ocean wave power generation, and electric vehicles.



Marcin Wardach was born in Poland in 1980. He graduated and received the Ph.D. degree from the Electrical Department, Szczecin University of Technology, Szczecin, in 2004 and 2009, respectively. From 2020 until now, he has been an Associate Professor with the Faculty of Electrical Engineering, West Pomeranian University of Technology in Szczecin. Since 2024, he has served as Vice-Dean for Organization and Development and Head of the Department of Electrical Machines and Drives at the Faculty of Electrical Engineering, West Pomeranian University of Technology in Szczecin. From 2019 to 2025, he worked as an electrical machine designer at mPower Sp. z o.o. company. His research interests include the design of electrical machines and drives, especially unconventional and hybrid excited. He is the author of over 100 scientific papers and post-conference publications. Since 2022, he has been the President of the Szczecin Branch of the Association of Polish Electrical Engineers (SEP). He is also a member of the Polish Society of Theoretical and Applied Electrical Engineering.



Javokhir Toshov currently works at the Department of Mining Electromechanics, Tashkent State Technical University, Uzbekistan. Toshov does research in Mechanical Engineering and Mining Engineering. Department of Electronic Devices Manufacturing Technologies, Faculty of Electronic and Automation Engineering, Tashkent State Technical University, Tashkent 100095, Uzbekistan; Department of Theoretical and Experimental Physics, Faculty of Physics, Karshi State University, Karshi 180119, Uzbekistan.



Xing Wang received the B.S. degree from China University of Mining and Technology, Xuzhou Jiangsu, China, in 1996, and M.S. degree from China University of Mining and Technology, Xuzhou Jiangsu, in 1999. In 2007, she became an Associate Professor with China University of Mining and Technology, Xuzhou. She is a holder of four US Patents, nine Australian Patents, two Canadian Patents, four Russian Patents, 12 Chinese Invention Patents, three Chinese Utility Model Patents, and authored 15 papers.



Ali Asghar Memon is professor in Electrical Engineering at Mehran University of Engineering and Technology Jamshoro, Pakistan. He holds B.E and M.E in Electrical Engineering from Mehran University and Ph.D. from University of Leeds, UK. Memon is head of Electrical Machine and Drives group at Mehran University. He has been member of National Curriculum Review Committee in Pakistan. Memon has been serving as an expert evaluator for National Research Project for Universities (NRPU), Post doc fellowship and project(s) under Technology Development Fund (TDF), under Higher Education Commission (HEC), Government of Pakistan. Memon is a keynote speaker and reviewer of prestige international research journals. Memon's interests include modeling and simulation of switched reluctance machines and inverters.



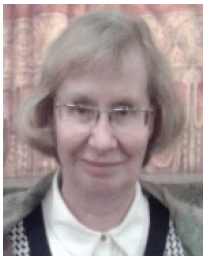
Bodrenkov Evgenii Alexandrovich received the B.S. and M.S. degree from Federal State Budgetary Educational Institution of Higher Education Amur State University, Ph.D. degrees from Federal State Autonomous Educational Institution of Higher Education Peter the Great St. Petersburg Polytechnic University.



Popov Stanislav Olegovich received the M.S. degree in the field of "Electric power plants and automation of power systems" in 2008, and Ph.D. in Technical Sciences. He has been an associate professor at the Institute of Energy, from 2008 to present in SPBSTU.



Nikolay Korovkin (Member, IEEE) received the M.S., Ph.D., and Doctorate degrees in electrical engineering from the State Polytechnic University, Saint Petersburg, Russia, in 1977, 1984, and 1995, respectively. He is currently a Professor with the Institute of Energy, Peter the Great Saint Petersburg Polytechnic University, Saint Petersburg. Since 1996, he has been an Academician with the Academy of Electrotechnical of Russian Federation, Saint Petersburg. He has about 300 published and reviewed works in Russia and abroad. His main research interests include the inverse problems in electromagnetics, systems described by stiff equations, ill conditioned problems, optimization of power networks, optimization of the location FACTS and PMU-devices, SMART grid technologies, methods for the analysis of reliability and ensuring power balance in EPS, methods of multicriteria optimization and their application to steady-state processes in power networks, transients in transmission line systems, impulse processes in linear and nonlinear systems, problems of the electromagnetic prediction of earthquakes, and identification of the behavior of the biological objects under the influence of the electromagnetic fields.



Sakhno Liudmila (Member, IEEE) received the B.S., M.S., and Ph.D. degrees from Russia Polytechnic Institute, Saint Petersburg, Russia, in 1972, 1974, and 1982, respectively, and the Doctors degree in electromechanics and electrical apparatus from St. Petersburg State Technical University, Saint Petersburg, in 2006. She is currently a Professor of Higher School of High Voltage Power Engineering, Peter the Great Saint Petersburg Polytechnic University, Saint Petersburg. She has about 200 published and reviewed works in Russia and abroad. Her research interests include the electromagnetic problems in power transformers, the skin effect and the proximity effect in the windings of converter transformers, electromagnetic and thermal characteristics of arc and resistance welding transformers, mechanical strength of structural elements under the action of loads, and field-circuit modeling in high frequency resistance spot welding systems. She obtained eight Russian Federation Patents.



Emmanuel Karapidakis is an Electrical and Computer Engineer. He was Dean at School of Engineering from 2019 to 2025, and Director of Energy, Environment and Climate Change Institute – IEECC (ieecc.hmu.gr) in Hellenic Mediterranean University – HMU (hmu.gr). Since 2022, he is President of the Board in Hellenic Association of Electricity Storage Systems HAESS (www.haess.gr). His research interest focuses on Energy Systems, Power Systems Operation, Diverse & Dispersed Generation, Micro-Grids, Renewable Energy Technologies, Energy Storage, and Energy Markets. He is/was scientific coordinator (PI) in 12 European financed projects, 15 National programs, and several private funded projects, with more than 8 million euros in total. He has published more than 120 papers (Scopus Author ID 6506872824) in prestigious journals and scientific conferences, and four scientific book chapters. From 2011 to 2015, he was Member of the Board in Regional Council of Innovation, and from 2015 to 2017, Member of Board in Energy Planning Council at Region of Crete.



Aris Dimeas is an Assistant Professor at the School of Electrical and Computer Engineering of the National Technical University of Athens (NTUA), with more than 20 years of experience in power systems operation, smart grids, and energy system digitalization. His expertise spans distribution and transmission system operation, renewable energy integration, microgrids, flexibility markets, artificial intelligence applications, and advanced control and decision-support software. He has played a leading technical and coordination role in more than 30 EU-funded research and innovation projects (H2020 and Horizon Europe), collaborating closely with TSOs, DSOs, regulators, industry, and the European Commission. His work bridges research and real-world deployment, with demonstrated impact on system supervision, resilience, market design, and datadriven grid operation, while his scientific contributions include high-impact publications in leading IEEE and international journals.



Sherif Moussa is the Dean of the School of Engineering, Applied Science, and Technology at the Canadian University Dubai (CUD), UAE. He earned his Ph.D. in Electrical and Computer Engineering from the University of Québec at Trois-Rivières, Canada, and his M.Sc. in Electrical and Computer Engineering from the University of Waterloo, Canada. Since joining CUD in 2007, Moussa has led the School's remarkable growth, overseeing the launch and accreditation of several engineering and computing programs, including Mechatronics Engineering, Computer Science, Cybersecurity, Software Design, Power and Renewable Energy Engineering, and the M.Sc. in Artificial Intelligence. His leadership has also advanced international collaborations, notably with Queen's University and the University of Ottawa, and strengthened CUD's engagement with industry partners in emerging technologies. Moussa's research interests span wireless communication, computer networks, machine learning, and digital systems design. He has published widely in international journals and conferences, serves on technical committees, and is the recipient of the 2015 CUD Research Excellence Award. He is also the founder of CUD's Robotics Club and a strong advocate for innovation and experiential learning in engineering education.



Habes Ali Khawaldeh (Member, IEEE) received the B.E. degree in electrical and computer engineering from The Hashemite University, Jordan, in 2009, and the M.S. degree in electrical power engineering from Yarmouk University, in 2013. In 2022, Habes Ali Khawaldeh received his Ph.D. degree in power electronics engineering from the Faculty of Engineering and Information Technology, University of Technology Sydney (UTS), Australia. Since 2018, he has been a Casual Academician with UTS for various power electronics subjects. Since July 2009, he has been working as an electrical engineer with different companies in Jordan. He was a part-time Faculty Member with Yarmouk University for various power electronics subjects. He was a full-time Faculty Member with Al-Hussein Bin Talal University from 2015 to 2018. His current research interests include renewable energy (RE) systems, power converter design for RE applications, battery systems, multi-port DC/DC converters, and energy conversion systems for the smart grid. He received a Grant from Al al-Bayt University for his Ph.D. degree. He is currently a reviewer for several IEEE, IET, and Elsevier journals. Currently, Habes Ali Khawaldeh is an assistant professor at the University of Al al-Bayt in Jordan.

Electromagnetic Analysis of a Novel Two-Degree-of-Freedom Tubular Linear Rotary Switched Reluctance Machine

Cheng Liu[1], Hao Chen[1,2,3,4], Marcin Wardach[5], Javokhir Toshov[6], Xing Wang[2,3], Bodrenkov Evgenii Alexandrovich[7], Popov Stanislav Olegovich[7], Nikolay Korovkin[7], Sakhno Liudmila[7], Mohamed Orabi[8], Mahmoud A. Gaafar[8], Emmanuel Karapidakis[9], Aris Dimeas[10], Sherif Moussa[11], and Habes Ali Khawaldeh[12]

[1]School of Electrical
Engineering China University of Mining and Technology, Xuzhou 221116, China
Chengliu97@cumt.edu.cn, hchen@cumt.edu.cn

[2]Shenzhen Research Institute
China University of Mining and Technology, Shenzhen 515100, China
3512@cumt.edu.cn

[3]Jiangsu Province Foreign Expert Workshop on New Energy Power Generation and Electric Transportation
Xuzhou 221008, China

[4]International Joint Research Center of Central and Eastern European Countries on
New Energy Electric Vehicle Technology and Equipment
Xuzhou 221008, China

[5]Department of Electrical Machines and Drives
West Pomeranian University of Technology, Sikorskiego 37, 70-313 Szczecin, Poland

[6]Tashkent State Technical University
University Street No2, 100095 Tashkent, Uzbekistan

[7]The Institute of Energy
Peter the Great Saint Petersburg Polytechnic University, Saint Petersburg, Russia

[8]Electrical Engineering Department
Faculty of Engineering, Aswan University, Aswan, Egypt

[9]School of Engineering
Hellenic Mediterranean University, Estavromenos Campus, 71004 Heraklio, Crete, Greece

[10]Athens National University of Technology
Greece

[11]School of Engineering
Canadian University Dubai, 117781, Sheikh Zayed Road, Dubai, United Arab Emirates
[12]The Renewable Energy Engineering Department
Faculty of Engineering, Al al-Bayt University, Mafraq, Jordan
*Corresponding author

Abstract **–** A novel two-degree-of-freedom tubular linear-rotary switched reluctance machine (TLRSRM) is proposed, and its electromagnetic characteristics are investigated. First, based on energy conversion principles, the topology and working mechanism of the TLRSRM are explained. Structural dimensions are determined using conventional motor design experience. Next, a 3D finite element model (FEM) and a structural validation process are established to verify the electromagnetic feasibility of the topology. The magnetic field distributions are compared between the unaligned and aligned positions. Furthermore, parameter sweeping is

Submitted On: January 16, 2026
Accepted On: June 12, 2026

1054-4887 © ACES

https://doi.org/10.13052/2026.ACES.J.410603

applied to systematically analyze static electromagnetic characteristics. These include the nonlinear variation of inductance, flux saturation behavior, and electromagnetic force output in a twodimensional position-current parameter space. Finally, the multi-degree-of-freedom coupling mechanism is quantitatively analyzed. Simulation results of both static and dynamic performances successfully confirm the structural feasibility of the proposed topology, thereby establishing a solid theoretical framework for subsequent optimization and control.

Index Terms – 3D finite element model, magnetic field distribution, static electromagnetic characteristics, switched reluctance machine.

I. INTRODUCTION

The increasing demand for drive system integration and multi-degree-of-freedom motion control in the fields of intelligent manufacturing, wind-wave co-generation system and other ocean energy utilization, the traditional single-degree-of-freedom motors have been unable to meet the requirements of efficient drive under complex working conditions due to the limitations of single function, high system complexity, and low space utilization. In this context, multi-degree-of-freedom motors have become a research hotspot in the field of motors due to their advantages of compact structure, high integration, and flexible motion control. Among them, switched reluctance motors (SRMs) show great potential in the application of multi-degree-of-freedom drive systems by virtue of their simple structure, high fault tolerance, and high environmental adaptability. However, the existing research on multi-degree-of-freedom SRMs still faces technical bottlenecks such as complex electromagnetic coupling, large torque pulsation, and imperfect design theory, which urgently need to realize performance enhancement through topological innovation and theoretical breakthroughs [1–4].

As an emerging topology, the two-degree-of-freedom tubular linear-rotary switched reluctance machine (TLRSRM) can realize the cooperative control of rotary and linear motions at the same time, which is of significant application value in the fields of automated robotic arms and intelligent conveyor systems. Currently, most of the related research focuses on the performance optimization of single-degree-of-freedom SRMs, while the research on TLRSRMs is still in its infancy, and its topology design methodology, electromagnetic coupling mechanism, and performance optimization strategy are yet to be explored in depth [5–7].

The magnetic circuit structure, TLRSRM can be composed mainly of rotary and linear magnetic circuits, so its structure can be studied from conventional radial switched reluctance motor (RSRM) and linear switched reluctance motor (LSRM). LSRM include various configurations tailored for various industrial applications. Among them, tubular linear switched reluctance motor (TLSRM) represent a special topology characterized by a cylindrical structure. The TLSRM offers two distinct advantages over single- and double-sided LSRMs that enhance its performance and utility. The coaxial arrangement of the tubular stator sleeve and tubular actuator allows the TLSRM to achieve a higher force density ratio (thrust output per unit volume) than conventional LSRM designs. This geometric configuration optimizes the flux path and promotes more efficient electromagnetic coupling, thereby maximizing thrust generation capability within a compact envelope [8–11].

Reference [12] provides an optimal design method for RSRMs through 2D finite element electromagnetic analysis and finite element thermal analysis, which improves the performance and reduces the manufacturing cost of RSRMs. Reference [13] performed a multi-objective optimization of a bilateral SRLM applied for wave power generation. A single-phase tubular permanent magnet linear generator (TPMLG) with a novel structure is presented in [14], the mover parts move in a reciprocating linear motion by the leaf springs. A two-degree-of-freedom double-stator linear-rotary SRM for an industrial robot is proposed in [15]. It can perform individual rotary motion, linear reciprocating motion, and helical motion.

Due to the limited literature on two-degree-of-freedom (2DOF) SRMs, this paper proposes a novel TLRSRM topology to achieve simultaneous linear and rotary motion. Based on energy conversion principles and established motor design methodologies, a structural design model of the proposed machine is developed. Furthermore, considering its unique structural features, a 3D finite element analysis (3D FEA) is performed via simulation software. The electromagnetic characteristics – including magnetic flux density, flux linkage, inductance, and static torque – are thoroughly investigated. The results validate the rationality and feasibility of the proposed topology.

II. STRUCTURE AND OPERATING PRINCIPLE OF TLRSRM

The proposed TLRSRM 3D structural model is shown in Fig. 1. This motor innovatively integrates rotational and linear drive functions into a single unit, with the topological design of its rotary and linear sections forming the core of the system. The rotary section employs a three-phase concentrated winding with a 12/10 stator-rotor pole configuration. Utilizing a conventional axial flux disc motor structure, it offers significant advantages such as a flat, compact profile

and short axial dimensions, making it suitable for space-constrained applications. Simultaneously, the concentrated winding structure reduces winding copper losses by shortening end lengths, thereby improving motor efficiency. The stator of the linear section comprises four pairs of tooth poles extending radially from the stator yoke of the rotary section's axial motor. Opposite-polarity windings are applied to each pair of tooth poles, generating transverse flux perpendicular to the direction of motion of the moving element. By alternately energizing windings at different phases, reluctance torque is induced between the moving element and stator tooth poles, driving the moving element to perform linear motion along the axial direction. This design effectively mitigates lateral leakage flux issues, reduces end-effect influences, and ensures the stability and precision of linear motion. Furthermore, the symmetrical distribution of the stator pole structure helps balance electromagnetic forces, which minimizes vibration and noise during rotor operation.

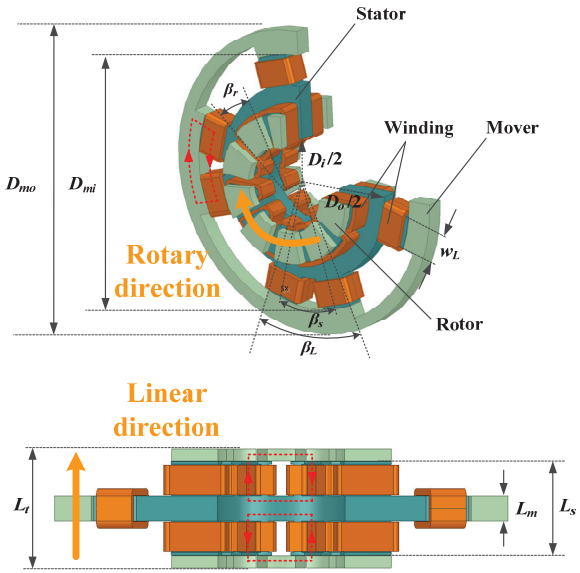


Fig. 1. 3D views of proposed TLRSRM model.

Additionally, the red dashed lines in Fig. 1 represent magnetic flux paths. It can be observed that the rotating section adopts an axial flux disc structure, where the rotor poles and axially symmetric stator teeth form the main magnetic circuit. This circuit closes through the stator yoke, achieving a uniform axial magnetic field distribution. The interaction between the three-phase concentrated windings and the rotor poles generates electromagnetic torque to drive rotation. The linear section operates similarly to conventional transverse flux motors. Magnetic flux lines originate from the stator yoke, traverse the stator poles and air gap, and form a radially closed circuit through the rotor ferromagnetic ring. The reverse winding generates an alternating-polarity magnetic field, establishing multiple independent magnetic circuits in the radial plane. These closed magnetic circuits run parallel to the stator cross-section and perpendicular to the rotor's direction of motion.

When the windings are energized, electromotive forces (EMF) are simultaneously induced on both the rotor and stator surfaces of the TLRSRM, thereby establishing independent current loops. These loops generate rotational torque and axial thrust concurrently. This integrated electromechanical design allows the motor to execute combined rotary-linear motion in both motoring and generating operational modes.

Based on the design experience of conventional axial flux SRMs and radial switched reluctance linear motors [16], the structural parameters of the TLRSRM of this paper are shown in Table 1.

Table 1: Structure parameters of the TLRSRM

Item	Unit	Value
Rated power	kW	1.5
Mover outer diameter/D_{mo}	mm	360
Mover inner diameter/D_{mi}	mm	300
Stator yoke outer diameter/D_o	mm	230
Stator yoke inner diameter/D_i	mm	101
Linear stator pole width/w_L	mm	40
Linear stator pole length/L_m	mm	20
Stator stack length/L_s	mm	74
Motor stack length/L_t	mm	94.8
Rotor pole arc/β_r	deg	25
Linear mover pole arc/β_L	deg	45
Linear stator tooth pitch/β_s	deg	30
Linear air gap thickness	mm	0.5
Rotary air gap thickness	mm	0.8
Winding conductor diameter	mm	2

III. STATIC ANALYSIS OF TLRSRM

In this paper, the flowchart of 3D modeling and analysis of the TLRSRM system using finite element software ANSYS is shown in Fig. 2 with the following steps.

- A geometric model of the TSRLM is established based on the pre-determined geometric dimension table. The geometric parameters in the model were configured according to the motor dimension specifications, ensuring precise mapping of the physical structure into the digital model.
- Physical properties of the TSRLM are set, including mechanical properties, material properties,

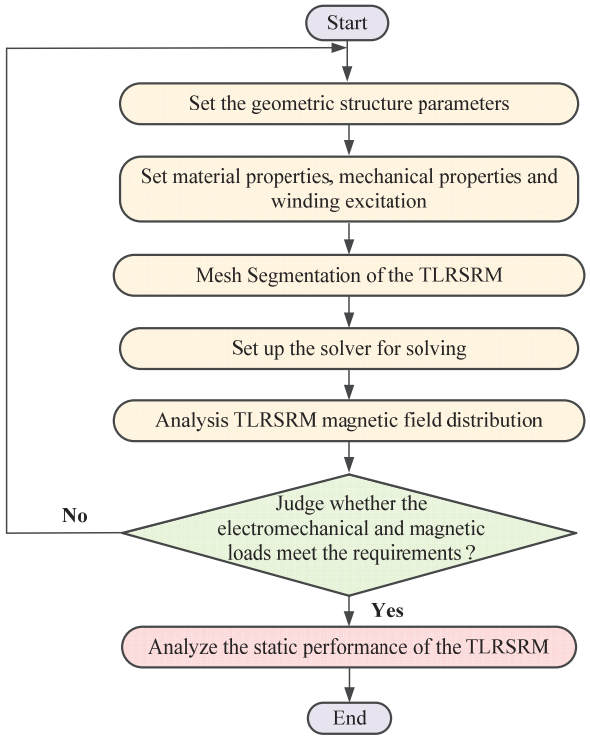


Fig. 2. Flow chart of finite element analysis.

and winding excitation of each component of the TSRLM.

- A customized mesh dissection of the TSRLM is performed and the geometric properties, physical properties, and dissection of the finite element model (FEM) are examined.
- A suitable solver (e.g., Maxwell 3D static/dynamic solver) is configured to perform electromagnetic field calculations on the meshed model. Then 3D magnetic flux distribution is analyzed to evaluate whether the designed electric load (current density, $J \leq 6A/mm^2$) and magnetic load (core flux density) meet design specifications. Specifically, the stator/rotor core flux density is checked against the saturation threshold (typically $\leq$1.8 T for silicon steel) to avoid excessive iron loss and magnetic nonlinearity, ensuring the motor operated within the optimal magnetic working range.
- After obtaining a well-designed motor structure, the FEM of TSRLM is analyzed for static performance and the data obtained from the simulation is processed in the next step.

Equal scale 3D FEM of the TLRSRM proposed in this paper from point to line and surface is performed according to the structural dimension in Table 1. The results of the mesh dissection of the $1/4$ geometric model of the TLRSRM are shown in Fig. 3. It can be observed that the mesh density in the FEM is custom adjusted according to the magnetic field distribution characteristics. Specifically, regions with complex magnetic field gradients (including stator pole tips, edges of the kinematic yoke, and air gap) are assigned fine meshes to capture rapid spatial variations in magnetic flux density and magnetic force. These critical regions, which are prone to magnetic saturation and field distortion, require high-resolution discretization to ensure accurate electromagnetic field calculations. In contrast, regions with relatively uniform or low magnetic field strengths (e.g., unsaturated cores and mechanical supports) employ coarser meshes to balance computational efficiency and solution accuracy.

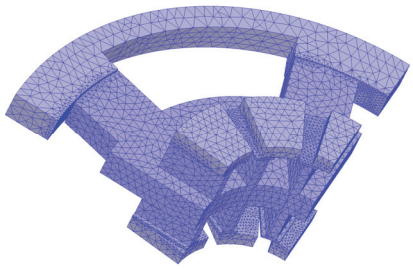
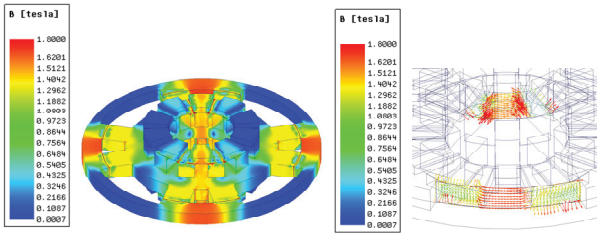


Fig. 3. Mesh sections for the 1/4 model of the TLRSRM.

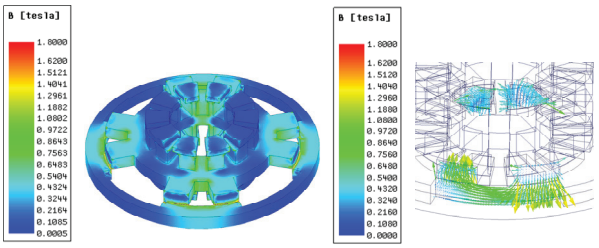
In rotary motion, when one of the phase windings is energized, the rotor position goes from unaligned to aligned, rotating one cycle in the angular range of (0°, 18°). In linear motion, excited by current from a single-phase winding, the actuator travel can be -20 mm to 0 mm or 0 mm to 20 mm, defining the position where the actuator's ferromagnetic ring and stator are fully aligned as the 0 mm position. The -20 mm position is the point at which the movable element moves negatively in the axial direction by 20 mm, and the movable element ferromagnetic ring and stator are perfectly misaligned when the movable element is in this position.



(a) (b)

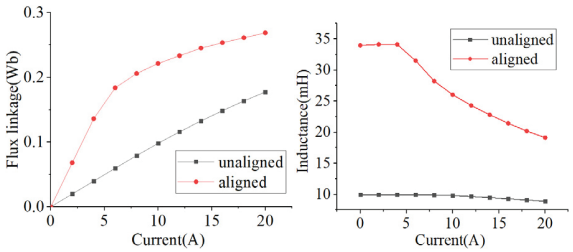
Fig. 4. TLRSRM in aligned position: (a) magnetic flux density map and (b) flux linkage distribution.

Figures 4 and 5 show the magnetic field distribution in the aligned and unaligned positions of the motor at rated operating conditions. Included here are the stator



(a) (b)

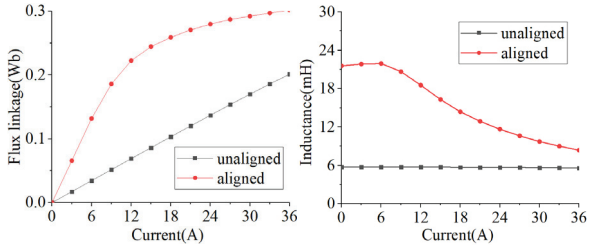
Fig. 5. TLRSRM in unaligned position: (a) magnetic flux density map and (b) flux linkage distribution.



(a) (b)

Fig. 7. Static characteristics of linear motion: (a) flux linkage at critical locations and (b) inductance at critical locations.

and rotor in rotational motion, and the stator and mover in linear motion. It can be seen that, when in the aligned position, there is less air leakage and the magnetic chain passes almost entirely through the rotor/motor. The air gap and the stator poles to form a closed loop, at which time the magnetic induction intensity in all parts of the TLRSRM reaches its maximum value. The motor has a high magnetic flux density, especially in the stator tooth poles and the magnetically conductive yoke section of the mover, with a high degree of core saturation. The maximum value of stator-rotor magnetic density is about 1.7 T, which meets the design requirements. From the same direction of flux flow at the air gap in Fig. 4 (b), it can be seen that the stator and rotor are more saturated at the air gap contact area, which is due to the smaller contact area. From Fig. 5, it is clearly observed that the overall core of the motor is less saturated with magnetic density, which is due to the inability of the flux path generated by the windings to form a closed path in the core. In linear motion, the area of the stator and the mover in the air gap contact area is almost zero, and there is more air leakage. In rotary motion, the air gap length between neighboring rotor blocks is too large, and the reluctance is larger.



(a) (b)

Fig. 6. Static characteristics of rotary motion: (a) flux linkage at critical locations and (b) inductance at critical locations.

Figures 6 and 7 illustrate the variations in magnetic flux linkage and phase inductance of the motor at two critical rotor positions: the unaligned and aligned configurations. For these measurements, a representative phase winding was selected for the rotating component, while a pair of stator pole windings was chosen for the linear section. At low excitation currents, the flux linkage exhibits a linear increase with current, and the inductance remains approximately constant at both positions, indicating that the magnetic circuit operates within the linear region of the core material's B-H curve. However, as the current exceeds the saturation threshold, the flux linkage at the aligned position begins to deviate from linearity, and the inductance gradually decreases. In contrast, the unaligned position shows no significant change in either parameter, maintaining linear behavior even at higher currents. This discrepancy arises because the aligned position experiences higher magnetic flux density in the stator and rotor cores, leading to localized saturation as the current increases. Once the core material reaches its saturation point (typically 1.8–2.0 T for silicon steel), the rate of change of magnetic flux with respect to current diminishes, resulting in the observed nonlinearity in flux linkage and inductance.

To comprehensively analyze the static characteristics across all rotor positions, Figs. 8 and 9 present 3D surface plots of inductance and flux linkage as functions of both current and rotor position, using the rotational motion as a case study. These plots reveal that the flux linkage exhibits a consistent trend with respect to rotor position across different current levels, indicating that the spatial distribution of the magnetic field is preserved despite variations in excitation magnitude.

Based on 3D finite element static simulations, the electromagnetic output characteristics of the two-degree-of-freedom TLRSRM are systematically analyzed as functions of rotor/stator position and excitation current, with the results presented in Figs. 10 and 11. Regarding the rotary motion characteristics, the static torque curve indicates that, as the rotor rotates from the unaligned to the aligned position, the electromagnetic torque exhibits a typical nonlinear pattern, initially rising and then falling. Specifically, at a rotor position angle of 18°, where the rotor pole centerline coincides with the stator slot centerline, the rate of change of

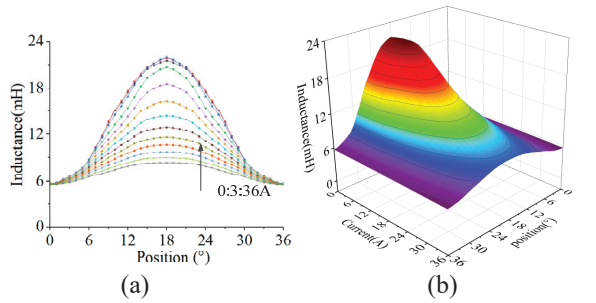


Fig. 8. Variation of inductance characteristics in rotary motion: (a) 2D variation curve and (b) 3D variation curve.

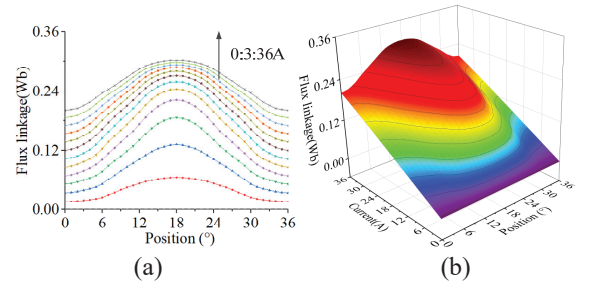


Fig. 9. Variation of flux linkage characteristics in rotary motion: (a) 2D variation curve and (b) 3D variation curve.

inductance reaches its peak and the magnetic reluctance is maximized, resulting in the maximum electromagnetic torque. Conversely, at the 0° position, complete alignment between the stator and rotor poles minimizes the magnetic reluctance, causing the electromagnetic torque to drop to zero. This behavior is consistent with the fundamental operating principle of SRMs.

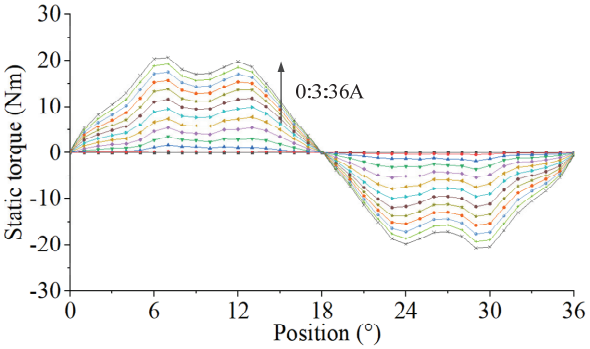


Fig. 10. Static torque curve for rotary motion.

In terms of linear motion characteristics, the static thrust curve shows a similar trend to that of rotary motion, which verifies the consistency of the electromagnetic force generation mechanism of this motor under multi-degree-of-freedom motion. Thanks to the

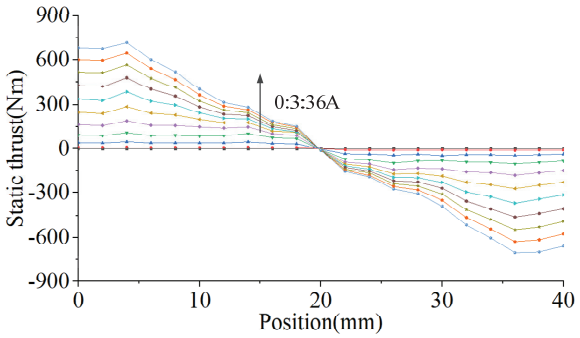


Fig. 11. Static thrust curves for linear motion.

accurate modeling of the motor end effect by the 3D finite element method, the static electromagnetic force results obtained from the simulation have high accuracy and reliability. Further parametric analysis shows that, with the increase of the excitation current, the curve shape of the electromagnetic force with respect to the position remains stable, but its amplitude tends to increase significantly. It is worth noting that when the excitation current exceeds a certain threshold, the growth rate of the electromagnetic force with the current gradually slows down due to the gradual saturation of the motor core, which is a characteristic that needs to be paid attention to in practical engineering design to avoid the performance degradation brought about by the saturated core. The above results not only reveal the changing law of electromagnetic force of TLRSRM under multi-degree-of-freedom motion, but also provide an important theoretical basis for the optimization design of the motor and the development of control strategies.

To further investigate the coupling effect between the linear and rotary windings on the motor's torque performance, the influence of energized linear windings on rotary motion is analyzed as an example. Figure 12 (a) shows the static torque variation when only the linear windings are supplied with rated current and the mover is in the aligned position. Figure 12 (b) illustrates the average static torque of the rotary motion under different excitation states of the linear windings, including no excitation, double excitation, and reverse excitation. Additionally, Fig. 12 (c) presents the electromagnetic torque variation of the rotary motion when the linear windings are supplied with rated current while the rotary windings are not excited.

As can be seen from Fig. 12 (a), the rotary torque waveform generated by the rotary windings remains almost unchanged regardless of whether the linear windings are excited. Additionally, it can be observed that under the excitation of the linear winding current and with no excitation applied to the rotary winding, the peak-to-peak value of the rotary torque is approximately 12 μNm. Therefore, when only the linear winding is

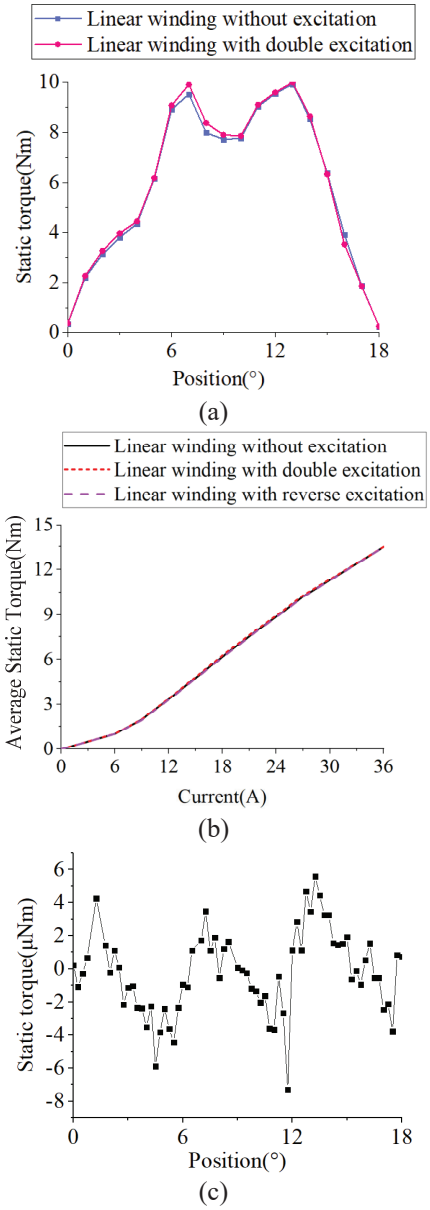


Fig. 12. Flux density distribution of TLRSRM: (a) static torque waveform, (b) static average torque variation with different currents, and (c) static torque of the linear winding under rated excitation with the rotary winding de-energized.

supplied with the rated current and the mover is in the aligned position, the influence of the linear winding on the rotary motion is minimal, indicating a low coupling effect.

IV. DYNAMIC PERFORMANCE ANALYSIS OF TLRSRM

To further evaluate the transient driving capabilities and multi-degree-of-freedom operational performance of the proposed TLRSRM, a comprehensive dynamic system model is established in MATLAB/Simulink. To retain the highly non-linear electromagnetic characteristics of the machine while ensuring computational efficiency, two-dimensional look-up tables (2D LUTs) of the non-linear flux linkage and static electromagnetic forces (torque and thrust) obtained from the prior analysis are implemented into the dynamic solver.

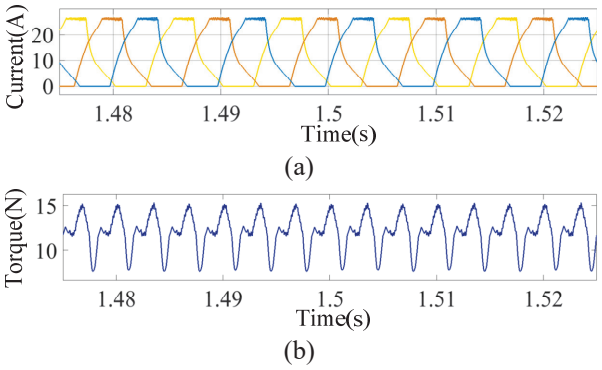


Fig. 13. Dynamic performance of rotary motion at 600 r/min: (a) phase current waveform and (b) torque waveform.

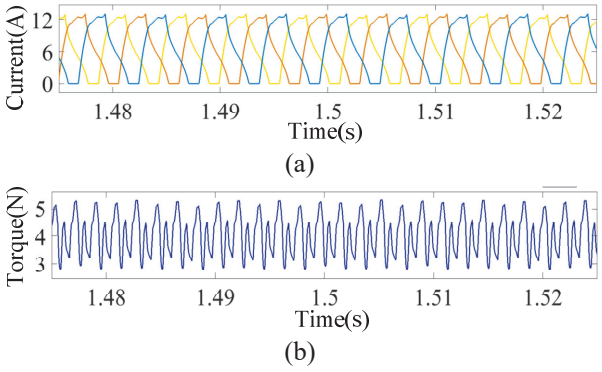


Fig. 14. Dynamic performance of rotary motion at 1000 r/min: (a) phase current waveform and (b) torque waveform.

The transient dynamic performance of the rotary motion is investigated under two typical control modes, namely current chopping control (CCC) and single pulse control (SPC). Under the CCC mode, the machine operates at a low rotational speed of 600 r/min with a preset rated chopping current of 15 A, and the corresponding transient phase current and dynamic torque waveforms are illustrated in Fig. 13. Under the high-speed SPC mode, the machine runs at 1000 r/min under an adjustable load torque of 4 N·m, where the phase current exhibits a typical single-pulse waveform shape due to the elevated back EMF, as shown in Fig. 14. For a

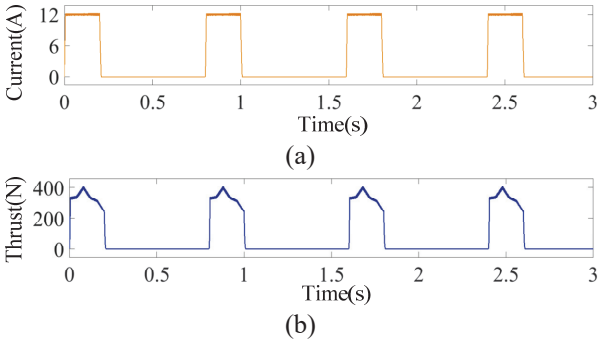


Fig. 15. Fig. 15. Dynamic performance of linear motion at 0.05 m/s: (a) phase current waveform and (b) thrust waveform.

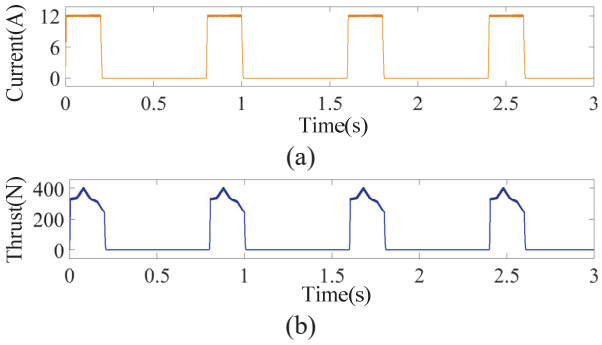


Fig. 16. Dynamic performance of linear motion at 0.1 m/s: (a) phase current waveform and (b) thrust waveform.

fair comparison, both operational modes are configured with a DC bus voltage of 96 V and identical turn-on and turn-off angles. The simulation results demonstrate that the dynamic torque effectively tracks the command values with acceptable ripples, verifying the excellent rotational drive capability.

Similarly, the transient dynamic characteristics of the linear motion are evaluated at different mover translation speeds of 0.05 m/s and 0.1 m/s. For both speed configurations, a DC bus voltage of 96 V and identical turn-on and turn-off positions are maintained. Figures 15 and 16 display the transient single-phase current and dynamic thrust waveforms, respectively. It can be observed that a reliable and robust dynamic thrust output is consistently maintained, which proves the feasibility of the linear actuation.

V. CONCLUSION

This study investigates the electromagnetic characteristics of a novel two-degree-of-freedom TLRSRM. By combining 3D finite element parameter sweeps with system-level Simulink dynamic simulations, the structural feasibility and operational rationality of the proposed topology are comprehensively verified. Under low excitation, the inductance and flux linkage exhibit near-linear behavior, whereas localized magnetic saturation under high currents introduces distinct nonlinear characteristics at the aligned position. Furthermore, the electromagnetic cross-coupling effect between the rotary and linear sections is quantitatively analyzed.

The dynamic performance further demonstrates the robust driving capabilities of the machine under typical control schemes. In the rotary mode, the phase currents and dynamic torque effectively track the operational demands under both CCC (600 r/min, 15 A) and SPC (1000 r/min, 4 N·m) modes with identical turn-on and turn-off angles. In linear mode, reliable and stable dynamic thrust outputs are consistently maintained at translation speeds of 0.05 m/s and 0.1 m/s under a 96 V DC bus voltage. Characterized by a compact structure and efficient electromagnetic performance, this TLRSRM framework provides a solid theoretical foundation for subsequent optimization and shows significant potential in advanced applications such as marine energy utilization.

ACKNOWLEDGMENT

This work is supported by the National Natural Science Foundation of China International (regional) cooperation and exchange projects NSFC-RSF under Grant W2412064 and the Shenzhen Collaborative Innovation Special Plan International Cooperation Research Project under Grant GJHZ20240218114300002.

REFERENCES

[1] H. Chen, R. Nie, and X. Li, "A transverse-flux single-phase tubular switched reluctance linear machine with 4 poles," *IEEE Transactions on Applied Superconductivity*, vol. 31, no. 8, pp. 1–4, Nov. 2021.

[2] K. Manohar and K. Srichandan, "Analysis of quadrupole magnetic field reluctance-based launcher with different coil switching patterns," *IEEE Transactions on Plasma Science*, vol. 51, no. 5, pp. 1370–1376, May 2023.

[3] L. Zhang, L. Yan, X. Wei, H. Su, Z. Dong, and L. Li, "Stress analysis of a flat linear switched reluctance motor with double excitation windings," in *CSAA/IET International Conference on Aircraft Utility Systems*, Nanchang, China, pp. 1240–1245, 2022.

[4] W. Ding, H. Fu, and Y. Hu, "Characteristics assessment and comparative study of a segmented-stator permanent-magnet hybrid-excitation SRM drive with high-torque capability," *IEEE Transactions on Power Electronics*, vol. 33, no. 1, pp. 482–500, Jan. 2018.

[5] R. Nie, J. Si, Y. Jia, P. Wang, S. Xu, and J. Liang, "Comprehensive comparison of mover-PM and stator-PM linear-rotary generators for wind-wave combined energy conversion system," *IEEE Transactions on Industry Applications*, vol. 60, no. 4, pp. 6170–6185, July-Aug. 2024.

[6] H. Chen, Y. Zhan, and R. Nie, "Multiobjective optimization design of single-phase tubular switched reluctance linear launcher," *IEEE Transactions on Plasma Science*, vol. 47, no. 5, pp. 2431–2437, May 2019.

[7] H. Chen, R. Nie, and H. Wang, "A transverse flux single-phase tubular-switched reluctance linear launcher with eight-pole structure," *IEEE Transactions on Plasma Science*, vol. 47, no. 5, pp. 2331–2338, May 2019.

[8] D. Wang, C. Shao, X. Wang, and C. Zhang, "Performance characteristics and preliminary analysis of low-cost tubular linear switch reluctance generator for direct drive WEC," *IEEE Transactions on Applied Superconductivity*, vol. 26, no. 7, pp. 1–5, Oct. 2016.

[9] D. H. Wang, X. H. Wang, C. L. Shao, and L. X. Xiong, "Design aspects of a high thrust density dual stator yokeless linear switched reluctance machine for harsh conditions," in *2015 IEEE International Conference on Applied Superconductivity and Electromagnetic Devices*, Shanghai, China, pp. 468–469, 2015.

[10] H. Chen, Z. Li, W. Yan, and R. Nie, "Flux characteristics analysis of a single-phase tubular switched reluctance linear launcher based on 3D magnetic equivalent circuit," *IEEE Transactions on Plasma Science*, vol. 47, no. 5, pp. 2507–2513, May 2019.

[11] S. Xu, X. Jiang, J. Si, R. Nie, and P. Wang, "A two-degree-of-freedom double-stator linear-rotary switched reluctance motor for an industrial robot," in *2023 26th International Conference on Electrical Machines and Systems*, Zhuhai, China, pp. 3666–3671, 2023.

[12] W. Wu, J. B. Dunlop, S. J. Collocott, and B. A. Kalan, "Design optimization of a switched reluctance motor by electromagnetic and thermal finite-element analysis," *IEEE Transactions on Magnetics*, vol. 39, no. 5, pp. 3334–3336, Sep. 2003.

[13] S. Zhao, H. Chen, R. Nie, and J. Liu, "Multi-objective optimal design of double-sided switched reluctance linear generator for wave power generation," *Compel*, vol. 38, no. 6, pp. 1948–1963, 2019.

[14] H. Chen, Y. Zhan, H. Wang, and R. Nie, "A tubular permanent magnet linear generator with novel structure," *IEEE Transactions on Plasma Science*, vol. 47, no. 6, pp. 2995–3001, June 2019.

[15] S. Xu, X. Jiang, J. Si, R. Nie, and P. Wang, "A two-degree-of-freedom double-stator linear-rotary switched reluctance motor for an industrial robot," in *26th International Conference on Electrical Machines and Systems (ICEMS)*, Zhuhai, China, pp. 3666–3671, 2023.

[16] F. Yu, H. Chen, W. Yan, V. F. Pires, J. F. A. Martins, P. Rafajdus, A. Musolino, L. Sani, M. P. Aguirre, M. A. Saqib, M. Orabi, and X. Li, "Design and multiobjective optimization of a double-stator axial flux SRM with full-pitch winding configuration," *IEEE Transactions on Transportation Electrification*, vol. 8, no. 4, pp. 4348–4364, Dec. 2022.



Cheng Liu received the B.S. degree in electrical engineering and automation from Hubei University of Technology, Wuhan, Hubei, China, in 2020, and the M.S. degree in electrical engineering from Hubei University of Technology, Wuhan, Hubei, in 2023. He is currently pursuing a Ph.D. degree in electrical engineering at China University of Mining and Technology, Xuzhou. His research interests include switched reluctance motor design control, ocean wave power generation, and electric vehicles.



Hao Chen (SM'08) received the B.S. and Ph.D. degrees from the Department of Automatic Control, Nanjing University of Aeronautics and Astronautics, Nanjing, China, in 1991 and 1996, respectively. In 1998, he became an Associate Professor with the School of Information and Electrical Engineering, China University of Mining and Technology, Xuzhou, where he has been a Professor since 2001. From 2002 to 2003, he was a Visiting Professor at Kyungsung University, Busan, Korea. Since 2008, he has also been an Adjunct Professor at the University of Western Australia, Perth, Australia. He is the author of one book and has also authored more than 190 papers. He is the holder of 15 US Patents, 23 Australian Patents, one Danish Patent, seven Canadian Patents, three South African Patents, 10 Russian Patents, 86 Chinese Invention Patents, and six Chinese Utility Model Patents. His current research interests include motor control, linear launcher, electric vehicles, electric traction, servo drives, and wind power generator control.

Chen was the recipient of both the Prize of Science and Technology of Chinese Youth and the Prize of the Fok Ying Tong Education Foundation for Youth Teachers in 2004. He was awarded first prize in the Science and Technology advanced of Province and Ministry once, second prize in the Science and Technology advanced of Province and Ministry seven times, and third prize in Science and Technology Advanced of

Province and Ministry 14 times. He became the Chinese New Century Hundred-Thousand Ten-Thousand Talents Engineering National Talent in 2007, and won the Government Especial Allowance of People's Republic of China State Department since 2006.



Marcin Wardach was born in Poland in 1980. He graduated and received the Ph.D. degree from the Electrical Department, Szczecin University of Technology, Szczecin, Poland, in 2004 and 2009, respectively. From 2020 until now, he has served as Associate Professor with the Faculty of Electrical Engineering, West Pomeranian University of Technology, in Szczecin. Since 2024, he has served as Vice-Dean for Organization and Development and Head of the Department of Electrical Machines and Drives at the Faculty of Electrical Engineering, West Pomeranian University of Technology, in Szczecin. From 2019 to 2025, he worked as an electrical machine designer at mPower Sp. z o.o. company. His research interests include the design of electrical machines and drives, especially unconventional and hybrid excited. He is the author of over 100 scientific papers and post-conference publications. Since 2022, he has been President of the Szczecin Branch of the Association of Polish Electrical Engineers (SEP). He is also a member of the Polish Society of Theoretical and Applied Electrical Engineering.



Javokhir Toshov currently works at the Department of Mining Electromechanics, Tashkent State Technical University, Uzbekistan. Javokhir does research in Mechanical Engineering and Mining Engineering in the Department of Electronic Devices Manufacturing Technologies, Faculty of Electronic and Automation Engineering, Tashkent State Technical University, Tashkent 100095, Uzbekistan; Department of Theoretical and Experimental Physics, Faculty of Physics, Karshi State University, Karshi 180119, Uzbekistan.



Xing Wang received the B.S. degree from China University of Mining and Technology, Xuzhou Jiangsu, China, in 1996, and M.S. degree from China University of Mining and Technology, Xuzhou Jiangsu, in 1999. In 2007, she became an Associate Professor with China University of Mining and Technology, Xuzhou. She is a holder of four US Patents, nine Australian Patents, two Canadian Patents, four Russian Patents, 12 Chinese Invention Patents, three Chinese Utility Model Patents, and has authored 15 papers.



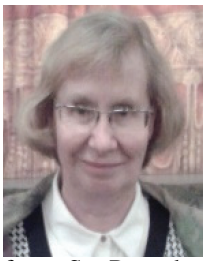
Bodrenkov Evgenii Alexandrovich received the B.S. and M.S. degree from Federal State Budgetary Educational Institution of Higher Education, Amur State University, and Ph.D. degrees from Federal State Autonomous Educational Institution of Higher Education, Peter the Great St. Petersburg Polytechnic University.



Popov Stanislav Olegovich received the M.S. degree in the field of "Electric power plants and automation of power systems" in 2008, and Ph.D. in Technical Sciences. He has been an associate professor at the Institute of Energy, from 2008 to present in SPBSTU.



Nikolay Korovkin (Member, IEEE) received the M.S., Ph.D., and Doctorate degrees in electrical engineering from the State Polytechnic University, Saint Petersburg, Russia, in 1977, 1984, and 1995, respectively. He is currently a Professor with the Institute of Energy, Peter the Great Saint Petersburg Polytechnic University, Saint Petersburg. Since 1996, he has been an Academician with the Academy of Electrotechnical of Russian Federation, Saint Petersburg. He has about 300 published and reviewed works in Russia and abroad. His main research interests include the inverse problems in electromagnetics, systems described by stiff equations, ill conditioned problems, optimization of power networks, optimization of the location FACTS and PMU-devices, SMART grid technologies, methods for the analysis of reliability and ensuring power balance in EPS, methods of multicriteria optimization and their application to steady-state processes in power networks, transients in transmission line systems, impulse processes in linear and nonlinear systems, problems of the electromagnetic prediction of earthquakes, and identification of the behavior of the biological objects under the influence of the electromagnetic fields.



Sakhno Liudmila (Member, IEEE) received the B.S., M.S., and Ph.D. degrees from Russia Polytechnic Institute, Saint Petersburg, Russia, in 1972, 1974, and 1982, respectively, and the Doctorate degree in electromechanics and electrical apparatus from St. Petersburg State Technical University, Saint Petersburg, in 2006. She is currently a Professor of Higher School of High Voltage Power Engineering, Peter the Great Saint Petersburg Polytechnic University, Saint Petersburg. She has about 200 published and reviewed works in Russia and abroad. Her research interests include the electromagnetic problems in power transformers, the skin effect and the proximity effect in the windings of converter transformers, electromagnetic and thermal characteristics of arc and resistance welding transformers, mechanical strength of structural elements under the action of loads, and field-circuit modeling in high frequency resistance spot welding systems. She has eight Russian Federation Patents.



Mohamed Orabi (Senior Member, IEEE) received the Ph.D. degree in power electronics from Kyushu University, Fukuoka, Japan, in 2004. He is currently a Professor with the Department of Electrical Engineering, Faculty of Engineering, Aswan University, Aswan, Egypt, where he is also the Founder and the Director of the Aswan Power Electronics Application Research Center. He is the Deputy Dean for the Postgraduate Studies and Research. His current research interests include high-frequency DC-DC converters and power factor correction converters for LEDs and electric vehicles applications, integrated power management, analysis and modeling of nonlinear circuits, and inverter control and design for renewable energy applications. Orabi was the Chair of the IEEE Power Electronics Egypt Chapter until 2020. He is a Guest Editor for *IEEE Journal of Emerging and Selected Topics in Power Electronics*.



Mahmoud A. Gaafar (Senior Member, IEEE) received the B.Sc. and M.Sc. degrees in electrical engineering from Aswan University, Aswan, Egypt, in 2004 and 2010, respectively, and the Ph.D. degree in electrical and electronics engineering from Kyushu University, Fukuoka, Japan, in 2017. In 2017, he joined the Aswan Power Electronics Applications Research Center (APEARC), Aswan University. He is currently an Assistant Professor with the Department of Electrical Engineering, Faculty of Engineering, Aswan University. He has been involved in several projects related to power electronics applications. His current research interests include the design and control of power electronics converters for photovoltaic, motor drives, and battery-based systems. Gaafar is also a member of the IEEE Power Electronics Society. He was a recipient of the Baek-Hyun Award in 2018 from the Korean Institute of Power Electronics for his academic contribution to the field of power electronics.



Emmanuel Karapidkis is an Electrical and Computer Engineer. He was Dean at School of Engineering from 2019 to 2025, and Director of Energy, Environment and Climate Change Institute – IEECC (ieecc.hmu.gr) in Hellenic Mediterranean University HMU (hmu.gr). Since 2022, he has been President of the Board in Hellenic Association of Electricity Storage Systems – HAESS (www.haess.gr). His research interests focus on energy systems, power systems operation, diverse & dispersed generation, micro-grids, renewable energy technologies, energy storage, and energy markets. He is/was scientific coordinator (PI) in 12 European financed projects, 15 National programs and several private funded projects, with more than 8 million euros in total. He has published more than 120 papers (Scopus Author ID 6506872824) in prestigious journals and scientific conferences, and four scientific book chapters. From 2011 to 2015, he was a Member of the Board in Regional Council of Innovation, and from 2015 to 2017, Member of the Board in Energy Planning Council at Region of Crete.



Aris Evangelos Dimeas is an Assistant Professor at the School of Electrical and Computer Engineering of the National Technical University of Athens (NTUA), with more than 20 years of experience in power systems operation, smart grids, and energy system digitalization. His expertise spans distribution and transmission system operation, renewable energy integration, microgrids, flexibility markets, artificial intelligence applications, and advanced control and decision-support software. He has played a leading technical and coordination role in more than 30 EU-funded research and innovation projects (H2020 and Horizon Europe), collaborating

closely with TSOs, DSOs, regulators, industry, and the European Commission. His work bridges research and real-world deployment, with demonstrated impact on system supervision, resilience, market design, and data-driven grid operation, while his scientific contributions include high-impact publications in leading IEEE and international journals.



Sherif Moussa is Dean of the School of Engineering, Applied Science, and Technology at the Canadian University Dubai (CUD), UAE. He earned his Ph.D. in Electrical and Computer Engineering from the University of Québec at Trois-Rivières, Canada, and his M.Sc. in Electrical and Computer Engineering from the University of Waterloo, Canada. Since joining CUD in 2007, Moussa has led the School's remarkable growth, overseeing the launch and accreditation of several engineering and computing programs, including mechatronics engineering, computer science, cybersecurity, software design, power and renewable energy engineering, and the M.Sc. in Artificial Intelligence. His leadership has also advanced international collaborations, notably with Queen's University and the University of Ottawa, and strengthened CUD's engagement with industry partners in emerging technologies. Moussa's research interests span wireless communication, computer networks, machine learning, and digital systems design. He has published widely in international journals and conferences, serves on technical committees, and is the recipient of the 2015 CUD Research Excellence Award. He is also the founder of CUD's Robotics Club and a strong advocate for innovation and experiential learning in engineering education.



Habes Ali Khawaldeh (Member, IEEE) received the B.E. degree in electrical and computer engineering from The Hashemite University, Jordan, in 2009, and the M.S. degree in electrical power engineering from Yarmouk University, Jordan, in 2013. In 2022, Habes Ali Khawaldeh received his Ph.D. degree in power electronics engineering from the Faculty of Engineering and Information Technology, University of Technology Sydney (UTS), Australia. Since 2018, he has been a Casual Academician with UTS for various power electronics subjects. Since July 2009, he has been working as an electrical engineer with different companies in Jordan. He was a part-time Faculty Member with Yarmouk University for various power electronics subjects. He was a full-time Faculty Member with Al-Hussein Bin Talal University from 2015 to 2018. His current research interests include renewable energy (RE) systems, power converter design for RE applications, battery systems, multi-port DC/DC converters, and energy conversion systems for the smart grid. He received a Grant from Al al-Bayt University for his Ph.D. degree. He is currently a reviewer for several IEEE, IET, and Elsevier journals. Currently, Habes Ali Khawaldeh is an assistant professor at the University of Al al-Bayt in Jordan.

A Lumped Parameter Thermal Network Model for Dual-Stator Mover-PM Linear-Rotary Generators

Chenxi Li, Rui Nie*, Shuai Xu, Yanqi Wei, Peixin Wang, and Jikai Si

School of Electrical and Information Engineering
Zhengzhou University, Zhengzhou 450001, China
lcx010707@163.com, nierui@zzu.edu.cn, xszzu2020@zzu.edu.cn,
weiyanqi@zzu.edu.cn, wangpeixin@zzu.edu.cn, sijikai@zzu.edu.cn
*Corresponding Author

Abstract – Mover-permanent magnet linear-rotary generators (MPMLRGs) with dual-stator topology and two degrees of freedom (2-DOF) have attracted growing interest due to their high integration and compactness, enabling coupled linear-rotary motion for direct-drive energy conversion and multifunctional actuation systems. However, the coupled linear-rotary motion and unsymmetric dual-stator topology lead to complex thermal behaviors, and the associated thermal characteristics remain insufficiently investigated compared to electromagnetic studies. In this paper, a lumped-parameter thermal network (LPTN) model is developed for a dual-stator MPMLRG to accurately capture its asymmetric heat transfer and temperature rise under helical motion. A novel approach is proposed to determine the air-gap convective heat transfer coefficients under coupled linear-rotary operation, along with a time-weighted correction method to account for the partial axial overlap of stator-mover surfaces. The thermal model is validated against 3-D thermal finite element analysis (FEA), showing good agreement while significantly reducing computational effort. The results provide useful insights into the thermal management of the dual-stator MPMLRG and establish a foundation for future design optimization and cooling enhancement.

Index Terms – Dual-stator topology, lumped-parameter thermal network, permanent magnet linear-rotary generator, thermal analysis.

I. INTRODUCTION

Permanent-magnet linear-rotary generators (PMLRGs) have attracted increasing attention in compact directdrive electromechanical conversion systems, such as wind-wave combined energy conversion (WWCEC), advanced manufacturing, and robotic actuation [1–5]. Linear-rotary integration enables high torque/thrust density with reduced transmission complexity, which is particularly attractive for marine energy applications requiring high integration and reliability [6]. However, offshore environments are typically characterized by strong reciprocating loads, high humidity and salinity, and limited cooling capability, where excessive temperature rise may cause irreversible permanent-magnet demagnetization and accelerated insulation aging, thus threatening long-term operational reliability [7, 8]. Therefore, thermal modeling and temperature prediction are critical for mover-permanent magnet linear-rotary generators (MPMLRGs) design and safe operation.

Although the electromagnetic performance of PMLRGs has been extensively investigated, studies on their thermal behaviors remain relatively limited. Representative configurations, such as dual-stator and dual-rotor PMLRGs employing alternately arranged toroidal and arc-shaped permanent magnets, have been reported in [9, 10], demonstrating the feasibility of compact linear-rotary integration. However, for MPMLRGs, the coupled helical motion and asymmetric structure lead to time-varying air-gap convection and nonuniform heat-transfer paths, posing significant challenges to accurate temperature prediction and thermal design.

Thermal analysis of electrical machines is commonly performed using computational fluid dynamics (CFD), the finite element method (FEM), and lumped-parameter thermal network (LPTN) models [11–13]. CFD is often used to evaluate convective heat transfer coefficients, while FEM provides accurate temperature distributions but is computationally expensive for rapid design iterations and optimization studies [14]. In contrast, LPTN offers a practical balance between accuracy and efficiency and has been widely used for fast thermal evaluation. Most existing LPTN studies, however, focus on conventional single degree-of-freedom (1-DOF) rotary or linear machines, and their extension to two degrees of freedom (2-DOF) linear-rotary generators (LRGs) has rarely been addressed. For instance,

Submitted On: January 29, 2026
Accepted On: July 23, 2026

1054-4887 © ACES

https://doi.org/10.13052/2026.ACES.J.410604

equivalent thermal networks have been established for various machine types, including flux-switching permanent-magnet double-rotor machines [15], brushless doubly-fed generators [16], surface-mounted and interior permanent magnet synchronous motors [17], oil-cooled segmented-stator machines [18], and dual-radial-ventilated permanent magnet synchronous generators [19]. Despite these advances, an LPTN framework that explicitly captures motion-coupled air-gap convection and asymmetric overlap-induced heat-transfer variation for dual-stator MPMLRG is still lacking. Different from conventional air-gap thermal models that assume pure rotational motion and full axial overlap, the proposed LPTN explicitly incorporates the coupled linear-rotary kinematics and the timevarying effective air-gap exposure unique to dual-stator MPMLRG.

To bridge this gap, this paper develops an LPTN model for a dual-stator MPMLRG that explicitly accounts for coupled helical motion and asymmetric air-gap geometry. In particular, the proposed model improves temperature prediction accuracy by incorporating motion-coupled air-gap convection and the effective heat-transfer variation induced by partial axial overlap between the mover and stator surfaces. The main contributions of this work are summarized as follows:

1. A method is proposed to determine air-gap convective heat transfer coefficients under coupled helical motion by extending classical empirical correlations to the 2-DOF operating condition.
2. A time-weighted correction approach is introduced to account for the partial axial overlap between the mover and stator surfaces caused by structural asymmetry.
3. The proposed LPTN model is validated against 3-D transient thermal finite element analysis (FEA), demonstrating close agreement with significantly reduced computation time.

The remainder of this paper is organized as follows. Section II introduces the machine structure and material data. Section III presents the loss models. Section IV describes the LPTN modeling process, including the proposed air-gap heat transfer coefficient calculation and timeweighted correction method. Section V presents the LPTN results and the 3-D FEA verification. Section VI concludes the paper and discusses potential future work.

II. TOPOLOGY OF THE DUAL-STATOR MPMLRG

A. Structure

The configuration of the dual-stator MPMLRG is shown in Fig. 1. The machine consists of an outer stator, a shared mover, and an inner stator, enabling integrated rotary and linear energy conversion in a compact structure. Permanent magnets are mounted on both the outer and inner surfaces of the mover, classifying the machine as a moverpermanent-magnet topology.

The outer stator and mover outer surface form the rotary generation unit (RGU), while the inner stator and mover inner surface constitute the linear generation unit (LGU). Both units adopt a 15-slot/20-pole configuration and are mechanically coupled through the common mover yoke. Concentrated windings are employed in the outer stator for rotary generation, whereas ring-shaped windings are arranged in the inner stator for linear generation. Correspondingly, arc-shaped and ring-shaped permanent magnets are radially magnetized with alternating polarities on the mover surfaces.

This dual-armature, dual-winding architecture provides improved integration, enhanced fault tolerance, and flexible control capability while maintaining structural compactness. The key geometric and electrical parameters are summarized in Table 1.

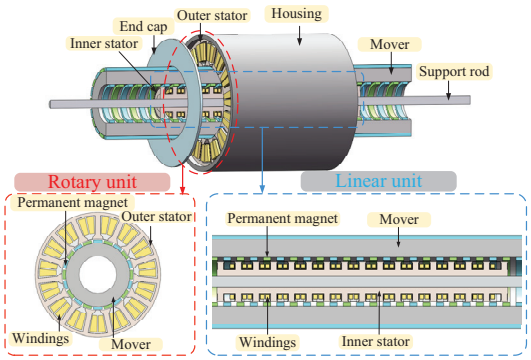


Fig. 1. Structure of the MPMLRG.

B. Materials

The material properties of the MPMLRG significantly affect both electromagnetic and thermal behaviors. The permanent magnets are N48, and the stator and mover cores are made of laminated silicon steel 50W470. Both the RGU and LGU stator cores employ axially laminated silicon steel sheets. Although axial lamination may not be optimal for all magnetic flux paths in tubular linear machines, it is adopted in this study, and its influence on the thermal model is reflected through the anisotropic thermal conductivities assigned to the laminated cores. A discussion on the influence of lamination orientation in tubular linear machines can be found in [20].

Thermal modeling of the stator slots is nontrivial due to the composite winding region. Therefore, an equivalent thermal conductivity approach is adopted to represent the anisotropic heat conduction of the slot

Table 1: Key parameters of the MPMLRG

Parameter		Symbol	Value
RGU	Outer diameter of outer stator	D_{so1}	150 mm
	Inner diameter of outer stator	D_{si1}	86 mm
	Outer diameter of mover	D_{mo}	84 mm
	Length of outer stator	l_{os}	150 mm
	Outer stator pole height	h_{sp1}	22.5 mm
	Outer stator yoke height	h_{sy1}	3.7 mm
	Air-gap thickness	$l_{\text{air-gap 1}}$	1 mm
	Rated speed	ω	300 rpm
	Number of turns per phase	N_{ph1}	$175(d = 2.0$ mm$)$
	Resistance of phase winding	R_{ph1}	0.468Ω
LGU	Outer diameter of inner stator	D_{so2}	36 mm
	Inner diameter of inner stator	D_{si2}	10 mm
	Inner diameter of mover	D_{mi}	39 mm
	Length of inner stator	l_{is}	262.5 mm
	Inner stator pole height	h_{sp2}	6 mm
	Inner stator yoke height	h_{sy2}	22 mm
	Air-gap thickness	$l_{\text{air-gap2}}$	1.5 mm
	Rated speed	v	1 m/s
	Number of turns per phase	N_{ph2}	$125(d = 1.5$ mm$)$
	Resistance of phase winding	R_{ph2}	0.167Ω

Table 2: Material thermal data

Model Region	Thermal Conductivity (W/(m·K))			Density (kg/m^3)	Specific Heat (J/(kg·K))
	Direction X	Direction Y	Direction Z		
Stator slots of RGU	0.23	0.23	276.06	5514.34	405.9
Stator slots of LGU	273.05	273.05	0.19	6411.22	403
Permanent magnet	9	9	7	7500	400
Lamina ted core	35	35	2	7650	450
Support rod	47	47	47	7850	470
Housin g	90	90	90	2700	900
End cap	0.3	0.3	0.3	920	1900

Note: X, Y, and Z denote the local radial, circumferential, and axial directions, respectively.

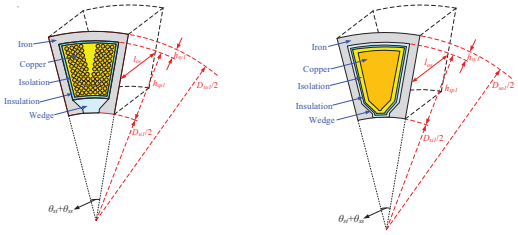


Fig. 2. Dimensions of the RGU stator slot: (a) individual slot geometry and (b) equivalent slot model.

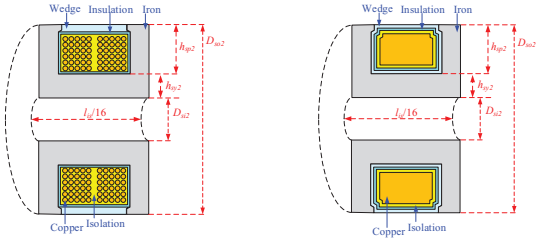


Fig. 3. Dimensions of the LGU stator slot: (a) individual slot geometry and (b) equivalent slot model.

region. As shown in Figs. 2 and 3, the slot region is homogenized by combining the copper conductors, insulation, impregnation materials, wedges, and slot fillers into an equivalent anisotropic medium. The homogenized slot regions correspond to the equivalent stator-slot materials used in the thermal model. Owing

to the different winding configurations, the RGU and LGU stator slots exhibit different principal thermal conductivity directions. The RGU winding is mainly arranged along the axial direction, whereas the annular winding of the LGU provides higher equivalent thermal conductivity within the plane of the winding layers. The equivalent conductivities are determined from the slot geometry, material fractions, and a standard series model. Consequently, the detailed material distribution inside each slot is represented by an equivalent homogeneous anisotropic region in the thermal model.

The thermal conductivities, densities, and specific heats used in the transient thermal analysis are summarized in Table 2.

III. LOSS MODELS

Accurate loss estimation is essential for thermal analysis because the losses act as heat sources. In this section, the losses of the MPMLRG under different operating conditions are analyzed using both FEM and analytical methods.

A. Copper loss

The MPMLRG operates at relatively low electrical frequencies (50 Hz for RGU and 41.67 Hz for LGU under rated conditions). Therefore, only DC resistance is considered, and copper loss is calculated as follows:

$$P = mI_{ph}^2 R_{ph}, \tag{1}$$

where m is phase number, I_{ph} and R_{ph} are phase current (RMS) and phase resistance, respectively.

B. Core loss

According to the Steinmetz formula, the core loss can be expressed as [21]:

$$P_{FeH} = \int_{V_c} \left(\sum_{n=1}^{N} C_H (n\omega_s) B_n^2 \right) dV, \tag{2}$$

$$P_{FeE} = \int_{V_c} \left(\sum_{n=1}^{N} C_E (n\omega_s)^2 B_n^2 \right) dV, \tag{3}$$

where P_{FeH} and P_{FeE} represent the hysteresis and eddy-current losses (W/kg), V_c is the volume of the laminated iron core, B_n is the amplitude of the nth harmonic flux density, N is the total number of harmonics, ω_s denotes the fundamental electrical angular frequency (rad/s), the angular frequency of the nth harmonic is $n\omega_s$, and C_H and C_E are the hysteresis and eddy-current loss coefficients. In this study, $C_H = 183.674$ and $C_E = 1.224$, which were obtained by nonlinear fitting of the loss data for 50W470 silicon steel.

C. Permanent magnet eddy current loss

The magnetic field in the MPMLRG can be divided into two components: the main field, generated by the mover-mounted permanent magnets, which rotates and translates synchronously with the mover and is therefore approximately stationary in the permanent magnet reference frame, contributing negligibly to the permanent magnet eddy-current loss; and the harmonic field, which lacks such synchronism and consequently induces electromotive force (EMF), eddy currents, and associated losses in the permanent magnets of both the RGU and the LGU. The eddy-current loss in the mover-permanent magnets, resulting from harmonic components of the air-gap magnetic field, is quantified by (4) over one alternating-magnetization period, as described in [22]:

$$P_e = \frac{1}{T_e} \int_0^{T_e} \sum_{e=1}^{N_e} J_e^2 \frac{1}{\sigma_r} \Delta_e l_a dt \tag{4}$$

where P_e denotes the rotor eddy current loss [W], J_e is the current density in each element $[\mathrm{A/m^2}]$, Δ_e is the element area $[\mathrm{m^2}]$, l_a is the mover axial length [m], σ_r is the conductivity of the eddy current zone [S/m], and T_e is the time corresponding to an alternating magnetization period in each element.

D. Heat generation

To evaluate the thermal behavior of the 2-DOF MPMLRG under helical motion, five representative operating cases are considered by simultaneously varying the rotational and translational speeds of the mover around the rated condition. The volumetric heat generation rates of major components are given in Table 3. Case 1 corresponds to the rated speeds of 300 rpm and 1.0 m/s, while in Cases 2–5 the rotational speed is increased in steps of 50 rpm and the linear speed in steps of 0.2 m/s. For all cases, the RGU and LGU load resistances are set to 5 Ω and 1 Ω, respectively. The resulting losses are converted into volumetric heat generation rates and applied as heat sources in the LPTN and FEA models.

Table 3: Volumetric heat generation rates of major components

Motor Part	Heat Generation (W/m^3)				
	Case 1	Case 2	Case 3	Case 4	Case 5
Stator of RGU	10513.53	12085.01	13861.75	15418.34	16588.97
Winding of RGU	165496.42	201620.49	241031.21	266156.82	290465.48
PM of RGU	2437.40	3335.63	4595.64	5772.04	6974.32
Mover	42.49	59.29	80.92	100.64	108.76
PM of LGU	670.24	961.91	1028.13	1060.38	1066.33
Stator of LGU	207225.95	302137.07	415043.91	560906.21	692365.80
Winding of LGU	39518.48	55733.89	75263.31	99711.47	124060.68

IV. LUMPED PARAMETER THERMAL NETWORK MODEL

To facilitate numerical analysis, the motor structure is discretized into thermal nodes based on material properties and geometry. Thermal resistances between nodes are calculated according to their spatial arrangements and heat pathways. Losses from components are proportionally distributed to corresponding nodes. Steady-state and transient heat transfer equations are formulated and solved using MATLAB to obtain the temperature at each node.

To simplify the three-dimensional temperature field while maintaining sufficient accuracy, the following assumptions are adopted: (i) circumferential temperature symmetry is assumed; (ii) heat transfer is dominated by conduction, whereas radiation and skin effects are neglected; and (iii) the short end windings of the RGU are ignored.

Based on these assumptions, the machine is partitioned into representative thermal regions, each modeled as a thermal node located at its geometric center. Heat exchange between nodes is represented by thermal resistances. The resulting LPTN is illustrated in Fig. 4, where nodes are assigned to the stator yoke, stator slots, stator teeth, permanent magnets, mover yoke, air gaps, support rod, housing, end caps, and internal air regions of both the RGU and LGU.

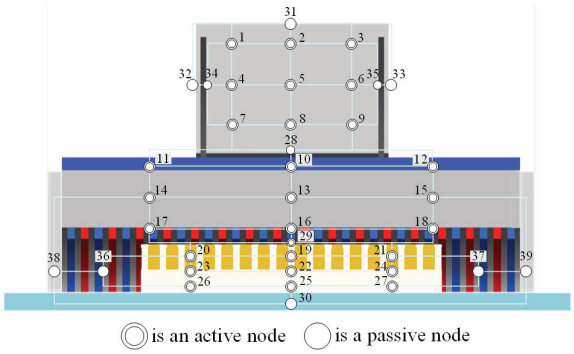


Fig. 4. Key thermal nodes of the MPMLRG cross-section.

A. Steady-state and transient thermal network method

The steady-state thermal behavior of the motor is modeled by formulating a linear algebraic system derived from the nodal energy balance equations. In this framework, the motor is discretized into multiple thermal nodes, each corresponding to a specific structural region. The inter-nodal heat conduction is captured by a global thermal conductance matrix G_s [23], constructed as the inverse of the thermal resistances between physically connected nodes. The internal heat generation due to electromagnetic losses is represented by a source vector Q_s, uniformly distributed across the corresponding nodes. The steady-state temperature distribution T_s is then obtained by solving:

$$G_s \cdot T_s = Q_s, \tag{5}$$

where T_s denotes the vector of steady-state nodal temperatures. Owing to the localized heat-transfer paths, G_s is symmetric and sparse, and its conductance topology (Fig. 5) provides an efficient representation of the steady-state thermal behavior of the MPMLRG.

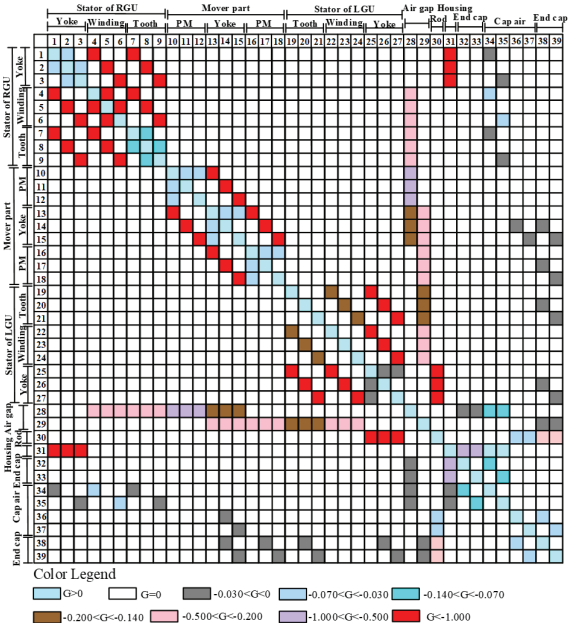


Fig. 5. Thermal conductance network between different components.

The transient thermal model describes the time-dependent temperature evolution by incorporating both internodal thermal conductance and thermal capacitance, the latter determined by material density, specific heat, and volume. The resulting dynamic thermal behavior is governed by the following first-order differential equation:

$$C_t \cdot \frac{dT_t}{dt} + G_t \cdot T_t = Q_t(t), \tag{6}$$

where C_t is the diagonal thermal capacitance matrix, G_t is the thermal conductance matrix, $T_t(t)$ represents the instantaneous nodal temperature vector, and $Q_t(t)$ denotes the time-dependent heat generation vector. This formulation captures both heat diffusion across components and energy accumulation due to thermal inertia.

B. Thermal resistance and thermal capacitance

Thermal resistance in electric machines can be categorized into two types: conduction thermal resistance

and convection thermal resistance. Conduction thermal resistance occurs within the solid components of the machine. As shown in Fig. 6, based on the fundamental law of heat conduction, the thermal conduction resistances of the two models are derived as follows [24].

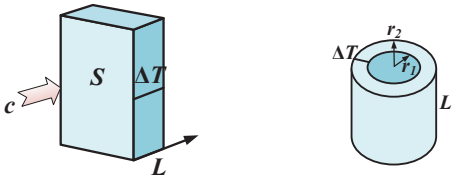
The thermal resistance of the flat plate conduction model is given by:

$$R = \frac{\Delta T}{Q} = \frac{L}{\lambda S}. \tag{7}$$

The thermal resistance of the cylindrical conduction model is given by:

$$R = \frac{\Delta T}{Q} = \int_{r_1}^{r_2} \frac{dr}{2\lambda \pi r L} = \frac{1}{2\pi\lambda L} \ln \frac{r_2}{r_1}, \tag{8}$$

where L is the length along the direction of heat flow [m], λ denotes the thermal conductivity of the material [W/(m·K)], and S represents the cross-sectional area for heat conduction [m^2].



(a) (b)

Fig. 6. Two types of conduction resistance models.

Thermal capacitance C can be given as:

$$C = mc_p, \tag{9}$$

where m denotes body mass and c_p is specific heat capacity.

As shown in Fig. 7, the nodes denote different components of the MPMLRG interconnected along the actual heat-transfer paths to establish the simplified LPTN. Based on well-established lumped-parameter thermal modeling theory, the thermal resistances and thermal capacitances of each node are determined from the corresponding geometry and material properties, and only the general formulation is presented here for conciseness.

C. Air gap heat transfer coefficient

The convective heat transfer within the air gap is evaluated through the following approach. For unified expression, the outer and inner boundaries of each cylindrical air gap are denoted as r_1 and r_2. Initially, the air-gap Taylor number T_{ag}, defined using the mean radius $r_g = (r_1 + r_2)/2$, and the geometry factor F_g [25] are calculated by:

$$Ta_g = \omega r_g^{0.5} (r_1 - r_2)^{1.5} / v_{air}, \tag{10}$$

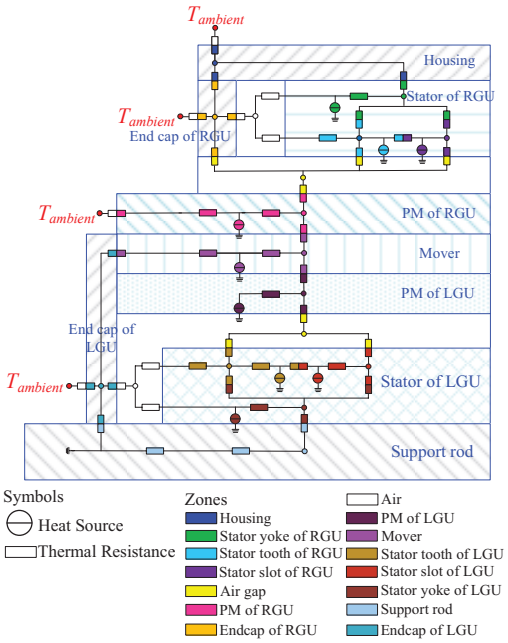


Fig. 7. Simplified LPTN for the MPMLRG.

and

$$F_g = \frac{\pi^2}{41.19\sqrt{S}} \left(1 - \frac{r_1 - r_2}{2r_g}\right)^{-1}, \tag{11}$$

where ω denotes the mover's angular velocity and v_{air} is the kinematic viscosity of air. The structural parameter S is given by:

$$S = 0.0571 \times \left[1 - 0.652 \times \frac{(r_1 - r_2)/r_g}{1 - (r_1 - r_2)/(2r_g)}\right] + 0.00056 \times \left[1 - 0.652 \times \frac{(r_1 - r_2)/r_g}{1 - (r_1 - r_2)/(2r_g)}\right]^{-1}. \tag{12}$$

Subsequently, the air-gap Nusselt number Nu_g is obtained as a function of $(Ta_g/F_g)^2$, as shown in (13). When $(Ta_g/F_g)^2 < 1700$, thermal convection is negligible, and heat transfer across the air gap is dominated by conduction. For $1700 < (Ta_g/F_g)^2 < 10^4$, the flow in the gap becomes laminar with vortex formation, while for $10^4 < (Ta_g/F_g)^2 < 10^7$, turbulent flow governs the convective heat exchange.

$$Nu_g = \begin{cases} \dfrac{2(r_1 - r_2)/r_{ro}}{\ln[1 + (r_1 - r_2)/r_{ro}]}, & \text{for } \dfrac{Ta_g^2}{F_g^2} < 1700 \\ 0.128(Ta_g^2/F_g^2)^{0.367}, & \text{for } 1700 < \dfrac{Ta_g^2}{F_g^2} < 10^4 \\ 0.409(Ta_g^2/F_g^2)^{0.241}, & \text{for } 10^4 < \dfrac{Ta_g^2}{F_g^2} < 10^7. \end{cases} \tag{13}$$

Based on the calculated Nusselt number, the air-gap convective heat transfer coefficient h_g can be derived accordingly as:

$$h_g = k_{air}\frac{Nu_g}{2g}. \tag{14}$$

Referring to (11) and the dimensional parameters listed in Table 1, the geometry factor of outer and inner airgap for the analyzed MPMLRG at rated speed is calculated to be $F_g^{(\mathrm{RGU})} = 1.01190 \approx 1$ and $F_g^{(\mathrm{LGU})} = 1.041667 \approx 1$, respectively. The air's kinematic viscosity is taken as $v_{air} = 1.5 \times 10^{-5}$ and the air-gap thermal conductivity is $k_{air} = 0.023\ \mathrm{W/(m \cdot K)}$. According to (10), the corresponding air-gap Taylor numbers under the operating condition of a mover speed of $n = 300$ rpm are calculated as: $Ta_g^{(\mathrm{RGU})} = 13.65382, Ta_g^{(\mathrm{LGU})} = 16.66085$.

Since $(Ta_g^{(\mathrm{RGU})})^2/(F_g^{(\mathrm{RGU})})^2 \approx 180 < 1700$, and $(Ta_g^{(\mathrm{LGU})})^2/(F_g{}^{(\mathrm{LGU})})^2 \approx 243 < 1700$, heat transfer within the air gap is dominated by thermal conduction rather than convection. As a result, the air-gap convective heat transfer coefficient is calculated as: $h_g^{(\mathrm{RGU})} = 46.54556\ \mathrm{W/(m^2 \cdot K)}, h_g^{(\mathrm{LGU})} = 31.92737\ \mathrm{W/(m^2 \cdot K)}$. In this regime, $Nu_g \approx 1$, and the resulting h_g represents the conduction-dominated equivalent heat-transfer coefficient across the air gap (i.e., $h_g \approx k_{air}/\delta$). It should be noted that this formulation represents an equivalent heat-transfer coefficient across the air gap, which is commonly adopted in electrical machine thermal modeling when the air flow remains weak.

By substituting the thresholds $(Ta_g^{(\mathrm{RGU})})^2/(F_g^{(\mathrm{RGU})})^2$ and $(Ta_g^{(\mathrm{LGU})})^2/(F_g{}^{(\mathrm{LGU})})^2 = 1700, 10^4$, and 10^7 into (13), the corresponding boundary mover speeds for the RGU and LGU are determined to be 916, 2223, and 70308 rpm, and 793, 1923, and 60828 rpm, respectively, which indicates that the analyzed operating range is well within the conduction-dominated regime.

However, in the case of MPMLRG, the mover undergoes both rotational and translational motions simultaneously, resulting in a helical trajectory. To more accurately represent the convective flow driven by such compound motion, an effective air-gap velocity can be defined as:

$$u_{eff} = \sqrt{u_\theta^2 + u_z^2}, \tag{15}$$

where $u_\theta = \omega r_{gap}$ is the tangential velocity and u_z is the linear velocity of the mover. According to forced convection theory, the convective heat transfer coefficient is proportional to velocity raised to a power n, typically $n = 0.8$ for turbulent forced convection of gases:

$$h \propto u^n. \tag{16}$$

Consequently, the original convective coefficient can be corrected as:

$$h_{g,new} = h_g \cdot \left(\frac{u_{eff}}{u_\theta}\right)^{0.8}. \tag{17}$$

This correction allows the model to incorporate the enhancement in heat transfer caused by the superimposed translational motion of the mover.

To further explore the influence of motion parameters on air-gap heat transfer performance, the same five operating conditions (Cases 1–5) introduced in section III part D are adopted. These include the rated operating condition (Case 1) and four additional cases with increased rotational and linear speeds. In each case, the corresponding Taylor number and Nusselt number are calculated, and the convective heat transfer coefficients of both the air gaps of RGU and LGU are evaluated accordingly.

As shown in Fig. 8, the convective heat transfer coefficients of both air gaps increase with speed due to enhanced forced convection.

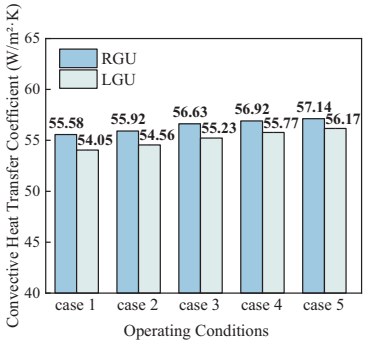


Fig. 8. Air-gap convective heat transfer coefficients.

Due to the dual-stator configuration of the MPMLRG, the outer and inner stators have axial lengths of 150 mm and 262.5 mm, respectively, whereas the mover spans a total of 400 mm. During operation, the mover undergoes a compound motion consisting of rotation and linear translation, resulting in a helical trajectory along the axial direction. Because of the mismatch in axial dimensions, not all portions of the mover surface are continuously enclosed by the stator cores. This partial air-gap exposure is illustrated schematically in Fig. 9, where the helical motion path and bidirectional travel of the mover are shown. Specifically, only a segment of the mover's outer surface forms an active air gap with the outer stator, while the rest is exposed to ambient air. A similar condition applies to the inner air gap.

To accurately represent this intermittent contact during motion, the convective heat transfer coefficients

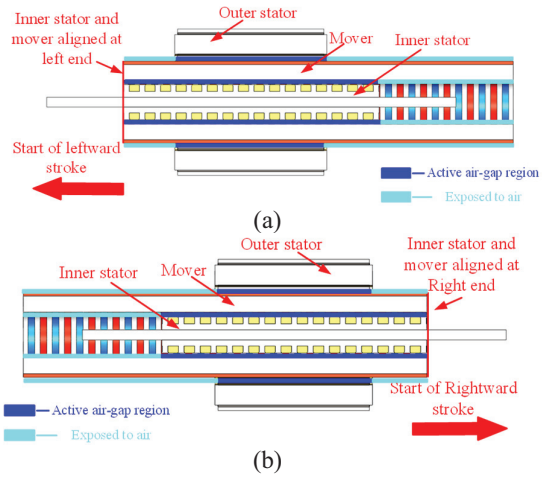


Fig. 9. Relative positions between the mover and stator during reciprocating motion: (a) left stroke limit and (b) right stroke limit.

of the inner and outer air gaps are modified using a time-weighted approach, expressed as:

$$\bar{h}_g = \eta \cdot h_g + (1-\eta) \cdot h_{air}, \tag{18}$$

where η is the effective contact ratio determined by the axial coverage of the stator relative to the mover and h_{air} is the natural convection heat transfer coefficient for the exposed surfaces. This method ensures the thermal model reflects realistic boundary conditions during coupled motion.

V. LPTN MODEL SOLVING AND 3-D FEA VERIFICATION

The proposed LPTN model predicts the average temperature of lumped components rather than detailed spatial distributions. Therefore, a 3-D thermal FEA model is established to obtain the temperature field and to validate the accuracy of the LPTN predictions. The heat transfer coefficients used in the FEA are consistent with those derived from the thermal network modeling in section IV.

A. Establishment of finite element model

The temperature distributions obtained from the 3-D thermal model implemented in ANSYS Workbench are shown in Fig. 10. The ambient temperature is set to 22°C.

At the rated operating condition, thermal behaviors are observed in the RGU and LGU. In the RGU, the stator iron and windings exhibit the highest temperatures, whereas the mover and permanent magnets remain significantly cooler due to partial exposure to ambient air. Similarly, in the LGU, the stator and windings

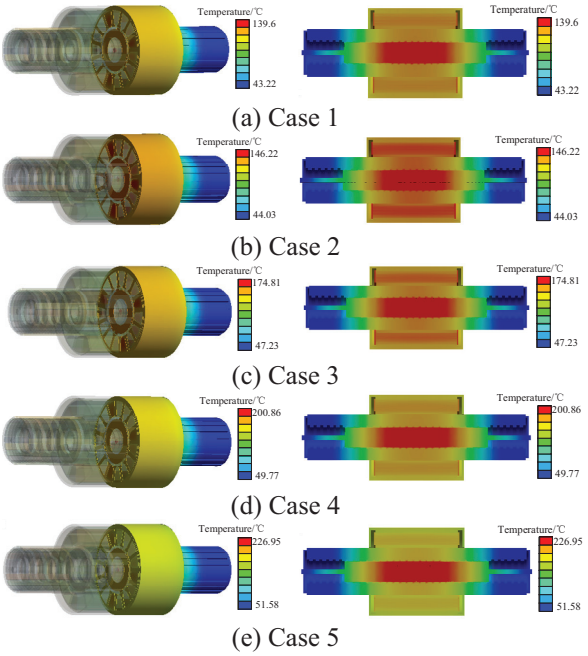


Fig. 10. 3-D temperature distribution and cross-section of MPMLRG @ five operating cases.

experience higher temperature rise, while the permanent magnets remain at relatively low temperatures. Although the LGU winding generates higher losses, its temperature is comparable to that of the RGU owing to the annular winding configuration, which enhances heat conduction to the stator core. However, the enclosure of the inner stator by the mover restricts heat dissipation, leading to a slightly higher temperature rise.

With increasing operating speed, the temperatures of both the RGU and LGU increase monotonically, indicating that natural convection alone is insufficient to offset the additional heat generation. At Case 5, severe thermal stress is observed, particularly in the stator windings, with the LGU inner winding becoming the most thermally critical component. In contrast, the mover and permanent magnets remain within a relatively safe temperature range.

It should be noted that these results are obtained under natural convection cooling only. At high operating speeds, excessive winding temperatures may compromise insulation reliability and reduce machine lifetime. Therefore, enhanced thermal management measures, such as winding impregnation or improved cooling strategies, are required for practical applications.

B. Steady-state LPTN

As shown in Fig. 11, the computing results of steady-state LPTN are compared with the results of FEA.

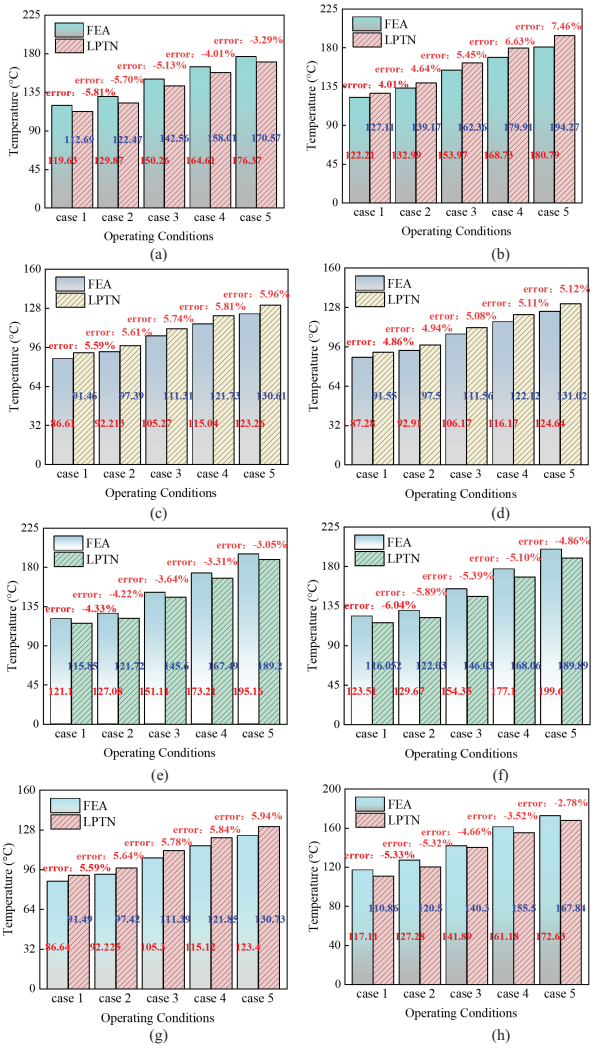


Fig. 11. Comparison of steady-state temperature of major components in the MPMLRG predicted by the LPTN and 3-D FEA: (a) RGU stator, (b) RGU winding, (c) RGU PM, (d) LGU PM, (e) LGU stator, (f) LGU winding, (g) mover, and (h) housing.

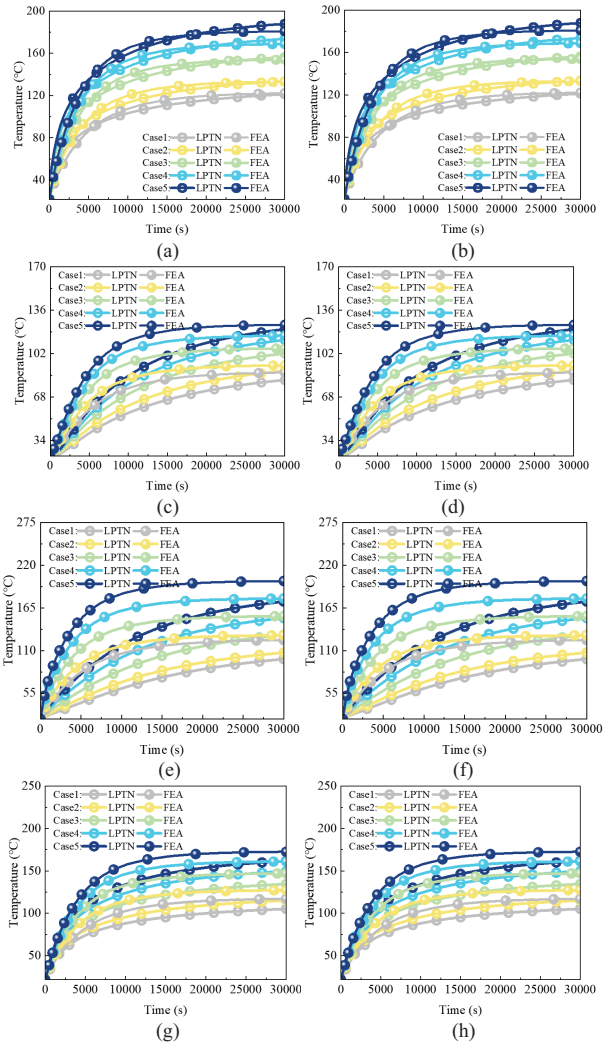


Fig. 12. Comparison of transient temperature of major components in the MPMLRG predicted by the LPTN and 3-D FEA: (a) RGU stator, (b) RGU winding, (c) RGU PM, (d) LGU PM, (e) LGU stator, (f) LGU winding, (g) mover, and (h) housing.

It can be observed that the results of the LPTN calculation are in close agreement with those of the FEA, confirming the accuracy of the proposed LPTN model for the MPMLRG. The largest discrepancy is observed in the winding of the RGU, which is mainly attributed to the geometric simplifications adopted in the LPTN model. Nevertheless, the overall agreement demonstrates that the proposed model can provide reliable temperature prediction for engineering applications.

VI. TRANSIENT LPTN

As shown in Fig. 12, the computing results of transient LPTN are compared with the results of FEA.

It can be observed that the final steady-state results of both methods are in good agreement; however, the temperature predicted by the LPTN reaches steady-state more slowly than that of the FEA. This discrepancy mainly arises from the intrinsic modeling assumptions of the LPTN. In the LPTN, multiple local heat-transfer paths are represented by equivalent thermal resistances and thermal capacitances. The spatial averaging smooths local temperature gradients and increases the effective thermal inertia of each thermal node, thereby slowing the predicted heat diffusion process. In contrast, the FEA explicitly resolves the distributed temperature field and local heattransfer paths, allowing local regions to respond more rapidly to thermal excitation. Consequently, the LPTN exhibits a slightly slower transient response while maintaining good agreement with the FEA under steady-state conditions. This characteristic

does not affect its suitability for thermal design and steady-state temperature prediction.

VII. CONCLUSION

A lumped-parameter thermal network model for the dual-stator MPMLRG was developed and validated against 3-D FEA. Both methods reveal that stator windings are the most thermally critical components, with the inner stator winding of the LGU exhibiting the highest temperature due to limited heat dissipation. The LPTN demonstrates good agreement with FEA in steady-state prediction, though it slightly underestimates transient dynamics owing to simplified thermal inertia representation. At high operating speeds, winding overheating becomes significant, underscoring the necessity of enhanced cooling strategies. Future work will integrate advanced cooling methods and couple the LPTN with dynamic electromagnetic loss models to support reliability assessment and design optimization. Future work will include experimental validation on a prototype to further verify the proposed thermal model under practical operating conditions.

ACKNOWLEDGMENT

This work was supported by the National Natural Science Foundation of China (52577073), the Natural Science Foundation of Henan (252300421095), the China Postdoctoral Science Foundation (2026T190135, 2025M780487), and the Henan Province Key R&D and promotion projects (Scientific and Technological Breakthrough) (262102241045).

REFERENCES

[1] M. A. Mueller, J. Burchell, Y. C. Chong, O. Keysan, A. McDonald, M. Galbraith, and E. J. P. Echenique Subiabre, "Improving the thermal performance of rotary and linear air-cored permanent magnet machines for direct drive wind and wave energy applications," *IEEE Trans. Energy Convers.*, vol. 34, no. 2, pp. 773–781, June 2019.

[2] L. Xu, C. Zhang, and X. Zhu, "Decoupling control of a dual-stator linear and rotary permanent magnet generator for offshore joint wind and wave energy conversion system," *IET Electric Power Appl.*, vol. 4, no. 4, pp. 561–569, Apr. 2020.

[3] L. Szabó, "On the use of rotary-linear generators in floating hybrid wind and wave energy conversion systems," in *Proc. IEEE Int. Conf. Autom., Quality Testing, Robot. (AQTR)*, Cluj-Napoca, Romania, pp. 1–6, 2018.

[4] E. D. Stoutenburg and M. Z. Jacobson, "Reducing offshore transmission requirements by combining offshore wind and wave farms," *IEEE J. Ocean. Eng.*, vol. 36, no. 4, pp. 552–561, Oct. 2011.

[5] E. D. Stoutenburg and M. Z. Jacobson, "Reducing offshore transmission requirements by combining offshore wind and wave farms," *IEEE J. Ocean. Eng.*, vol. 36, no. 4, pp. 552–561, Oct. 2011.

[6] L. Szabó, "On the use of rotary-linear generators in floating hybrid wind and wave energy conversion systems," in *Proc. IEEE Int. Conf. Autom.*, *Quality Testing, Robot*, Cluj-Napoca, Romania, pp. 1–6, 2018.

[7] N. A. Bhuiyan and A. Mcdonald, "Optimization of offshore direct drive wind turbine generators with consideration of permanent magnet grade and temperature," *IEEE Trans. Energy Convers.*, vol. 34, no. 2, pp. 1105–1114, June 2019.

[8] X. Song, J. Zhao, J. Song, F. Dong, L. Xu, and J. Zhao, "Local demagnetization fault recognition of permanent magnet synchronous linear motor based on S-transform and PSO-LSSVM," *IEEE Trans. Power Electron.*, vol. 35, no. 8, pp. 7816–7825, Aug. 2020.

[9] L. Xu, X. Zhu, C. Zhang, L. Zhang, and L. Quan, "Power oriented design and optimization of dual-stator linear-rotary generator with Halbach PM array for ocean energy conversion," *IEEE Trans. Energy Convers.*, vol. 36, no. 4, pp. 3414–3426, Dec. 2021.

[10] F. Xing, W. Jian, and L. Ming, "Design and analysis of linear-rotary permanent magnet generator for wind-wave combined power generation system," in *Proc. 20th Int. Conf. Electr. Mach. Syst. (ICEMS)*, Sydney, NSW, Australia, pp. 1–6, Aug. 2017.

[11] S. Nateg, O. Wallmark, M. Leksell, and S. Zhao, "Thermal analysis of a PMaSRM using partial FEA and lumped parameter modeling," *IEEE Trans. Energy Convers.*, vol. 27, no. 2, pp. 477–488, June 2012.

[12] A. B. Nachouane, A. Abdelli, G. Friedrich, and S. Vivier, "Numerical study of convective heat transfer in the end regions of a totally enclosed permanent magnet synchronous machine," *IEEE Trans. Ind. Appl.*, vol. 53, no. 4, pp. 3538–3547, July-Aug. 2017.

[13] J. Huang, Y. Xu, L. Xiao, L. Zhuo, G. Yu, and J. Zou, "Study of thermal field analysis methods of oil-filled motors," *IEEE Trans. Appl. Supercond.*, vol. 34, no. 8, pp. 1–5, Nov. 2024.

[14] J. Bao, B. L. J. Gysen, K. Boynov, J. J. H. Paulides, and E. A. Lomonova, "Torque ripple reduction for 12-stator/10-rotor-pole variable flux reluctance machines by rotor skewing or rotor teeth non-uniformity," *IEEE Trans. Magn.*, vol. 53, no. 11, pp. 1–5, Nov. 2017.

[15] L. Mo, T. Zhang, and Q. Lu, "Thermal analysis of a flux-switching permanent-magnet double-rotor machine with a 3-D thermal network model," *IEEE Trans. Appl. Supercond.*, vol. 29, no. 2, pp. 1–5, Mar. 2019.

[16] X. Jiang, Y. Zhang, S. Jin, F. Zhang, and C. Gerada, "A novel thermal network model used for temperature calculation and analysis on brushless

doubly-fed generator with winding encapsulating structure," *IEEE Trans. Ind. Appl.*, vol. 55, no. 2, pp. 1473–1483, Mar.-Apr. 2019.

[17] J. Si, S. Zhao, H. Feng, Y. Hu, and W. Cao, "Analysis of temperature field for a surface-mounted and interior permanent magnet synchronous motor adopting magnetic-thermal coupling method," *CES Trans. Electr. Mach. Syst.*, vol. 2, no. 1, pp. 166–174, Mar. 2018.

[18] R. Camilleri, D. A. Howey, and M. D. McCulloch, "Predicting the temperature and flow distribution in a direct oil-cooled electrical machine with segmented stator," *IEEE Trans. Ind. Electron.*, vol. 63, no. 1, pp. 82–91, Jan. 2016.

[19] V. Ruuskanen, J. Nerg, M. Niemelä, J. Pyrhönen, and H. Polinder, "Effect of radial cooling ducts on the electromagnetic performance of the permanent magnet synchronous generators with double radial forced air cooling for direct-driven wind turbines," *IEEE Trans. Magn.*, vol. 49, no. 6, pp. 2974–2981, June 2013.

[20] G. Cipriani, M. Corpora, V. Di Dio, A. Musolino, R. Rizzo, and L. Sani, "A comparison among different kinds of stator lamination in tubular linear machines," *Progress in Electromagnetics Research M*, vol. 50, pp. 95–104, 2016.

[21] A. Belahcen and A. Arkkio, "Comprehensive dynamic loss model of electrical steel applied to FE simulation of electrical machines," *IEEE Trans. Magn.*, vol. 44, no. 6, pp. 886–889, June 2008.

[22] X. Zhang, H. Zhang, W. Li, C. Gerada, D. Gerada, and J. Li, "Thermal barrier for high-voltage permanent magnet synchronous motor with aircooling hybrid ventilation systems," in *Proc. 22nd Int. Conf. Elect. Mach. Syst.*, Harbin, China, pp. 1–4, 2019.

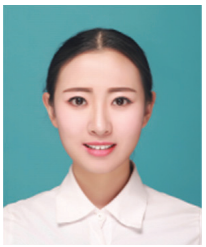
[23] Q. Chen, D. Liang, L. Gao, Q. Wang, and Y. Liu, "Hierarchical thermal network analysis of axial-flux permanent-magnet synchronous machine for electric motorcycle," *IET Electr. Power App.*, vol. 12, no. 6, pp. 859–866, July 2018.

[24] J. Pyrhönen, T. Jokinen, and V. Hrabovcová, *Design of Rotating Electrical Machines*. Chichester: John Wiley & Sons, 2008.

[25] D. A. Howey, P. R. N. Childs, and A. S. Holmes, "Air-gap convection in rotating electrical machines," *IEEE Trans. Ind. Electron.*, vol. 59, no. 3, pp. 1367–1375, Mar. 2012.



Chenxi Li was born in Sichuan, China, in 2001. She received the B.S. degree in electrical engineering and automation from Henan University of Technology, Zhengzhou, in 2023. She is currently working toward the M.S. degree in the School of Electrical Engineering at Zhengzhou University, Zhengzhou. Her research interests include renewable energy generation technologies and thermal analysis of two-degree-of-freedom motors.



Rui Nie received the B.S. degree in electrical engineering from Henan Polytechnic University, Jiaozuo, China, in 2015, and the Ph.D. degree in electrical engineering from China University of Mining and Technology, Xuzhou, in 2020. She is currently a Research Fellow at Zhengzhou research interests include two-degree-of-freedom machines, linear motor and renewable energy generation technologies.



Shuai Xu received the B.S. degree in electrical engineering and automation and the Ph.D. degree in electrical engineering from China University of Mining and Technology, Xuzhou, China, in 2014 and 2019, respectively. Since 2021, he has been an Associate Professor at Zhengzhou University. His research interests include motor design and control.



Yanqi Wei received the Ph.D. degree in electrical engineering from Zhengzhou University, Zhengzhou, China, in 2024. He is currently a Postdoctoral Researcher with the School of Electrical and Information Zhengzhou University. His research interests include the design, analysis, axial-flux permanent-magnet motors.



Peixin Wang received the B.S. and M.S. degrees from Henan Polytechnic University, Jiaozuo, China, in 2016 and 2018, respectively, and the Ph.D. degree from Southeast University, Nanjing, in 2022. He is currently a Lecturer at Zhengzhou University. His research interests include air-gap flux modulation theory and the design and analysis of special machines.



Jikai Si received the B.S. degree in electrical engineering and automation from Jiaozuo Institute of Technology, Jiaozuo, China, in 1998, the M.S. degree from Henan Polytechnic University, Jiaozuo, in 2005, and the electrical engineering from China University of Mining and Technology, He is currently a Distinguished Professor at Zhengzhou University. His include the theory and control of special motors.

Electromagnetic Analysis of a 12-Pole Single-Phase Switched Reluctance Linear Motor

Hao Chen[1,2,3], Denis Kotin[4], Aris Dimeas[5], Emmanuel Karapidakis[6], Olimjon Toirov[7], Liu Jingfu[2], Zhao Wenmin[2], Xing Wang[1,3*], and Sherif Moussa[8]

[1]International Cooperation Joint Laboratory of New Energy Power Generation and Electric Vehicles of Jiangsu Province Colleges and Universities, Xuzhou 221008, China
hchen@cumt.edu.cn, 3512@cumt.edu.cn

[2]School of Electrical Engineering
China University of Mining and Technology, Xuzhou 221116, China
hchen@cumt.edu.cn, liujinfu99@cumt.edu.cn

[3]Shenzhen Research Institute
China University of Mining and Technology, Shenzhen 515100, China

[4]Department of Electric Drive and Industry Automation
Novosibirsk State Technical University, 630073, 20 Prospekt K. Marksa, Novosibirsk, Russia
d.kotin@corp.nstu.ru

[5]Athens National University of Technology
Greece
karapidakis@hmu.gr

[6]School of Engineering, Hellenic Mediterranean University
Estavromenos Campus, 71004 Heraklio, Crete, Greece
karapidakis@hmu.gr

[7]Tashkent State Technical University
University Street No. 2, 100095 Tashkent, Uzbekistan
olimjon.t@mail.ru

[8]School of Engineering, Canadian University Dubai
117781, Sheikh Zayed Road, Dubai, United Arab Emirates
smoussa@cud.ac.ae

***Abstract* –** A novel modular 12-pole transverse-flux tubular switched reluctance linear machine (TSRLM) is proposed in this paper. The machine adopts a U-shaped modular-stator structure with windings arranged on the stator yoke, which shortens magnetic flux paths, reduces magnetic reluctance, and improves iron core utilization. A three-dimensional finite-element model is established to analyze the electromagnetic characteristics of the proposed TSRLM, including flux linkage, static electromagnetic force, and magnetic field distribution. On this basis, a sensitivity-based single-objective optimization is conducted to determine the structural parameters of the motor. Then, a 12-pole TSRLM prototype is fabricated, and dynamic motoring experiments are carried out under different current chopping limits. Experimental results agree well with simulation results, validating the accuracy of the finite-element model and the feasibility of the proposed design.

***Index Terms* –** Finite-element analysis, modular-stator, transverse-flux, tubular switched reluctance linear machine.

I. INTRODUCTION

Switched reluctance motors (SRMs) are special electric machines with high robustness, simple manufacturing processes, low cost, simple construction, strong fault tolerance, wide speed regulation range, and good adaptability to harsh operating environments [1–3].

Submitted On: March 23, 2026
Accepted On: May 27, 2026

1054-4887 © ACES

https://doi.org/10.13052/2026.ACES.J.410605

Owing to these merits, SRMs have attracted increasing attention from researchers worldwide in recent years [4–7]. Flat-type linear machines are affected by both lateral end effects and longitudinal end effects [8]. The lateral end effect arises from the unequal lengths of the primary and secondary parts, while the longitudinal end effect is caused by the finite machine length resulting from the interruption of the magnetic circuit at the longitudinal ends. The longitudinal end effect leads to differences between the magnetic circuits of the end phases and the middle phases, resulting in inductance imbalance among phases. Consequently, phase currents and output forces become unbalanced, which aggravates electromagnetic force ripple and reduces the service life of the machine.

By rotating a flat-type SRLM through one full revolution along a circular path perpendicular to the direction of motion, a tubular switched reluctance linear motor (TSRLM) can be obtained [9, 10]. The cross-sectional structure of the TSRLM is highly similar to that of a rotary switched reluctance motor (RSRM). By combining the advantages of tubular machines and SRLMs, the TSRLM inherently eliminates lateral end effects, thereby reducing analytical complexity. Moreover, the tubular structure eliminates the normal electromagnetic force between the stator and the mover, effectively addressing the eccentricity problem inherent in flat-type linear machines. As a result, a smaller air gap can be adopted, leading to a significant improvement in electromagnetic force density.

Over the more than four decades of development of SRMs, their performance has gradually become sufficient to meet practical application requirements. However, conventional SRMs have long faced difficulties in large-scale manufacturing, resulting in low production efficiency and increased manufacturing costs. To address this issue, the concept of modular machine design has been proposed. Compared with traditional SRMs, modular SRMs exhibit advantages such as lower cost, higher torque capability, strong fault tolerance, and reduced losses. Modularization is conducive to expanding production scale, improving manufacturing efficiency, shortening production cycles, and further promoting the development of SRMs, thereby significantly enhancing their industrial competitiveness. Wang et al. [11] proposed a novel modular secondary-side SRLM with annular windings. The stator is composed of multiple mutually independent ferromagnetic modules, and the stator yoke is eliminated to effectively isolate adjacent magnetic blocks. Only one phase armature winding is placed in each stator slot, and no inter-phase insulation is required, which reduces manufacturing cost and significantly improves iron core utilization. As a result, the overall performance of the machine is effectively enhanced. In [1]], two segmented E-shaped rotors with different structures are comprehensively analyzed. Ding et al. [13] proposed a modular-rotor SRM with an E-shaped stator configuration. The stator is composed of six mutually independent E-shaped stator modules, with the windings arranged on the stator yokes. The rotor is divided into three segments corresponding to the stator poles, and the three segmented rotors are mounted on a common shaft without any angular displacement. Ruba et al. [14] proposed a modular-stator SRM with high fault tolerance and conducted a dynamic simulation study. The machine is a four-phase SRM, with two stator modules per phase. The winding of each stator module is wound around the corresponding stator yoke, and the two winding modules of each phase are positioned at diametrically opposite locations along the circumference. Adjacent stator modules are separated by non-magnetic spacers.

In summary, although tubular switched reluctance linear machines and modular SRM topologies have been extensively investigated, most existing studies focus either on modular concepts in rotary SRMs or on conventional tubular linear structures, while the combination of modular-stator topology and transverse-flux tubular SRLMs remains insufficiently explored. Moreover, issues related to electromagnetic characteristics, magnetic field distribution, and experimental validation of such modular tubular structures are still not fully addressed. Motivated by these considerations, this paper proposes a novel 12-pole modular TSRLM with U-shaped stator topology. The structural configuration and operating principle of the proposed machine are introduced in detail. A three-dimensional finite-element model is established to analyze its electromagnetic characteristics, including flux linkage, static electromagnetic force, and magnetic field distribution. Furthermore, a prototype is fabricated and experimentally tested to validate the proposed design and the accuracy of the modeling approach. The results demonstrate the feasibility and effectiveness of the proposed modular TSRLM structure.

II. STRUCTURE AND PRINCIPLE OF MS-6P-TSRLG

A. Basic structure of MS-6P-TSRLG

The modular TSRLM proposed in this paper inherits the typical characteristics of SRLMs, and its overall shape and structure are highly similar to those of a conventional RSRM, especially in terms of the cross-sectional configuration. Owing to the very low magnetic permeability of air, both the stator and mover cores are fabricated by stacking silicon steel laminations. The structure of the 12-pole TSRLM is illustrated in

Fig. 1. Figure 1 (a) shows the cross-sectional view of the 12-pole TSRLM and the corresponding magnetic flux paths. The stator consists of six U-shaped modular-stator units, and adjacent stator modules are separated by stator spacers made of non-magnetic material, which effectively suppresses magnetic leakage between modules. The windings are wound around the stator yokes of the U-shaped modules and connected in an NSNSNSNSNSNS sequence using conductors with a diameter of 1.5 mm. The entire machine includes five stator ferromagnetic rings, which are mechanically connected by fastening bolts passing through the stator spacing rings.

The mover structure is shown in Fig. 1 (b). Each mover ferromagnetic ring contains six gear-shaped salient poles. These poles are inserted into the openings of the modular-stator cores, such that each mover pole and each U-shaped stator module together form a closed stator slot structure. This configuration is conducive to establishing an effective magnetic circuit and helps to enhance the thrust density of the machine. The mover assembly consists of five ferromagnetic rings uniformly mounted on the shaft with specified spacing. The ferromagnetic materials used for both the stator and the mover are 50DW470 silicon steel laminations. The shaft material is the same as the non-magnetic material used between adjacent stator modules. Similarly, non-magnetic materials are inserted between adjacent stator ferromagnetic rings and between adjacent mover ferromagnetic rings to prevent the formation of axial magnetic flux.

The proposed 12-pole TSRLM is a transverse-flux machine, in which the plane of the magnetic circuit is perpendicular to the direction of motion. Once axial magnetic flux is generated, mutual coupling may occur between adjacent ferromagnetic rings, leading to severe distortion of axial flux lines and degradation of machine performance. To avoid this phenomenon, non-magnetic materials are employed to separate the stator ferromagnetic rings.

The structure of the 12-pole TSRLM in this paper is illustrated in Fig. 1. When the windings are energized, closed magnetic flux paths are established through the ferromagnetic materials and air gaps. The magnetic flux paths mainly consist of two loops. One loop passes through the stator yoke of the U-shaped module, the stator pole of the U-shaped module, and the air gap g_1 between the stator pole and the mover pole. The other loop passes through the stator yoke of the U-shaped module, the stator pole of the U-shaped module, and the air gap g_2 between the stator pole and the mover yoke. These closed magnetic circuits are formed within each U-shaped stator pole, which effectively shortens the magnetic path, reduces magnetic reluctance, and significantly improves the overall performance of the machine.

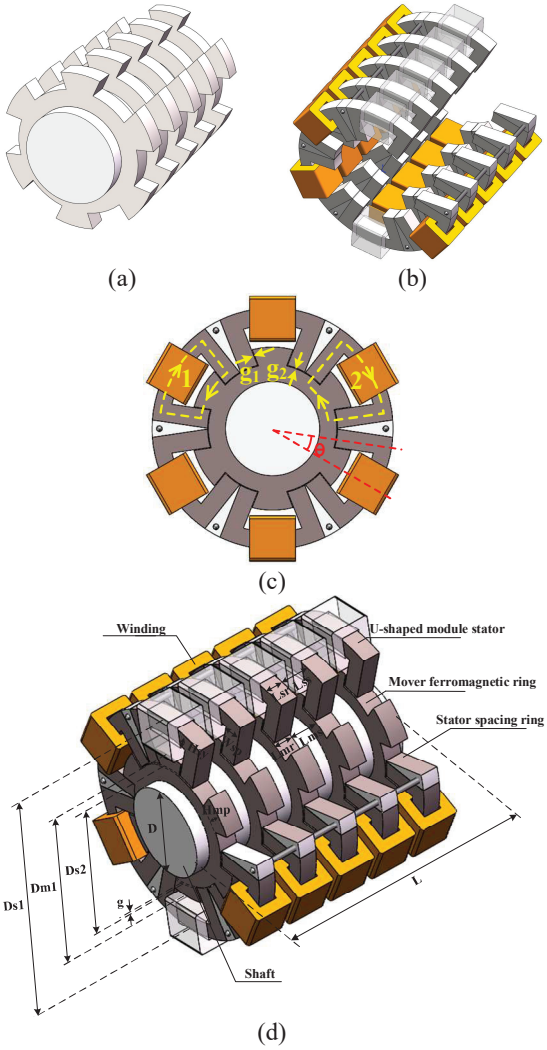


Fig. 1. Structure of the 12-pole TSRLM: (a) segmented mover, (b) segmented stator, (c) stator cross-section, and (d) overall structure.

In conventional machines, the windings are typically placed on the stator poles, and the number of turns that can be accommodated is constrained by two factors: the available stator slot space in the cross-sectional direction and the axial spacing between two adjacent stator ferromagnetic rings. In such configurations, two winding modules are usually arranged in each stator slot, and the allowable number of turns is determined by the smaller of the two available spaces, namely the stator slot area and the axial spacing between the ferromagnetic rings.

In contrast, in the 12-pole TSRLM proposed in this paper, the windings are wound around the stator

yoke. As a result, only one winding module is placed in each stator slot in a given stator cross-section. This configuration eliminates the limitation imposed by the stator slot space in the cross-sectional direction, and the winding accommodation is determined solely by the axial spacing between adjacent stator rings. This winding arrangement significantly reduces manufacturing complexity, facilitates an increase in the number of winding turns, and consequently enhances the overall performance of the machine.

B. Principle of the 12-pole TSRLM

The TSRLM is a reluctance-based machine and differs fundamentally from conventional electrical machines. As the mover travels, the magnetic reluctance of the TSRLM varies continuously, causing the magnetic field energy to change with the mover position. During operation, the TSRLM follows the principle of minimum reluctance, that is, the magnetic flux always tends to close along the path with the minimum magnetic reluctance. Owing to this operating mechanism, its structure and working principle are markedly different from those of conventional machines. Figure 2 illustrates the structural principle of the 12-pole TSRLM. The operating process can be described as follows.

When switches S1 and S2 are turned on, the DC power supply U energizes the windings. The radial electromagnetic force generated by the distorted magnetic field tends to drive the mover toward the position where the central axis of the mover pole aligns with that of the stator pole, namely the aligned position. When the mover reaches this aligned position, the magnetic reluctance and leakage flux are minimized, and the corresponding flux linkage, electromagnetic force, and inductance reach their maximum values within one mover period. As the mover continues to move and deviates from the aligned position, the magnetic reluctance and leakage flux increase, while the flux linkage, electromagnetic force, and inductance decrease accordingly. Excitation of the stator windings always produces a radial electromagnetic force that tends to align the central axes of the stator and mover poles, thereby driving the mover back toward the aligned position.

The direction of the excitation current in the windings does not affect the direction of motion of the machine, which allows the use of a relatively simple power converter topology. When switches S1 and S2 are turned off, the winding current flows through the freewheeling diodes VD1 and VD2, and the remaining electrical energy is fed back to the power supply U. This energy recovery process is beneficial for improving the overall efficiency of the system.

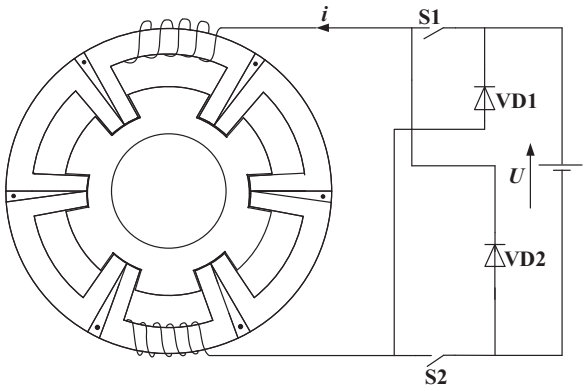


Fig. 2. Structural schematic diagram of the 12-pole TSRLM.

III. ELECTROMAGNETIC ANALYSIS OF THE 12-POLE TSRLM

A. Electromagnetic characteristic curves of the 12-pole TSRLM

The finite-element model established in this paper is shown in Fig. 3. Among them, the ferromagnetic materials for both the stator and rotor parts are all 50DW470.

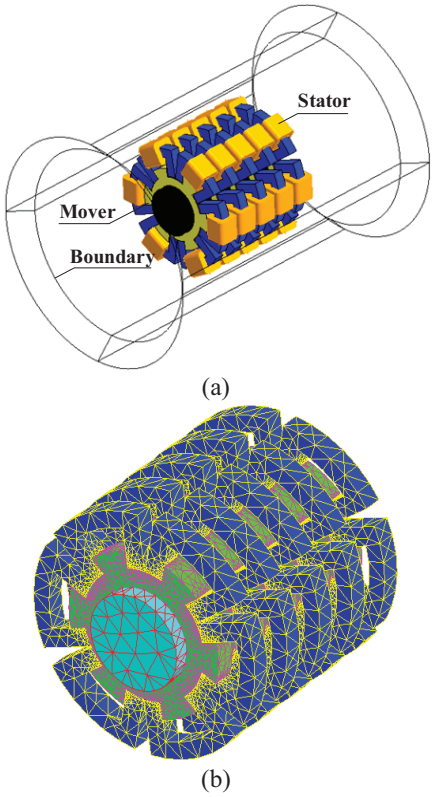


Fig. 3. Finite-element model of the 12-pole TSRLM: (a) model and its boundaries and (b) model after meshing.

For the 12-pole TSRLM investigated in this paper, one mover period is 10 mm, and the mover stroke ranges from −5 mm to 5 mm. Following conventional design practice, the position at which the central axis of the stator pole is perfectly aligned with that of the mover pole is defined as the 0 mm position, i.e., the aligned position. Taking the 0 mm position as the reference, the mover travels 5 mm in the negative direction to the −5 mm position and 5 mm in the positive direction to the 5 mm position. At both the −5 mm and 5 mm positions, the stator and mover poles are completely misaligned, corresponding to the unaligned positions.

The settings of the TSRLM finite-element model are modified by assigning the excitation current in the range of 0–15 A with a step size of 1 A, and restricting the mover position to the range of −5 mm to 0 mm with a step size of 0.5 mm. As the mover position varies, the finite-element model is remeshed, and the flux linkage and magnetic co-energy are calculated for different current levels at each mover position. By repeating this procedure sequentially, accurate finite-element results are obtained. Figure 3 shows the three-dimensional surfaces of the flux linkage and magnetic co-energy as functions of mover position and excitation current, obtained from the finite-element analysis.

According to Fig. 4 (a), at a given mover position, the flux linkage increases overall with increasing current and, near the aligned position, the magnetic circuit exhibits a clear tendency toward saturation as the current rises. For a given current level, when the mover travels from the unaligned position at −5 mm to the aligned position at 0 mm, the flux linkage increases and reaches its maximum at the 0 mm position. During transition from the unaligned position to the aligned position, the magnetic circuit gradually approaches saturation, and the flux linkage exhibits pronounced nonlinear characteristics. The variation trend of flux linkage when the mover moves from the 5 mm position toward 0 mm is completely symmetric to that observed when the mover moves from −5 mm toward 0 mm. Moreover, for different current levels, the flux linkage exhibits the same variation trend with respect to the mover position.

As shown in Fig. 4 (b), the variation trends of the magnetic co-energy with respect to mover position and current are consistent with those shown in Fig. 3 (a); therefore, they are not repeated here.

Figure 5 shows the static electromagnetic force curves within one mover period under different mover positions and excitation current levels. Five static electromagnetic force curves corresponding to excitation currents of 3 A, 6 A, 9 A, 12 A, and 15 A are presented. As can be observed from Fig. 5, for a given current level, when the mover travels from the −5 mm position toward the 0 mm position, the magnitude of the static electromagnetic force gradually decreases. When the mover reaches the 0 mm position, where the magnetic reluctance is minimized, the electromagnetic force becomes zero.

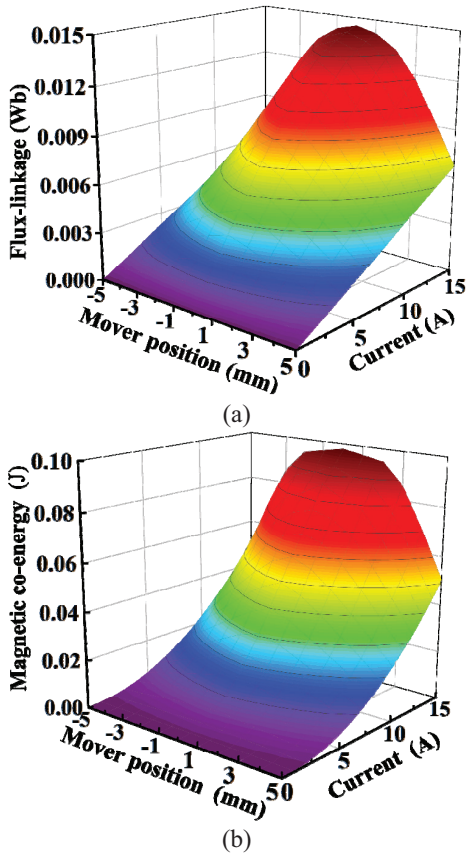


Fig. 4. Three-dimensional curves of flux linkage and magnetic energy of the 12-pole TSRLM varying with current and mover position: (a) calculation results of flux-linkage and (b) calculation results of magnetic co-energy.

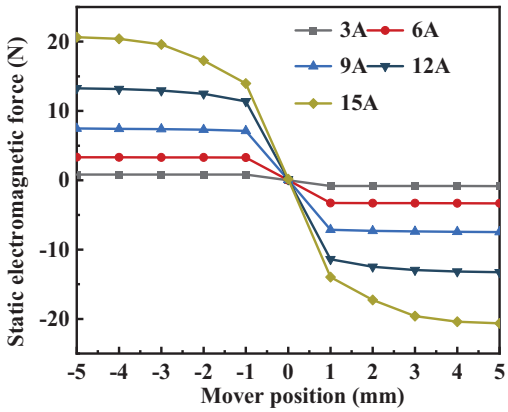


Fig. 5. Static electromagnetic force curves under different mover positions and currents.

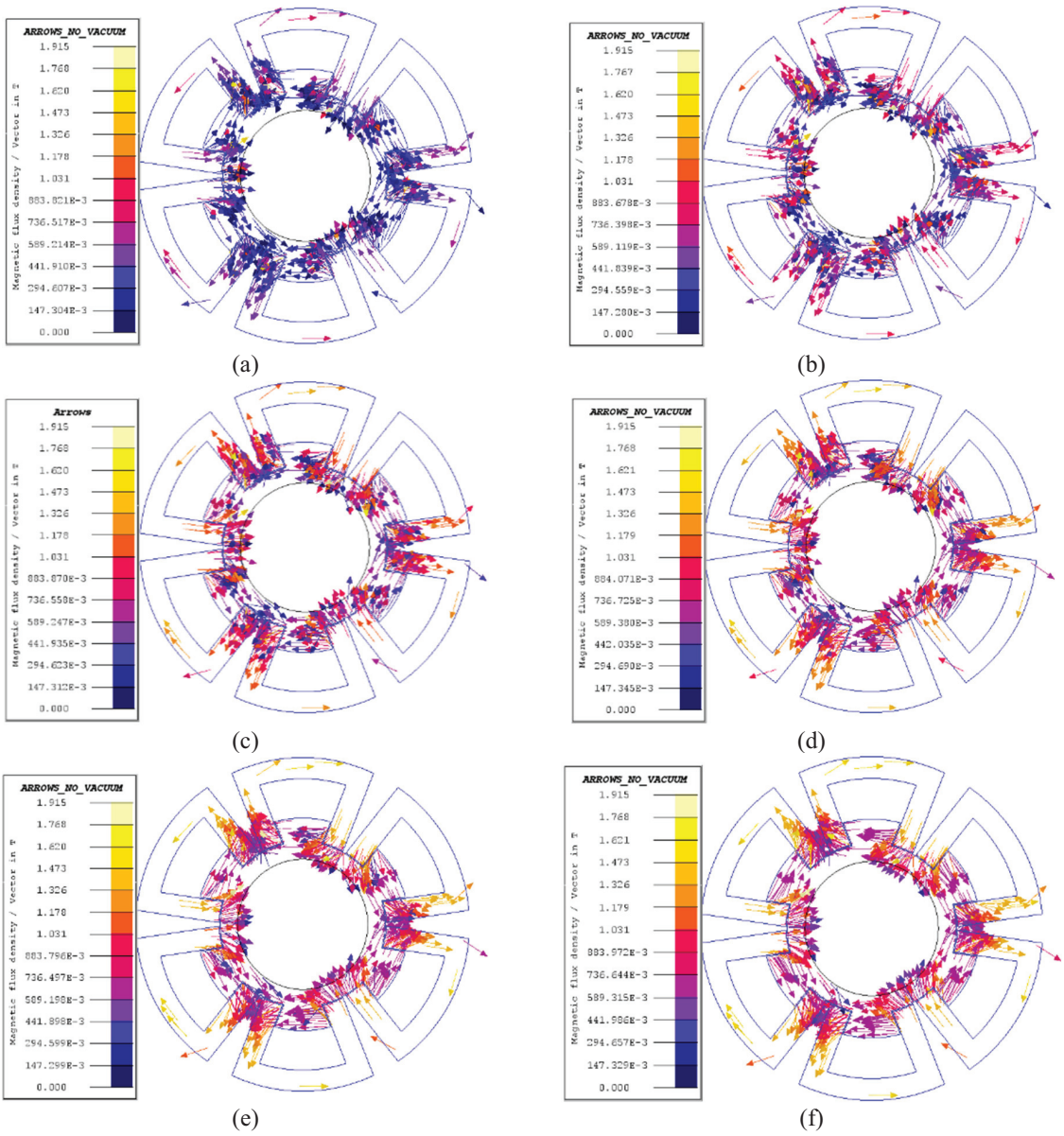


Fig. 6. Flux paths of the 12-pole TSRLM in different mover positions: (a) −5 mm, (b) −4 mm, (c) −3 mm, (d) −2 mm, (e) −1 mm, and (f) 0 mm.

For different excitation current levels, the variation trend of the static electromagnetic force with respect to the mover position remains consistent. However, as the excitation current increases, the magnitude of the static electromagnetic force increases accordingly.

B. Analysis of the magnetic field of 12-pole TSRLM

Electromagnetic field analysis of the TSRLM is a fundamental step in machine design and provides the basis for subsequent optimization of the TSRLM. Based on the initial dimensions of the TSRLM, a finite-element model is established in the FLUX software and static analyses are carried out. Figure 6 shows the magnetic flux path distributions of the TSRLM at different mover positions. Since the motion processes and corresponding finite-element results in the ranges of (−5 mm, 0) and (0, 5 mm) are completely symmetric, only the magnetic flux distributions within the (−5 mm, 0) range are presented in Fig. 5. In this analysis, the excitation current is set to 15 A.

The proposed TSRLM is a transverse-flux machine that effectively avoids longitudinal end effects between adjacent ferromagnetic rings, which commonly affect linear machines. The magnetic flux circuit distributions clearly illustrate the density of magnetic field lines.

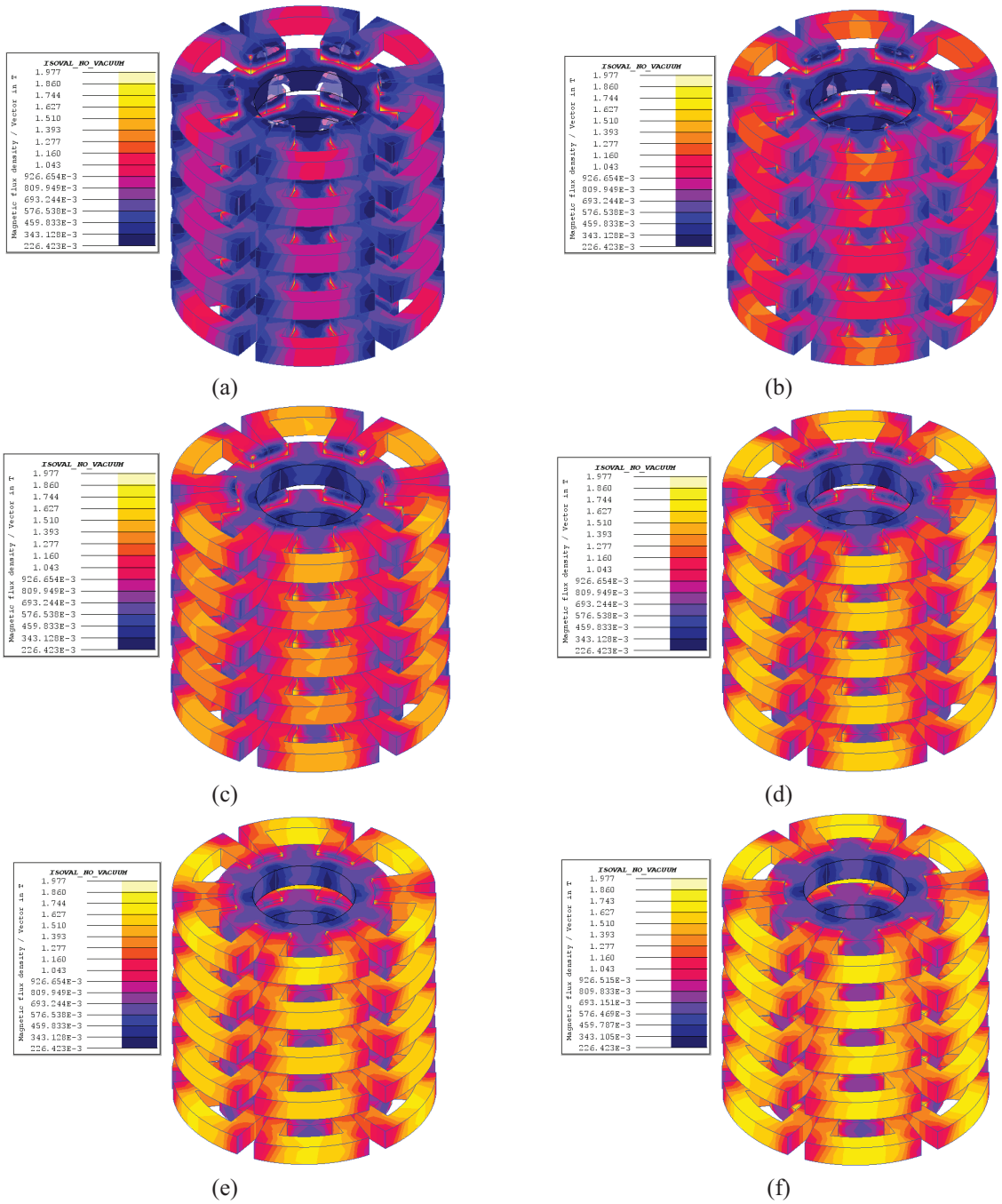


Fig. 7. Magnetic flux density distribution of the 12-pole TSRLM in different mover positions: (a) −5 mm, (b) −4 mm, (c) −3 mm, (d) −2 mm, (e) −1 mm, and (f) 0 mm.

The arrow directions indicate the orientation of the magnetic flux, while the arrow colors represent the magnitude of the magnetic flux density at the corresponding mover positions. Colors closer to the top of the color scale indicate higher magnetic flux density, whereas colors closer to the bottom indicate lower magnetic flux density. As the mover travels from the −5 mm position to the 0 mm position, the magnetic flux density gradually increases. This is because, at the 0 mm position, the central axes of the stator poles and mover poles are fully aligned, and the magnetic flux lines form closed loops through the stator yoke, stator poles, mover yoke or mover poles, and the air gap, resulting in minimal leakage flux in the air. Consequently, the magnetic flux density reaches its maximum within one mover period at this position.

When the mover moves from the 0 mm position toward the −5 mm position, although the magnetic flux lines still form closed loops through the stator yoke, stator poles, mover yoke or mover poles, and the air gap, the distortion of the flux lines causes the leakage flux in the air to gradually increase. At the −5 mm or 5 mm positions, corresponding to the unaligned positions, the leakage flux reaches its maximum value.

Although the magnetic flux path distributions can clearly illustrate the flux orientation and the relative variation of magnetic flux density at different mover positions, they only provide a qualitative evaluation of the magnetic field intensity. By means of three-dimensional finite-element analysis, the magnetic flux density contour plots corresponding to an excitation current of 15 A and mover positions ranging from −5 mm to 0 mm can be obtained, as shown in Fig. 7, enabling a quantitative analysis of the magnetic flux density based on specific numerical values.

From the magnetic flux density contour plots, the saturation level of the iron core can be directly observed. The color scale associated with the contour plots indicates the magnitude of the magnetic flux density in different regions of the machine. Colors closer to the top of the scale represent higher magnetic flux density, corresponding to stronger magnetic field intensity and a higher degree of saturation, whereas colors closer to the bottom represent lower magnetic flux density, indicating weaker magnetic field intensity and a lower degree of saturation. Since the performance of SRMs can be fully exploited when operating under saturated conditions, these flux density distributions provide an effective means to assess the operating state of the machine. Based on such assessments, appropriate measures can be proposed to further enhance the performance of the machine.

As shown in Fig. 7, the relative positional relationship between the stator ferromagnetic rings and the mover ferromagnetic rings can be clearly observed at different mover positions. From the color distribution in different regions of the cross-section, it can be seen that the magnetic flux density is highest in the stator yoke, followed by the stator poles, while the magnetic flux density in the mover is comparatively lower. As the mover travels from the −5 mm position to the 0 mm position, the magnetic flux density in the ferromagnetic parts increases progressively; however, the increase in flux density is more pronounced in the stator than in the mover.

Since the 0 mm position corresponds to the aligned position, the leakage flux is minimal and the magnetic flux density reaches its maximum at this position. Nevertheless, even with the stator yoke in the 0 mm position, only a small portion of the iron core reaches a flux density of approximately 1.6 T, while most regions remain significantly unsaturated. Therefore, it can be concluded that the performance of the machine has not yet reached its optimal level, and further improvements can be achieved through appropriate optimization of the machine design.

IV. SENSITIVITY-BASED SINGLE-OBJECTIVE OPTIMIZATION

In the optimization process in this paper, the single-objective optimization adopts the sensitivity analysis method. The objective function is the average electromagnetic force, and the design variables are the stator inner diameter (31-38 mm), height of the rotor magnetic pole (2–5 mm), width of the stator magnetic pole (4–5 mm), and thickness of the stator yoke (3.4–5.4 mm). By traversing the step sizes of each variable (such as 1 mm, 0.2 mm, 0.1 mm, 0.2 mm, which represent the minimum mesh length of each component, respectively), the corresponding average electromagnetic force is calculated, and the parameter corresponding to the maximum value is selected as the optimal solution.

In sensitivity analysis with average electromagnetic force as the optimization objective, the first parameter considered was the stator inner diameter, which affects the available space for winding placement. The winding space, in turn, influences the electrical loading characteristics of the motor. With all other structural parameters kept constant, the stator inner diameter was varied uniformly from 31 mm to 38 mm in 1 mm increments. During this variation, the mover's outer diameter also changed correspondingly; the effects of the mover's outer diameter variation and the stator inner diameter variation on motor performance can be considered equivalent. Therefore, this can be regarded as the influence of a single parameter (stator inner diameter) on electromagnetic force. A corresponding finite-element model was built to analyze this effect, and the resulting trend of the average electromagnetic force under different stator inner diameters is shown in Fig. 8.

As shown in Fig. 8, when the stator inner diameter increases from 31 mm to 34 mm, the average electromagnetic force rises from 13.260 N to 13.875 N. This increase is attributed to shortening of the magnetic flux path as the stator inner diameter enlarges, which reduces magnetic reluctance and consequently increases the output force. When the stator inner diameter further increases from 34 mm to 38 mm, the average electromagnetic force slightly decreases from 13.875 N to 13.750 N. Throughout the entire variation range, the average electromagnetic force exhibits a small fluctuation, with a range of 0.615 N. Therefore, stator inner

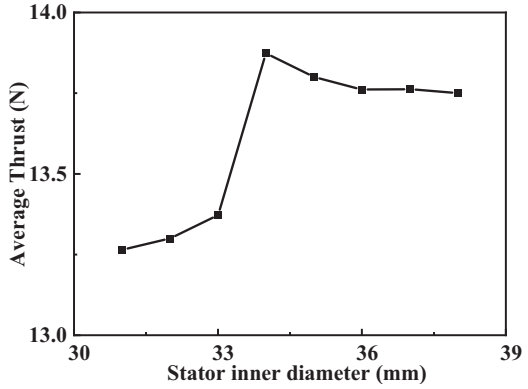


Fig. 8. Average electromagnetic force under different stator inner diameters.

diameter was ultimately selected as 34 mm, corresponding to the maximum average electromagnetic force.

During sensitivity analysis of the mover pole height, the stator inner diameter of the 12-pole TSRLM finite-element model was modified to the optimized value of 34 mm, while all other structural parameters remained unchanged. Subsequently, mover pole height was varied, causing the mover yoke thickness to change correspondingly. This variation can equivalently be considered as the effect of a single structural parameter, i.e., mover pole height. Mover pole height was varied from 2 mm to 5 mm in 0.2 mm increments. The corresponding trend of average electromagnetic force with respect to mover pole height is shown in Fig. 9.

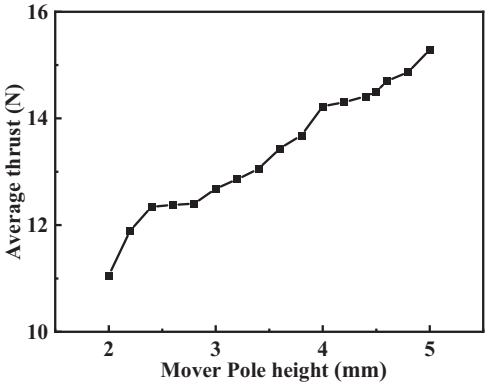


Fig. 9. Average electromagnetic force with respect to mover pole height.

As shown in Fig. 9, average electromagnetic force increases with the increase of mover pole height, exhibiting a relatively steep trend. The average electromagnetic force monotonically rises from 10.701 N to 14.952 N, with a range of 4.251 N. This behavior is attributed to the increased overlap area between the stator and mover poles, which enhances the effective magnetic flux path. However, increasing the mover pole height reduces the spacing between adjacent stator poles, which complicates the manufacturing process, and an excessive pole height may also compress the stator slots, limiting the space available for winding placement. Considering these factors comprehensively, the mover pole height was ultimately set to 4.5 mm, corresponding to an average electromagnetic force of 14.21 N.

Stator pole width affects both magnetic flux density and utilization efficiency of the ferromagnetic material in the 12-pole TSRLM. During sensitivity analysis of the stator pole width, the stator inner diameter and mover pole height in the finite-element model were set to 34 mm and 4.5 mm, respectively, while all other structural parameters remained unchanged. Stator pole width was then varied from 4 mm to 5 mm in 0.1 mm increments. The corresponding trend of the average electromagnetic force with respect to stator pole width is shown in Fig. 10.

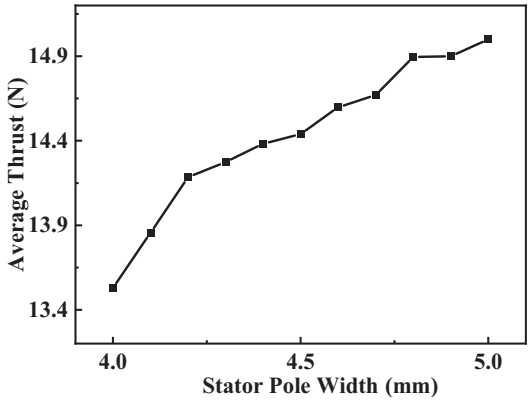


Fig. 10. Average electromagnetic force with respect to stator pole width.

From Fig. 10, when the stator pole width increases from 4 mm to 4.2 mm, average electromagnetic force rises steeply from 13.561 N to 14.201 N. As the stator pole width further increases from 4.2 mm to 4.7 mm, growth of the average electromagnetic force slows down, and when the width increases from 4.7 mm to 5.0 mm, the growth trend further attenuates. Overall, the curve exhibits a monotonic trend, with a range of 1.450 N in average electromagnetic force. A stator pole width that is too small may hinder the formation of an effective magnetic path, whereas an excessively large width reduces the spacing between the winding and adjacent poles, significantly increasing manufacturing difficulty. Moreover, an oversized stator pole width constrains the size of the stator slots, limiting the space available for winding placement. Considering these factors comprehensively, stator pole width was ultimately determined to be 4.8 mm.

Similar to stator pole width, the stator yoke thickness also affects formation of the effective magnetic circuit. During sensitivity analysis of the stator yoke thickness, the stator inner diameter, mover pole height, and stator pole width in the finite-element model were set to 34 mm, 4.5 mm, and 4.8 mm, respectively. All other structural parameters were kept constant, while the stator yoke thickness was varied from 3.4 mm to 5.4 mm with a step size of 0.2 mm. The corresponding trend of the average electromagnetic force with respect to the stator yoke thickness is shown in Fig. 11.

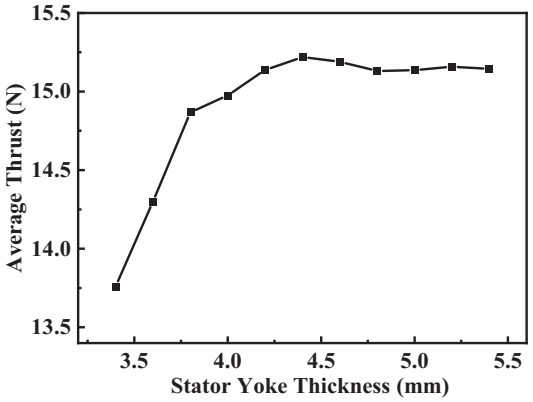


Fig. 11. Average electromagnetic force with respect to stator yoke thickness.

As shown in Fig. 11 when stator yoke thickness increases from 3.4 mm to 4.4 mm, the average electromagnetic force exhibits a relatively steep increase, rising from 13.751 N to 15.201 N. When yoke thickness further increases from 4.4 mm to 5.4 mm, the growth of the average electromagnetic force becomes much more gradual, approaching an almost constant value. The range of the average electromagnetic force is 1.480 N. An excessively thick stator yoke compresses the stator slot size, reducing the space available for winding placement, and may also prevent the core from reaching magnetic saturation, which increases the motor mass and leads to underutilization of the core, ultimately degrading motor performance. Considering these factors comprehensively, stator yoke thickness was finally selected as 4.4 mm. The structural parameters after single objective optimization are presented in Table 1.

Figure 12 shows the output electromagnetic force waveforms of the 12-pole TSRLM before and after optimization. It can be observed that the optimized TSRLM exhibits a significant improvement in output electromagnetic force compared with the pre-optimization design. Calculations indicate that the average electromagnetic force over half a mover pole pitch increased from 12.73 N before optimization to 14.69 N after optimization, representing a 15.4% improvement. This result

Table 1: Structural parameters of 12-pole TSRLM

Structural Parameter	Size	Structural Parameter	Size
Stator outer diameter	63.0 mm	Mover yoke thickness	4.5 mm
Stator inner diameter	34.0 mm	Mover pole height	4.5 mm
Mover outer diameter	42.6 mm	Stator spacing ring thickness	8.0 mm
Shaft diameter	24.6 mm	Mover ferromagnetic ring thickness	5.5 mm
Stator yoke thickness	4.4 mm	Mover spacing ring thickness	7.5 mm
Stator pole width	4.8 mm	Air-gap length	0.2 mm
Stator ferromagnetic ring thickness	5.0 mm	Mover stack length	65.0 mm
Stator module angle	43/2°		

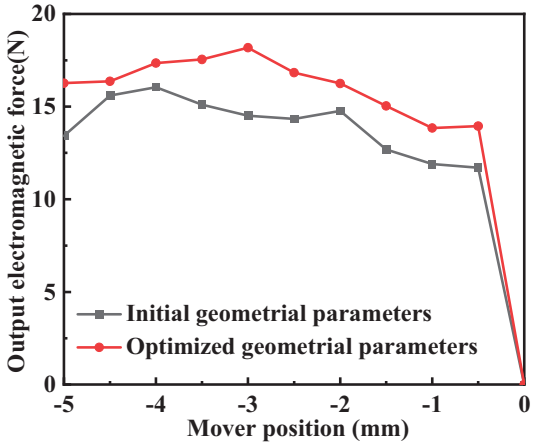


Fig. 12. Comparison curves of output electromagnetic force of the 12-pole TSRLM before and after single objective optimization.

demonstrates the effectiveness of the single-objective optimization.

V. EXPERIMENTAL VERIFICATION

A prototype of the 12-pole TSRLM after single-objective optimization was fabricated, and both the hardware test bench and the machine test platform were designed and established, as shown in Fig. 13. In this system, a DC rotary motor is used as the prime mover. Its torque is regulated by the magnetic powder brake, and the rotary motion is converted into reciprocating linear

motion through a crank-slider mechanism connected to the TSRLM mover, thereby driving the TSRLM to operate under reciprocating motion.

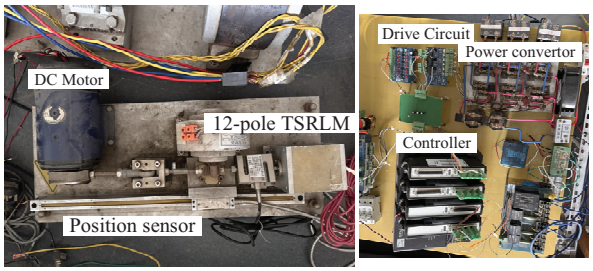


Fig. 13. The 12-pole TSRLM and hardware experiment platform.

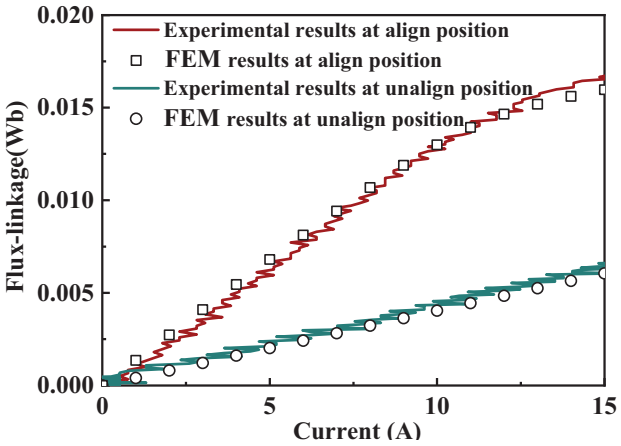
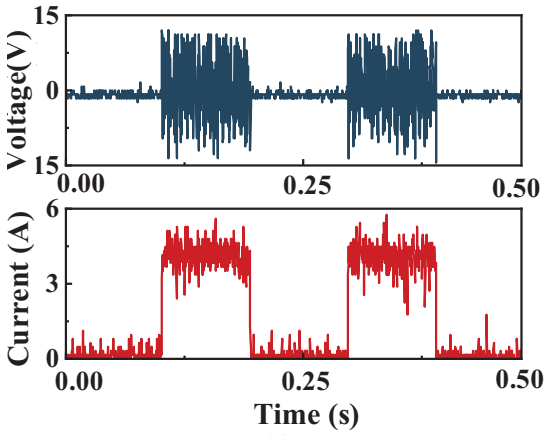
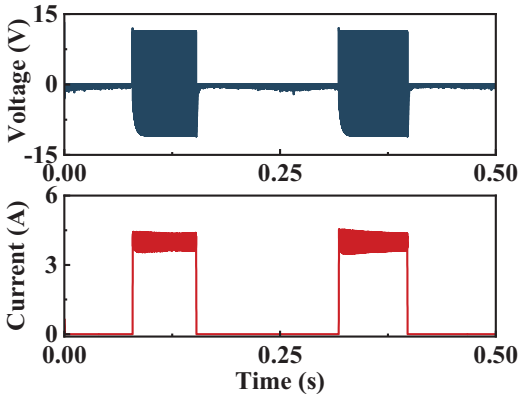


Fig. 14. Comparison of magnetization curves at special mover positions.



(a)



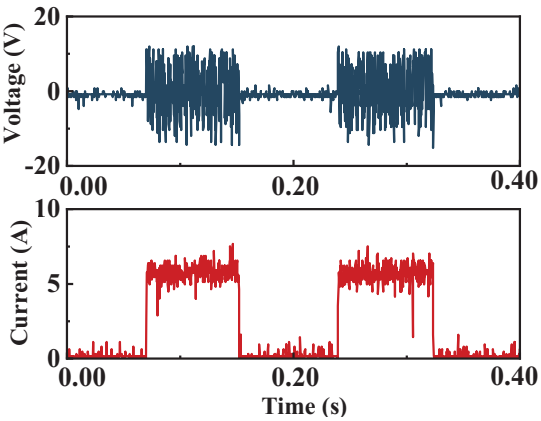
(b)

Fig. 15. Comparison of experiment and simulation under 4 A current chopping limit: (a) experimental curve under 4 A current chopping limit and (b) simulation curve under 4 A current chopping limit.

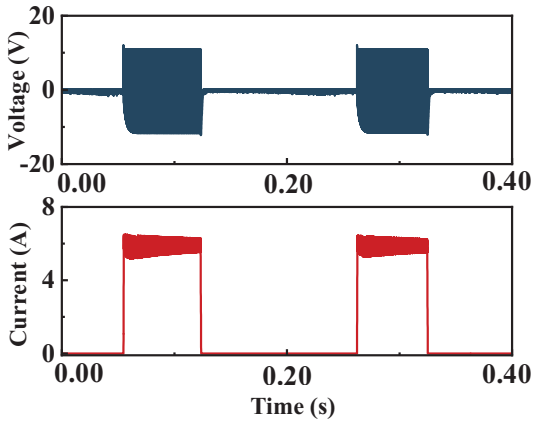
Based on the hardware experimental platform described above, static tests were conducted on the proposed 12-pole TSRLM. The static tests include static flux linkage measurements as well as voltage and current measurements. During the static flux linkage test, the mover of the machine was fixed at the aligned position (0 mm) and the unaligned positions (−5 mm or 5 mm), respectively. A 12-V phase voltage was then instantaneously applied to the phase winding of the TSRLM, and the corresponding voltage and current waveforms were recorded. The measured voltage and current data were processed, and the flux linkage was calculated using the known voltage balance equation.

Comparison between the experimental results and the finite-element calculation results is shown in Fig. 14. It can be observed that the experimentally obtained magnetization curves agree well with those predicted by finite-element analysis, with a discrepancy of less than 5%. In the high-current region, the flux linkage values obtained from the finite-element model are slightly lower than the experimental results. This discrepancy may be attributed to the neglect of leakage flux caused by longitudinal end effects in the finite-element model, which leads to an underestimation of the magnetization curves at both aligned and unaligned positions. In addition, manufacturing tolerances and assembly imperfections may also contribute to the observed differences.

Dynamic tests were carried out on the 12-pole TSRLM prototype, which also served to verify the accuracy of the MATLAB/Simulink dynamic simulation model. The DC supply voltage was set to 12 V, and a current chopping control strategy was adopted. The current chopping limits were set to 4 A and 6 A, respectively, and the corresponding winding voltage and winding current waveforms were measured. Using the same control strategy and identical current chopping limits, the winding voltage and current waveforms were obtained from the MATLAB/Simulink dynamic simulation model. Comparisons between the measured and simulated waveforms are presented in Figs. 15 and 16.



(a)



(b)

Fig. 16. Comparison of experiment and simulation under 6 A current chopping limit: (a) experimental curve under 6 A current chopping limit and (b) simulation curve under 6 A current chopping limit.

From the comparison results, it can be observed that the measured waveforms agree well with the simulated ones. As the current chopping limit increases, the winding current increases accordingly, leading to a higher output electromagnetic force. Consequently, the operating speed of the 12-pole TSRLM also increases. The motoring performance tests not only validate the dynamic performance of the TSRLM prototype but also confirm the accuracy and effectiveness of the finite-element analysis and dynamic simulation models.

VI. CONCLUSION

This paper presents a modular transverse-flux tubular switched reluctance linear machine based on U-shaped stator topology. The proposed modular structure effectively shortens magnetic flux paths and enhances iron core utilization, resulting in improved electromagnetic characteristics. A three-dimensional finite-element analysis is performed to investigate the electromagnetic behavior of the machine, and a simple single-objective optimization is employed to enhance the average electromagnetic force. A 12-pole TSRLM prototype is manufactured and experimentally tested. The close agreement between experimental and simulation results confirms the correctness of the electromagnetic modeling and the feasibility of the proposed machine design. With its modular structure, simple configuration, and good manufacturability, the proposed TSRLM provides a promising solution for high-performance linear electric drive applications.

ACKNOWLEDGMENTS

This work is supported by the National Natural Science Foundation of China International (regional) co-operation and exchange projects NSFC-RSF under Grant W2412064.

REFERENCES

[1] H. Chen, J. Liu, C. Liu, X. Wang, A. Musolino, M. Shamiyev, and A. O. Pulatov, "A novel tubular double stator switched reluctance linear launcher," *IEEE T. Plasma Sci.*, vol. 53, no. 10, pp. 2677–2681, Oct. 2025.

[2] J. Liu, H. Chen, X. Wang, P. Wheeler, V. F. Pires, J. F. A. Martins, A. Musolino, Y. Gorbounov, and H. Torkaman, "Switched reluctance linear motor force ripple suppression based on fixed frequency implicit generalized predictive self-correction controller," *IEEE Transactions on Energy Conversion*, pp. 1–18, 2024.

[3] Q. Sun, J. Wu, and C. Gan, "Optimized direct instantaneous torque control for SRMs with efficiency improvement," *IEEE Transactions on Industrial Electronics*, vol. 68, no. 3, pp. 2072–2082, Mar. 2021.

[4] R. Yang, X. Wang, Z. Huang, and Y. Ma, "Torque ripple minimization control of switched reluctance motor based on online torque sharing function," *IEEE Transactions on Power Electronics*, vol. 40, no. 4, pp. 4878–4888, 2025.

[5] J. Cai, X. Dou, A. D. Cheok, W. Ding, Y. Yan, and X. Zhang, "Model predictive control strategies in switched reluctance motor drives – An overview," *IEEE Transactions on Power Electronics*, vol. 40, no. 1, pp. 1669–1685, 2025.

[6] S. Tavakolian, G. Fang, S. Dhale, and B. N. Mobarakeh, "Fixed-switching model-free predictive current control of switched reluctance motor using parameter estimation," in *2024 IEEE Transportation Electrification Conference and Expo (ITEC)*, 2024.

[7] A. Walz-Lange and G. Schullerus, "Sensorless control of a switched reluctance machine based on switching frequency evaluation," *IEEE Transactions on Industry Applications*, vol. 58, no. 4, pp. 4768–4777, 2022.

[8] R. Nie, H. Chen, J. Liu, W. Zhao, S. Zhao, J. Tian, X. Wang, and Y. Huo, "Peak current compensation for reducing the negative impact of LEE on SRLM," *IET Electric Power Applications*, vol. 14, no. 6, pp. 1030–1040, June 2020.

[9] H. Chen, R. Nie, J. Liu, W. Zhao, Z. Yuan, and J. Tian, "A novel tubular switched reluctance linear machine shielding from longitudinal end magnetic effect," *IEEE Transactions on Applied Superconductivity*, vol. 30, no. 4, pp. 1–7, 2020.

[10] D. Wang, C. Shao, and X. Wang, "Design and performance evaluation of a tubular linear switched reluctance generator with low cost and high thrust density," *IEEE Transactions on Applied Superconductivity*, vol. 26, no. 7, pp. 1–5, 2016.

[11] D. Wang, D. Zhang, X. Du, and X. Wang, "Unitized design methodology of linear switched reluctance motor with segmental secondary for long rail propulsion application," *IEEE Transactions on Industrial Electronics*, vol. 65, no. 12, pp. 9884–9894, 2018.

[12] W. Ding, Y. Hu, T. Wang, and S. Yang, "Comprehensive research of modular e-core stator hybrid-flux switched reluctance motors with segmented and nonsegmented rotors," *IEEE Transactions on Energy Conversion*, vol. 32, no. 1, pp. 382–393, 2017.

[13] W. Ding, Y. Hu, Q. Ze, X. Liu, and Y. Liu, "A novel modular E-core stators and segmental rotors switched reluctance machine for electric vehicles," in *2014 Ninth International Conference on Ecological Vehicles and Renewable Energies (EVER)*, pp. 1–8, 2014.

[14] M. Ruba, I. Benþia, and L. Szabó, "Modular fault tolerant switched reluctance machine-design and dynamic simulations," in *12th International Conference on Optimization of Electrical and Electronic Equipment*, pp. 441–446, 2010.



Hao Chen received the B.S. and Ph.D. degrees in electrical engineering from the Department of Automatic Control, Nanjing University of Aeronautics and Astronautics, Nanjing, China, in 1991 and 1996, respectively. He is with the School of Electrical and Power Engineering, China University of Mining and Technology, Xuzhou, where he has been a professor since 2001. From 2002 to 2003, he was a Visiting Professor with Kyung sung University, Busan, South Korea. Since 2008, he has also been an Adjunct Professor with The University of Western Australia, Perth, WA, Australia. He has authored one book and more than 200 articles. He holds 15 U.S. patents, 23 Australian patents, one Danish patent, seven Canadian patents, three South African patents, 10 Russian patents, 66 Chinese invention patents, and six Chinese utility model patents. His current research interests include motor control, linear launcher, electric vehicles, electric traction, servo drives, and wind power generator control. Chen was a recipient of the Prize of Science and Technology of Chinese Youth and the Prize of the Fok Ying Tong Education Foundation for Youth Teachers in 2004. He was awarded the First Prize in the Science and Technology Advanced of Province and Ministry once, the Second Prize in the Science and Technology Advanced of Province and Ministry nine times, and the Third Prize in the Science and Technology Advanced of Province and Ministry 14 times. He became the Chinese New Century Hundred-Thousand Ten-Thousand Talents Engineering National Talent in 2007, and won the Government Especial Allowance of People's Republic of China State Department in 2006.



Denis Kotin received the B.S., M.S., and Cand. Tech. Sc. in the Department of Electric Drive and Industry Automation, Faculty Mechatronics and Automation, Novosibirsk State Technical University, Russia, in 2005, 2007, and 2010, respectively. Since 2015, is the Head of the Department of Electric Drive and Industry Automation. Research interests include automatic control of AC electric drives and power electronic devices, and he has authored more than 160 scientific publications.



Aris Dimeas is an Assistant Professor at the School of Electrical and Computer Engineering of the National Technical University of Athens (NTUA), with more than 20 years of experience in power systems operation, smart grids, and energy system digitalization. His expertise spans distribution and transmission system operation, renewable energy integration, microgrids, flexibility markets, artificial intelligence applications, and advanced control and decision-support software. He has played a leading technical and coordination role in more than 30 EU-funded research and innovation projects (H2020 and Horizon Europe), collaborating closely with TSOs, DSOs, regulators, industry, and the European Commission. His work bridges research and real-world deployment, with demonstrated impact on system supervision, resilience, market design, and data-driven grid operation, while his scientific contributions include high-impact publications in leading IEEE and international journals.



Emmanuel Karapidakis is an Electrical and Computer Engineer. He was Dean at School of Engineering from 2019 to 2025, and Director of Energy, Environment and Climate Change Institute IEECC, in Hellenic Mediterranean University HMU. Since 2022, he is President of the Board in Hellenic Association of Electricity Storage Systems HAESS. His research interests focus on energy systems, power systems operation, diverse & dispersed generation, micro-grids, renewable energy technologies, energy storage, and energy markets. He is/was scientific coordinator (PI) in 12 European financed projects, 15 National programs, and several private funded projects, with more than 8 million euros in total. He has published more than 120 papers (Scopus Author ID 6506872824) in prestigious journals and scientific conferences, and four scientific book chapters. From 2011 to 2015, he was Member of the Board in Regional Council of Innovation, and from 2015 to 2017, Member of Board in Energy Planning Council at Region of Crete.



Olimjon Toirov received his Ph.D. (2012) and D.Sc. (2018) in Technical Sciences (Energy Systems and Complexes) from the Institute of Energy and Automation, Academy of Sciences of Uzbekistan, and Tashkent State Technical University (TSTU), respectively. He was awarded the academic title of Full Professor in 2020. He has held research and leadership positions at the Institute of Energy and Automation, Uzbekenergo, AGH University of Science and Technology (Poland), and TSTU, where he served as Head of the Electrical Machines and Drives Department (2019–2024) and has been Dean of the Faculty of Electrical Engineering since 2024. His research interests include electric drive systems, renewable and green energy, energy efficiency, asynchronous generator control, and electromechanical system optimization. He has led and participated in over 65 industrial and research projects, implemented control systems in major industrial enterprises, and received more than 12 international research grants. Toirov has authored over 300 publications, including patents, textbooks, and monographs, with more than 40 papers indexed in Web of Science and Scopus. He has supervised one D.Sc., five Ph.D., and numerous undergraduate and master's students. His honors include national scientific awards, the Scopus Uzbekistan Award (2023), and the Shuhrat medal (2024). He currently serves on national expert councils and editorial boards of scientific journals.



Liu Jingfu received the B.S. degree in Mechanical and Electrical Engineering, from Northeast Forestry University, Harbin, Heilongjiang, China, in 2017, the M.S. degree from the School of Electrical Engineering, China University of Mining and Technology, Xuzhou, Jiangsu, in 2021. He is currently pursuing a Ph.D. degree in electrical engineering at China University of Mining and Technology, Xuzhou. His research interests include switched reluctance linear motor control, ocean wave power generation, and electric vehicles.



Zhao Wenmin received the B.S. degree in automation from the Taiyuan University of Technology, Taiyuan, China, in 2017. She is currently pursuing the master's degree in electrical engineering with the China University of Mining and Technology, Xuzhou. Her current research interests include motor design and optimization.



Xing Wang received the B.S. degree from China University of Mining and Technology, Xuzhou Jiangsu, China, in 1996, and M.S. degree from China University of Mining and Technology, Xuzhou Jiangsu, in 1999. In 2007, she became an Associate Professor with China University of Mining and Technology, Xuzhou. She is a holder of four US Patents, nine Australian Patents, two Canadian Patents, four Russian Patents, 12 Chinese Invention Patents, three Chinese Utility Model Patents, and has authored 15 papers.



Sherif Moussa is Dean of the School of Engineering, Applied Science, and Technology at the Canadian University Dubai (CUD), UAE. He earned his Ph.D. in Electrical and Computer Engineering from the University of Québec at Trois-Rivières, Canada, and his M.Sc. in Electrical and Computer Engineering from the University of Waterloo, Canada. Since joining CUD in 2007, Moussa has led the School's remarkable growth, overseeing the launch

and accreditation of several engineering and computing programs, including Mechatronics Engineering, Computer Science, Cybersecurity, Software Design, Power and Renewable Energy Engineering, and the M.Sc. in Artificial Intelligence. His leadership has also advanced international collaborations, notably with Queen's University and the University of Ottawa, and strengthened CUD's engagement with industry partners in emerging technologies. Moussa's research interests span wireless communication, computer networks, machine learning, and digital systems design. He has published widely in international journals and conferences, serves on technical committees, and is the recipient of the 2015 CUD Research Excellence Award. He is also the founder of CUD's Robotics Club and a strong advocate for innovation and experiential learning in engineering education.

Unified 3D Analytical Models of Surface-Inserted Axial Flux Machines With Odd-/Even-Piece Halbach Arrangements

Youyuan Ni[1], Jinsong Zou[1], Yong Lin[1], and Anbang Wang[2]

[1]School of Electrical Engineering & Automation
Hefei University of Technology, Hefei 230009, China
nyy@hfut.edu.cn, 2024110327@mail.hfut.edu.cn, linyong@hfut.edu.cn

[2]Yangzhou Haitong Electronic Technology Co. Ltd.
Yangzhou 225001, China
delsuner@163.com

Abstract – Considering the 3-dimensional (3D) air-gap fringing field, unified 3D analytical models equivalent to linear machines are proposed for surface-inserted axial flux machines (SIAFMs) with odd-/even-piece Halbach arrangements. The 3D scalar potential governing equations for several regions can be uniquely solved according to Fourier decomposition coefficient matrixes derived from field boundary conditions. Based on this, the electromagnetic parameters can be derived. Predictions indicate that, compared with the non-optimized SIAFMs with three-/four-piece Halbach arrangements, the optimized SIAFMs with three-/four-piece Halbach arrangements exhibit excellent electromagnetic performances. The 3D finite element (FE) and analytical predictions for the SIAFM models are compared.

Index Terms – Odd-/even-piece Halbach arrangements, surface-inserted axial flux machine, unified 3D analytical model.

I. INTRODUCTION

Different from the non-optimized radial flux permanent magnet (PM) machines, axial flux machines with PMs have not only smaller volume but also higher torque and power density although they may lead to larger torque ripple [1, 2]. With the progress and development of society, especially extensive use of rare earth materials and improvement of control techniques, more axial flux machines, which are used in fields like electric vehicles, aerospace, and wind power [2–4], are needed.

A great variety of academic research on surface-mounted axial flux machines (SMAFMs) with PMs is carried out with the aim of improving their performance. Halbach arrangements that not only weaken torque ripple but also gather the magnetic field [4], are used for SMAFMs in [4–9], and the combination of magnet circumferential displacement with various pole-arc ratios and magnet axial shape design are utilized to reduce pulsating torque in [10]. Surface-inserted axial flux machines (SIAFMs) with different thickness Halbach magnets and soft magnetic materials are proposed in [11]. Axial flux machines combining surface-inserted and surface-mounted magnets are analyzed in [7].

As a numeric solution approach, the 3-dimensional (3D) finite element (FE) analysis takes a long computation time, especially for optimization. In order to reduce the computing time, a few approaches have been presented. An approach with 2-dimensional (2D) scalar potential equivalent to linear motor for SMAFM is proposed in [5, 12, 13]. A 2D analytical model with vector potential is presented for achieving the magnetic field in SMAFMs with Halbach arrangements in [14, 15], and a method with 2D vector potential equivalent to linear machine is proposed in [4, 6, 16–18]. However, these approaches, except [13, 17], ignore the fringing effect in radial direction, and the methods with correction coefficient proposed in [13, 17] still have a degree of error. Then, 3D scalar potential techniques based on Bessel function in [18–20] or virtual argument Bessel function in [8, 9, 21] are presented. These 3D techniques can only solve the fields in SMAFMs and have non-negligible errors with the equivalent method in [7]. In addition, an equivalent method with the 3D scalar potential equivalent to linear motors has been proposed in [22–25], but it cannot be used for SIAFMs. The approach proposed in [26] only applies to surface-inserted radial flux PM machines.

In this paper, unified 3D analytical models are proposed for SIAFMs with odd-/even-piece Halbach arrangements. By means of solving the Fourier decomposition of boundary condition matrix in equivalent linear machines, the field governing equations in different regions are solved. The stator slotting effect is taken into account by Carter's coefficient. Different from 2D radial flux machines, the air-gap fringing effect for SIAFMs

Submitted On: March 09, 2026
Accepted On: June 15, 2026

1054-4887 © ACES

https://doi.org/10.13052/2026.ACES.J.410606

needs to be considered and the air-gap fringing field is analyzed. According to the solved magnetic fields, the electromagnetic performances are obtained. Computation results demonstrate that the optimized pieced Halbach arrangement SIAFMs have better performance than the corresponding non-optimized ones. A comparison of 3D FE and analytical predictions demonstrates that the proposed 3D analytical model is valid.

II. 3D PHYSICAL MODEL FOR HALBACH SIAFMS

A. Geometrical parameters for Halbach arrangements

Figures 1 (a) and (b) show the design parameters of the odd-/even-piece Halbach arrangements for SIAFMs. For the odd/even-piece Halbach, $\alpha_1, \ldots$, and α_λ are the arc ratios of all the magnet pieces. Regardless of odd- or even-piece number, α is the proportion of polar arcs between two rotor teeth, α_0 is the arc ratio of all the N or S magnets. For both odd- and even-piece Halbach arrangements, the magnetization angles between the axial symmetric axis and the magnetization directions are defined as $\theta_1, \ldots$, and $\theta_{\lambda+1}$. In particular, for the odd-piece Halbach, $\theta_1 = 0°$. If θ_1 is equal to zero for the even-piece Halbach, the even-piece Halbach is equivalent to the odd-piece Halbach.

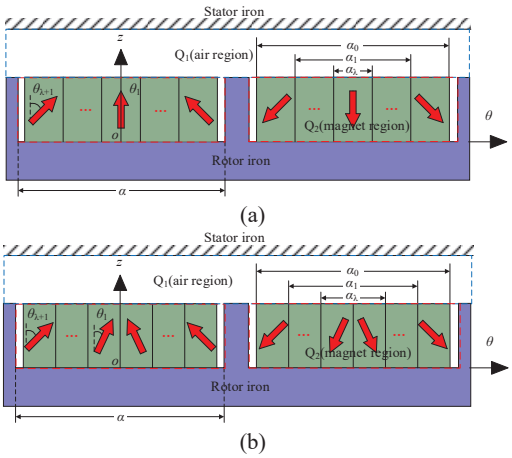


Fig. 1. Design parameters of surface-inserted odd-/even-piece Halbach arrangements: (a) odd-piece Halbach and (b) even-piece Halbach.

Figure 2 clearly exhibits the 3D structure of single rotor and double stator SIAFM with three-piece Halbach arrangements. In the cylindrical coordinate systems, the 3D analytical equations of SIAFM models can be hardly solved. As a consequence, for easy solution of the 3D field distributions in SIAFMs with Halbach arrangements, the cylindrical coordinate system is converted to the spatial Cartesian one. However, due to the difference

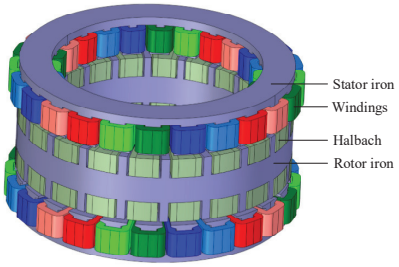


Fig. 2. 3D structure of SIAFM with three-piece Halbach arrangements.

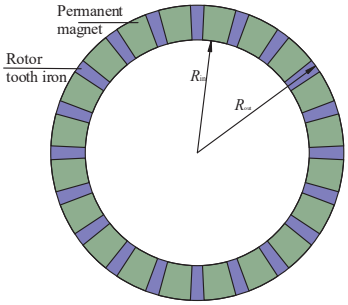


Fig. 3. Top view of SIAFM.

between inner and outer diameters, the unfolded ring cannot be strictly equivalent to a rectangle. In order to ensure the rigor and accuracy of the equivalent calculation, the PMs can be divided into n_t (an odd number) circular cylinder slices with unequal inner and outer radii but equal differences between inner and outer radii. From inside to outside, the circular cylindrical regions are numbered as $1, \ldots, j, \ldots$, and n_t. Therefore, the average radius of the j-th circular cylinder can be computed as

$$R_j = R_{\text{in}} + (j-1)\frac{R_{\text{out}} - R_{\text{in}}}{n_t} + \frac{1}{2}\frac{R_{\text{out}} - R_{\text{in}}}{n_t}, \quad (1)$$

where R_{in} and R_{out} are the inner and outer radii, respectively, as shown in Fig. 3.

B. Magnetization parameters for Halbach arrangements

The double Fourier decomposition of magnetization by trigonometric functions are one key point of the analytical model. However, because of the special circumstances of the rotor teeth, polar distance cannot be used as half a cycle of magnetization components. Through the mirror method, the length between the rotor teeth can be considered as half a cycle of the magnetization components. In the spatial Cartesian coordinate system, the three magnetization components in x-, y-, and z-directions for odd-piece Halbach (given three-piece Halbach as an example) between $-l/2$ to $3l/2$ can

be expressed as

$$\begin{cases} M_x^j = \dfrac{B_{re}}{\mu_0}\sin(\theta_2) & -\dfrac{\alpha_0 l}{2\alpha} < x < -\dfrac{\alpha_1 l}{2\alpha} \\ M_y^j = 0 & -\dfrac{qn_t}{2} < y < \dfrac{qn_t}{2} \\ M_z^j = \dfrac{B_{re}}{\mu_0}\cos(\theta_2) \end{cases}, \tag{2}$$

$$\begin{cases} M_x^j = 0 & -\dfrac{\alpha_1 l}{2\alpha} < x < \dfrac{\alpha_1 l}{2\alpha} \\ M_y^j = 0 & -\dfrac{qn_t}{2} < y < \dfrac{qn_t}{2} \\ M_z^j = \dfrac{B_{re}}{\mu_0} \end{cases}, \tag{3}$$

$$\begin{cases} M_x^j = -\dfrac{B_{re}}{\mu_0}\sin(\theta_2) & \dfrac{\alpha_1 l}{2\alpha} < x < \dfrac{\alpha_0 l}{2\alpha} \\ M_y^j = 0 & -\dfrac{qn_t}{2} < y < \dfrac{qn_t}{2} \\ M_z^j = \dfrac{B_{re}}{\mu_0}\cos(\theta_2) \end{cases}, \tag{4}$$

$$\begin{cases} M_x^j = -\dfrac{B_{re}}{\mu_0}\sin(\theta_2) & -\dfrac{\alpha_0 l}{2\alpha} + l < x < -\dfrac{\alpha_1 l}{2\alpha} + l \\ M_y^j = 0 & -\dfrac{qn_t}{2} < y < \dfrac{qn_t}{2} \\ M_z^j = -\dfrac{B_{re}}{\mu_0}\cos(\theta_2) \end{cases}, \tag{5}$$

$$\begin{cases} M_x^j = 0 & -\dfrac{\alpha_1 l}{2\alpha} + l < x < \dfrac{\alpha_1 l}{2\alpha} + l \\ M_y^j = 0 & -\dfrac{qn_t}{2} < y < \dfrac{qn_t}{2} \\ M_z^j = -\dfrac{B_{re}}{\mu_0} \end{cases}, \tag{6}$$

$$\begin{cases} M_x^j = \dfrac{B_{re}}{\mu_0}\sin(\theta_2) & -\dfrac{\alpha_1 l}{2\alpha} + l < x < \dfrac{\alpha_0 l}{2\alpha} + l \\ M_y^j = 0 & -\dfrac{qn_t}{2} < y < \dfrac{qn_t}{2} \\ M_z^j = -\dfrac{B_{re}}{\mu_0}\cos(\theta_2) \end{cases}, \tag{7}$$

$$\begin{cases} M_x^j = 0 \\ M_y^j = 0 \\ M_z^j = 0 \end{cases} \quad \text{others}, \tag{8}$$

$$\begin{cases} l = \dfrac{\alpha\pi R_j}{p} \\ q = \dfrac{R_{\text{out}} - R_{\text{in}}}{n_t} \end{cases}, \tag{9}$$

where M_x^j, M_y^j, and M_z^j are x-, y-, and z-axis components of the j-th group of magnets, B_{re} is PM remanence, μ_0 is vacuum permeability, p is pole-pair number, and h is PM length in the axial direction.

Using double Fourier decomposition, the magnetizations in regions $\mathrm{Q}_0(-1/2 \le x \le 3/2$ and $qn_t \le z \le qn_t)$ are expressed by

$$\begin{cases} M_x^j = \displaystyle\sum_{m=0}^{\infty}\sum_{i=1,3,5}^{\infty} M_{xmi}^j \sin(\omega_i^j x)\cos\left\{\omega_m^j\left[\left(y + \left(j - \dfrac{n_t+1}{2}\right)q\right]\right\}\right. \\ M_y^j = 0 \\ M_z^j = \displaystyle\sum_{m=0}^{\infty}\sum_{i=1,3,5}^{\infty} M_{zmi}^j \cos(\omega_i^j x)\cos\left\{\omega_m^j\left[\left(y + \left(j - \dfrac{n_t+1}{2}\right)q\right]\right\}\right. \end{cases}, \tag{10}$$

where i is an odd number, m is a nonnegative integer, and ω_m^j and ω_i^j can be given as

$$\begin{cases} \omega_m^j = \dfrac{m\pi}{R_{\text{out}} - R_{\text{in}}} \\ \omega_i^j = \dfrac{ip}{\alpha R_j} \end{cases}, \tag{11}$$

where M_{zmi}^j and M_{xmi}^j are the Fourier decomposition coefficients and can be written as

$$M_{xmi}^j = \begin{cases} \dfrac{1}{lqn_t}\displaystyle\iint_Q M_x^j \sin(\omega_i^j x) & m \ne 0 \\ \quad \cos\left\{\omega_m^j\left[\left(y + \left(j - \dfrac{n_t+1}{2}\right)\dfrac{q}{n_t}\right]\right\}\right. \mathrm{d}x\mathrm{d}y, & \\ \dfrac{1}{2lqn_t}\displaystyle\iint_Q M_x^j \sin(\omega_i^j x)\mathrm{d}x\mathrm{d}y & m = 0 \end{cases}, \tag{12}$$

$$M_{zmi}^j = \begin{cases} \dfrac{1}{lqn_t}\displaystyle\iint_Q M_z^j \cos(\omega_i^j x) & \\ \quad \cos\left\{\omega_m^j\left[\left(y + \left(j - \dfrac{n_t+1}{2}\right)\dfrac{q}{n_t}\right]\right\}\right. \mathrm{d}x\mathrm{d}y\mathrm{y}, & m \ne 0 \\ \dfrac{1}{2lqn_t}\displaystyle\iint_Q M_z^j \cos(\omega_i^j x)\mathrm{d}x\mathrm{d}y, & m = 0 \end{cases}. \tag{13}$$

III. 3D ANALYTICAL MODEL FOR HALBACH SIAFMS

A. Slotless 3D field prediction

In order to ensure the feasibility of 3D field calculation, several assumptions are made: infinite permeability for the stators and rotor, linear demagnetization property for PM, and neglected eddy current.

The whole 3D solution domain consists of air region $\mathrm{Q}_1(-q/2 < y < q/2$ and $h < z < h+g)$ and magnet region $\mathrm{Q}_2(-l/2 + l/\alpha \le x \le 3l/2 + l/\alpha, -q/2 < y < q/2$ and $0 < z < h)$. The 3D governing equations in these

two regions are written as

$$\begin{cases} \dfrac{\partial^2\varphi_1^j}{\partial x^2}+\dfrac{\partial^2\varphi_1^j}{\partial y^2}+\dfrac{\partial^2\varphi_1^j}{\partial z^2}=0, & \text{in } Q_1 \\ \dfrac{\partial^2\varphi_2^j}{\partial x^2}+\dfrac{\partial^2\varphi_2^j}{\partial y^2}+\dfrac{\partial^2\varphi_2^j}{\partial z^2}=\dfrac{1}{\mu_r}\dfrac{\partial M_x^j}{\partial x}, & \text{in } Q_2 \end{cases}, \quad (14)$$

where μ_r is relative permeability of PMs, φ is scalar potential, subscript numbers denote the region, superscript j means j-th group of magnets, and g is axial length of air gap. In the linear analytical model, permeability of the magnet is generally considered as a constant.

In a Cartesian coordinate system, according to the symmetry and period boundary conditions, with setting a zero scalar potential value on the interface, the 3D scalar potential equations are expressed as

$$\begin{cases} \varphi_1^j(x,y,z)=-\varphi_1^j(x+\pi R_j/p,y,z) \\ \varphi_2^j(x,y,z)=-\varphi_2^j(x+\alpha\pi R_j/p,y,z) \\ \varphi_{1,2}^j(x,y,z)=\varphi_{1,2}^j(x,y+2R_{\text{out}}-2R_{\text{in}},z) \\ \varphi_1^j(x,y,h+g)=\varphi_2^j(x,y,0)=0 \end{cases}. \quad (15)$$

On the basis of (15) and the separation of variables, general solutions of 3D scalar potential equations for (14) are

$$\begin{cases} \varphi_1^j=\displaystyle\sum_{m=0}^{\infty}\sum_{n=1,3}^{\infty}A_{1mn}^j(e^{k_1^j z}-e^{2k_1^j h+2k_1^j g-k_1^j z})\cos(\omega_n^j x) \\ \qquad\times\cos\left\{\omega_m^j\left[\left(y+\left(j-\dfrac{n_t+1}{2}\right)q\right]\right\}\right. \\ \varphi_2^j=\displaystyle\sum_{m=0}^{\infty}\sum_{i=1,3}^{\infty}\left[A_{2mi}^j(e^{k_2^j z}-e^{-k_2^j z})-\frac{\omega_i^j M_{xmi}^j}{\mu_r k_2^{j^2}}(1-e^{-k_2^j z})\right] \\ \qquad\times\cos(\omega_i^j x)\cos\left\{\omega_m^j\left[\left(y+\left(j-\dfrac{n_t+1}{2}\right)q\right]\right\}\right. \end{cases}, \quad (16)$$

$$\begin{cases} k_1^j=\sqrt{\omega_m^{j^2}+\omega_n^{j^2}} \\ k_2^j=\sqrt{\omega_m^{j^2}+\omega_i^{j^2}} \end{cases}, \quad (17)$$

$$\begin{cases} \omega_m^j=\dfrac{m\pi}{R_{\text{out}}-R_{\text{in}}} \\ \omega_n^j=\dfrac{np}{R_j} \\ \omega_i^j=\dfrac{ip}{\alpha R_j} \end{cases}, \quad (18)$$

where A_{1mn}^j and A_{2mi}^j are unknown coefficients of the j th group of magnets depending on the boundary conditions and n is an odd number.

Moreover, in the 3D spatial Cartesian coordinates, the relationships between scalar potential, magnetic field intensity, and flux density are

$$\begin{cases} H_x=-\dfrac{\partial\varphi}{\partial x} \\ H_y=-\dfrac{\partial\varphi}{\partial y} \\ H_z=-\dfrac{\partial\varphi}{\partial z} \end{cases}, \quad (19)$$

$$\begin{cases} B_x=-\mu_0\mu_r\dfrac{\partial\varphi}{\partial x}+\mu_0 M_x \\ B_y=-\mu_0\mu_r\dfrac{\partial\varphi}{\partial y}+\mu_0 M_y \\ B_z=-\mu_0\mu_r\dfrac{\partial\varphi}{\partial z}+\mu_0 M_z \end{cases}, \quad (20)$$

For the unique solution of undetermined coefficients in (16), the 3D boundary conditions between two different regions are applied as

$$\begin{cases} H_{1x,y}^j(x,y,h)=H_{2x,y}^j(x,y,h) \\ B_{1z}^j(x,y,h)=B_{2z}^j(x,y,h) \end{cases}, \quad (21)$$

where subscript numbers denote the region, and subscript letters denote the x-, y-, and z-axis components.

Because of the rotor teeth being in the magnet region, Fourier decompositions are made for the boundary conditions. Separate Fourier decomposition coefficients need to be in agreement. Thus, (21) can be expanded as

$$\begin{cases} \displaystyle\int_{-\frac{l}{2\alpha}}^{\frac{l}{2\alpha}}\int_{-\frac{qq_t}{2}}^{\frac{qn_t}{2}}H_{1x}^j(x,y,h)\sin(\omega_n^j x) \\ \qquad\times\cos\left\{\omega_m^j\left[\left(y+\left(j-\dfrac{n_t+1}{2}\right)q\right]\right\}\right.\mathrm{d}x\mathrm{d}y \\ =\displaystyle\int_{-\frac{l}{2}}^{\frac{l}{2}}\int_{-\frac{qn_t}{2}}^{\frac{qn_t}{2}}H_{2x}^j(x,y,h)\sin\left(\omega_n^j x\right) \\ \qquad\times\cos\left\{\omega_m^j\left[\left(y+\left(j-\dfrac{n_t+1}{2}\right)q\right]\right\}\right.\mathrm{d}x\mathrm{d}y \\ \displaystyle\int_{-\frac{l}{2}}^{\frac{l}{2}}\int_{-\frac{qn_t}{2}}^{\frac{qn_t}{2}}B_{1z}^j(x,y,h)\cos\left(\omega_i^j x\right) \\ \qquad\times\cos\left\{\omega_m^j\left[\left(y+\left(j-\dfrac{n_t+1}{2}\right)q\right]\right\}\right.\mathrm{d}x\mathrm{d}y \\ =\displaystyle\int_{-\frac{l}{2}}^{\frac{l}{2}}\int_{-\frac{qn_t}{2}}^{\frac{qn_t}{2}}B_{2z}^j(x,y,h)\cos\left(\omega_i^j x\right) \\ \qquad\times\cos\left\{\omega_m^j\left[\left(y+\left(j-\dfrac{n_t+1}{2}\right)q\right]\right\}\right.\mathrm{d}x\mathrm{d}y \end{cases}. \quad (22)$$

According to (16)–(20), both the magnetic field intensity components H_{1x}^j and H_{2x}^j and the flux density

components B_{1z}^j and B_{2z}^j in (22) are the superposition of multiple harmonics. Therefore, considering the orthogonality of trigonometric functions, (22) can be simplified to a matrix equation as

$$\begin{bmatrix} \mathbf{A}_{1m}^j \\ \mathbf{A}_{2m}^j \end{bmatrix} = \begin{bmatrix} \mathbf{C}_m^j & \mathbf{D}_m^j \\ \mathbf{E}_m^j & \mathbf{F}_m^j \end{bmatrix}^{-1} \cdot \begin{bmatrix} \mathbf{G}_m^j \\ \mathbf{H}_m^j \end{bmatrix}, \tag{23}$$

where $\mathbf{A}_{1m}^j$ is a matrix with $(n_{\max}+1)/2 \times 1, \mathbf{A}_{2m}^j$ is a matrix with $(i_{\max}+1)/2 \times 1$, $\mathbf{C}_m^j$ is a matrix with $(n_{\max}+1)/2 \times (n_{\max}+1)/2$ related to m and n, $\mathbf{D}_m^j$ is a matrix with $(n_{\max}+1)/2 \times (i_{\max}+1)/2$ related to m, i and n, $\mathbf{E}_m^j$ is a matrix with $(i_{\max}+1)/2 \times (n_{\max}+1)/2$ related to m, i and $n, \mathbf{F}_m^j$ is a matrix with $(i_{\max}+1)/2 \times (i_{\max}+1)/2$ related to m and $i, \mathbf{G}_m^j$ is a matrix with $(n_{\max}+1)/2 \times 1$ related to m, i and n, and $\mathbf{H}_m^j$ is a matrix with $(i_{\max}+1)/2 \times 1$ related to m and i. Note that the elements in $\mathbf{G}_m^j$ are the superposition of different i values. In fact, for different values of m, the left term with unknown coefficients in (23) is rewritten as

$$\begin{bmatrix} \mathbf{A}_1^j \\ \mathbf{A}_2^j \end{bmatrix} = \begin{bmatrix} \mathbf{A}_{1m=0}^j & \mathbf{A}_{1m=1}^j & \cdots & \mathbf{A}_{1m=m_{\max}^j}^j \\ \mathbf{A}_{2m=0}^j & \mathbf{A}_{2m=1}^j & \cdots & \mathbf{A}_{2m=m_{\max}^j}^j \end{bmatrix}, \tag{24}$$

where $\mathbf{A}_{1m}^j$ is a matrix with $(n_{\max}+1)/2 \times m, \mathbf{A}_{2m}^j$ is a matrix with $(i_{\max}+1)/2 \times m$, and subscript max denotes the maximum value.

Once the field due to j-th group of magnets is calculated, the total flux densities are the superposition of flux density generated by multiple groups of magnets and are given as

$$\begin{cases} \boldsymbol{B}_{1\text{sum}} = \sum_{j=1}^{n_t} \boldsymbol{B}_1^j \\ \boldsymbol{B}_{2\text{sum}} = \sum_{j=1}^{n_t} \boldsymbol{B}_2^j \end{cases}. \tag{25}$$

B. Slotted 3D field prediction

Considering the slotting influence, an equivalent approach is brought in. Figure 4 shows five flux paths denoted (a)–(e), where γ is an angle and $x_1, x_2, x_3, x_4, x_{rb}$, x_{rc}, and x_{rd} are length parameters. Accounting for the shortest magnetic circuit principle, it is worth noting that there exist at most five paths. The expressions of these flux paths are given as

$$\begin{cases} \eta_{\text{a}} = g \\ \eta_{\text{b}} = g + \dfrac{\pi x_{r\text{b}}}{2} \\ \eta_{\text{c}} = g + x_3 + 2\pi x_{rc} \cdot \dfrac{\gamma + 90}{360} \\ \eta_{\text{d}} = g + x_4 \cdot \tan\gamma + \dfrac{\pi x_{r\text{rd}}}{2} + x_3 \\ \eta_{\text{e}} = g + x_1 - x_2 \end{cases}. \tag{26}$$

The magnetic conductance expressions of five paths are

$$\begin{cases} \Lambda_{\text{a}} = \mu_0 \displaystyle\int_{S_a} \frac{1}{\eta_a} \text{d}S = \frac{\mu_0 S_a}{g} \\ \Lambda_{\text{b}} = \mu_0 \displaystyle\int_{S_b} \frac{1}{\eta_b} \text{d}S = \frac{2\mu_0 (R_{\text{out}} - R_{\text{in}})}{\pi} \ln\left(1 + \frac{\pi x_\alpha}{2g}\right) \\ \Lambda_{\text{c}} = \mu_0 \displaystyle\int_{S_c} \frac{1}{\eta_c} \text{d}S = \frac{\mu_0 (R_{\text{out}} - R_{\text{in}})}{k_p} \\ \qquad \times \ln\left[1 + \dfrac{k_p (x_\beta - x_\alpha)}{g + x_3 + k_p x_\alpha}\right] \\ \Lambda_{\text{d}} = \mu_0 \displaystyle\int_{S_d} \frac{1}{\eta_d} \text{d}S = \frac{2\mu_0 (R_{\text{out}} - R_{\text{in}})}{\pi} \\ \qquad \times \ln\left[1 + \dfrac{\pi (x_\delta - x_\beta)}{k_t + \pi x_{r\text{d}}}\right] \\ \Lambda_{\text{e}} = \mu_0 \displaystyle\int_{S_e} \frac{1}{\eta_e} \text{d}S = \frac{\mu_0 S_e}{g + x_1 - x_3} \end{cases}, \tag{27}$$

where $S_{\text{a}}, S_{\text{b}}, S_{\text{c}}, S_{\text{d}}$, and S_{e} are the areas of five paths, x_α, x_β, and x_δ are the specific values for the equal lengths for paths (b) and (c), those for paths (c) and (d) and those for paths (d) and (e), respectively. In addition, k_p and k_t are written as

$$\begin{cases} k_p = \dfrac{\pi(\gamma + 90)}{180} \\ k_t = 2g + 2x_4 \cdot \tan\gamma + 2x_3 \end{cases}. \tag{28}$$

Instead of the slotted stator, the equivalent area S_f, the air gap length η_f, and the magnetic conductance Λ_f for the slotless stator are given as

$$\begin{cases} S_f = \pi \left(R_{\text{out}}^2 - R_{\text{in}}^2\right) \dfrac{1}{2N_s} \\ \eta_f = g_f \\ \Lambda_f = \mu_0 \displaystyle\int_{S_f} \frac{1}{\eta_f} \text{d}S = \frac{\mu_0 S_f}{g_f} \end{cases}. \tag{29}$$

With the same total magnetic conductance, the equivalent air gap can be written as

$$g_f = \frac{\mu_0 S_f}{\Lambda_{\text{a}} + \Lambda_{\text{b}} + \Lambda_{\text{c}} + \Lambda_{\text{d}} + \Lambda_{\text{e}}} = C_s \cdot g, \tag{30}$$

where C_S is Carter's coefficient and is computed by

$$C_S = \frac{\mu_0 S_f}{g \cdot (\Lambda_{\text{a}} + \Lambda_{\text{b}} + \Lambda_{\text{c}} + \Lambda_{\text{d}} + \Lambda_{\text{e}})}. \tag{31}$$

For a period of one slot with $2l_c = 2\pi(R_{\text{out}} + R_{\text{in}})/2N_s$, the coefficient C_s' related to C_S can be defined

as

$$C_s' = \begin{cases} Cs & \frac{\pi}{N_s}\frac{R_{\text{out}}+R_{\text{in}}}{2} - \beta < x < \frac{\pi}{N_s}\frac{R_{\text{out}}+R_{\text{in}}}{2} + \beta, \\ 1 & \text{others} \end{cases} \tag{32}$$

where β is the circumferential length of one half of slot and N_s is the stator slot number.

In order to predict the slotted model, using Fourier decomposition, the coefficient is expressed as

$$C_s' = \sum_{n_{cs}=0}^{\infty} c_{sn} \cos\left(n_{cs}\frac{\pi x}{l_c}\right), \tag{33}$$

where n_{cs} is a nonnegative integer and c_{sn} can be defined by

$$C_{sn} = \begin{cases} \frac{1}{l_c}\int_0^{2l_c} C_s' \cos\left(n_{cs}\frac{\pi x}{l_c}\right) \mathrm{d}x & n_{cs} \neq 0 \\ \frac{1}{2l_c}\int_0^{2l_c} C_s' \mathrm{d}x & n_{cs} = 0 \end{cases}. \tag{34}$$

Thus, the slotted flux density in the air-gap is calculated as

$$\boldsymbol{B}_{1\text{slotted}} = \frac{\boldsymbol{B}_{1\text{sum}}}{C_s'}. \tag{35}$$

As shown in Fig. 2, considering the winding end being in the 3D solution region, the air-gap fringing effect for SIAFMs needs to be considered. As shown in Fig. 5, there exists the air-gap fringing magnetic field. The air-gap fringing field coefficient is defined as

$$C_{\text{fr}} = 1 + \frac{\pi(2|y| - qn_t)}{4g}. \tag{36}$$

In order to calculate the back-EMF, according to (16), (19), (20), and (25), the slotless flux density in the axial direction at $z = h+g$ can be written as

$$B_{1z}|_{h+g} = -2\mu_0 \sum_{j=1}^{n_t}\sum_{m=0}^{\infty}\sum_{n=1,3}^{\infty} A_{1mn}^j k_1^j e^{k_1^j(h+g)} \cos(\omega_n^j x) \times \cos\left\{\omega_m^j\left[\left(y + \left(j - \frac{n_t+1}{2}\right)q\right]\right\}, \tag{37}$$

where A_{2mi}^j and B_{2mi}^j are the undetermined coefficients in the region of the layer magnets near the air-gap.

And the ranges of region Q_3 influencing the back EMF of the s-th slot are $W - R_j\alpha_{cp}/2 < x < W + R_j\alpha_{cp}/2$ and $q < \mathrm{y} < q$

$$W = W(t) = R_j[-\omega_r t + \alpha_{cp}(s-1)], \tag{38}$$

$$\alpha_{cp} = \frac{2\pi}{N_s}, \tag{39}$$

$$\omega_r = \frac{2\pi n_e}{60}, \tag{40}$$

where n_e is the rated rotational speed.

Therefore, the slotted flux density in the axial direction at $z = h+g$ can be expressed as

$$B_{1z}'|_{h+g} = \begin{cases} \frac{B_{1z}|_{h+g}}{C_s C_{\text{fr}}} \begin{cases} W - \frac{R_j\alpha_{cp}}{2} \le x \le W - \frac{R_j\alpha_{cp}}{2} + \beta \\ -qn_t \le y \le -\frac{qn_t}{2} \text{ or } \frac{qn_t}{2} \le y \le qn_t \end{cases} \\ \frac{B_{1z}|_{h+g}}{C_{\text{fr}}} \begin{cases} W - \frac{R_j\alpha_{cp}}{2} + \beta \le x \le W + \frac{R_j\alpha_{cp}}{2} - \beta \\ -qn_t \le y \le -\frac{qn_t}{2} \text{ or } \frac{qn_t}{2} \le y \le qn_t \end{cases} \\ \frac{B_{1z}|_{h+g}}{C_s C_{\text{fr}}} \begin{cases} W + \frac{R_j\alpha_{cp}}{2} - \beta \le x \le W + \frac{R_j\alpha_{cp}}{2} \\ -qn_t \le y \le -\frac{qn_t}{2} \text{ or } \frac{qn_t}{2} \le y \le qn_t \end{cases} \\ \frac{B_{1z}|_{h+g}}{C_s} \begin{cases} W - \frac{R_j\alpha_{cp}}{2} \le x \le W - \frac{R_j\alpha_{cp}}{2} + \beta \\ -\frac{qn_t}{2} \le y \le \frac{qn_t}{2} \end{cases} \\ B_{1z}|_{h+g} \begin{cases} W - \frac{R_j\alpha_{cp}}{2} + \beta \le x \le W + \frac{R_j\alpha_{cp}}{2} - \beta \\ -\frac{qn_t}{2} \le y \le \frac{qn_t}{2} \end{cases} \\ \frac{B_{1z}|_{h+g}}{C_s} \begin{cases} W + \frac{R_j\alpha_{cp}}{2} - \beta \le x \le W + \frac{R_j\alpha_{cp}}{2} \\ -\frac{qn_t}{2} \le y \le \frac{qn_t}{2} \end{cases} \end{cases}. \tag{41}$$

Then, using the slotted flux density, the flux linkage for the s-th coil with N-turn is written as

$$\Psi = N\Phi = N\iint_{Q_3} B_{12}'|_{h+g} \mathrm{d}S. \tag{42}$$

In addition, the back EMF of each coil can be obtained as

$$e_s = -\partial\Psi/\partial t = 4Nu_0 \sum_{j=1}^{n_t}\sum_{m=0}^{+\infty}\sum_{n=1,3}^{+\infty} \times A_{1mn}^j k_1^j e^{k_1^j(h+g)} \omega_r R_j \cdot Int(t) \cdot Int, \tag{43}$$

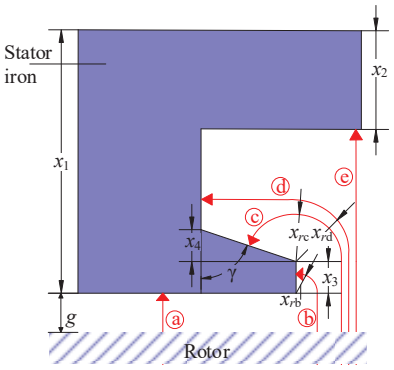


Fig. 4. Ideal paths in one half of slot and tooth.

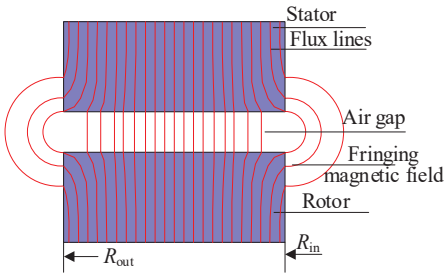


Fig. 5. Air-gap fringing magnetic field for SIAFMs.

where

$$Int(t) = \sin\{\omega_n R_j[-\omega_r t + \alpha_{cp}(s-1)\} \times \left\{\frac{2}{C_s}\sin\left(\frac{\omega_n \beta}{2}\right)\cos\left[\frac{\omega_n(R_j\alpha_{cp}-\beta)}{2}\right] + \sin\left[\frac{\omega_n(R_j\alpha_{cp}-2\beta)}{2}\right]\right\}, \quad (44)$$

$$Int = \begin{cases} qn_t + \frac{4g}{\pi}\ln\left(1+\frac{\pi q n_t}{4g}\right), & m=0 \\ 2\frac{\sin\left(\frac{\omega_m q n_t}{2}\right)}{\omega_m} \times \cos\left[\omega_m\left(j-\frac{n_t+1}{2}\right)q\right] + Int_1 + Int_2, & m\neq 0 \end{cases}, \quad (45)$$

$$\begin{cases} Int_1 = \int_{-qn_t}^{-qn_t/2}\frac{1}{C_{fr}} \cdot\cos\left\{\omega_m\left[y+\left(j-\frac{n_t+1}{2}\right)q\right]\right\}dy \\ Int_2 = \int_{qn_t/2}^{qn_t}\frac{1}{C_{fr}} \cdot\cos\left\{\omega_m\left[y+\left(j-\frac{n_t+1}{2}\right)q\right]\right\}dy \end{cases}. \quad (46)$$

Figure 6 exhibits the stator coil distribution and the current directions of a 20-pole/ 24-slot SIAFM. The instantaneous balanced three phase back-EMFs are written as

$$\begin{cases} e_A = 2(-e_1+e_2+e_7-e_8-e_{13}+e_{14}+e_{19}-e_{20}) \\ e_B = 2(e_3-e_4-e_9+e_{10}+e_{15}-e_{16}-e_{21}+e_{22}) \\ e_C = 2(-e_5+e_6+e_{11}-e_{12}-e_{17}+e_{18}+e_{23}-e_{24}) \end{cases}, \quad (47)$$

where e_A, e_B, and e_C are the three-phase back-EMFs, and the subscripts $1, 2, \ldots, 24$ are the coil numbers.

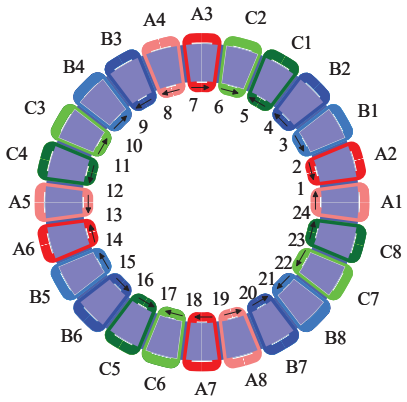


Fig. 6. Coil distribution and current directions of 20-pole/24-slot SIAFMs.

Therefore, the electromagnetic torque for SIAFMs is

$$T_e = \frac{e_A i_A + e_B i_B + e_C i_C}{\omega_r}, \quad (48)$$

where i_A, i_B, and i_C are the instantaneous three-phase currents.

Table 1: Design parameters of SIAFMs

Symbol	Parameter	Value
R_1/R_2	Inner/outer radii of rotor iron	52/68
r_1/r_2	Inner/outer radii of magnets	52/68
p/N_s	Numbers of pole-pairs and slot	20/24
I	Rated phase current	4 A
N	Number of coil turns	16
α_0	Arc ratio of whole pole magnets	0.7
α	Arc ratio of distance between	0.7
g	Air gap length	1 mm
h	Magnet thickness	5 mm
B_{re}/μ_r	Magnet property	1.1
n_e	Rated rotational speed	3000
P_N	Rated power	270 W

IV. OPTIMIZATION RESULTS AND FE VALIDATION

Table 1 lists the main design parameters of 20-pole/ 24-slot SIAFMs. In order to obtain the relatively better performance of the SIAFMs, optimization is made. The optimization object with the maximum average electromagnetic torque and the optimization constraint conditions are written as

$$\begin{cases} \text{Max}\{\text{Average}[T_e(\alpha_1,\ldots,\alpha_\lambda,\theta_1,\ldots,\theta_{\lambda+1})]\} \\ \text{Subject to.} \begin{cases} 0 \le \alpha_1,\ldots,\alpha_\lambda \le \alpha_0 \le 1 \\ 0^\circ \le \theta_1,\ldots,\theta_{\lambda+1} \le 90^\circ \end{cases} \end{cases}. \quad (49)$$

Based on the parameter scanning technique, Fig. 7 shows the analytically obtained average electromagnetic torque against two optimization variables (magnetization angle and pole-arc ratio) for the three-piece Halbach arrangements, and Fig. 8 shows that against three optimization variables (two magnetization angles and pole-arc ratio) for the four-piece Halbach arrangements, respectively.

Table 2: Optimized parameters for three-/four-piece Halbach

Optimized Parameters	Three-Piece	Four-Piece
α_1	0.29	0.39
θ_1	/	17.1°
θ_2	53.0°	60.0°
$T_{\max}$(Nm)	0.847	0.862

According to Figs. 7 and 8, for the three-/four-piece Halbach SIAFM, the optimization variables and the largest average value of electromagnetic torque are given in Table 2.

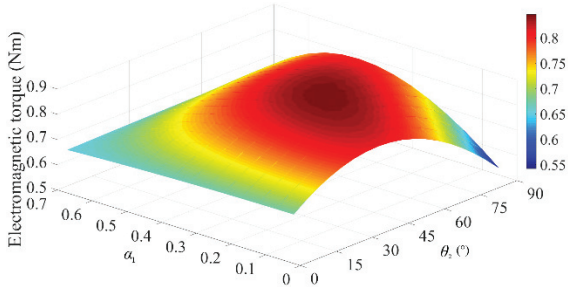


Fig. 7. Analytically obtained average electromagnetic torque against pole-arc ratio and magnetization angle for three-piece Halbach.

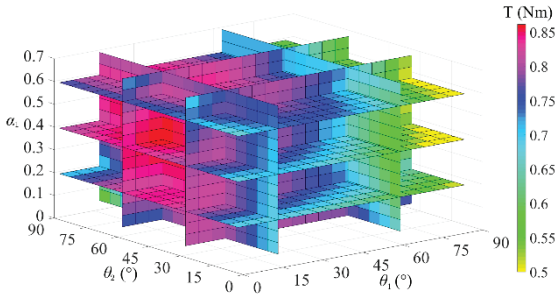


Fig. 8. Analytically obtained average electromagnetic torque against pole-arc ratio and two magnetization angles for four-piece Halbach.

Figure 9 shows a comparison of axial flux density waveforms of SIAFMs with optimized three-/four-piece Halbach arrangements at different radii by 3D FE and

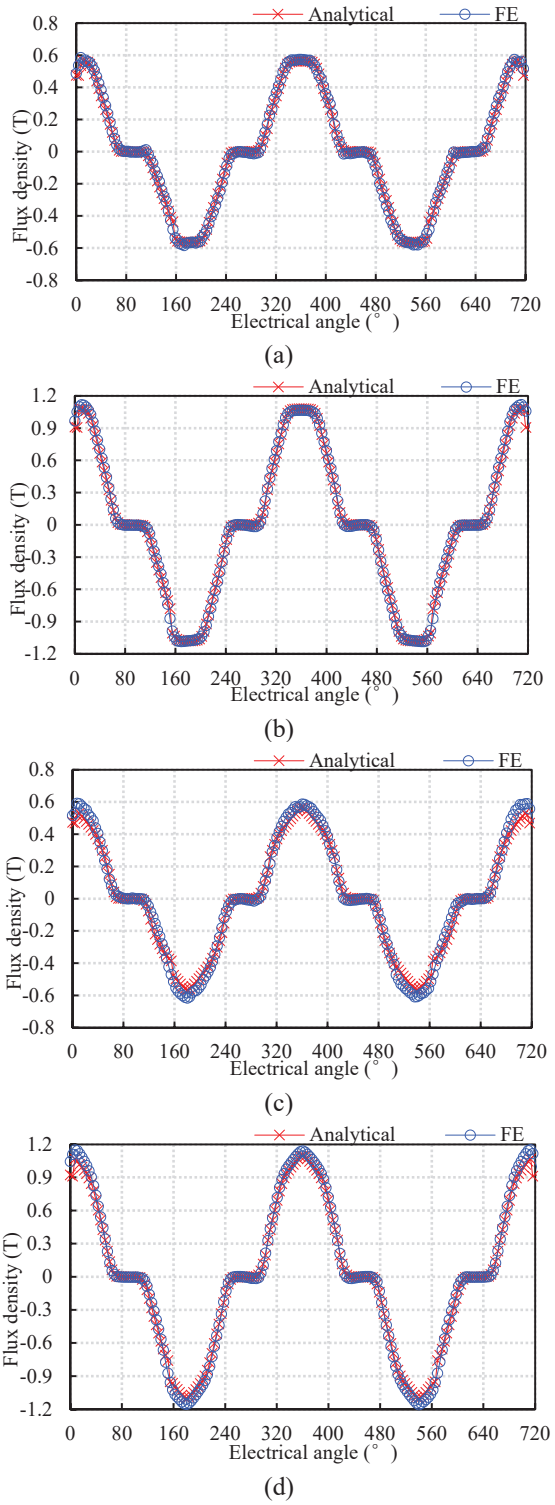


Fig. 9. Flux density waveform comparison of SIAFMs with optimized three-/four-piece Halbach arrangements at different radii in the radial direction and at 5.5 mm (axial air gap center) in axial direction by 3D analytical and FE models: (a) three-piece at 26 mm, (b) three-piece at 30 mm, (c) four-piece at 26 mm, and (d) four-piece at 30 mm.

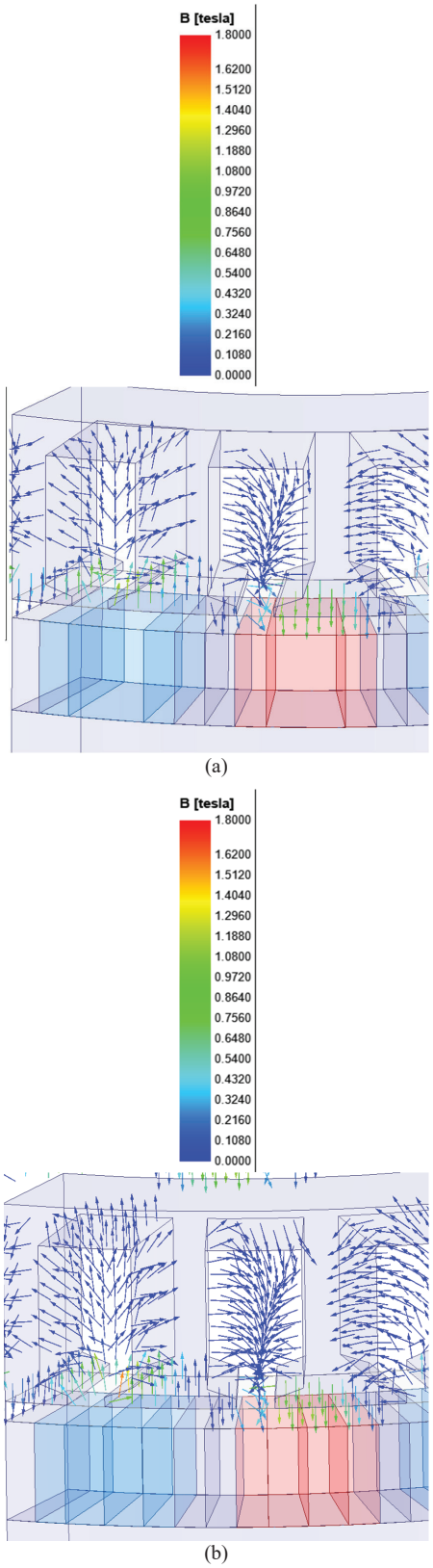


Fig. 10. Magnetic flux density vector of SIAFMs with optimized three-/four-piece Halbach arrangements in 3D FE models: (a) three-piece and (b) four-piece.

analytical models to verify the feasibility of the method by equivalent reluctance coefficients. It can be seen that, independent of the radius, each two waveforms calculated by two models are in great agreement.

Figure 10 shows the magnetic flux density vector of air gap and slots in SIAFMs with optimized three-/four-piece Halbach arrangements in 3D FE models. Figure 11 presents the comparison of no-load back-EMF waveforms for SIAFMs with optimized three-/four-piece Halbach arrangements from 3D FE and analytical models. It is clearly seen that great accuracy can be achieved with the use of Carter's coefficient and the air-gap fringing field coefficient for SIAFMs.

Because the amplitude of reluctance torque for SIAFMs is lower than 1 mNm, its waveform is not given. Compared with the electromagnetic torque, its value can be ignored. Figure 12 shows that the instantaneous electromagnetic torque waveforms for 3D FE and analytical models are in good agreement for SIAFMs with both three- and four-piece Halbach arrangements. Thus, the proposed 3D analytical models are validated.

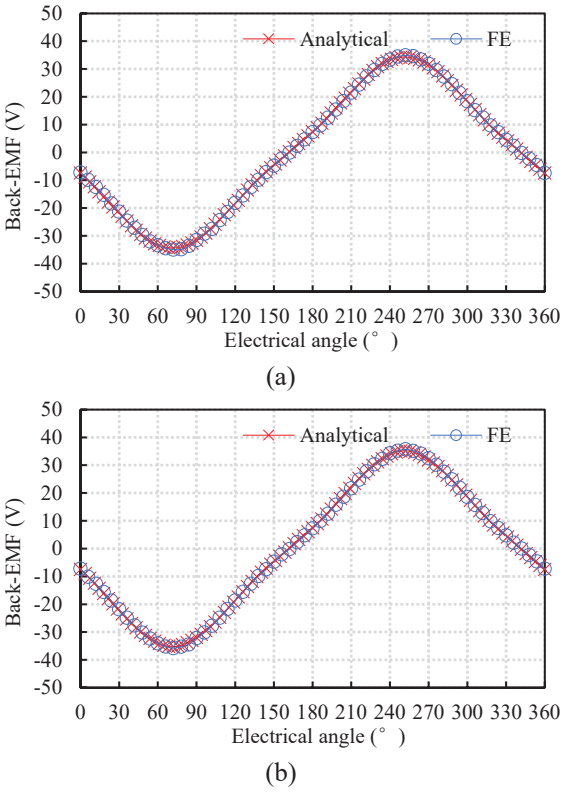


Fig. 11. Comparison of back-EMF waveforms of SIAFMs with optimized three-/four-piece Halbach arrangements by 3D FE and analytical models: (a) three-piece Halbach and (b) four-piece Halbach.

Due to the presence of the radial air gap edge magnetic field, accuracy values of analytical models

with/without air gap edge magnetic field are different. For SIAFMs with optimized three-/four-piece Halbach arrangements, the errors in back-EMF amplitude reduce from 9.22%/8.97% to 1.61%/1.34%, respectively. In terms of the average electromagnetic torque, the errors decrease from 7.73%/8.03% to 0.06%/0.35%, respectively.

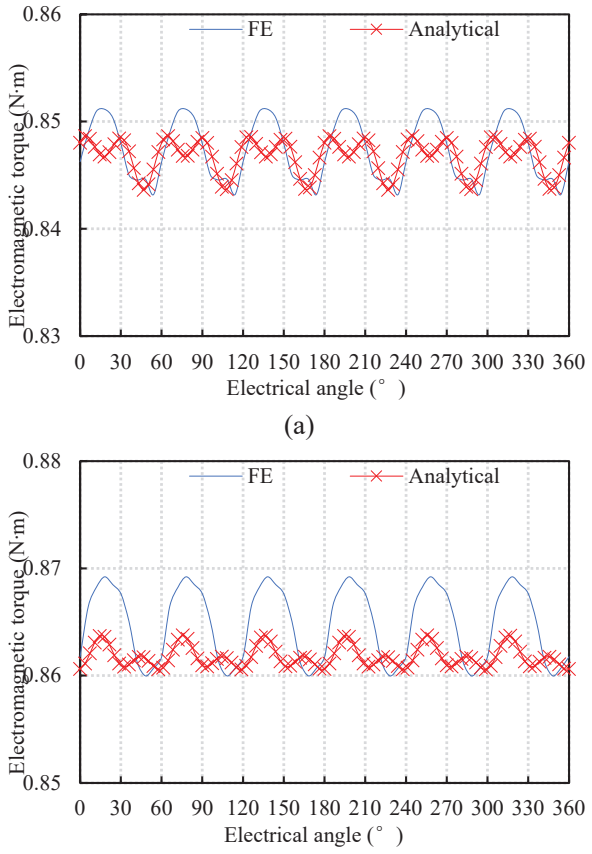


Fig. 12. Comparison of electromagnetic torque waveforms of SIAFMs with optimized three-/four-piece Halbach arrangements for 3D FE and analytical models: (a) three-piece Halbach and (b) four-piece Halbach.

V. OPTIMIZATION RESULTS AND FE VALIDATION FOR SMAFMS

Similarly, Figs. 13 (a) and (b) show the PM design parameters of 2D cross section for the proposed surface-mounted odd-/even-piece Halbach arrangements, and the PM design parameters are same as those for surface-inserted odd-/even-piece Halbach arrangements. In particular, if $\alpha = 1$, the SIAFMs are equivalent to the SMAFMs.

Figure 14 shows a comparison of axial flux density of slotted SMAFMs with optimized three-/four-piece Halbach arrangements by FE and 3D analytical models. It can be seen that the waveforms calculated by the two models referred to above are in great agreement.

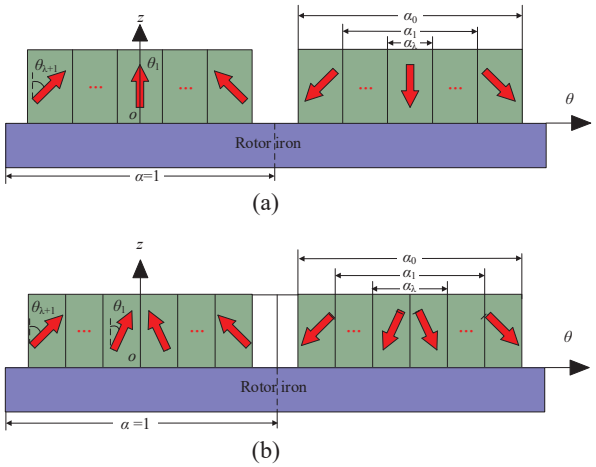


Fig. 13. Design parameters of surface-mounted odd-/even-piece Halbach arrangements: (a) odd-piece Halbach and (b) even-piece Halbach.

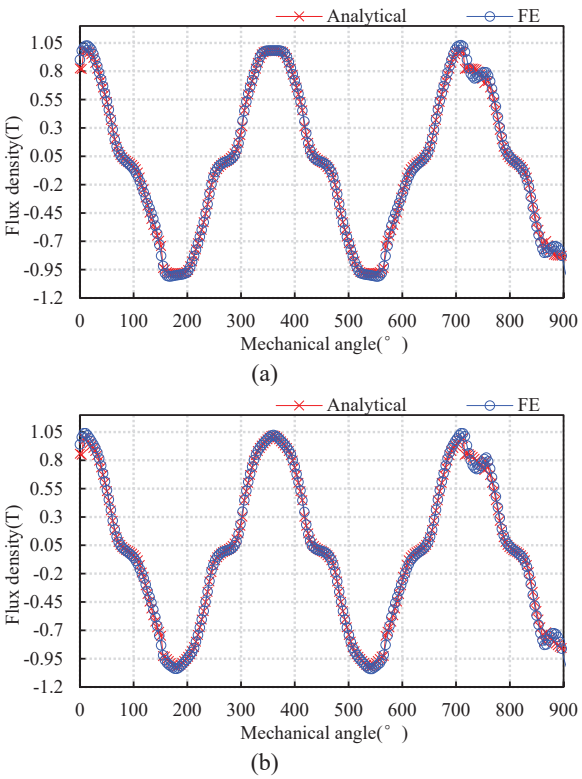


Fig. 14. Flux density waveform comparison of SMAFMs with optimized three-/four-piece Halbach arrangements by FE and 3D analytical models: (a) three-piece and (b) four-piece.

Figure 15 presents a comparison of no-load back-EMF waveforms of slotted SMAFMs with optimized

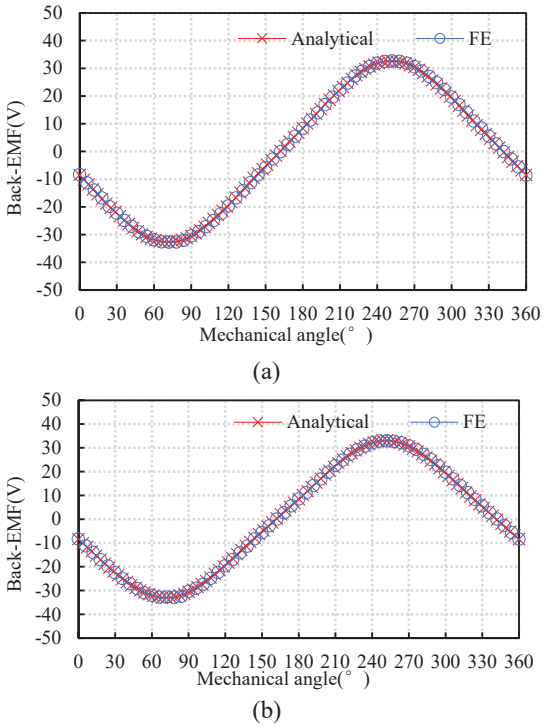


Fig. 15. Comparison of back-EMF waveforms of SMAFMs with optimized three-/four-piece Halbach arrangements by FE and 3D analytical models: (a) three-piece Halbach and (b) four-piece Halbach.

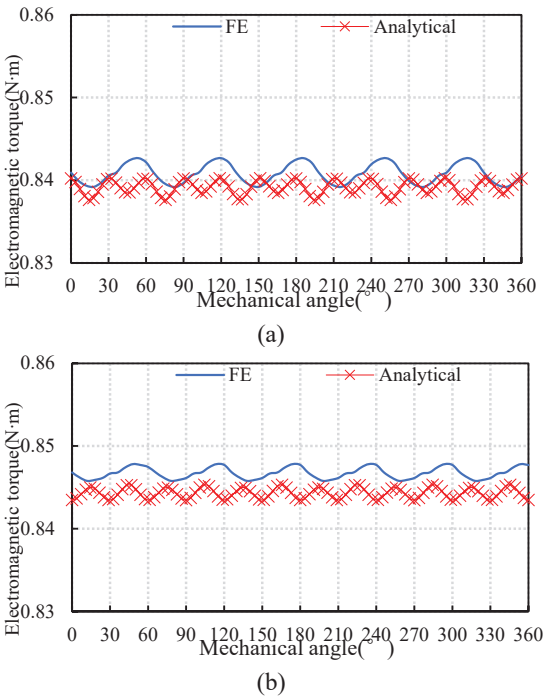


Fig. 16. Comparison of electromagnetic torque waveforms of SMAFMs with optimized three-/four-piece Halbach arrangements by FE and 3D analytical models: (a) three-piece Halbach and (b) Four-piece Halbach.

three-/four-piece Halbach arrangements from FE and 3D analytical models. It can be clearly seen that the use of Carter's coefficient and the air-gap outside leakage magnetic field coefficient for slotted SMAFMs exhibit great computation accuracy.

Figure 16 shows that instantaneous electromagnetic torque waveforms from FE and 3D analytical models are in excellent agreement for SMAFMs with both three- and four-piece Halbach arrangements. Thus, the 3D analytical models proposed above are validated.

VI. ANALYTICAL COMPARISON WITH NON-OPTIMIZED HALBACH SIAFMS

To analyze the effects of the optimized variables and methods mentioned in section IV, this section compares the traditional Halbach array with the optimized Halbach array in terms of back EMF, harmonics, and electromagnetic torque. Figures 17 (a) and (b) show the PM design parameters of the non-optimized three-/four-piece Halbach arrangements for SIAFMs, and the detailed parameter values are listed in Table 3.

Table 3: PM parameters for non-optimized SIAFMs with three-/four-piece Halbach arrangements

Symbol	Three-Piece	Four-Piece	
		Combination 1	Combination 2
α	0.7	0.7	0.7
α_0	0.7	0.7	0.7
α_1	7/30	0.35	0.35
$\theta_1(^\circ)$	0	30	45
$\theta_2(^\circ)$	45	45	60

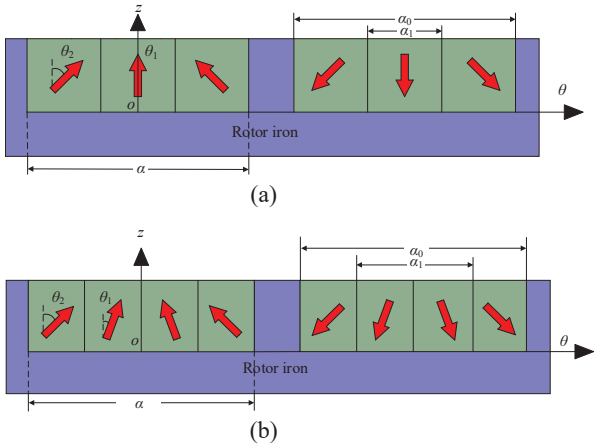


Fig. 17. Design parameters of non-optimized three-/four-piece Halbach arrangements for SIAFMs: (a) three-piece Halbach and (b) four-piece Halbach.

The prediction shows that for four-piece Halbach, the performance of combination 1 is better than that

of combination 2. Therefore, combination 1 is chosen for the comparison with the optimized results. Figure 18 exhibits and compares the back-EMF for the non-optimized/optimized 3D SIAFM models with three-/four-piece Halbach arrangements.

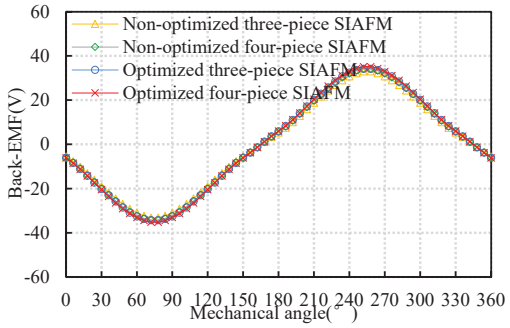


Fig. 18. Comparison of back-EMF waveforms for SIAFMs with non-optimized/proposed three-/four-piece Halbach.

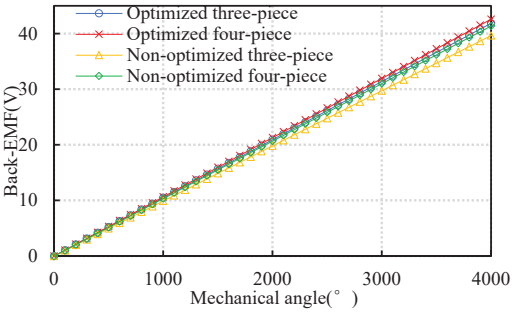


Fig. 19. Comparison of fundamental component of back-EMF with respect to speed for SIAFMs with non-optimized/proposed three-/four-piece Halbach.

Figure 19 exhibits and compares the differences of fundamental component of back-EMF with respect to speed for SIAFMs with non-optimized/optimized three-/four-piece Halbach. Tables 4 and 5 list the back-EMF harmonics, total harmonic distortion (THD), and fundamental amplitude (FA) for the non-optimized/optimized SIAFMs with Halbach arrangements. It can be clearly observed that the back-EMFs of the optimized 3D SIAFM models have higher fundamental and less harmonic components than those of the non-optimized ones. Compared with the values of the electromagnetic torque, it can be seen that the amplitudes of cogging torque waveforms for both Halbach arrays are small and can be ignored.

Figure 20 compares the instantaneous electromagnetic torque for the 3D SIAFM models with non-optimized/optimized Halbach arrangements. As far as the electromagnetic torque values are concerned, the optimized model parameters are much better.

Table 4: Back-EMF harmonics for non-optimized/optimized three-/four-piece Halbach

Harmonic Order	Three-Piece		Four-Piece	
	Non-Optimized	Optimized	Non-Optimized	Optimized
1	100.00%	100.00%	100.00%	100.00%
3	10.71%	9.49%	9.96%	9.73%
5	0.05%	0.13%	0.09%	0.12%
7	0.26%	0.04%	0.16%	0.03%
9	0.43%	0.04%	0.31%	0.31%
11	0.17%	0.35%	0.20%	0.08%
13	0.22%	0.18%	0.21%	0.17%
15	0.04%	0.04%	0.03%	0.01%
17	0.01%	0.01%	0.01%	0.01%

Table 5: Back-EMF parameters for non-optimized/optimized three-/four-piece Halbach

	Three-Piece		Four-Piece	
	Non-Optimized	Optimized	Non-Optimized	Optimized
FA (V)	29.73	31.39	31.01	31.94
THD	10.58%	9.50%	9.97%	9.74%

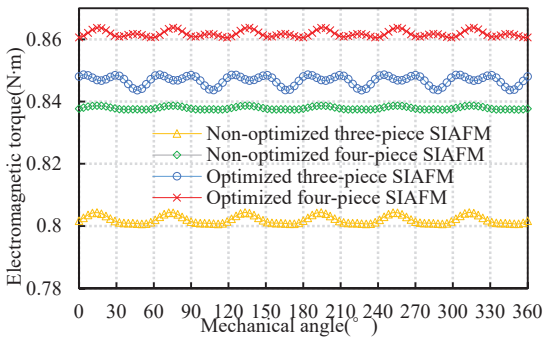


Fig. 20. Comparison of torque waveforms for SIAFMs with non-optimized/optimized three-/four-piece Halbach.

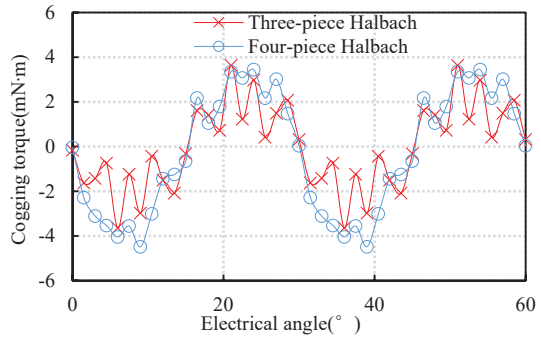


Fig. 21. Cogging torque for SIAFMs with three-/four-piece Halbach.

Figure 21 shows the cogging torque for the 3D SIAFM models with proposed three-/four-piece Halbach. Figure 22 exhibits the efficiency of the machine over whole speed and torque range for the 3D SIAFM models. When the 3D SIAFM models are in constant

power operation, the current and speed are inversely proportional. Therefore, as can be seen from the Fig. 22, the efficiency increases with the increase of speed.

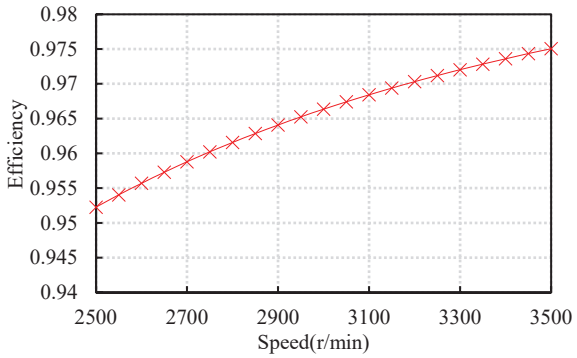


Fig. 22. Efficiency of SIAFMs over whole speed and torque range.

VII. DISCUSSION

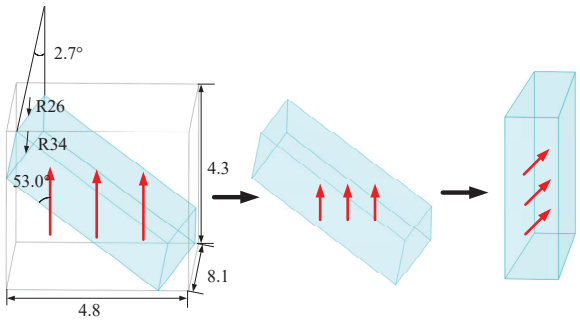


Fig. 23. Manufacturing process of one Halbach magnet.

The manufacture of a Halbach magnet with specific magnetization angle is difficult and time-consuming and expensive. Taking one Halbach magnet segment with a specific magnetization angle as an example, the manufacturing process is shown in Fig. 23. First, a relatively large rectangular prism with parallel magnetization is manufactured. Second, the required portion of magnet is exactly cut out. Third, this magnet segment with a specific magnetization direction is placed at the desired position. Finally, all the magnet segments of Halbach array are assembled using a kind of superglue. For magnet bonding, it is essential to choose a suitable adhesive, depending on the magnet material, service environment, and strength requirements. Epoxy resin adhesive is one of the commonly used options, offering high strength, heat resistance, and chemical resistance. However, it requires mixing of two components (A and B) and has a relatively long curing time (typically 24 hours). It is often used for permanent bonding of neodymium (rare-earth) magnets and ferrite magnets to metals or plastics.

A considerable part of each magnet segment is redundant and wasteful. It can be also seen that the manufacturing process is complex and expensive. Although Halbach arrays possess excellent electromagnetic performance, their practical implementation is restricted by complicated and costly manufacturing techniques. This work focuses on applying the 3D analytical model to axial flux PM machines, using a rectangular coordinate system for derivation to avoid the complicated calculations with Bessel functions in cylindrical coordinates. It also unifies surface-mounted and surface-inserted structures into one model to evaluate the application value of Halbach arrays in axial flux PM machines. Since our research focuses on analytical modeling and design analysis rather than experimental prototyping, no physical prototype is developed in this work.

VIII. CONCLUSION

Different from 2D radial flux machines, the air-gap fringing effect for SIAFMs needs to be considered. Accounting for the air-gap fringing field, unified 3D analytical models are proposed for SIAFMs with odd-/even-piece Halbach arrangements. In order to obtain the correct analytical solution with high accuracy, the slotting effect is taken into account by Carter's coefficient. Based on the proposed 3D analytical models, the constructed equations according to the interface conditions between different regions are solved and the optimized electromagnetic performances of SIAFMs with Halbach arrangements are obtained. The comparison of 3D analytical and FE predictions shows good agreement. The proposed 3D analytical models can be applied for design and optimization of SIAFMs with any-piece Halbach arrangements.

REFERENCES

[1] A. Echle, A. Neubauer, and N. Parspour, "Design and comparison of radial flux and axial flux brushless DC motors for power tool applications," in *2018 XIII International Conference on Electrical Machines (ICEM)*, Alexandroupoli, Greece, pp. 125–130, 2018.

[2] A. S. Patil and R. T. Ugale, "Design and comparative analysis of axial flux and radial flux permanent magnet brushless DC motor for a 2-wheeler electric vehicle application," in *2022 IEEE Conference on Interdisciplinary Approaches in Technology and Management for Social Innovation (IATMSI)*, Gwalior, India, pp. 1–4, 2022.

[3] S. Kumar, W. Zhao, Z. S. Du, T. A. Lipo, and B.-I. Kwon, "Design of ultrahigh speed axial-flux permanent magnet machine with sinusoidal back EMF for energy storage application," *IEEE Trans. Magn.*, vol. 51, no. 11, pp. 1–4, Nov. 2015.

[4] J. Zhu, G. Li, D. Cao, Z. Zhang, and S. Li, "Comparative analysis of coreless axial flux permanent

magnet synchronous generator for wind power generation," *J. Electr. Eng.*, vol. 15, no. 2, pp. 727–735, 2020.

[5] B. Guo, Z. Djelloul-Khedda, and F. Dubas, "Nonlinear analytical solution in axial flux permanent magnet machines using scalar potential," *IEEE Trans. Industr. Electron*, vol. 71, no. 4, pp. 3383–3393, 2024.

[6] B. Guo, Y. Huang, F. Peng, and J. Dong, "An analytical model for axial flux permanent magnet machines with Halbach array," *Chin. Soc. Electr. Eng.*, vol. 39, no. 1, pp. 289–295+343, 2019.

[7] Y. Cao, L. Feng, R. Mao, and K. Li, "Analysis of analytical magnetic field and flux regulation characteristics of axial-flux permanent magnet memory machine," *IEEE Trans. Magn.*, vol. 58, no. 9, pp. 1–9, 2022.

[8] P. Jin, Y. Yuan, Q. Xu, S. Fang, H. Lin, and S. L. Ho, "Analysis of axial-flux Halbach permanent-magnet machine," *IEEE Trans. Magn.*, vol. 51, no. 11, pp. 1–4, 2015.

[9] T. Okita and H. Harada, "3D analytical model of axial-flux permanent magnet machine with segmented multipole-Halbach array," *IEEE Access*, vol. 11, pp. 2078–2091, 2023.

[10] S. Wu, S. Zuo, X. Wu, F. Lin, and J. Shen, "Magnet modification to reduce pulsating torque for axial flux permanent magnet synchronous machines," *Applied Computational Electromagnetics Society (ACES) Journal*, vol. 31, no. 3, pp. 294–303, 2016.

[11] L. Yang, K. Yang, S. Sun, Y. Luo, F. Xiong, and C. Luo, "Study on the influence of a combined-Halbach array for the axial flux permanent magnet electrical machine with yokeless and segmented armature," *IEEE Trans. Magn.*, vol. 60, no. 3, pp. 1–5, 2024.

[12] Y. Huang, B. Guo, Y. Guo, J. Zhu, A. Hemeida, and P. Sergeant, "Analytical modeling of axial flux PM machines with eccentricities," *Int. J. Appl. Electromagn. Mech.*, vol. 53, no. 4, pp. 757–777, 2017.

[13] F. Yi, C. Zhang, S. Qiu, L. Wu, and G. Yang, "Quasi-3D analytical method of open-circuit magnetic field for yokeless and segmented armature machine," *IEEE Trans. Magn.*, vol. 59, no. 12, pp. 1–10, 2023.

[14] H. Tiegna, A. Bellara, Y. Amara, and G. Barakat, "Analytical modeling of the open-circuit magnetic field in axial flux permanent-magnet machines with semi-closed slots," *IEEE Trans. Magn.*, vol. 48, no. 3, pp. 1212–1226, 2012.

[15] A. Bellara, Y. Amara, G. Barakat, and P. Reghem, "Analytical modelling of the magnetic field in axial flux permanent magnet machines with semi-closed slots at no load," in *XIX International Conference on Electrical Machines (ICEM)*, Rome, Italy, pp. 1–6, 2010.

[16] W. Xu, Y. Hu, Y. Zhang, and J. Wang, "Design of an integrated magnetorheological fluid brake axial flux permanent magnet machine," *IEEE Trans. Transp. Electrif.*, vol. 10, no. 1, pp. 1876–1886, 2024.

[17] M. Sun, R. Tan, X. Han, and W. Tong, "Analysis and modeling for open circuit air gap magnetic field prediction in axial flux permanent magnet machines," *Chin. Soc. Electr. Eng.*, vol. 38, no. 5, pp. 1525–1533, 2018.

[18] F. Zhao, Z. Shao, and H. Fan, "Analytical calculation and low-order component optimization of axial electromagnetic force for an axial flux motor," *IEEE Trans. Magn.*, vol. 59, no. 11, pp. 1–5, 2023.

[19] J. H. Kim, Y. S. Kwon, S. Lee, B. M. Kang, J. M. Park, J. M. Sung, and J. Y. Yoon, "3D hybrid segmented layer modeling of on-load magnetic fields and torques for coreless axial-flux permanent magnet synchronous motor," *IEEE Trans. Energy Convers.*, vol. 38, no. 3, pp. 1815–1826, 2023.

[20] Y. Huang, B. Ge, J. Dong, H. Lin, J. Zhu, and Y. Guo, "3D analytical modeling of no-load magnetic field of ironless axial flux permanent magnet machine," *IEEE Trans. Magn.*, vol. 48, no. 11, pp. 2929–2932, 2012.

[21] P. Jin, Y. Yuan, M. Jin, S. Fang, H. Lin, H. Yang, and S. L. Ho, "3D analytical magnetic field analysis of axial flux permanent-magnet machine," *IEEE Trans. Magn.*, vol. 50, no. 11, pp. 1–4, 2014.

[22] A. Zerioul, L. Hadjout, Y. Ouazir, H. Bensaidane, A. Benbekai, and O. Chaouch, "3D analytical model to compute the electromagnetic torque of axial flux magnetic coupler with a rectangular-shaped magnet," in *2018 International Conference on Electrical Sciences and Technologies in Maghreb (CISTEM)*, Algiers, Algeria, pp. 1–4, 2018.

[23] B. Dolisy, S. Mezani, T. Lubin, and J. Lévêque, "A new analytical torque formula for axial field permanent magnets coupling," *IEEE Trans. Energy Convers.*, vol. 30, no. 3, pp. 892–899, 2015.

[24] B. Dolisy, T. Lubin, S. Mezani, and J. Lévêque, "Three-dimensional analytical model for an axial-field magnetic coupling," *Prog. Electromagn. Res.*, vol. 35, pp. 173–182, 2014.

[25] A. Hemeida and P. Sergeant, "Analytical modeling of surface PMSM using a combined solution of Maxwell's equations and magnetic equivalent circuit," *IEEE Trans. Magn.*, vol. 50, no. 12, pp. 1–13, 2014.

[26] Z. Q. Zhu, D. Howe, and Z. P. Xia, "Prediction of open-circuit airgap field distribution in brushless machines having an inset permanent magnet rotor topology," *IEEE Trans. Magn.*, vol. 30, no. 1, pp. 98–107, 1994.



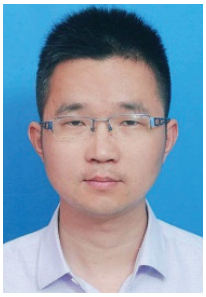
Youyuan Ni received the B.Eng. and Ph.D. degrees in electrical engineering from the Hefei University of Technology, Hefei, China, in 1999 and 2006, respectively. Since 2006, he has been with Hefei University of Technology, where he is currently an associate professor. His current research interest includes design and control of electric machines.



Jinsong Zou received the B.Eng. degree in electrical engineering and automation from Jiangsu University, Zhenjiang, China, in 2022. He is currently working toward the M.E. degree in electrical engineering with Hefei University of Technology. His current research interests include design of permanent magnet machines.



Yong Lin received the B.Eng. and M.S. degrees from Hefei University Technology of China in 1995 and 2002, respectively, both in automation engineering. He is currently an associate researcher. His research interests include automotive control systems and system modeling and simulation.



Anbang Wang received the B.Eng. and Ph.D. degrees from Hefei University of Technology, Hefei, China, in 2002 and 2016, respectively. Since 2016, he has been with Yangzhou Haitong Electronic Technology Co. Ltd., where he currently serves as an engineer. His research interests include power electronics and electric machine control.

Design and Open-Circuit Fault Analysis of Modular E-Type Stator Switched Reluctance Motor for High-Reliability Applications

Hao Chen[1,8*], Xin Liu[1], Sergei Brovanov[2], Jason Gu[3], Sherif Moussa[4], Marcin Wardach[5], Javokhir Toshov[6], Ali Asghar Memon[7], and Xing Wang[8]

[1]School of Electrical Engineering
China University of Mining and Technology, Xuzhou 221116, China
hchen@cumt.edu.cn, li_uxin@163.com

[2]Novosibirsk State Technical University
Novosibirsk 630073, Russia
brovanov@corp.nstu.ru

[3]Electrical and Computer Engineering
Dalhousie University, Halifax NS B3J 2X4, Canada
jason.gu@dal.ca

[4]School of Engineering
Canadian University Dubai, 117781 Sheikh Zayed Road, Dubai, United Arab Emirates
smoussa@cud.ac.ae

[5]Department of Electrical Machines and Drives
West Pomeranian University of Technology in Szczecin, Sikorskiego 37, 70-313 Szczecin, Poland
Marcin.Wardach@zut.edu.pl

[6]Tashkent State Technical
University University Street No2, 100095 Tashkent, Uzbekistan
javokhir.toshov@yandex.ru

[7]Mehran University of Engineering and Technology
Department of Electrical Engineering, Jamshoro, Pakistan
ali.asghar@faculty.muet.edu.pk

[8]Jiangsu Province Foreign Expert Workshop on New Energy Power Generation and Electric Transportation
Xuzhou 221008, China
3512@cumt.edu.cn
*Corresponding author

Abstract – This study proposes a modular switched reluctance motor (SRM), featuring an E-shaped stator core structure, suitable for high-reliability applications. The stator comprises six independent E-shaped cores with windings mounted on the core yokes. A two-dimensional simplified model evaluates static performance, including torque, magnetic flux (MMF), and inductance under both normal and winding fault conditions. Simulation results demonstrate the high reliability of the designed SRM.

Index Terms – E-type stator, reliability, stator modularization, switched reluctance motor, winding fault.

I. INTRODUCTION

Switched Reluctance Motors (SRMs) have gained widespread application in industrial fields and high-reliability scenarios due to their simple structure, centralized and independent windings, good heat dissipation performance, strong geometric adaptability, high fault tolerance, the absence of windings and permanent magnets in the rotor, and superior rotor temperature resistance. However, these motors also have issues such as low torque density, large torque pulsation, and significant noise and vibration, which limit their further promotion in industry. To enhance the industrial appeal of SRMs, various effective approaches have been proposed

Submitted On: February 02, 2026
Accepted On: June 09, 2026

1054-4887 © ACES

https://doi.org/10.13052/2026.ACES.J.410607

in research, including optimizing the conventional motor structure [1, 2], improving control strategies [3, 4], and using active materials such as piezoelectric actuators [5]. In recent years, many scholars have also been dedicated to exploring special rotor or stator structures with specific properties to further improve the comprehensive application performance of SRMs.

In reference [6], a new type of single-pole winding segmented rotor SRM was studied. This structure can significantly increase the magnetic flux (MMF) per revolution of the motor, thereby greatly enhancing the torque density. Compared with the traditional SRM, its average torque has increased by 40%. Based on this, reference [7] further proposed a 12/16-pole dual rotor single stator axial flux segmented rotor SRM for electric vehicles. This design has more rotor segments than stator slots, thereby increasing the torque density while reducing the end length of the windings, achieving the compactification of the motor structure.

In 2010, a single-phase C-type iron core hybrid magnetic circuit SRM for wind power generation was successfully developed [8]. This motor, based on the traditional SRM, achieved better controllability, stronger fault tolerance, and a lighter rotor weight, and there was no mutual coupling between the phase windings. In the literature [9, 10], a new type of two-phase E-type iron core SRM composed of two segmented stator cores was proposed. In this configuration, the MMF path formed by the phase excitation is shorter, thus reducing the required MMF for driving. Compared with the traditional two-phase SRM, it significantly reduces copper loss and iron loss, and has higher efficiency and average torque. The literature [11] introduced a new structure of disc-type SRM for high torque density applications. This motor adopts a double-sided stator design, which improves output torque and noise control compared to traditional small-sized SRM. Additionally, based on the innovative concept of non-circular stator pole, the literature [12] proposed a new stator pole structure aimed at further increasing the average torque. In the literature [13], a new SRM using stator and rotor core winding was studied. Analysis shows that, under the same output torque, this motor can achieve a higher speed than traditional SRM. The literature [14] proposed a simple stator SRM based on C-type iron core, and the research results show that this structure performs well in terms of torque and efficiency, and provides greater flexibility for winding design; however, this study only provides analytical results and did not conduct prototype experiments for verification. To reduce torque pulsation and improve efficiency, the literature [15] proposed a stator pole surface design with non-uniform air gap and added pole shoes on the rotor pole side. The literature [16] introduced a double-layer phase-segmented isolated SRM for high torque and low flux applications. This motor consists of three independent magnetic modules and has higher starting torque and efficiency than traditional SRM, suitable for key fields such as aerospace. The literature [17] proposed a π-type iron core permanent magnet-assisted SRM for electric vehicle traction. Its stator adopts a segmented isolated iron core structure, shortening the MMF path and effectively reducing core loss. Compared with traditional SRM, this π-type structure motor's average torque increased by 23%, and torque pulsation decreased by 41%.

This paper presents a modular E-type iron core stator type of new SRM suitable for high-reliability applications. This structure provides a larger slot space, making the winding process more convenient. Additionally, each E-type stator unit is independent, facilitating the separate manufacturing and winding through an automated process, thereby significantly reducing the winding manufacturing cost. Moreover, the abundant slot space also offers greater flexibility for the design of the MMF of the turns and phases, helping to achieve higher torque output.

II. E-TYPE STATOR SWITCHED RELUCTANCE MOTOR STRUCTURE

The E-type stator SRM is a special type of machine. Figure 1 shows the modular E-type stator structure of the SRM machine. The stator is composed of six independent modular E-type sections. Both the stator and rotor of the motor are manufactured by laminating silicon steel sheets. Two winding coils are wound together in each left yoke frame and right yoke frame of each E-type stator. The two opposite E-type modular stators form one phase in the motor. The four coils in one phase are connected in series to form a single-phase winding, as shown in Fig. 2. It can also be divided into two phases (A1 and A2) and connected to two power converters as two separate channels, which can be used for fault-tolerant applications. In this motor, since the stator modules are independent and evenly distributed, it can effectively shorten the MMF path and improve the efficiency.

To clearly explain the working principle of the proposed modular E-type stator SRM, the terms "alignment position" and "non-alignment position" are first defined. As shown in Fig. 1, when a rotor segment is perfectly aligned with the centerline of the left (or right) pole of the E-type iron core module, the inductance reaches its maximum value, and this position is called the alignment position; when the rotor segment is located between two adjacent stator modules and is completely offset from the stator pole, the inductance is at its minimum, and this position is called the non-alignment position.

The generation of positive torque requires applying current to the ascending region of the inductor, which is the process from the non-aligned position to the aligned position. For the 18/12-pole structure in this paper, the ascending region of the inductor for each phase (formed by two opposite E-type modules connected in series) corresponds to a mechanical angle of 15°. To fully utilize the ascending region of the inductor and avoid entering the descending region, the conduction angle is set as the non-aligned position of phase A (mechanical angle 0°), and the turn-off angle is set as 30° mechanical angle. Commutation sequence: Phase A conducts from 0° to 30°, Phase B conducts from 30° to 60°, Phase C conducts from 60° to 90°, and then the cycle repeats. Commutation timing: Phase A conducts from 0° to 30°, Phase B conducts from 30° to 60°, Phase C conducts from 60° to 90°, and then the cycle repeats. The current conduction angle (30° mechanical angle) corresponds to an electrical angle of 90°, and the current pulse is strictly synchronized with the rotor position. This commutation logic ensures that each phase generates positive torque within its inductor ascending region.

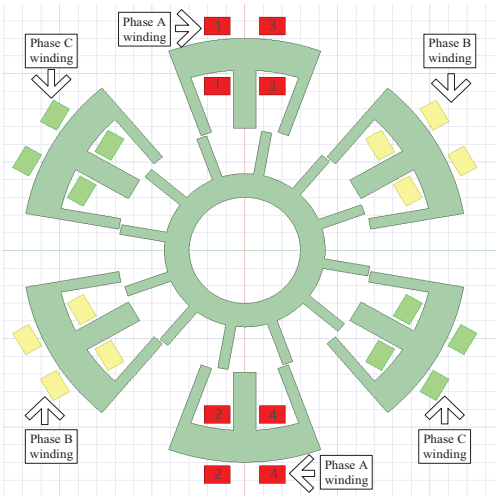


Fig. 1. Stator and rotor structure of the motor.

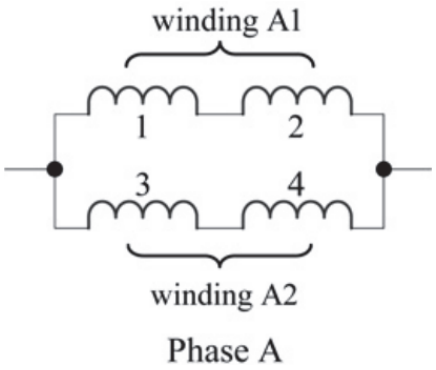


Fig. 2. Diagram of phase A winding connection.

III. DESIGN OF MAIN DIMENSIONS OF E-TYPE STATOR SWITCHED RELUCTANCE MOTOR

In order to ensure that the rotor has the self-starting capability for forward and reverse rotation, when the stator and rotor teeth are completely aligned, it is necessary to ensure that there is a certain overlap between adjacent stator and rotor teeth of the same phase. Therefore, the pole arc needs to meet the relevant necessary conditions, as shown in equation (1):

$$\begin{cases} \min(\beta_r, \beta_s) \geq \dfrac{2\pi}{qN_r} \\ \beta_r + \beta_s \leq \dfrac{2\pi}{N_r} \end{cases}, \tag{1}$$

where β_s and β_r represent the stator pole arc and the rotor pole arc, respectively. The slender shape of the motor is as shown in equation (2):

$$l = \frac{l_a}{D_a}, \tag{2}$$

where l_a represents the core length and D_a represents the rotor diameter. When the value of l is relatively small, the motor takes on a short and thick shape, resulting in a higher copper consumption during the manufacturing process; the motor's rotational inertia is larger, and it is easier for heat to dissipate inside the motor. Based on the design experience of SRM, the value of l generally ranges from 0.5 to 3. In this paper, the value of l is set at 1.

Based on the design experience of SRM, the range of the ratio of the outer diameter of the rotor to the stator is:

$$\frac{D_a}{D_s} = 0.5 \sim 0.55. \tag{3}$$

The electromagnetic power equation of the motor is:

$$\begin{cases} P_e = qUI_mK_d \\ I_m = K_mI/K_i \\ K_d = N_r\theta_d/2\pi \end{cases}, \tag{4}$$

where I_m represents the current amplitude, K_i is the peak current coefficient, K_m is the square wave current coefficient, U represents the voltage, K_d is the load coefficient, and θ_d is the current conduction angle during the rising phase of the winding inductance.

Ignoring the resistance of the windings on the stator, the maximum MMF can be expressed by the average MMF density of the stator poles:

$$\psi_m = N_{ph}\Phi \approx N_{ph}B_{ps}D_a \sin\frac{\beta_s}{2}l_\delta, \tag{5}$$

where l_δ is the calculated length of the armature and B_{ps} is the average MMF density of the stator poles. Ignoring leakage flux, by combining equations (4) and (5), we can obtain:

$$D_a^2 l_\delta = \frac{60 K_i P_{em}}{\pi N_r K_m A B_{ps} n \sin \beta_s / 2}. \tag{6}$$

The other parameters of the E-type modular stator SRM include the outer diameter of the stator (D_s), the outer diameter of the rotor (D_a), the yoke height between the stator and the rotor (h_{cs} and h_{cr}), and the length of the core (l_a). Based on the determination of D_a and l_a, other parameters can be calculated. According to equation (1), the sub-pole arc β_s is initially set at 10° and the rotor pole arc β_r is set at 10.65°. The remaining parameters can be calculated using the following equations:

Stator pole width:

$$b_{ps} = (D_a + 2g) \sin \frac{\beta_s}{2}. \tag{7}$$

Rotor pole width:

$$b_{pr} = D_a \sin \frac{\beta_r}{2}. \tag{8}$$

Stator yoke height:

$$h_{cs} = (0.5 \sim 0.75) b_{ps}. \tag{9}$$

Rotor yoke height:

$$h_{cr} = (0.5 \sim 1) b_{pr}. \tag{10}$$

Based on the aforementioned calculation method, the initial design flowchart for the motor described in this paper is shown in Fig. 3. Using the calculated data and parameter selection criteria, the parameters for each section of the SRM were determined, as shown in Table 1.

IV. FINITE ELEMENT SIMULATION CALCULATIONS AND PERFORMANCE COMPARISON

In the design of SRMs, fault tolerance is a critical characteristic. Analysis is conducted using the software Maxwell 2D. Bearing failures in SRMs can be eliminated through regular maintenance schedules, while the primary failures in these motors center on winding faults. Consequently, the impact of short-circuit or open-circuit faults in SRM windings on torque performance warrants significant attention. This paper analyzes torque data variations under missing excitation faults in windings and explores the mechanism enabling continued motor operation.

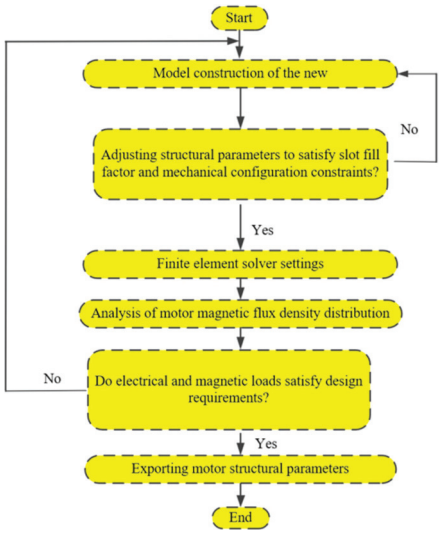


Fig. 3. Motor structural design flowchart.

Table 1: Specific parameters of the designed motor

Definition	Value
Number of stator poles	18
Number of rotor segments	12
Outer stator outer diameter	120 mm
Inner stator outer diameter	69 mm
Stator teeth slot width	6.088 mm
Stator pole length	16.5 mm
Stator yoke length	9 mm
Rotor pole pitch coefficient	0.5
Rotor pole length	12.3 mm
Air gap length	0.5 mm
Winding turns per teeth	50

The finite element simulation adopts the commutation angle setting described in section II. Taking phase A as an example, the current excitation is applied within the rotor mechanical angle range of 0° to 30° (with the non-aligned position of phase A set as the 0° reference). The torque-rotor position curves shown in Fig. 4 (normal operation) and Fig. 5 (winding A1 failure) are obtained under this conduction scheme. For instance, when the rotor position angle is 5° and the current is 5 A, the normal torque is 0.01676 N · m (as shown in Fig. 4) and, at this time, the inductance is still in the rising zone, so the torque is positive. If the current is applied beyond 30° (i.e., entering the inductance decline zone), a negative torque will be generated. This is avoided through the correct commutation logic. Therefore, the clear relationship between the current time (i.e., the conduction angle interval) and the rotor position is the core for generating positive torque. The results from

Figs. 4–8 jointly verify that the proposed E-type stator SRM can stably output positive torque under the above commutation logic.

In the fault-tolerant research of SRM, the winding faults are mainly classified into open-circuit faults and short circuit faults. This paper focuses on open-circuit faults (i.e., the winding is disconnected from the power supply, and the excitation current is zero). The reason for choosing open-circuit faults is that this fault mode can most directly verify the magnetic circuit independence and the continued operation capability of the remaining healthy windings in the modular E-type stator SRM proposed, and it can be simulated and analyzed without additional protective hardware.

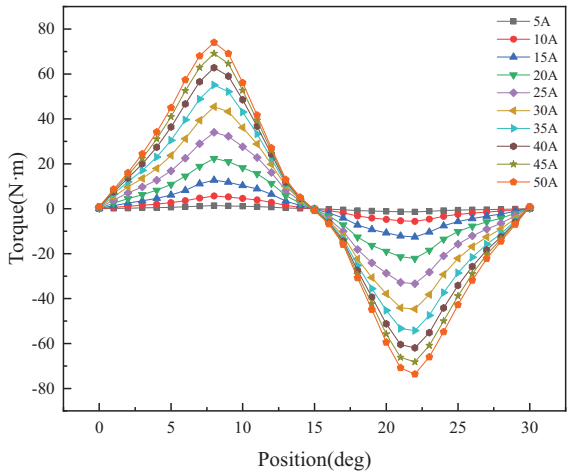


Fig. 4. Normal torque characteristic curve.

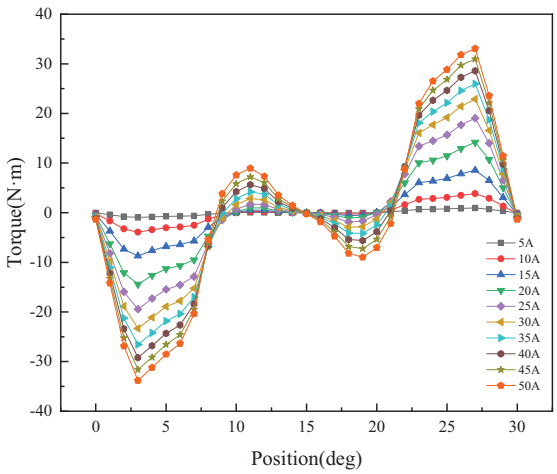


Fig. 5. Torque characteristic curve when winding A1 is faulty.

During normal operation, the A1 and A2 windings are energized, generating independent and symmetrical MMF loops within the E1 and E2 modules. The two magnetic paths are not coupled in space. When the A1 winding experiences an open-circuit fault, the E1 module has no energizing current and the MMF is zero. However, the A2 winding can still normally establish the MMF, forming a complete circuit along the E2 module and the corresponding rotor section, thereby providing a continuous electromagnetic torque.

First, compare the torque data under normal operation and phase-loss fault conditions. From the data in Figs. 4 and 5, it can be seen that in the case of fault in winding A1, the torque values are generally lower than the normal situation. For example, at the rotor position angle of 0 degrees and current of 5 A, the normal torque is 0.01676 Nm, while the phase-loss torque is −0.03647 Nm, indicating that the phase-loss not only reduces the torque output but also introduces a negative torque region. Similarly, at different currents and positions, the amplitude of the phase-loss torque decreases and the fluctuations increase. This is mainly because the torque of the SRM is generated by multiple phase windings together. When winding A1 is faulty, the total torque synthesis decreases, and the torque pulsation increases, resulting in a decrease in the average torque and unstable operation.

The reason for the torque difference under the phase loss fault lies in the working principle of the SRM. During normal operation, each phase winding is excited in sequence, and the magnetic resistance change caused by the rotor position variation is utilized to generate continuous torque. When phase A1 is missing, it does not contribute to the torque, so the torque output depends on the remaining phases. However, the excitation of the remaining phases may not fully cover all rotor positions, resulting in low torque or negative torque at certain positions. Moreover, due to magnetic circuit coupling, the phase loss may change the flux distribution, further affecting the torque characteristics.

Despite the torque performance degradation caused by phase loss, the motor can continue to operate. This is because the designed SRM structure possesses inherent fault tolerance. Each phase winding is relatively independent in both electrical and magnetic circuits, so a fault in winding A1 does not directly affect the operation of other phases. The remaining phase windings can continue to generate torque, driving the rotor rotation. Although output torque decreases and pulsation increases, the motor can maintain operation in many applications, especially if the load demands are not high or the control system can adjust the current to compensate for the torque loss. Furthermore, the designed SRM features a simple structure and robustness that ensures reliability under fault conditions.

To validate the magnetic circuit and operating principle of the modular E-shaped core stator in the novel

switch reluctance motor, a finite element analysis model was constructed based on the motor structural parameters provided in Table 1. This model was used to evaluate the electromagnetic performance of the new SRM. Figure 6 illustrates the finite element model structure of the modular novel motor and its magnetic field distribution characteristics under excitation conditions.

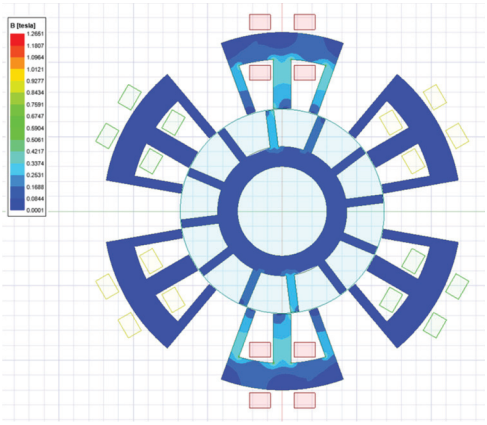
Analysis of the MMF density distribution reveals that the magnetic field distribution in the tooth regions and winding areas of both the stator and rotor cores is relatively uniform, with no significant localized saturation observed. It should be noted that peak MMF density is primarily concentrated near the pole tips adjacent to the air gap, a distribution characteristic consistent with the physical principles governing magnetic field control. Simulation results indicate that, throughout the entire operating cycle, the maximum MMF density in the core material consistently remains below 1.01 T. This data not only demonstrates the efficient utilization of magnetic materials but also validates the rationality and reliability of the proposed motor structure from an electromagnetic design perspective.

From the MMF density distribution in Fig. 6, it can be seen that the maximum MMF density of the iron core of the motor in this study is 1.01–1.27 T, which is significantly lower than the 1.5–1.7 T commonly used in conventional motor designs. This choice was not accidental but was based on the following considerations: (a) to reserve magnetic circuit saturation margin for the current increase of the remaining healthy windings in case of open-circuit faults; (b) to reduce core loss and improve efficiency; (c) to reduce radial magnetic suction pulsation and suppress noise and vibration; (d) to maintain the linearity of the magnetic circuit near the normal operating point for easier control.

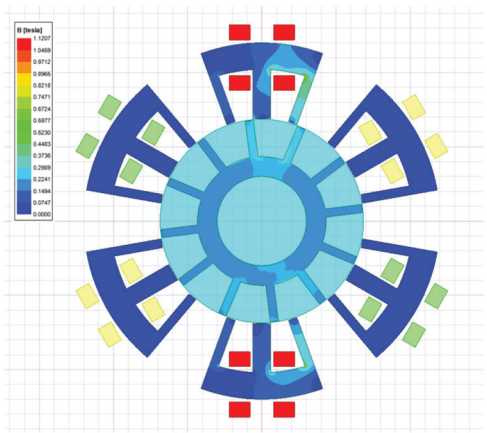
If higher requirements are imposed on volume and weight, the iron core size can be reduced by increasing the MMF density. For example, if the maximum MMF density is raised to 1.5 T, the stator tooth width and yoke height can be reduced accordingly, and the core volume is expected to shrink by approximately 35%. However, the cost is a significant increase in iron loss (about 2.5 times), and the torque pulsation and noise levels also increase. Therefore, the conservative MMF density design adopted in this study is more suitable for high-reliability and low-noise applications; for applications that require high power density, the motor can be optimized for high MMF density in subsequent work.

The core electromagnetic characteristics of SRMs are embodied in key parameters such as MMF linkage, inductance, and output torque. Figures 7 and 8 illustrate the variation patterns of MMF linkage and inductance across a single stator pole with current changes under normal operating conditions and single-winding fault conditions.

Figure 7 shows the flux-current curves for a single stator pole at both aligned and non-aligned positions during a winding A1 fault. As illustrated, at low currents, the flux at both positions increases approximately linearly with current. As current continues to rise, the flux growth at the aligned position slows significantly, exhibiting a saturation trend, indicating that the pole tip region enters a state of local magnetic saturation. In contrast, the MMF at the non-aligned position maintains a consistent linear relationship throughout the entire current range. This comparison demonstrates that, under winding fault conditions, the spatial distribution characteristics of the motor's MMF remain consistent with

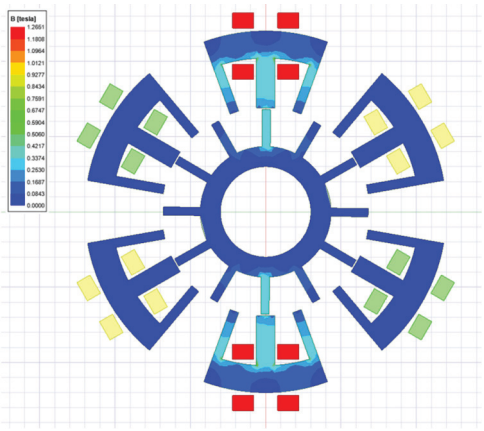


(a)

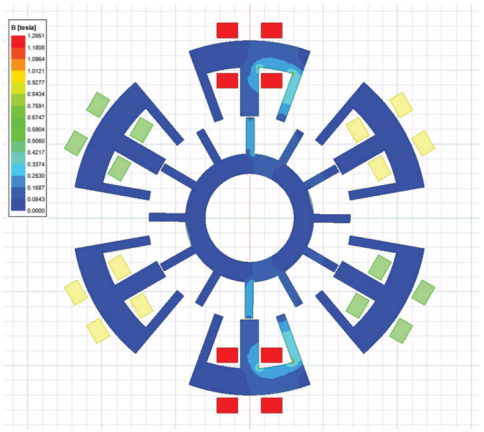


(b)

Fig. 6. Finite element model and magnetic field distribution: (a) normal magnetic flux density map misaligned position, (b) magnetic flux density cloud map during A1 winding fault – misaligned position, (c) normal magnetic flux density map – alignment position, and (d) magnetic flux density cloud map during A1 winding fault – alignment position.



(c)

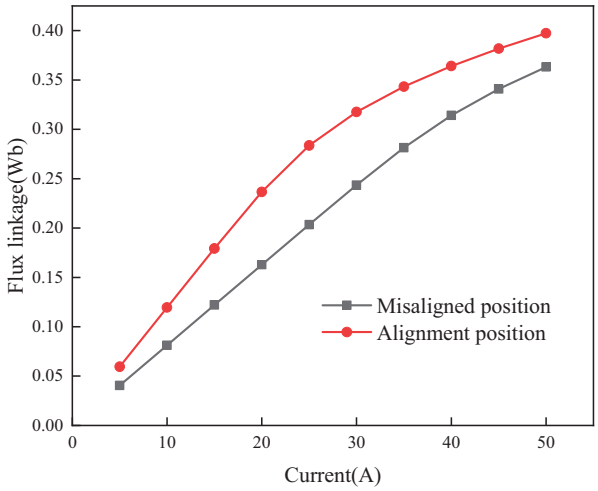


(d)

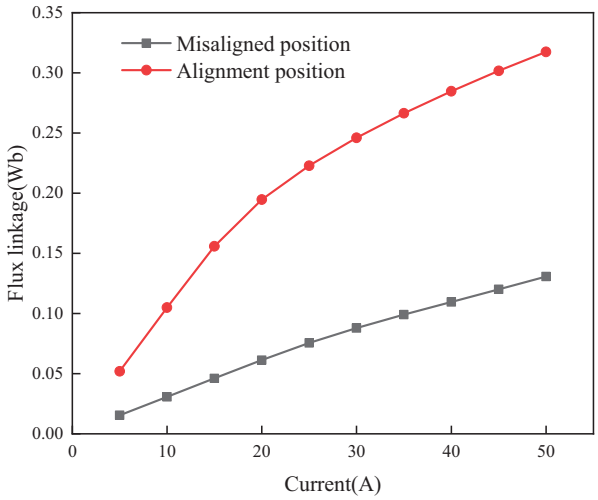
Fig. 6. (*Continued*).

normal operating conditions. The peak MMF density remains concentrated near the air gap at the aligned position, adhering to the fundamental physical principles of magnetic field distribution. This also indirectly reflects that the motor structure retains a certain degree of electromagnetic stability even under localized faults.

Figure 7 shows the pattern of the MMF as it varies with the current. In the normal operating condition (Fig. 7 (a)), the MMF at the aligned position (red line) linearly increases in the low current region. When the current exceeds 2 A, it enters the saturation region, and the slope of the curve gradually decreases. The MMF at the non-aligned position (black line) remains linear throughout the current range and is much lower than that at the aligned position (for example, at 2 A, the MMF at the non-aligned position is only 25% of that at the aligned position). This is in line with the basic characteristics of the SRM. When an A1 winding open-circuit fault occurs (Fig. 7 (b)), due to the absence of A1 winding excitation, the total phase MMF is halved, resulting in a decrease of approximately 20.7% in the MMF at the aligned position compared to the normal operating state (at 5 A current, it drops from 0.0605 Wb to 0.0480 Wb); while the MMF at the non-aligned position is almost unaffected (because the magnetic path at this position is mainly composed of air gaps, with a large magnetic resistance, and the effect of halving the number of windings can be ignored).



(a)

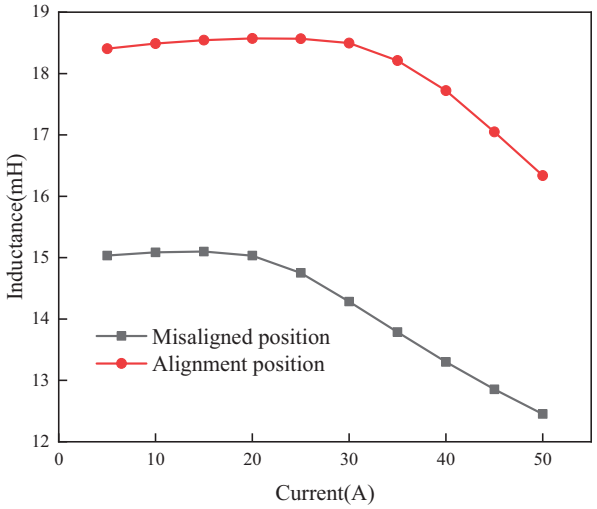


(b)

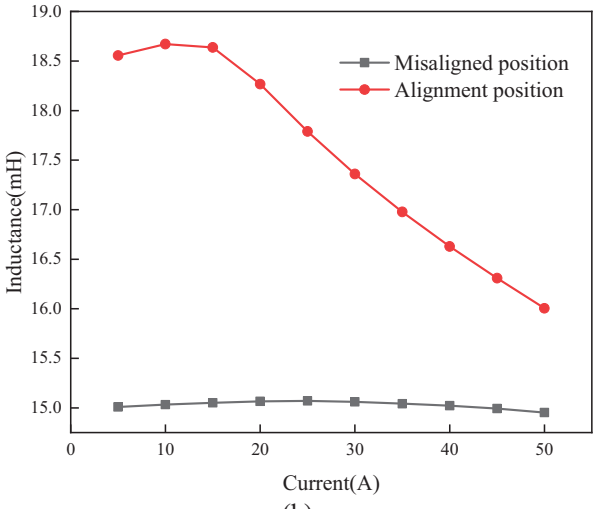
Fig. 7. Magnetic linkage curve diagram: (a) normal operation (both A1 and A2 are in normal excitation state) and (b) open-circuit fault in the A1 winding (A2 is operating normally; the current in A1 is zero).

Figure 8 further compares the inductance-current curves during normal operation and when winding A1 is faulty. During normal operation, the inductance at the aligned position remains stable at low currents but decreases significantly upon entering the saturation region. The inductance at the non-aligned position exhibits smooth variation across the entire current

range. After the A1 winding failure, the overall trend of the inductance curve remains unchanged. However, the inductance value at the aligned position in the saturation region slightly decreases, while the inductance characteristics at the non-aligned position remain virtually unaffected. These results indicate that the winding fault did not alter the inherent saturation characteristics of the motor's magnetic circuit. The distinct response differences between the aligned and non-aligned positions remain clearly discernible. This further confirms that the designed motor exhibits a certain degree of robustness against localized faults at the electromagnetic parameter level, providing a basis for analyzing the motor's fault-tolerant operation.



(a)



(b)

Fig. 8. Inductance curve graph: (a) normal operation (both A1 and A2 are in normal excitation state) and (b) open-circuit fault in the A1 winding (A2 is operating normally; the current in A1 is zero).

As can be seen from Table 2, the analytical values are in good agreement with the finite element values, and all relative errors are within 3%. The errors mainly result from the fact that the analytical model did not take into account the non-linear saturation of the core material and the edge effect of the tooth tips. This verification result indicates that although the analytical model contains certain approximations, its design accuracy is sufficient to meet the requirements of the initial engineering design, and it also provides a reliable initial size for the subsequent finite element optimization.

Table 2: Comparison of analytical calculation results with finite element simulation results (5 A)

Performance Indicators	**Analysis Calculation Value**	**Finite Element Simulation Values**	**Relative Error**
Aligned position magnetic link	0.0595 Wb	0.0580 Wb	2.5%
Its position inductance	12.4 mH	11.8 mH	2.5%
Non-aligned position inductor	2.78 mH	2.82 mH	1.4%

During the initial stage of excitation with lower currents, the MMF at both positions increases approximately linearly with the excitation current, while the corresponding inductance values remain largely constant. This indicates that the motor's magnetic circuit is operating within the linear region of the core material's magnetization curve. However, once the current exceeds a specific saturation threshold, the MMF growth at the aligned position slows significantly, exhibiting nonlinear saturation characteristics, and its inductance value decreases markedly. In contrast, the MMF and inductance at the misaligned position exhibit smooth variations across the entire current range, maintaining a consistently good linear relationship throughout.

V. CONCLUSION

The E-type stator modular structure of the SRM is relatively simple in terms of manufacturing and maintenance. The simulation results have proved the fault-tolerant capability and reliability of the proposed SRM. Even in the case of severe open-circuit faults in the windings, it can still perform the task well. Of course, in this situation, the torque pulsation of the SRM will become larger, the speed will decrease, and the period of low torque will be prolonged due to the increase in the number of current pulses missing. In the future,

studies will be conducted to reduce the torque pulsation through an appropriate current control system, increase the current in the remaining healthy windings of the stator, and further improve the reliability of the SRM.

ACKNOWLEDGMENT

This work was supported in part by the National Natural Science Foundation of China International (regional) cooperation and exchange projects NSFC-RSF under Grant W2412064.

REFERENCES

[1] W. Yan, W. Wang, H. Li, H. Chen, F. Yu, D. Zhang, H. Yang, and Q. Wang, "Investigation on different stator structures of the axial-radial flux switched reluctance motors," *IEEE Transactions on Industrial Electronics*, vol. 71, no. 6, pp. 5474–5484, June 2024.

[2] G. Wang, H. Chen, F. Yu, W. Yan, X. Wang, M. Benbouzid, A. Bresolin, M. P. Aguirre, H. Torkaman, M. Shamiev, Y. Tairov, M. Orabi, and M. A. Gaafar, "Design, analysis, and comparison of a novel axial flux modular-double-stator hybrid excitation SRM," *IEEE Transactions on Transportation Electrification*, vol. 10, no. 3, pp. 6100–6114, Sep. 2024.

[3] H. Chen, C. Fang, G. Guan, and N. Parspour, "Fault diagnosis for power converter in SRM drives based on current prediction," *IEEE Transactions on Industrial Electronics*, vol. 69, no. 12, pp. 13576–13585, Dec. 2022.

[4] F. Yu, H. Chen, W. Yan, and X. Wang, "Three-switch reconfigurable winding power converter and online mode-changeover methods for SRM speed range extension," *IEEE Transactions on Transportation Electrification*, vol. 11, no. 1, pp. 2061–2075, Feb. 2025.

[5] X. Ojeda, X. Mininger, H. B. Ahmed, M. Gabsi, and M. Lecrivain, "Piezoelectric actuator design and placement for switched reluctance motors active damping," *IEEE Trans. Energy Convers.*, vol. 24, no. 2, pp. 305–313, 2009.

[6] B. C. Mecrow, E. A. El-Kharashi, J. W. Finch, and A. G. Jack, "Segmental rotor switched reluctance motors with single-tooth windings," *IEE Proc. Electr. Power Appl.*, vol. 150, no. 5, pp. 591–599, 2003.

[7] R. Madhavan and B. G. Fernandes, "Axial flux segmented SRM with a higher number of rotor segments for electric vehicles," *IEEE Trans. Energy Convers.*, vol. 28, no. 1, pp. 203–213, 2013.

[8] A. Labak and N. C. Kar, "Designing and prototyping a novel five-phase pancake-shaped axial-flux SRM for electric vehicle application through dynamic FEA incorporating flux-tube modeling," *IEEE Transactions on Industry Applications*, vol. 49, no. 3, pp. 1276–1288, May–June 2013.

[9] C. Lee and R. Krishnan, "New designs of a two-phase E-core switched reluctance machine by optimizing the magnetic structure for a specific application: Concept, design, and analysis," *IEEE Trans. Ind. Appl.*, vol. 45, no. 5, pp. 1804–1814, 2009.

[10] C. Lee, R. Krishnan, and N. S. Lobo, "Novel two-phase switched reluctance machine using common-pole E-core structure: Concept, analysis, and experimental verification," *IEEE Trans. Ind. Appl.*, vol. 45, no. 2, pp. 703–711, 2009.

[11] F. Yu, H. Chen, W. Yan, V. F. Pires, J. F. A. Martins, P. Rafajdus, A. Musolino, L. Sani, M. P. Aguirre, M. A. Sagib, M. Orabi, and X. Li, "Design and multiobjective optimization of a double-stator axial flux SRM with full-pitch winding configuration," *IEEE Transactions on Transportation Electrification*, vol. 8, no. 4, pp. 4348–4364, Dec. 2022.

[12] S. Cai, Y. Wang, H. Chen, X. Yuan, L. Yu, Z. Zhang, C. H. T. Lee, "Design and analysis of a doubly salient wound field starter generator for cost-effective automobile application," *IEEE Transactions on Vehicular Technology*, vol. 71, no. 7, pp. 6900–6911, July 2022.

[13] K. Nakamura, T. Ono, H. Goto, T. Watanabe, and O. Ichinokura, "A novel switched reluctance motor with wound-cores put on stator and rotor poles," *IEEE Trans. Magn.*, vol. 41, no. 10, pp. 3919–3921, 2005.

[14] S. H. Mao and M. C. Tsai, "A novel switched reluctance motor with C-core stators," *IEEE Trans. Magn.*, vol. 41, no. 12, pp. 4413–4420, 2005.

[15] Y. K. Choi, H. S. Yoon, and C. S. Koh, "Pole-shape optimization of a switched reluctance motor for torque ripple reduction," *IEEE Trans. Magn.*, vol. 43, no. 4, pp. 1797–1800, 2007.

[16] H. Torkaman, E. Afjei, and M. S. Toulabi, "New double-layer-per-phase isolated switched reluctance motor: Concept, numerical analysis, and experimental confirmation," *IEEE Trans. Ind. Electron.*, vol. 59, no. 2, pp. 830–838, 2012.

[17] C. S. Kim, G. Lee, K. Lee, J. Lee, and Y. Cho, "Design of π core and π^2 core PM-aided switched reluctance motors," in *Proc. IEEE Int. Conf. Electric Vehicle*, Kuching, Malaysia, pp. 1–6, 2012.



Hao Chen (SM'08) received the B.S. and Ph.D. degrees from the Department of Automatic Control, Nanjing University of Aeronautics and Astronautics, Nanjing, China, in 1991 and 1996, respectively. In 1998, he became an Associate Professor with the School of Information and Electrical Engineering, China University of Mining and Technology, Xuzhou, where he has been a Professor since 2001. From 2002 to 2003, he was a Visiting Professor at Kyungsung

University, Busan, Korea. Since 2008, he has also been an Adjunct Professor at the University of Western Australia, Perth, Australia. He is the author of one book and has also authored more than 190 papers. He is the holder of 15 US Patents, 23 Australian Patents, one Danish Patent, seven Canadian Patents, three South African Patents, 10 Russian Patents, 86 Chinese Invention Patents, and six Chinese Utility Model Patents. His current research interests include motor control, linear launcher, electric vehicles, electric traction, servo drives, and wind power generator control.

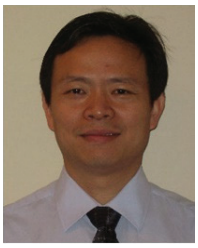
Chen was the recipient of both the Prize of Science and Technology of Chinese Youth and the Prize of the Fok Ying Tong Education Foundation for Youth Teachers in 2004. He was awarded first prize in the Science and Technology advanced of Province and Ministry once, second prize in the Science and Technology advanced of Province and Ministry seven times, and third prize in the Science and Technology advanced of Province and Ministry 14 times. He became the Chinese New Century Hundred-Thousand Ten-Thousand Talents Engineering National Talent in 2007, and won the Government Especial Allowance of People's Republic of China State Department in 2006.



Xin Liu obtained a master's degree in electrical engineering. Since 2024, he has been studying for a doctoral degree in electrical engineering at China University of Mining and Technology in Xuzhou, China. His research interests include switched reluctance drive, special motor design, power converters, and motor control.



Sergei Brovanov received the engineer degree from the Industrial Electronics Department, Novosibirsk Electrotechnical Institute, Russia, in 1987. In 1999, he became an Associate Professor in the Industrial Electronics Department, Novosibirsk State Technical University, where he has been a Professor since 2013. In 2004, he was a Visiting Professor at Ulsan University, South Korea. He is the author of one book and has also authored more than 150 papers. He has obtained 17 Russian patents. His current research interests include semiconductor converters, vector PWM of multilevel NPC converters, and semiconductor converters for electrical energy storage systems. In 1996–1997, he was awarded a scholarship from the Swiss Academy of Engineering Sciences. In 2023, he was awarded the State Prize of the Novosibirsk Region for the development of intelligent power electronic systems and devices. Brovanov currently is a professor in the electronics and electrical engineering department at Novosibirsk State Technical University.



Jason Gu (Senior Member, IEEE) received the B.Eng. degree in electrical engineering and information science from the University of Science and Technology of China, Hefei, China, in 1992, the M.A.Sc. degree in biomedical engineering from Shanghai Jiaotong University, Shanghai, in 1995, and the Ph.D. degree in electrical and computer engineering from the University of Alberta, Edmonton, AB, Canada, in 2001. He is currently a Professor of electrical and computer engineering with Dalhousie University, Halifax, NS. He is also a Cross-Appointed Professor with the School of Biomedical Engineering for his multidisciplinary research work. He is a Guest Professor with Shandong University, Jinan. His current research interests include robotics and teleoperation, biomedical engineering, rehabilitation engineering, neural networks, and control.



Sherif Moussa is the Dean of the School of Engineering, Applied Science, and Technology at the Canadian University Dubai (CUD), UAE. He earned his Ph.D. in Electrical and Computer Engineering from the University of Québec at Trois-Rivières, Canada, and his M.Sc. in Electrical and Computer Engineering from the University of Waterloo, Canada. Since joining CUD in 2007, Moussa has led the School's remarkable growth, overseeing the launch and accreditation of several engineering and computing programs, including mechatronics engineering, computer science, cybersecurity, software design, power and renewable energy engineering, and the M.Sc. in Artificial Intelligence. His leadership has also advanced international collaborations, notably with Queen's University and the University of Ottawa, and strengthened CUD's engagement with industry partners in emerging technologies. Moussa's research interests span wireless communication, computer networks, machine learning, and digital systems design. He has published widely in international journals and conferences, serves on technical committees, and was the recipient of the 2015 CUD Research Excellence Award. He is also the founder of CUD's Robotics Club and a strong advocate for innovation and experiential learning in engineering education.



Marcin Wardach was born in Poland in 1980. He graduated and received the Ph.D. degree from the Electrical Department, Szczecin University of Technology, Szczecin, Poland, in 2004 and 2009, respectively. From 2020 until now, he has been an Associate Professor with the Faculty of Electrical Engineering, West Pomeranian University of Technology in Szczecin. Since 2024, he has served as Vice-Dean for Organization and Development and Head of the Department of Electrical Machines and Drives at the Faculty of Electrical Engineering, West Pomeranian University of Technology in Szczecin. From 2019 to 2025, he worked as an electrical machine designer at Mpower Sp. z o.o. company. His research interests include the design of electrical machines and drives, especially unconventional and hybrid excited. He is the author of over 100 scientific papers and post-conference publications. Since 2022, he has been the President of the Szczecin Branch of the Association of Polish Electrical Engineers (SEP). He is also a member of the Polish Society of Theoretical and Applied Electrical Engineering.



Javokhir Toshov received the B.S. degree from Navoi State Mining Institute, Navoi, Uzbekistan, in 1999, and M.S. degree from Tashkent State Technical University, Tashkent, in 2002. Dr.Sci. in 2017, Professor of the Tashkent State Technical University since 2020. He has about 250 published and reviewed works. His current research interests include drilling control for drilling operations, as well as electrical installations and motors for mining equipment. For many years he worked as the dean of the energy faculty, and today he works as the head of the department at Tashkent State Technical University.



Ali Asghar Memon is professor in Electrical Engineering at Mehran University of Engineering and Technology Jamshoro, Pakistan. He holds B.E. and M.E. both in Electrical Engineering from Mehran University and Ph.D. from University of Leeds, UK. Memon is head of Electrical Machine and Drives group at Mehran University. He has been member of National Curriculum Review Committee in Pakistan. Memon has been serving as an expert evaluator for National Research Project for Universities (NRPU), Post doc fellowship and project(s) under Technology Development Fund (TDF), under Higher Education Commission (HEC), Government of Pakistan. Memon is keynote speaker and reviewer of prestige international research journals. Memons interests include modeling and simulation of switched reluctance machines and inverters.



Xing Wang received the B.S. degree from China University of Mining and Technology, Xuzhou Jiangsu, China, in 1996, and M.S. degree from China University of Mining and Technology, Xuzhou Jiangsu, in 1999. In 2007, she became an Associate Professor with China University of Mining and Technology, Xuzhou. She is a holder of four US Patents, nine Australian Patents, two Canadian Patents, four Russian Patents, 12 Chinese Invention Patents, three Chinese Utility Model Patents, and has authored 15 papers.

Performance Comparison Analysis of Modular Double-Stator Switched Reluctance Motor with Differing Winding Polarities

Fengyuan Yu[1,5], Hao Chen[1,2,3,*], Haidong Yan[4], Guanjun Wang[4], and Jun Bao[4]

[1]School of Electrical Engineering
China University of Mining and Technology, Xuzhou 221116, China
fyyu@cumt.edu.cn, hchen@cumt.edu.cn

[2]International Joint Research Center of Central and Eastern European Countries on New Energy Electric Vehicle Technology and Equipment
Xuzhou 221008, China

[3]Shenzhen Research Institute
China University of Mining and Technology, Shenzhen 518057, China

[4]Wuxi Institute of Inspection, Testing and Certification
Wuxi 214101, China
yhd@wxmtc.com, wgjcumt@126.com, jsmtc12@126.com

[5]School of Electrical Engineering and Automation
Jiangsu Normal University, Xuzhou 221116, China
*Corresponding author

Abstract – Modular double-stator switched reluctance motors offer the advantages of high torque density, low mutual coupling, and high reliability, making them promising candidates for electrified transportation applications. The dual-winding configuration enables both the inner and outer stator poles to be equipped with excitation windings. Variations in the excitation direction of these windings lead to distinct winding polarity distributions, thereby resulting in different magnetic flux paths and electromagnetic characteristics. This paper presents two typical polarity distributions for modular double-stator switched reluctance motors, namely NSNS and NSSN. Motor models are established in the finite element software Altair Flux to analyze the flux path, flux density, and static electromagnetic torque under both winding polarities. In addition, dynamic performance metrics including torque ripple, core loss, copper loss, and efficiency are evaluated under various rotor geometries and operating speeds. The influence of key rotor geometric parameters on the torque and efficiency characteristics of the two polarity configurations is also investigated.

Index Terms – Electromagnetic performance, finite element analysis, flux path, switched reluctance motor, winding polarity.

I. INTRODUCTION

Owing to the absence of permanent magnet and windings on the rotor, the switched reluctance motor (SRM) boasts advantages such as simple and robust construction, low manufacturing cost, and strong fault tolerance [1, 2]. Consequently, it has found applications in various fields including electric vehicles, electric aircraft, and wind power generation [3, 4]. However, due to its inherent reluctance torque nature, the torque and power performance of SRMs still lag behind those of permanent magnet motors and require improvement.

To enhance SRMs' performance, several novel motor structures, including double-stator SRM [5], segmentedrotor SRM [6], axial-flux SRM [7], and hybrid excitation SRM [8] configurations have been proposed. Among these, the double-stator SRM (DSSRM) improves the utilization of electromagnetic space and is characterized by high torque density. Nevertheless, the design process of its structural parameters often involves large phase inductance values or a high ratio of maximum to minimum inductance. The traditional SRM features a fixed magnetic circuit and a single operational mode. This often results in a limited constant-power speed range and a restricted operational region for DSSRMs, even when they possess high torque density characteristics. It is challenging to achieve both high

Submitted On: February 11, 2026
Accepted On: July 30, 2026

1054-4887 © ACES

https://doi.org/10.13052/2026.ACES.J.410608

torque density and a wide speed range simultaneously, which limits their application in scenarios demanding non-rare-earth motor systems that combine these two features.

In other types of motors, variable-flux motor structures have become a current research hotspot. Variable-flux motors enhance field-weakening capability, broaden the constant-power range, and enable wide-speed operation by introducing an additional controllable magnetic flux regulation variable to alter the main air-gap flux. Depending on the method of air-gap flux regulation, adjustable-flux motors include hybrid excitation, mechanical flux adjustment, variable stator winding configuration, and variable flux memory motors [9–12]. For SRMs, some scholars have achieved flux regulation by employing two separate sets of windings simultaneously. This approach aims to extend the motor's speed range while maintaining torque output capability at low speeds [13–16]. However, this scheme faces shortcomings such as a high slot fill factor, severe electromagnetic coupling, and complex decoupling control, which hinder the widespread adoption of this motor type.

Indeed, varying the energizing direction of the winding coils leads to distinct winding polarity distributions, which in turn affect motor performance. This paper investigates the influence of the winding coil energizing direction on the performance of modular DSSRMs. First, the motor structure is described and the feasible polarity configurations are identified. Second, a two-dimensional finite element model of the motor is developed in finite element software, and the flux paths, flux density, torque, flux linkage, and inductance characteristics under the two different winding polarities are analyzed using the finite element analysis method. Finally, the effect of rotor pole arc angle on the torque characteristics of the motors with the two polarity distributions is examined.

II. MOTOR STRUCTURE AND WINDING POLARITY DISTRIBUTION

Figure 1 illustrates the structural schematic of the modular double-stator switched reluctance motor. As can be observed, the inner stator, rotor, and outer stator are concentrically arranged from the innermost to the outermost layers. Both the inner and outer stators adopt the U-shaped modular structure, positioned on either side of the segmented rotor, which itself features a sector-shaped modular configuration. A total of eight U-shaped outer stator modules, eight U-shaped inner stator modules, and 14 sector-shaped rotor segments are uniformly distributed along the circumferential direction. The tooth poles of both the inner and outer U-shaped stators face the rotor. The pole numbers of the inner stator, rotor, and outer stator are 16, 14, and 16, respectively.

In addition, each tooth pole of both the outer and inner stators is equipped with excitation windings. It is worth noting that by varying the energizing directions of the excitation windings on the inner and outer stators, different polarity distribution characteristics can be achieved in the modular double-stator switched reluctance motor. In this paper, a single stator unit is formed by combining one U-shaped outer stator, the corresponding U-shaped inner stator positioned opposite to it, and the surrounding segmented rotor. When the excitation windings on the inner and outer stators are energized in the same direction, the polarity distribution of a single stator unit is NSNS.

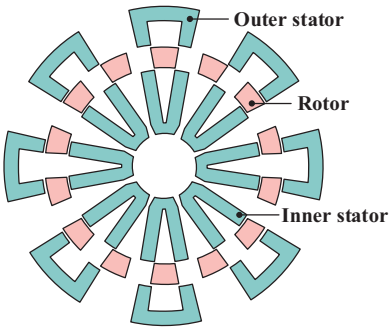


Fig. 1. Diagram of the modular double-stator switched reluctance motor structure.

Figure 2 presents a schematic diagram of the winding energizing directions for both the entire motor cross-section and a single stator unit under the NSNS polarity distribution. It can be observed that the tooth polarities of the outer U-shaped stator from left to right are N and S, while those of the inner U-shaped stator from left to right are also N and S. This indicates that the energizing direction of the excitation windings on the inner stator is identical to that on the outer stator.

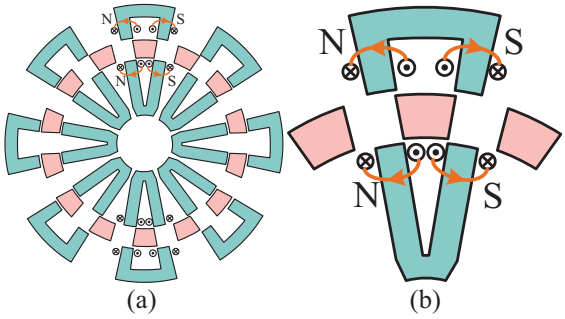
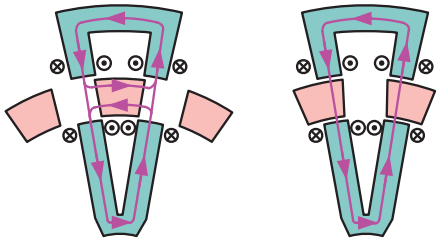


Fig. 2. Diagram of winding coil connection under NSNS polarity distribution: (a) cross-sectional view of the whole motor and (b) single inner/outer stator unit.

As can be seen, when the excitation windings on the inner and outer stators are energized in the same direction, corresponding to the NSNS polarity distribution, the magnetic flux forms a closed loop along the adjacent segmented inner stator teeth, segmented rotor, and segmented outer stator teeth, resulting in a relatively long flux path. Figures 3 (a) and (b) depict the flux paths at the rotor fully aligned and fully unaligned positions, respectively, under this polarity, with arrows indicating the direction of magnetic flux.

As shown in Fig. 3 (a), when the motor is at the rotor unaligned position under the NSNS polarity, the magnetic flux circulates through the segmented inner stator teeth, the air gap between two adjacent segmented rotor segments, and the segmented outer stator teeth, forming a closed annular loop. At this position, the motor exhibits the minimum inductance under this polarity. In contrast, Fig. 3 (b) illustrates that when the motor is at the rotor aligned position under the NSNS polarity, the magnetic flux flows through the segmented inner stator teeth, two adjacent segmented rotor segments, and the segmented outer stator teeth, again forming a closed annular loop. This corresponds to the position of maximum inductance under this polarity.

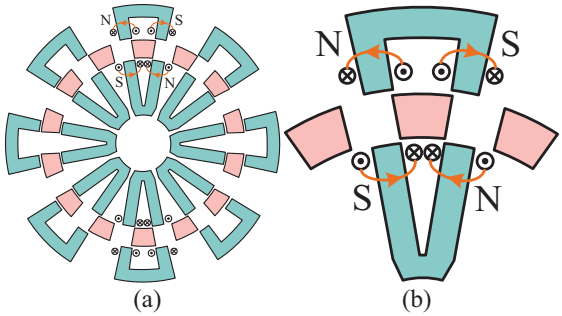


(a) (b)

Fig. 3. Diagram of the flux path under NSNS polarity distribution: (a) rotor electromagnetic unalignment position and (b) rotor electromagnetic alignment position.

When the excitation windings on the inner and outer stators are energized in opposite directions, the polarity distribution of a single stator unit becomes NSSN. A schematic representation of the winding energizing directions for both the full motor cross-section and a representative stator unit under the NSSN configuration is provided in Fig. 4.

As evident, the outer U-shaped stator teeth exhibit N and S polarities from left to right, while the inner U-shaped stator teeth display S and N polarities in the same orientation. This indicates that the excitation windings on the inner and outer stators are energized in opposite directions. By reversing the current direction in the inner stator windings, the proposed variable-flux-path double-stator switched reluctance motor can realize distinct magnetic flux path configurations. Under the

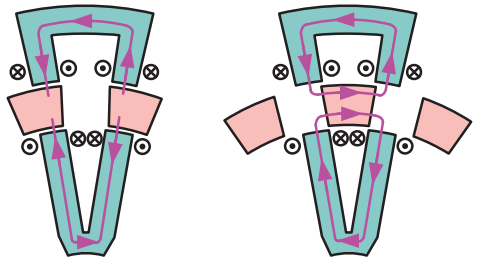


(a) (b)

Fig. 4. Diagram of winding coil connection under NSSN polarity distribution: (a) cross-sectional view of the whole motor and (b) single inner/outer stator unit.

NSSN polarity distribution, where the inner and outer stator excitations are opposing, the magnetic flux completes a closed loop via the adjacent segmented inner stator tooth, the segmented rotor, and the segmented outer stator tooth, forming a relatively short flux path. The flux path distributions at the fully aligned and fully unaligned rotor positions for this polarity are presented in Figs. 5 (a) and (b), respectively.

Figure 5 (a) reveals that at the unaligned position under NSSN polarity, the magnetic flux emanates separately from the segmented inner and outer stator teeth and cancels within the segmented rotor, thereby establishing a closed circuit. This rotor position yields the minimum inductance for this polarity. In contrast, Fig. 5 (b) shows that at the aligned position under NSSN polarity, the flux flows from the segmented inner stator tooth, through the segmented rotor, and into the segmented outer stator tooth, subsequently canceling within the rotor to close the loop. This electromagnetic alignment position corresponds to the maximum inductance condition under the NSSN polarity.



(a) (b)

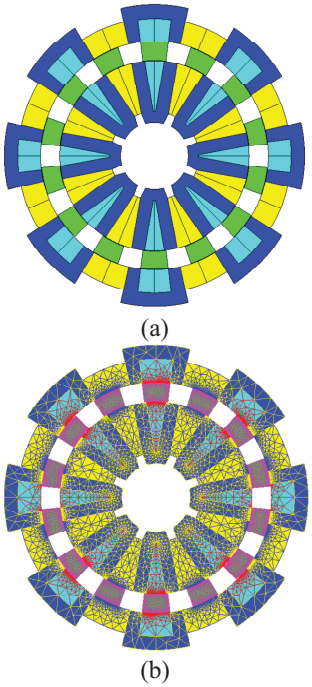
Fig. 5. Diagram of the flux path under NSSN polarity distribution: (a) rotor electromagnetic unalignment position and (b) rotor electromagnetic alignment position.

A comparative look at Figs. 3 and 5 reveals that, without any modification to the stator or rotor structure, simply altering the excitation direction of the inner stator windings enables two distinct magnetic flux paths.

This difference in flux routing gives rise to varying electromagnetic characteristics, which will be examined in detail via finite element analysis in the following section. It is worth noting that SNSN and SNNS represent additional feasible winding polarity configurations. However, since SNSN produces magnetic circuit behavior equivalent to that of NSNS, and SNNS mirrors the effect of NSSN, these two distributions are not addressed in the present study.

III. FINITE ELEMENT MODELLING AND STATIC ELECTROMAGNETIC PERFORMANCE ANALYSIS

To evaluate the performance of the modular double-stator switched reluctance motor under different winding polarity distributions, a two-dimensional finite element model was developed using the commercial simulation software Altair Flux 2020. The established finite element model and its corresponding meshing results are depicted in Fig. 6. Furthermore, the stator and rotor cores are fabricated from 50DW470 silicon steel sheets. The key structural parameters of the motor prototype are summarized in Table 1.



(a)

(b)

Fig. 6. Comparison of non-eccentric and static eccentric structures.

The static magnetic flux line and flux density behaviors are examined first. With the excitation magnetomotive force set to 900 ampere-turns and the excitation direction of the inner and outer stator windings set to be identical, the flux line distributions at the rotor unaligned and aligned positions under the NSNS polarity are reported in Fig. 7. Figure 8 offers the corresponding flux density contour maps for these two rotor positions.

As can be seen from Fig. 7, when the motor operates under the NSNS polarity configuration, a closed long flux loop is formed along the inner U-shaped segmented stator, two adjacent segmented rotor blocks, and the outer U-shaped segmented stator at the rotor aligned position, i.e., the maximum inductance position. A similar closed long loop is likewise observed at the minimum inductance position. The flux density contours presented in Fig. 8 are consistent with the flux line distributions, further confirming this behavior. These findings demonstrate that when the inner and outer stator windings are energized in the same direction, the magnetic flux path within each stator unit assumes a closed annular shape.

Table 1: Parameters of the modular double-stator switched reluctance motor

Motor Parameter	**Unit**	**Value**
Outer stator poles number	/	16
Inner stator poles number	/	16
Rotor poles number	/	14
Outer stator outer diameter	mm	200
Rotor outer diameter	mm	151
Inner stator outer diameter	mm	126
Outer stator yoke thickness	mm	9
Inner stator yoke thickness	mm	7
Outer stator pole arc angle	○	7
Inner stator pole arc angle	○	7
Rotor pole arc angle	○	14
Air-gap length	mm	0.5
Stacking length	mm	100

Additionally, by reversing the excitation directions of the inner and outer stator windings while maintaining the same magnetomotive force of 900 AT, the motor operates under the NSSN polarity distribution. Figure 10 exhibits the corresponding flux density contour maps at these two specific rotor positions.

As revealed in Fig. 9, under the NSSN polarity configuration, a closed short flux loop is formed at the rotor aligned position, i.e., the maximum inductance position, with magnetic flux traveling along the inner U-shaped segmented stator, the segmented rotor, and the outer U-shaped segmented stator, ultimately canceling within the segmented rotor. A similar closed short loop, also characterized by flux cancellation within the segmented rotor, is observed at the minimum inductance position. The flux density contours in Fig. 10 further corroborate these findings. This confirms that when the inner and outer stator windings are energized

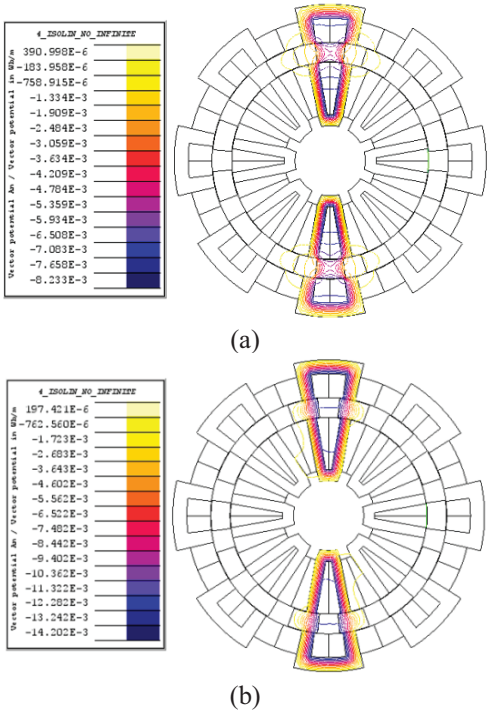


Fig. 7. Magnetic lines distribution at rotor special positions under NSNS polarity distribution: (a) rotor electromagnetic unalignment position and (b) rotor electromagnetic alignment position.

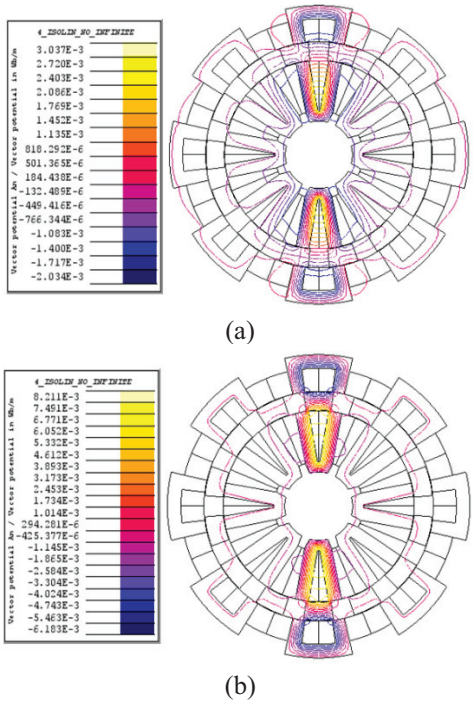


Fig. 9. Magnetic lines distribution at rotor special positions under NSSN polarity distribution: (a) rotor electromagnetic unalignment position and (b) rotor electromagnetic alignment position.

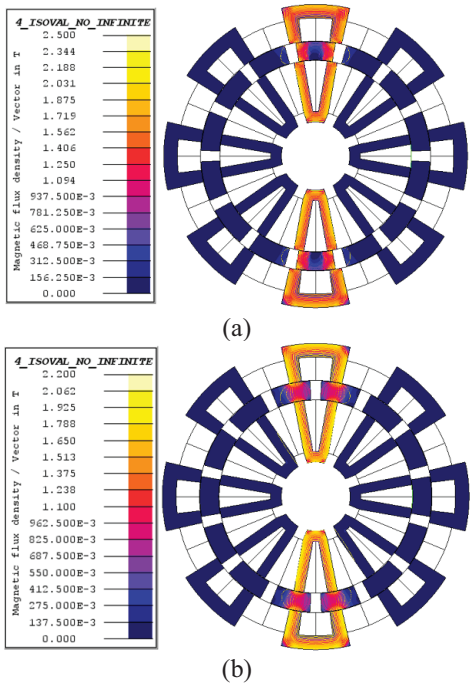


Fig. 8. Magnetic density maps at rotor special positions under NSNS polarity distribution: (a) rotor electromagnetic unalignment position and (b) rotor electromagnetic alignment position.

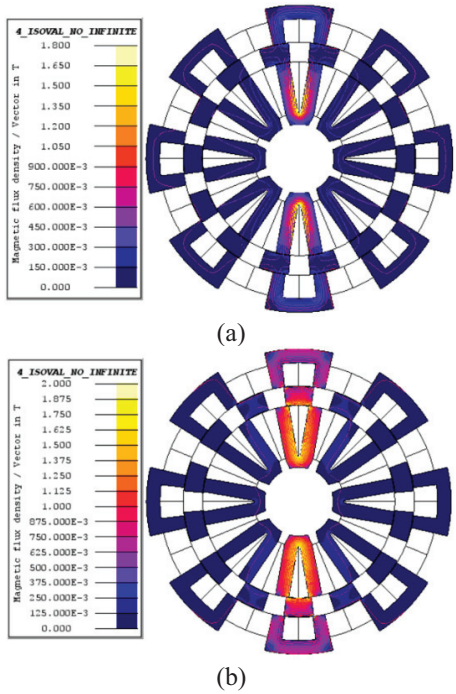


Fig. 10. Magnetic density maps at rotor special positions under NSSN polarity distribution: (a) rotor electromagnetic unalignment position and (b) rotor electromagnetic alignment position.

in opposite directions, the magnetic flux paths cancel each other within the intermediate segmented rotor of each stator unit. Then, the static electromagnetic torque characteristics of the motor are subsequently evaluated. In the finite element simulation, a fixed current was injected into phase A, with the excitation magnitude progressively increased from 20 A to 100 A, while the rotor position was swept from 0 to 180 electrical degrees. The resulting static torque profiles under the NSNS and NSSN polarity distributions are presented in Fig. 11. It can be observed that electromagnetic torque is generated under both winding polarity configurations; however, the torque waveforms exhibit distinct shapes.

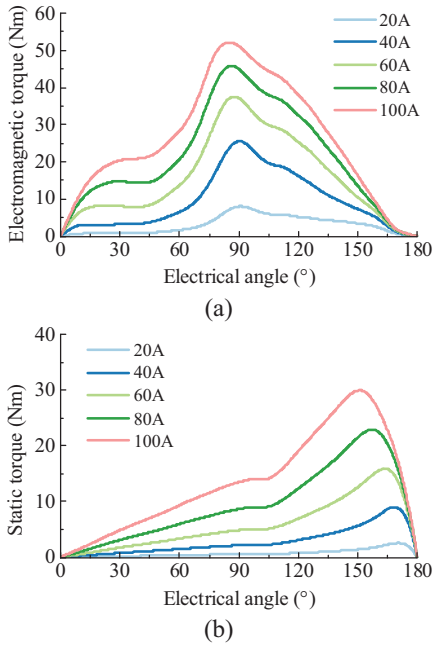


Fig. 11. Static torque waveforms of the motor in two winding polarity arrangement: (a) NSNS and (b) NSSN.

Table 2: Average torque values of the motor in two winding polarity arrangement

Winding Polarity	NSNS	NSSN
20 A	2.893 Nm	0.723 Nm
40 A	9.074 Nm	2.757 Nm
60 A	15.154 Nm	5.642 Nm
80 A	20.476 Nm	9.144 Nm
100 A	25.027 Nm	13.035 Nm

To quantitatively assess the static torque output, the average torque values were computed and are summarized in Table 2. The results indicate that, under the current electromagnetic dimensions, the static electromagnetic torque produced by the NSNS polarity consistently exceeds that of the NSSN polarity, irrespective of the applied excitation current level.

It should be noted that the consistently lower static torque output of the NSSN configuration observed in Fig. 11 and Table 2 is obtained under the baseline rotor pole arc angle of 14°. Under this geometry, the short flux path characteristic of the NSSN arrangement forces the magnetic flux to concentrate within a limited rotor region at the electromagnetically aligned position, as illustrated in Figs. 9 and 10. As the excitation current increases, this localized flux concentration causes the rotor segments to saturate more rapidly, thereby restricting the inductance variation ratio and limiting the torque-producing capability. In contrast, the NSNS configuration establishes a longer flux path that distributes the magnetic field over a larger iron core volume, alleviating local saturation and sustaining higher torque generation. This saturation mechanism explains the distinct torque gap between the two configurations at the baseline rotor geometry.

However, as revealed by the preceding flux path analysis, the magnetic fluxes generated by both the inner and outer stators pass through the inner segmented rotor. It is therefore necessary to investigate the influence of rotor dimensions on the static electromagnetic torque characteristics. It should be noted that rotor geometric parameters exert a significant influence on the electromagnetic performance of switched reluctance motors [17–20]. For the sector-shaped rotor employed in this modular double-stator configuration, both the rotor pole arc angle and the rotor radial thickness collectively determine the overall rotor dimensions and magnetic characteristics. To evaluate the sensitivity of motor performance to these key rotor geometric parameters, this section investigates the influence of the rotor pole arc angle and the rotor radial thickness on the static torque characteristics under both winding polarity configurations.

Firstly, parametric studies were conducted in the finite element software by varying the rotor pole arc angle from 10° to 20°, to observe the corresponding static torque behavior under the two winding polarity distributions. The resulting torque profiles are presented in Fig. 12. It is evident that the rotor pole arc angle exerts a substantial influence on the electromagnetic torque output. To further quantify the performance differences, Table 3 provides a comparative summary of the average static torque values under the two polarity configurations. Notably, as the rotor pole arc angle increases, the static electromagnetic torque under NSNS polarity exhibits a decreasing trend, whereas that under NSSN polarity increases progressively. When the rotor pole arc angle β_r is less than 19°, the torque produced by NSNS exceeds that of NSSN. However, once β_r reaches

20°, the NSSN configuration yields higher torque than NSNS.

The results in Figs. 12–13 and Table 3 further reveal that the rotor pole arc angle exerts a pronounced and opposite influence on the static torque of the two winding configurations. As the rotor pole arc angle β_r increases, the NSNS configuration experiences a progressive decrease in static torque, whereas the NSSN configuration exhibits a substantial torque increase. This behavior can be understood through the saturation mechanism discussed above. A larger rotor pole arc angle widens the rotor segment, which effectively reduces the magnetic flux density within the short flux path region of the NSSN configuration. The resulting alleviation of local saturation enhances the inductance variation ratio and boosts the torque-producing capability. Conversely, for the NSNS configuration, an excessively large rotor pole arc angle increases the overlap between adjacent rotor segments and the stator poles in the long flux path, which reduces the rate of change of inductance and diminishes the torque output. This explains why the torque ranking between the two configurations reverses when the rotor pole arc angle exceeds a certain threshold, underscoring the critical role of rotor geometry in determining the performance characteristics of the motor under each winding polarity configuration.

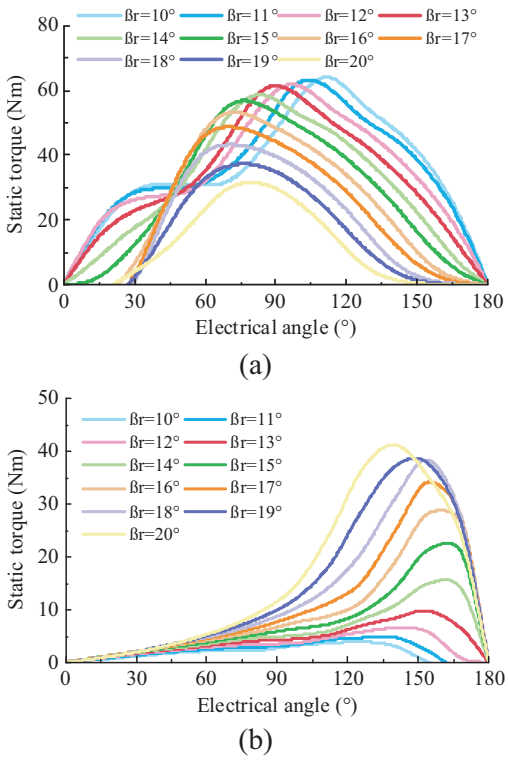


Fig. 12. Static torque waveforms variation with rotor pole arc angle in the two winding polarity arrangement: (a) NSNS and (b) NSSN.

Table 3: Average torque values variation with rotor pole arc angle in two winding polarity arrangement

Winding Polarity	NSNS	NSSN
$\beta_r = 15°$	25.751 Nm	7.053 Nm
$\beta_r = 16°$	22.396 Nm	8.733 Nm
$\beta_r = 17°$	19.531 Nm	10.326 Nm
$\beta_r = 18°$	16.307 Nm	11.885 Nm
$\beta_r = 19°$	13.416 Nm	13.296 Nm
$\beta_r = 20°$	10.424 Nm	14.504 Nm

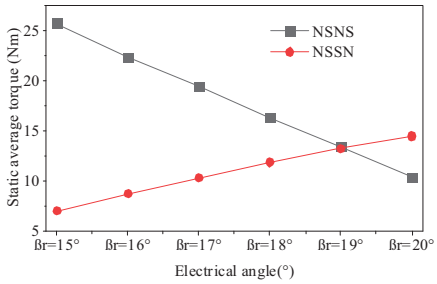


Fig. 13. Static torque waveforms variation with rotor pole arc in two working modes of the motor.

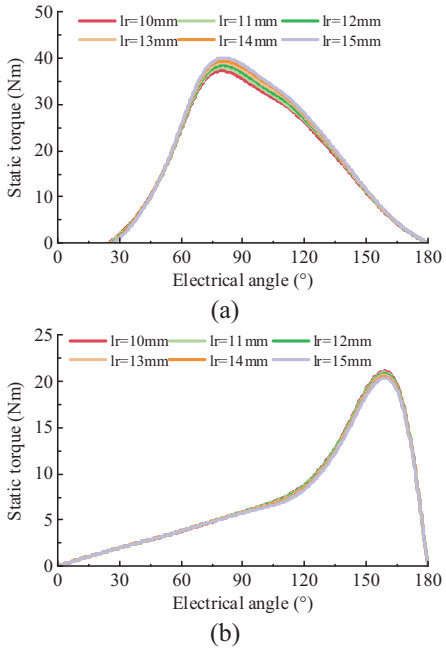


Fig. 14. Static torque waveforms variation with rotor thickness in the two winding polarity arrangement: (a) NSNS and (b) NSSN.

Furthermore, the rotor radial thickness l_r was varied from 10 mm to 15 mm. Figure 14 presents the static torque waveforms for both NSNS and NSSN winding polarity configurations as a function of rotor radial

thickness. It can be observed that for both configurations, variations in rotor radial thickness produce only minor changes in the static torque waveforms. This behavior differs notably from the pronounced influence of the rotor pole arc angle previously discussed. The limited sensitivity to rotor radial thickness can be understood from the saturation perspective established above: the radial thickness primarily affects the rotor yoke cross-sectional area along the radial direction, which is not the dominant constraint on the main flux path in either configuration. In the NSSN configuration, saturation is predominantly governed by the circumferential flux concentration within the rotor teeth region, while in the NSNS configuration, the longer flux path inherently distributes the magnetic field over a sufficient core volume. Therefore, increasing the rotor radial thickness within the investigated range contributes little to relieving the flux bottlenecks that limit torque production. These results indicate that while rotor geometry does affect the static performance of the motor, the rotor pole arc angle exerts a considerably stronger influence than the rotor radial thickness. To further evaluate the practical performance differences between the two winding configurations, the dynamic electromagnetic characteristics are investigated in the following section.

IV. DYNAMIC ELECTROMAGNETIC PERFORMANCE ANALYSIS

While the static torque analysis in the previous section reveals the inherent torque capability of the two winding polarity configurations, a dynamic performance assessment is essential for practical motor evaluation. Accordingly, this section investigates the dynamic torque response, torque ripple, and efficiency characteristics under both NSNS and NSSN polarity configurations across a range of operating speeds and load torques.

As a representative operating point, the dynamic torque behavior is first evaluated at a constant speed of 600 r/min with a DC bus voltage of 48 V. The drive was operated under single-pulse control (SPC) mode, with a conduction angle ranging from 0° to 6.43°. The rotor pole arc coefficient β_r was varied from 15° to 20°. Figure 15 presents the dynamic electromagnetic torque waveforms under both winding configurations as a function of the rotor pole arc coefficient for this operating condition. It can be observed from Fig. 15 that as the rotor pole arc angle β_r increases, the dynamic torque waveform under the NSNS polarity configuration exhibits a decreasing trend. In contrast, the dynamic torque under the NSSN polarity configuration is negatively correlated with the value of β_r. To provide a clearer qualitative and quantitative evaluation of the dynamic performance of the motor under the two winding configurations, the calculated results of average torque, torque ripple, core loss, copper loss, and efficiency are summarized in Table 4.

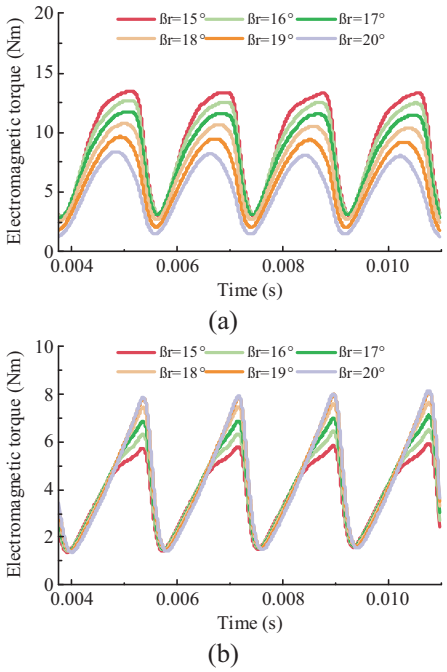


Fig. 15. Transient electromagnetic torque waveforms variation with rotor thickness in the two winding polarity arrangement: (a) NSNS and (b) NSSN.

Table 4: Results of the dynamic performance of the motor at 600 r/min under two different winding polarities

Winding Polarity	**NSNS**	**NSSN**		
Rotor pole arc	$\beta_r = 15°$	$\beta_r = 18°$	$\beta_r = 15°$	$\beta_r = 18°$
Average torque (Nm)	9.19	7.23	4.45	5.12
Torque ripple (%)	119.8	117.2	114.0	136.3
Electromagnetic power (W)	577.1	454.4	279.3	325.5
Power density (W/kg)	70.38	55.41	34.06	39.70
Copper loss (W)	150.8	129.5	77.6	72.3
Iron loss (W)	55.0	47.2	28.3	26.4
Efficiency (%)	73.7	72.0	72.5	76.5

As indicated in Table 4, at a speed of 600 r/min, the average torque values of the NSNS configuration at rotor pole arc angles of 15° and 18° are 9.19 Nm and 7.23 Nm, respectively. Under the same rotor pole arc angles, the NSSN configuration yields average torque values of 4.45 Nm and 5.12 Nm, respectively. Consequently, the NSNS configuration delivers higher average torque and electromagnetic power than the NSSN configuration. Nevertheless, the NSSN configuration exhibits relatively

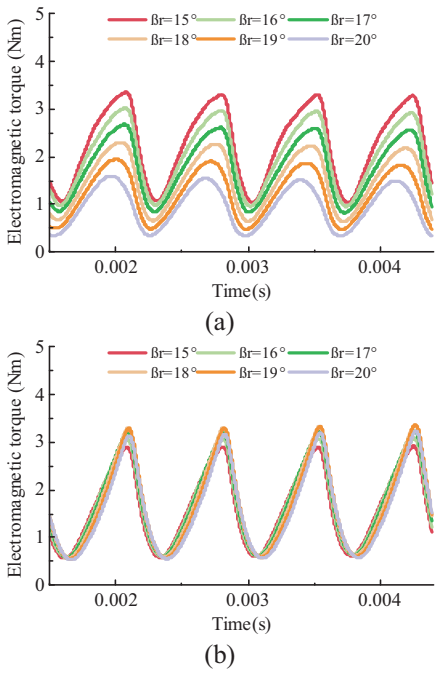


Fig. 16. Transient electromagnetic torque waveforms variation with rotor thickness in the two winding polarity arrangement: (a) NSNS and (b) NSSN.

lower copper loss and core loss. At a rotor pole arc angle of 18°, its operating efficiency reaches 76.5%, which is superior to the 72.0% efficiency of the NSNS configuration. It is also evident that the rotor pole arc angle exerts a pronounced influence on the performance of both winding configurations. When the rotor pole arc angle is 15°, the power density of the NSNS configuration exceeds that of the NSSN configuration by 106.6%; when the rotor pole arc angle increases to 18°, the advantage of the NSNS configuration reduces to only 39.6%. Subsequently, the speed was increased to 1500 r/min while maintaining the same applied voltage, control mode, and phase conduction width. Figure 16 presents the dynamic torque waveforms for the two winding configurations as a function of the rotor pole arc angle β_r. Similar to the trend observed in Fig. 15, the dynamic torque waveform of the NSNS configuration is positively correlated with the rotor pole arc angle β_r, whereas that of the NSSN configuration exhibits a negative correlation with β_r. The corresponding calculated results of average torque, torque ripple, losses, and efficiency at 1500 r/min are listed in Table 5.

As shown in Table 5, at a speed of 1500 r/min and a rotor pole arc angle of 15°, the average torque values of the NSNS and NSSN configurations are 2.24 Nm and 1.65 Nm, respectively, indicating a higher torque output for the NSNS configuration. However, at a rotor pole arc angle of 18°, the average torque of the NSNS configuration is 1.48 Nm, which falls below the 1.72 Nm produced by the NSSN configuration. This further confirms the significant influence of the rotor pole arc angle on motor performance. Additionally, the NSSN configuration exhibits relatively lower copper loss and core loss. At a rotor pole arc angle of 18°, its operating efficiency reaches 84.1%, exceeding the 80.8% efficiency of the NSNS configuration.

Table 5: Results of the dynamic performance of the motor at 1500 r/min under two different winding polarities

Winding Polarity	**NSNS**	**NSSN**		
Rotor pole arc	$\beta_r = 15°$	$\beta_r = 18°$	$\beta_r = 15°$	$\beta_r = 18°$
Average torque (Nm)	2.24	1.48	1.65	1.72
Torque ripple (%)	108.6	116.4	152.1	174.9
Electromagnetic power (W)	351.61	231.89	259.13	270.86
Power density (W/kg)	42.88	28.28	31.60	33.03
Copper loss (W)	36.9	28.7	31.6	26.8
Iron loss (W)	33.6	26.2	28.8	24.4
Efficiency (%)	83.3	80.8	81.1	84.1

In summary, based on the comparison of dynamic performance under different operating conditions, it can be concluded that the two winding configurations each possess distinct advantages. Generally, the NSNS configuration can produce higher torque output, while the NSSN configuration offers lower losses and higher efficiency. Therefore, the appropriate winding configuration should be selected according to the specific application requirements. The NSNS configuration is better suited for low-speed high-torque scenarios, whereas the NSSN configuration demonstrates superior efficiency under high-speed operating conditions. It should also be emphasized that the rotor pole arc angle exerts a substantial influence on motor performance. To maximize the potential of each configuration, a relatively small rotor pole arc coefficient is recommended for the NSNS configuration, while a larger rotor pole arc coefficient is preferable for the NSSN configuration.

V. CONCLUSION

This paper investigated the influence of winding polarity distribution on modular double-stator switched reluctance motor performance. Two polarity configurations, NSNS and NSSN, were realized by varying the excitation direction of the inner and outer stator windings. Finite element analysis was employed to compare flux paths, static torque, and dynamic performance including losses and efficiency. Results show that the NSNS configuration yields higher torque output, exceeding the NSSN configuration by 106.6% at 600

r/min with 15° rotor pole arc angle. Conversely, the NSSN configuration exhibits lower losses and achieves an efficiency of 84.1% at 1500 r/min with 18° rotor pole arc angle, outperforming the NSNS configuration by 3.3 percentage points. The rotor pole arc angle exerts opposite influences on torque for the two configurations, with NSNS torque decreasing and NSSN torque increasing as the pole arc angle grows. These findings indicate that the NSNS configuration is better suited for low-speed high-torque applications, while the NSSN configuration offers advantages in high-speed high-efficiency scenarios. The appropriate winding configuration and rotor pole arc angle should therefore be selected according to specific application requirements.

ACKNOWLEDGMENT

This work is supported by the National Natural Science Foundation of China International (regional) cooperation and exchange projects NSFC-RSF (W2412064), the Basic Research Program of Jiangsu Province (BK20251662), the China Postdoctoral Science Foundation (2024M763541), the Jiangsu Provincial Market Supervision Administration Science and Technology Plan Project (KJ2025017), and the Jiangsu Funding Program for Excellent Postdoctoral Talent (2024ZB008).

REFERENCES

[1] A. Hasnain, A. Somiruwan Gamwari, R. Resalayyan, K. Farokhi Sadabadi, and A. Khaligh, "Medium- and heavy-duty vehicle electrification: Trends and technologies," *IEEE Transactions on Transportation Electrification*, vol. 11, no. 1, pp. 3602–3616, Feb. 2025.

[2] P. Upadhyay and R. K, "Design of two-phase switched reluctance motor (SRM) for two-wheel electric vehicle and torque-density based comparison with three-phase SRM," *IEEE Transactions on Industry Applications*, vol. 60, no. 3, pp. 3912–3919, May–June 2024.

[3] A. Kumar, B. Singh, and G. Singh, "Modified direct torque control of solar fed sensorless switched reluctance motor drive for electric vehicle with regenerative braking," *IEEE Transactions on Industry Applications*, vol. 60, no. 2, pp. 3155–3164, Mar.–Apr. 2024.

[4] X. Shan, C. Gan, H. Ren, C. Zhang, H. Wang, J. Sun, S. Wang, and R. Qu, "Phase current reconstruction for Y-type converter fed switched reluctance motors drive with fault-tolerant ability," *IEEE Transactions on Power Electronics*, vol. 41, no. 4, pp. 4909–4920, Apr. 2026.

[5] W. Yan, H. Chen, S. Liao, Y. Liu, and H. Cheng, "Design of a low-ripple double-modular-stator switched reluctance machine for electric vehicle applications," *IEEE Transactions on Transportation Electrification*, vol. 7, no. 3, pp. 1349–1358, Sep. 2021.

[6] X. Sun, K. Diao, G. Lei, Y. Guo, and J. Zhu, "Study on segmented-rotor switched reluctance motors with different rotor pole numbers for BSG system of hybrid electric vehicles," *IEEE Transactions on Vehicular Technology*, vol. 68, no. 6, pp. 5537–5547, June 2019.

[7] W. Sun, Q. Li, L. Sun, and X. Jiang, "Study on magnetic shielding for performance improvement of axial-field dual-rotor segmented switched reluctance machine," *CES Transactions on Electrical Machines and Systems*, vol. 5, no. 1, pp. 50–61, Mar. 2021.

[8] G. Davarpanah, J. Faiz, H. Shirzad, and M. Lotfizadeh, "A modular hybrid excited switched reluctance motor with two groups of permanent magnets to enhance the performance of the motor," *IEEE Transactions on Energy Conversion*, vol. 39, no. 3, pp. 1686–1698, Sep. 2024.

[9] R. Jayarajan, N. Fernando, and I. U. Nutkani, "A review on variable flux machine technology: Topologies, control strategies and magnetic materials," *IEEE Access*, vol. 7, pp. 70141–70156, 2019.

[10] X. An, G. Liu, Q. Chen, and X. Sun, "New cost function design for robustness deadbeat model predictive control of a five-phase PMSM," *IEEE Transactions on Transportation Electrification*, vol. 11, no. 6, pp. 13934–13946, Dec. 2025.

[11] B. S. Abdel-Mageed, A. M. Aljehaimi, and P. Pillay, "Analysis of design topologies for variable flux permanent magnet motors," *IEEE Transactions on Industry Applications*, vol. 62, no. 1, pp. 939–955, Jan.–Feb. 2026.

[12] H. Hua, Z. Zhou, and W. Hua, "Investigation of dual-effect air-gap field regulation mechanism in variable flux memory machines," *IEEE Transactions on Industrial Electronics*, vol. 71, no. 8, pp. 8571–8580, Aug. 2024.

[13] L. Sun, H. Vansompel, Z. Zhang, and P. Sergeant, "Winding configurations of a switched reluctance generator system excited by circulating current," in *2022 International Conference on Electrical Machines (ICEM)*, Valencia, Spain, pp. 2067–207, 2022.

[14] X. Y. Ma, G. J. Li, G. W. Jewell, and Z. Q. Zhu, "Recent development of reluctance machines with different winding configurations, excitation methods, and machine structures," *CES Transactions on Electrical Machines and Systems*, vol. 2, no. 1, pp. 82–92, Mar. 2018.

[15] S. Pal, D. Roy, M. W. Rahaman, and M. Sengupta, "Investigations on vibration studies of a 4-phase double-sided axial flux switched reluctance motor with different terminal connections," in *2022 IEEE International Conference on Power Electronics, Drives and Energy Systems (PEDES)*, Jaipur, India, pp. 1–6, 2022.

[16] F. Ni, S. Niu, Z. Li, and X. Zhao, "Novel electrically excited doubly salient variable reluctance machine with high-order-harmonic winding," *IEEE Transactions on Magnetics*, vol. 59, no. 11, pp. 1–6, Nov. 2023.

[17] W. Yan, J. Hu, H. Li, H. Chen, Y. Wang, and Q. Wang, "Research on high-performance control method of double-stator switched reluctance generator," *IEEE/ASME Transactions on Mechatronics*, vol. 31, no. 2, pp. 1254–1264, Apr. 2026.

[18] B. Gecer, N. F. O. Serteller, and A. N. Akpolat, "Comprehensive analysis and measurements of switched reluctance motor," *Insight - Non-Destructive Testing and Condition Monitoring*, vol. 68, no. 1, pp. 54–60, Jan. 2026.

[19] H. Chen, C. Liu, X. Wang, N. Korovkin, S. Liudmila, P. S. Olegovich, and B. E. Alexandrovich, "Mathematical modeling and electromagnetic force analysis of novel tubular linear rotary switched reluctance machine," *IEEE Transactions on Plasma Science*, vol. 54, no. 1, pp. 270–278, Jan. 2026.

[20] S. Hussain, A. Kallaste, M. U. Naseer, H. Tiismus, M. Sarap, B. Asad, and T. Vaimann, "Design and prototyping of additively manufactured axial flux switched reluctance machine," *IEEE Transactions on Industry Applications*, vol. 62, no. 2, pp. 2587–2597, Mar.–Apr. 2026.



Fengyuan Yu received the Ph.D. degree from the School of Electrical Engineering, China University of Mining and Technology, Xuzhou, China, in 2023, where he was a Post-Doctoral Researcher from 2023 to 2026. Since 2026, he has been a Lecturer with the School of Electrical Engineering and Automation, Jiangsu Normal University, Xuzhou. His research interests include switched reluctance drive, special motor design, power converters, and motor control.



Hao Chen received his B.S. and Ph.D. degrees from the Department of Automatic Control, Nanjing University of Aeronautics and Astronautics, Nanjing, China, in 1991 and 1996, respectively. In 1998, he became an Associate Professor with the School of Information and Electrical Engineering, China University of Mining and Technology, Xuzhou, where he has been a Professor since 2001. From 2002 to 2003, he was a Visiting Professor at Kyungsung University, Busan, Korea. Since 2008, he has also been an Adjunct Professor at the University of Western Australia, Perth, Australia. He is the author of one book and has also authored more than 190 papers. He is the holder of 14 US Patents, 23 Australian Patents, one Danish Patent, seven Canadian Patents, three South African Patents, 10 Russian Patents, 44 Chinese Invention Patents and six Chinese Utility Model Patents. His current research interests include motor control, linear launcher, electric vehicles, electric traction, servo drives, and wind power generator control.

Chen was the recipient of both the Prize of Science and Technology of Chinese Youth and the Prize of the Fok Ying Tong Education Foundation for Youth Teachers in both 2004. He was awarded the first prize in the Science and Technology advanced of Province and Ministry once, the second prize in the Science and Technology advanced of Province and Ministry seven times, and the third prize in the Science and Technology advanced of Province and Ministry 14 times. He became the Chinese New Century Hundred-Thousand Ten-Thousand Talents Engineering National Talent in 2007 and won the Government Especial Allowance of People's Republic of China State Department in 2006.



Haidong Yan was born in May 1982. He has a master's degree in System Analysis and Integration from Nanjing University of Information Science & Technology, China. He is a Senior Engineer currently serving as the deputy director of Wuxi Institute of Inspection, Testing, and Certification. His research direction mainly focuses on electromagnetic metrology, new energy vehicle specialized metrology, and testing technology.



Guanjun Wang, male, born in September 1986, master's degree in Electronic and Communication Engineering from China University of Mining and Technology, China. Senior Engineer. Currently serving as the director of Electrical and Information M&R Department of Wuxi Institute of Inspection, Testing, and Certification. His research direction mainly focuses on electromagnetic metrology, new energy vehicle specialized metrology and testing technology.



Jun Bao was born in August 1971. He is a Full Senior Engineer, currently serving as the director of Wuxi Institute of Inspection, Testing and Certification, China. His primary research areas include inspection and testing technologies for new energy vehicles, as well as metrological test technologies.

A Dual-Port Integrated Switched Reluctance Motor Power Converter for Electric Vehicles With Flexible Braking and Energy Recovery

Chenhe Zhang[1], Hao Chen[1], Olimjon Toirov[2], Sherif Moussa[3], Habes Ali Khawaldeh[4], Marcin Wardach[5], Sergei Brovanov[6], Ali Asghar Memon[7], Emmanuel Karapidakis[8], and Aris Dimeas[9]

[1]School of Electrical Engineering
China University of Mining and Technology, Xuzhou 221116, China
1364573229@qq.com, hchen@cumt.edu.cn

[2]Tashkent State Technical University
University Street No2, 100095 Tashkent, Uzbekistan
olimjon.t@mail.ru

[3]School of Engineering
Canadian University Dubai, Dubai, UAE 117781, Sheikh Zayed Road, Dubai, United Arab Emirates
smoussa@cud.ac.ae

[4]The Renewable Energy Engineering Department
Faculty of Engineering, Al al-Bayt University, Mafraq, Jordan
habes.a.khawaldeh@aabu.edu.jo

[5]West Pomeranian University of Technology
Sikorskiego 37, 70-313 Szczecin, Poland
Marcin.Wardach@zut.edu.pl

[6]Novosibirsk State Technical University
Novosibirsk 630073, Russia
brovanov@corp.nstu.ru

[7]Mehran University of Engineering and Technology
Electrical Engineering, Jamshoro, Pakistan
Pakistanali.asghar@faculty.muet.edu.pk

[8]School of Engineering
Hellenic Mediterranean University, Estavromenos Campus, 71004 Heraklio, Crete, Greece

[9]Athens National University of Technology
Greece
*Corresponding author

Abstract – As environmental protection increasingly becomes a global focus, new energy vehicles have gradually emerged as a rising star in the modern transportation sector. They not only represent technological innovation but also carry the hope of achieving sustainable mobility. This paper proposes a novel dual-port integrated power converter, consisting of a front-end circuit and a traditional asymmetric half-bridge converter. By changing the operating state of the front-end circuit's switch transistors, different operating modes can be switched. In the motoring state, there are single-power supply mode and hybrid power supply mode, and the converter is reconfigured into a five-level converter. In the regenerative braking mode, there are moderate braking mode and severe braking mode, and energy recovery can be achieved in both modes, with the converter being reconfigured into a four-level converter. The power converter proposed in this paper can accommodate wide speed range regulation for both electric and braking operations, while also recovering energy from

Submitted On: January 18, 2026
Accepted On: June 10, 2026

1054-4887 © ACES

https://doi.org/10.13052/2026.ACES.J.410609

regenerative braking. It has been simulated and verified on a three-phase 12/8 switched reluctance motor, confirming its practicality and effectiveness.

Index Terms – Multilevel, regenerative braking, switched reluctance motor.

I. INTRODUCTION

Against the backdrop of actively addressing climate change and vigorously promoting energy transformation worldwide, electric vehicles are like a rising star, rapidly becoming the mainstream direction of the automotive industry's development with their significant advantages of cleanliness, environmental protection, high efficiency, and energy conservation, leading the transportation sector to accelerate towards a green, intelligent, and sustainable future. As one of the components of the power system of electric vehicles, the motor plays an extremely important role. The strong magnetic field characteristics of the permanent magnet in the permanent magnet synchronous motor make its structure more compact and capable of outputting greater power in a limited space, which is very suitable for the lightweight and high power needs of electric vehicles. However, its core cost lies in the permanent magnet, which is greatly affected by the high cost of rare earths. Thus, there is an urgent need for a rare earth free motor, and switched reluctance motors (SRMs) have received widespread attention in this field. The rotor has no permanent magnets and windings, and is made of stacked silicon steel sheets. The stator winding structure is simple, with a low failure rate and almost no maintenance required, which enables it to be applied in scenarios such as high speed, high temperature, and high torque.

SRM drive topology with multi-power supply and multi-port has the characteristics of integration, high reliability, and strong applicability, which has gradually attracted the attention of scholars and engineers. In addition, in high-speed operation, the traditional SRM drive system is usually limited by the constant DC bus voltage, which makes the excitation and demagnetization voltage fixed, and it is difficult to realize the rapid excitation and demagnetization of the winding, thus affecting the efficiency, output energy, and dynamic performance of the motor system. A multilevel power conversion circuit can realize the fast excitation and demagnetization of windings, which is an effective scheme to improve the driving performance of SRM [1].

Ali and Narimani suggested an eight-leg asymmetric three-level power converter, which divides the batteries into two groups and produces a similar working mode as the traditional three-level asymmetric converter. It has improved performance, reduced size, and is different from the series connected single battery pack. The proposed battery pack separate connection provides flexible control and fault tolerance for SRM driver [2]. Hu et al. proposed a SRM drive system for electric vehicles based on battery/super capacitor. The system has G2V and V2H/V2G functions. The power circuit of the motor drive system is composed of bidirectional two quadrant front-end DC/DC converter and SRM asymmetrical bridge converter. Through reasonable control and key parameter setting, good acceleration/deceleration, reversible drive, and braking characteristics are obtained [3]. A highly integrated modular converter for SRM of extended range electric vehicle is proposed by Xia and Bauman [4]. The converter can be realized by a standard industrial switch module, and can flexibly realize the energy conversion between SRM, battery, generator, and external AC power supply through front-end circuit. In the battery driven mode, the capacitor in parallel with the generator is naturally charged and discharged, which improves the phase voltage, accelerates the excitation and demagnetization process of SRM, and improves the torque capacity of SRM. In the generator driven mode, the battery also participates in the rapid excitation and demagnetization of SRM.

Yu et al. suggested a simplified dual-port driver for flux modulated SRM with flexible charging capability for electric vehicle applications in [5]. Using modular three-phase converter and auxiliary battery, the corresponding pulse width modulation (PWM) control method was studied, and a current regulator based on VPI was proposed, which further improved the performance of the motor, realized flexible power control and battery charging, and a variety of driving and charging modes. Phase current regulation of SRMs driven by traditional asymmetric half-bridge power converters (AHB) is limited by the supply voltage. Thus an improved capacitor voltage self-balancing active boost power converter is proposed by Han and Chen in [6]. The problems of an AHB power converter in different phases of each phase current were analyzed, the different working modes of the converter were studied, and the corresponding control strategies implemented.

A motor driver for a four-phase SRM with only two current sensors is presented in [7]. The driver uses an asymmetric half-bridge circuit, but each current of the two windings is detected by a current sensor, which enables the proposed SRM driver to provide additional charge/discharge functions without adding any additional circuit elements. Additional current sensors, implementation of the integrated driver, and proof of the results is provided. A modular three-port converter with simple structure is proposed in [8], which organically combines the generator, battery, and SRM. A

bidirectional front-end circuit with a photovoltaic (PV) power supply is designed in [9], which integrates the electrical components into a converter and realizes six driving modes and five charging modes to obtain multilevel voltage and increased torque capacity. A highly integrated solar assisted SRM drive system, which has the functions of electric drive reconfiguration of G2V and V2G/V2L, realizes flexible and efficient multi-mode energy transmission between SRM, battery pack, solar PV panel, and AC grid in [10]. In order to extend the driving range of electric vehicles, the use of PV panels on vehicles helps to reduce the dependence on on-board batteries. Based on the phase winding characteristics of SRM, a three-port converter is used to control the energy flow between PV cells, batteries, and SRMs in [11].

This paper is structured as follows. Section II introduces the components of the power converter. Section III gives its various working states and characteristics. Section IV is simulation verification, and section V draws conclusions.

II. STRUCTURE AND PERFORMANCE ANALYSIS OF THREE-PHASE SRM

The stator and rotor of SRM are of salient pole structure and are laminated by silicon steel sheets (reducing iron consumption). The rotor has no windings and permanent magnets, and the structure is simple and reliable. Single-phase, two-phase, three-phase, and four-phase structures are common, and three-phase SRM is the most widely used. The winding current is a unidirectional pulse current, which is provided by the power converter [12]. According to the law of conservation of energy and the law of electromagnetic induction, the voltage applied to each stator winding is equal to the sum of the resistance voltage drop and the induced electromotive force generated due to the change of flux linkage, and the relationship between the voltage, current, and flux linkage of phase k of the motor is:

$$U_s = i_k R + \frac{d\psi k}{dt}. \tag{1}$$

When the given excitation current is high, the electromagnetic characteristics will show nonlinearity due to the saturation of the magnetic core. In general, for the convenience of calculation, the mutual inductance between the windings of SRM is often not considered. The magnetic circuit and inductance are functions of current and rotor position. Flux linkage can be calculated by the product of winding inductance and current:

$$\psi_k = \psi_k(i_k, \theta) = L_k(i_k, \theta) i_k. \tag{2}$$

Combining Equations (1) and (2), there is an electric potential balance equation:

$$U_s = \left(L_k + i_k \frac{dl_k}{di_k} \right) \frac{di_k}{dt} + i_k \frac{dl_k}{d\theta} \frac{d\theta}{dt} + i_k R. \tag{3}$$

Equation (3) reveals that the terminal voltage of each phase winding in a SRM is balanced by three distinct voltage components within the circuit: the resistive voltage drop, the transformer electromotive force, and the motional electromotive force [13].

Given the magnetic circuit nonlinearity inherent in SRMs, the electromagnetic torque at an arbitrary operating point can be derived via the principle of virtual displacement – specifically, as the partial derivative of the magnetic co-energy with respect to the rotor position – and is expressed by:

$$T(\theta, i) = \frac{\partial W'(\theta, i)}{\partial \theta} = \frac{1}{2} i^2 \frac{dL}{d\theta}. \tag{4}$$

Combined with the piecewise linear model of inductance, the torque expression of each interval can be further derived. In non-overlapping/aligned areas, $\frac{dL}{d\theta} = 0$. Torque is zero. In overlapping areas:

$$\frac{dL}{d\theta} = \frac{L_{\max} - L_{\min}}{\theta_2 - \theta_1} = \mathrm{C}, \tag{5}$$

where C is a constant and torque is proportional to the square of the current. In addition, the equation of mechanical motion of the motor is:

$$J \frac{d\omega}{dt} = T_e - H\omega - T_L, \tag{6}$$

where J, H, ω, T_e, and T_L are moment of inertia, viscous coefficient, rotor angular velocity, electromagnetic torque, and load torque, respectively [14].

Let us take the 12/8 three-phase SRM (12-pole stator, 8-pole rotor, three-phase concentrated winding) as an example (see Fig. 1). Its core advantages lie in the stability of operation, fault tolerance, structural reliability, and wide speed regulation range. The stepping angle is 15° (half of 30° compared with 6/4 three-phase SRM), torque superposition is more continuous, fundamental frequency of torque ripple is increased, and low-speed stepping sense is weakened, which is conducive to improving the stability of operation and reducing vibration and noise [15].

Figure 2 shows a 3D diagram of a 12/8 three-phase SRM static flux linkage. The data in Fig. 2 is obtained through simulation in ANSYS, in which the current is simulated at the interval of 0 A to 100 A, and the rotor position is simulated at the interval of 0° to 45°. Intermediate data points are obtained by linear interpolation method. As can be seen from Fig. 2, the

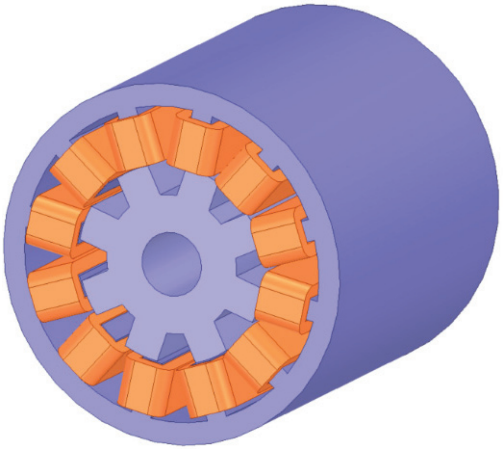


Fig. 1. Three-phase 12/8 SRM structure.

minimum value of the flux linkage appears in the fully misaligned position, while the maximum value appears in the fully aligned position. Flux linkage increases gradually in the range $0-22.5^\circ$ and decreases gradually in the range $22.5-45^\circ$.

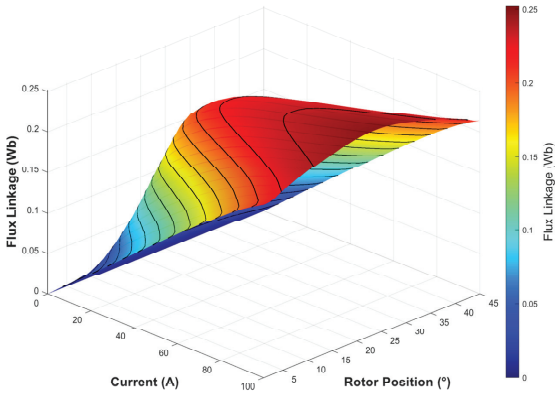


Fig. 2. Three-dimensional view of the static flux linkage of 12-8 SRM.

Figure 3 shows a three-dimensional view of its static torque. The data in Fig. 3 is obtained through ANSYS finite element simulation, in which the current simulation interval is 0 A to 100 A, the rotor position simulation interval is 0° to 45°, and the rotor angle cycle is 45°. It can be seen from Fig. 3 that the static torque of SRM is positive in the range $0-22.5^\circ$ and negative in the range $22.5-45^\circ$.

Figure 4 illustrates the variations in static torque and flux linkage of the SRM under single-phase excitation, with both parameters characterized across different rotor angles and winding currents. It is evident that the flux linkage magnitude of the SRM increases alongside the winding current during the rotor's movement from the unaligned to the aligned position relative to the excited

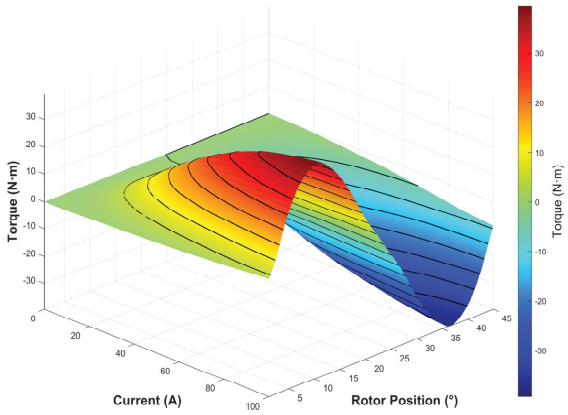


Fig. 3. Three-dimensional view of static torque of 12/8 SRM.

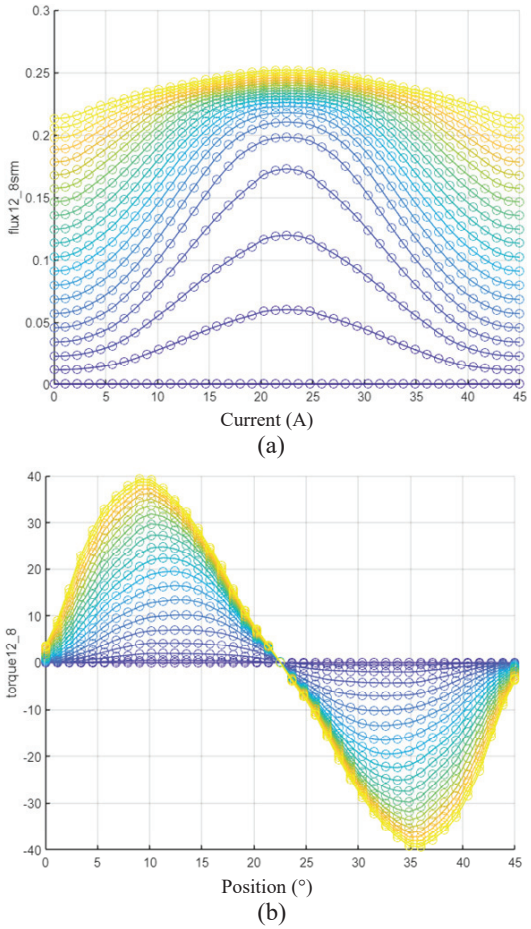


Fig. 4. Phase torque and phase flux linkage at different angles and currents: (a) static flux linkage line curve and (b) static torque curve.

stator pole. In particular, flux linkage at the unaligned position exhibits a linear relationship with the current, which indicates that the motor operates in a magnetically unsaturated state under this condition.

III. DRIVING CHARACTERISTICS OF DUAL-PORT INTEGRATED SRM POWER CONVERTER

Figure 5 shows the topology of the dual-port integrated SRM power converter proposed in this paper for a three-phase 12/8 structure SRM. It is mainly composed of front-end circuit and traditional AHB, taking into account the electric and braking states of electric vehicle operation, and can achieve energy recovery in the braking state. The front-end circuit includes four switch tubes, two diodes, a power supply, and a power battery. By controlling the on and off of the front-end circuit switch tubes, multiple functions and operating modes of the electric vehicle can be achieved. The electric vehicle power system based on SRM is shown in Fig. 6 [15].

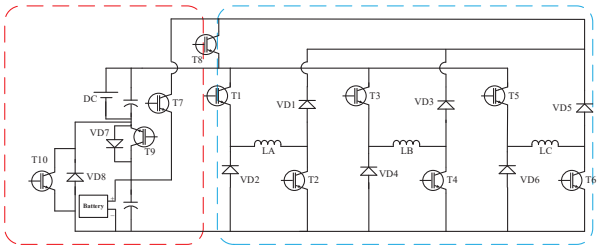


Fig. 5. Topology of dual-port integrated SRM converter.

The power converter proposed in this paper includes electric mode, multilevel mode, and hybrid power mode of power battery. Due to the addition of multilevel mode, the output torque and load capacity of the motor have been significantly improved. In the power drive mode, the battery does not participate in power supply, but rapid demagnetization can be achieved by increasing the demagnetization voltage through series connection of batteries. In hybrid driving mode, the motor is driven in series by a power source and a battery to improve its dynamic performance [16]. The power supply and battery can be matched according to different working conditions to improve dynamic performance. In addition, in the braking state, it is possible to achieve two modes of braking while also considering energy recovery. Moderate braking is excited by the power supply alone, and the battery recovers energy. Heavy braking is excited by both the power supply and the battery, while the battery recovers energy, to cope with different braking situations and achieve more flexible braking.

The proposed power converter has a total of six working states: power excitation, power demagnetization, hybrid excitation, hybrid demagnetization, zero voltage demagnetization, and energy recovery. The electric mode includes five working states, and the braking mode includes four working states. The components

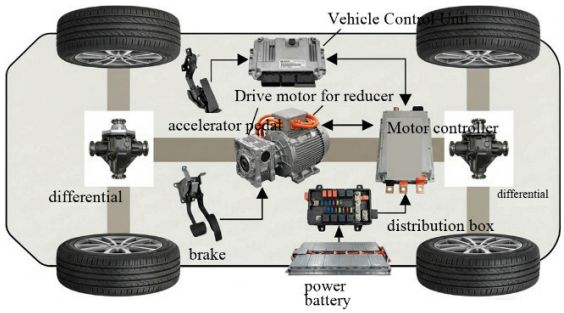


Fig. 6. Electric vehicle power system.

used in the power converter proposed in this article are shown in Table 1.

Table 1: Composition of power converter components [17]

Component	Type Number	Quantity
Mosfet	IRFP4668	10
Diode	RURG8060	8

A. Single power drive mode

In single power drive mode, there are three states: power excitation, zero voltage freewheeling, and power demagnetization, as shown in Fig. 7. In the excitation state of the power supply, the current passes through the asymmetric half-bridge circuit, flows through the negative pole of the power battery, and then forms an excitation circuit through the reverse diode VD_8 connected in parallel with the switching transistor T_{10}, and the current rises rapidly. The voltage applied to the winding at this time is U_{DC}, as shown by the red dotted line in Fig. 7. Afterwards, by controlling the switching tubes T_1, T_3, and T_5 separately, the A, B, and C phase windings are controlled for zero voltage freewheeling, resulting in zero winding voltage, as shown by the blue dotted line in the Fig. 7. In demagnetization mode, the control switch tubes T_8 and T_0 are turned on, and the phase current forms a demagnetization circuit through the switch tubes T_8 and T_{10}. A reverse voltage $-U_{DC}$ is applied to the winding for reverse demagnetization, as shown by the green dotted line in the Fig. 7. Therefore,

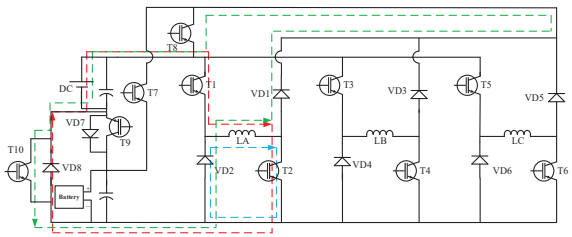


Fig. 7. Working status of power drive.

in the electric single power supply mode, only the T_8 and T_{10} switching tubes need to be controlled to conduct.

B. Hybrid driving mode

In hybrid driving mode, there are three states: hybrid excitation, zero voltage freewheeling, and hybrid demagnetization, as shown in Fig. 8. In this mode, the power supply is connected in series with the battery, and both the excitation voltage and demagnetization voltage are increased, achieving fast excitation and fast freewheeling, improving the output capability of the motor torque and enhancing the dynamic performance of the motor. In excitation mode, current flows through the switch T_9 and the AHB converter to form an excitation circuit, achieving fast excitation. The voltage applied to the winding is the sum of the power supply voltage and the battery voltage $U_{DC}+U_B$, as shown by the red dotted line in the Fig. 8. We can control the A, B, and C phase windings for zero voltage freewheeling by separately controlling the switching tubes T_1, T_3, and T_5, as shown by the blue dotted line in Fig. 8. In demagnetization mode, the current passes through the reverse diode VD_7 of the switching tubes T_8 and T_9 to form a circuit for demagnetization, achieving rapid demagnetization in the reverse direction. The voltage applied to the winding is $-(U_{DC}+U_B)$, as shown by the green dotted line in Fig. 8. Therefore, in the hybrid power supply mode of electric state, only the two switching tubes T_8 and T_9 need to be controlled to conduct.

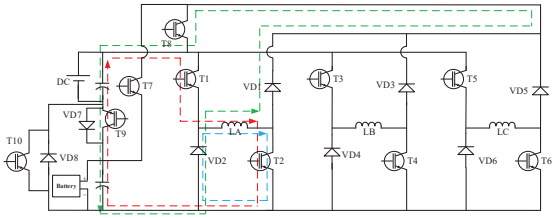


Fig. 8. Working status of hybrid drive.

C. Moderate braking mode

During normal braking, the SRM speed is low and the back electromotive force is small. A combination of current chopping control (CCC) and PWM is used to control the on-off of power devices through PWM signals, stabilizing the braking current at the set value and maintaining a constant braking torque. In normal situations where braking is required, power excitation can be used to apply voltage U_{DC} to the winding during the rise of the inductor, generating braking current. In the decrease interval of the inductor, negative torque and generating current can be generated to reduce the speed and charge the battery. Due to the combination of front-end circuit and traditional asymmetric half-bridge, phase overlap can be achieved in the braking state. In normal braking mode, when phase A recovers energy and phase B excites, the phase overlap situation is shown in Fig. 9.

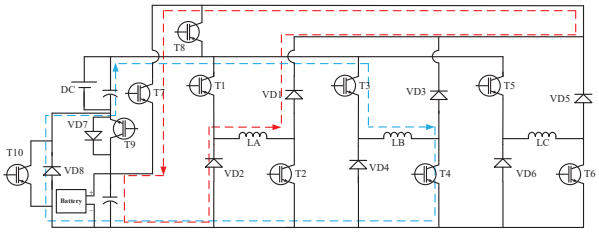


Fig. 9. Phase overlap under moderate braking conditions.

The blue dashed line in Fig. 9 indicates that the B-phase winding is being excited, and the switching tubes T_3 and T_4 are open, causing a rapid increase in winding current. The red dashed line indicates that the A-phase winding is undergoing energy recovery, and the braking energy flows to the battery through switch tube T_7.

D. Heavy braking mode

In emergency situations where strong braking is required, the power supply is connected in series with the battery and voltage $U_{DC}+U_B$ is applied to the winding during the rise of the inductance to jointly excite it, achieving a rapid increase in braking current and generating negative torque quickly. This can greatly improve the braking performance of the motor and, while ensuring braking, the braking energy can still be recovered by flowing through the switch tube T_7 to the battery. In heavy braking mode, when phase A recovers energy and phase B excites, the phase overlap situation is shown in Fig. 10.

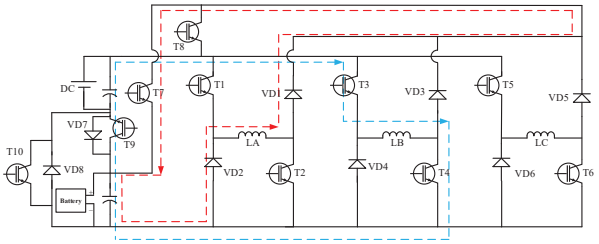


Fig. 10. Phase overlap under heavy braking conditions.

Similar to Fig. 9, the blue dashed line in Fig. 10 indicates that the B-phase winding is being excited, and the switching tubes T_3 and T_4 are open, causing the winding current to rise more rapidly. The red dashed line indicates that the A-phase winding is undergoing energy recovery, and the braking energy is still flowing to the battery through switch tube T_7.

E. Converter driving characteristics

The proposed switched reluctance power converter adopts different working states according to different operating conditions, as shown in Fig. 11.

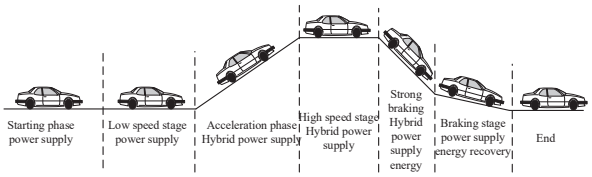


Fig. 11. Working modes under different working conditions.

In the starting and low-speed states, power supply is used for this condition, with power excitation and demagnetization [18]. Power batteries can be connected in series for demagnetization. In the rapid acceleration stage and high-speed stage, a hybrid driving mode is adopted, in which the power supply and battery are connected in series to participate, and the power supply and battery are connected in series to jointly excite and demagnetize, thereby increasing the excitation voltage and demagnetization voltage and improving the output performance of the motor. In the case of heavy braking, a multilevel SRM power converter can ensure the simultaneous use of two power sources during motor operation by mixing power and battery excitation, and recovering battery energy. We can select the appropriate conduction mode based on the current speed, torque error, and rotor position to achieve stable operation of the motor at low speeds and timely tracking of the required current value at high speeds, thus suppressing torque ripple. This multiple power supply mode enables the motor power converter to adapt to complex and changing working conditions, improve the efficiency and stability of motor operation, and is widely used in motor drive systems encountered in various complex working conditions of electric vehicles.

IV. SIMULATION RESULTS

A 1 kW three-phase 12/8-pole SRM was modeled in MATLAB/Simulink, and the proposed highly integrated converter was validated. The rated voltage of the motor is 96 V, The moment of inertia J is 0.01 $\mathrm{Kg \cdot m^2}$, and the friction coefficient D is 0.00032 $\mathrm{N \cdot m \cdot s/rad}$, the battery voltage U_B and power supply voltage U_{DC} were set to 36 V and 60 V, the battery capacity is 5.4 Ah, initial state-of-charge is 60%, respectively, and the load torque was set to 3 $\mathrm{N \cdot m}$. The electric mode adopted CCC, and the hysteresis current bandwidth was set to 1.5 A. Low-speed and high-speed operation were considered in the simulation. The motor section is shown in Fig. 12.

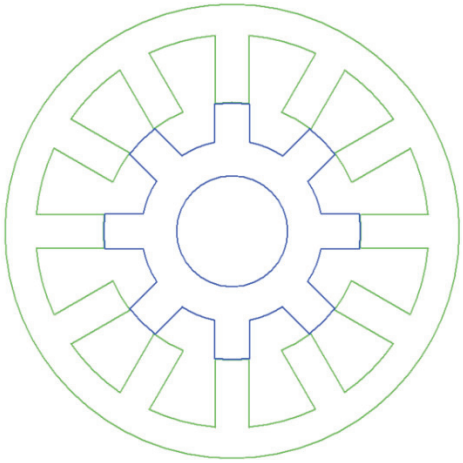


Fig. 12. 12/8 SRM section.

The motor adopts CCC current chopper control and obtains the reference current value I_{ref} through proportional-integral-derivative (PID) control. When the phase current reaches I_{max}, the power switch of that phase is turned off, the power supply is cut off, and the current is attenuated through the freewheeling diode. When the phase current drops to I_{min}, turn on the power switch and the current rises again. Cycle the above process to make the phase current fluctuate within the range $[I_{min}, I_{max}]$, achieving stable control of the current amplitude. The opening angle of the motor in this simulation is set to -5°, and the closing angle is set to 15°.

The single power drive mode is suitable for starting and low-speed states. When the motor rotates to 600 r/min, the speed diagram and torque diagram are shown in Fig. 13.

The winding voltage in single power mode is shown in Fig. 14. It can be seen that the winding voltage mainly varies between 0 V, 60 V, and -60 V, with an excitation state of 60 V. When the phase current reaches the reference current, it transitions to a freewheeling state of 0 V. When the phase reaches the turn off angle, the winding demagnetizes and the phase voltage is -60 V.

When the motor rotates to 1200 r/min, the speed diagram and torque diagram are shown in Fig. 15.

The winding voltage in single power mode is similar to Fig. 14. From Fig. 14, it can be seen that in single power drive mode, the motor speed can quickly increase to 1200 r/min and remain stable.

As shown in Fig. 16, in the single power excitation mode, when the target speed is 1600 r/min, the motor cannot reach the target speed and the torque ripple increases. With the conduction angle unchanged, the motor output is close to the limit. In the hybrid driving mode, the simulation results of the target speed of 1600 r/min are shown in Fig. 17. When the target speed

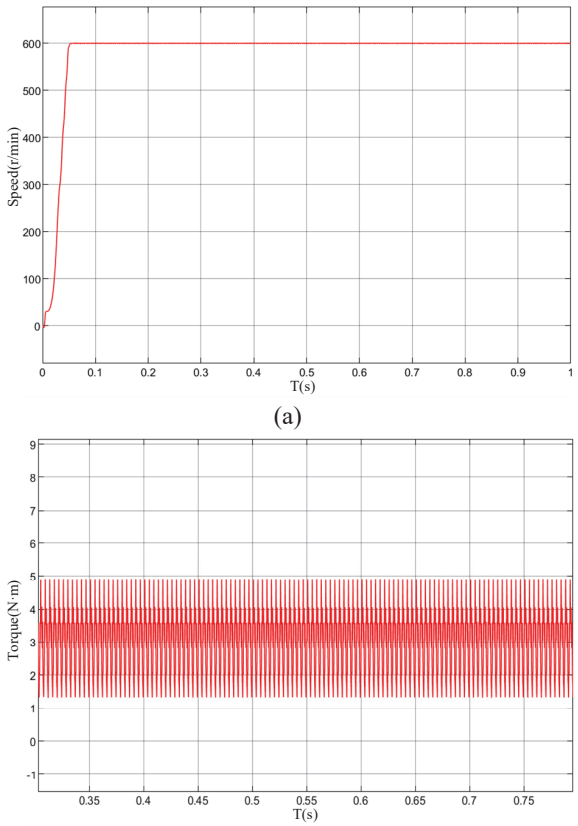


Fig. 13. Simulation results of a 600 r/min single power drive mode motor: (a) speed waveform diagram and (b) torque waveform diagram.

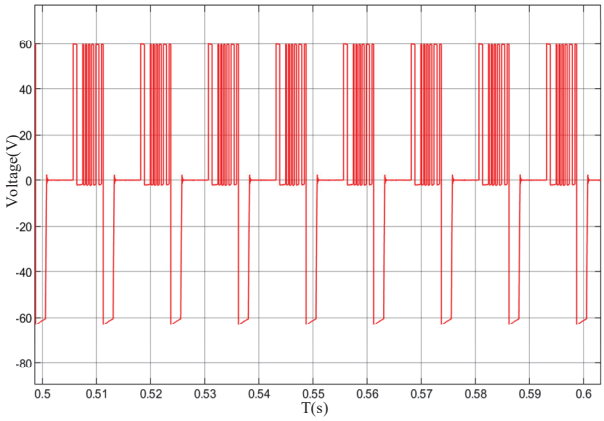


Fig. 14. Single power drive winding voltage.

remains constant at 1600 r/min and the load torque increases by 6 N · m, the simulation results are shown in Fig. 18.

By comparison, it can be seen that when using the hybrid mode, both the excitation voltage and demagnetization voltage are significantly increased. Under the same load torque, higher speeds can be achieved and

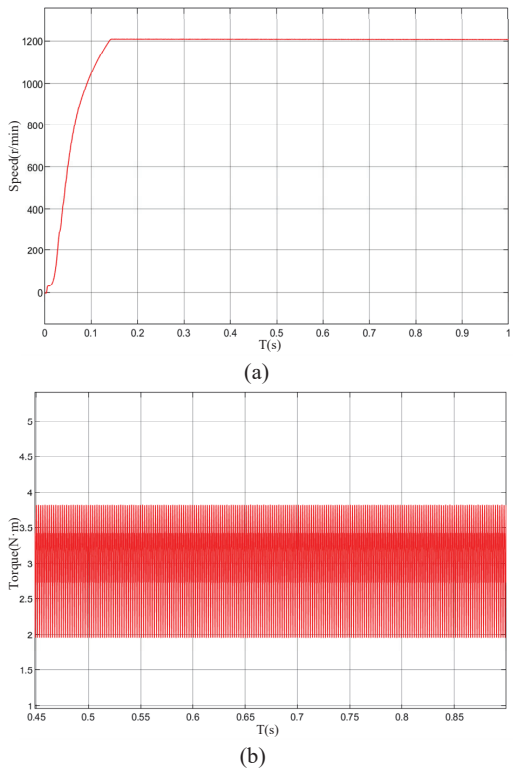


Fig. 15. Simulation results of a 1200 r/min single power drive mode motor: (a) speed waveform diagram and (b) torque waveform diagram.

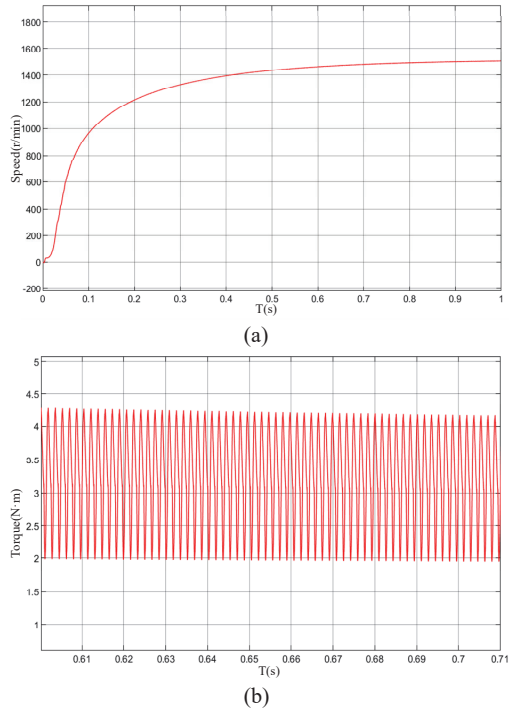
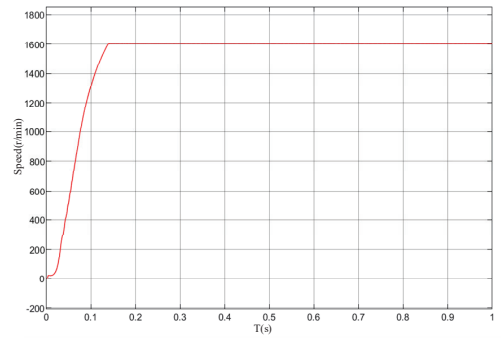
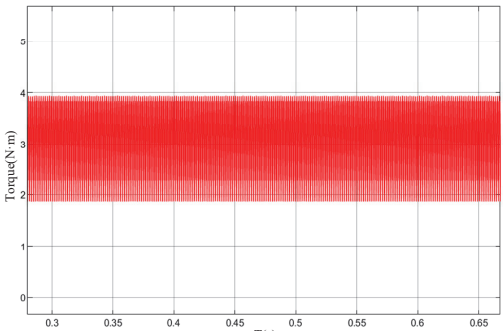


Fig. 16. Simulation results of a 1600 r/min single power drive mode motor: (a) speed waveform diagram and (b) torque waveform diagram.

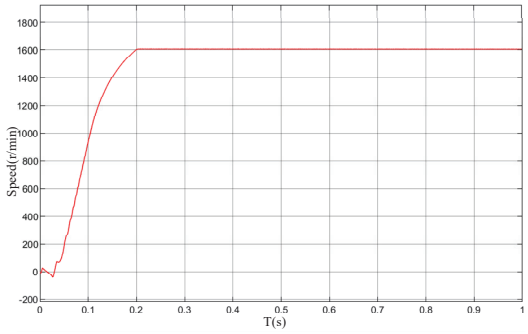


(a)

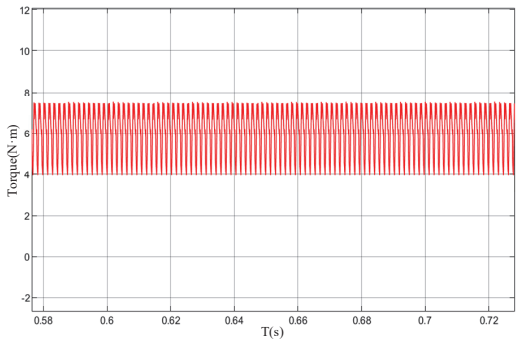


(b)

Fig. 17. Simulation results of a 1600 r/min hybrid drive mode motor: (a) speed waveform diagram and (b) torque waveform diagram.



(a)

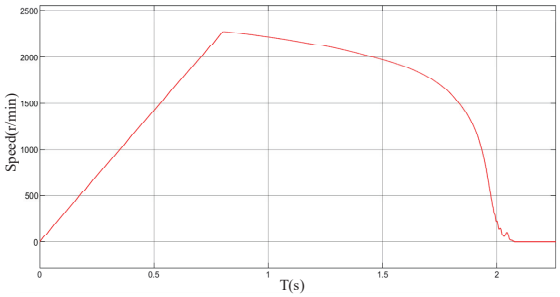


(b)

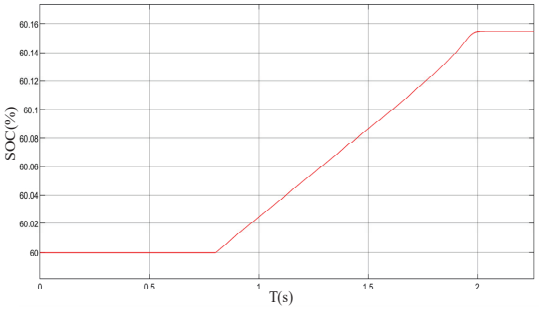
Fig. 18. Simulation results of load torque 6 N · m at a speed of 1600 r/min: (a) speed waveform diagram and (b) torque waveform diagram.

acceleration is faster. At the same time, larger output torque can be obtained while reducing torque ripple, greatly increasing the overall performance of the motor.

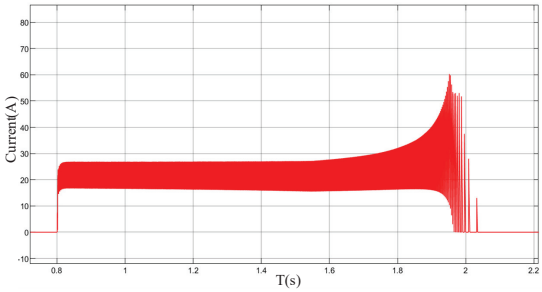
In the context of brake simulation, braking commences when the motor speed reaches 2200 r/min. Under moderate braking mode, the motor simulation results are shown in Fig. 19.



(a)



(b)

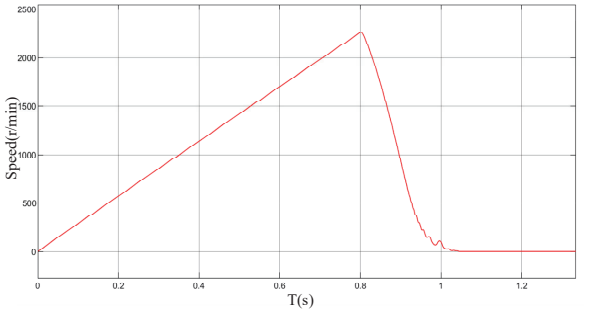


(c)

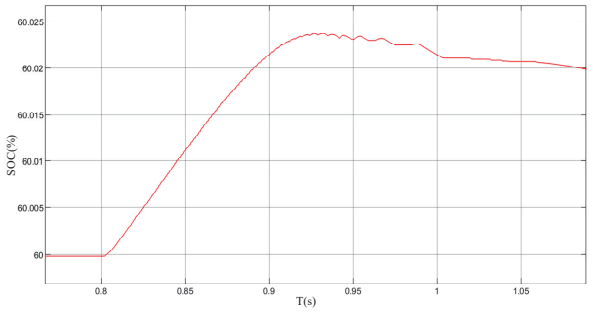
Fig. 19. Simulation results of moderate braking: (a) speed waveform diagram, (b) battery SOC, and (c) charging current waveform.

Load torque is still 3 N · m, motor speed rises from 0 to 2200 r/min at 0.8 s, and then starts braking. In the moderate braking mode, the motor is braked to 0 r/min at 2.05 s, and braking time is about 1.25 s. SOC of the power battery is initially 60% and, after recovery of the braking dynamic energy, battery SOC increases from 60% to 60.155%, as shown in Fig. 19 (b). Energy flows towards the battery, and the charging current of the battery is shown in Fig. 19 (c).

In heavy braking mode, as shown in Fig. 20, the motor speed rises from 0 to 2200 r/min at 0.8 s, and



(a)



(b)

Fig. 20. Simulation results of heavy braking: (a) speed waveform diagram and (b) battery SOC.

then starts braking. At 1.05 s, the motor was braked to 0 r/min, and the braking time was about 0.25 s. At the same time, the power battery recovered energy, and the battery SOC increased. During this braking process, the SOC of the battery increases from 60% to 60.024%, and the recovered energy is relatively less compared to moderate braking.

Compared with moderate braking, heavy braking can significantly improve the braking performance, so as to cope with the complex working conditions of electric vehicles and recover energy at the same time. The proposed converter has been effectively verified in terms of braking.

V. CONCLUSION

This paper proposes a dual-port integrated switched reluctance motor power converter for electric vehicles, which takes into account the electric and braking state of electric vehicles. By controlling the switching state of the front-end circuit, it can flexibly realize energy conversion between the battery, switched reluctance motor, and power supply. It not only improves the performance of the motor system under operating conditions, but also realizes the energy recovery function, realizes flexible driving and flexible braking, obtains multilevel voltage, increases torque capacity, and improves the dynamic performance of the motor as a whole. At the same time, this paper theoretically analyzes a switched reluctance motor under different working conditions, and carries out the simulation of electric and braking to verify the effectiveness of the converter.

ACKNOWLEDGMENT

This work is supported by the National Natural Science Foundation of China International (regional) cooperation and exchange projects NSFC-RSF under Grant W2412064.

REFERENCES

[1] H. Wang, *Speed Regulation and Control Technology of Switched Reluctance Motors*, 2nd ed. Beijing: Publishing House of Electronics Industry, 2014.

[2] N. Ali and M. Narimani, "A new three-level switched reluctance motor drive for electric vehicles," in *2024 IEEE 21st International Power Electronics and Motion Control Conference (PEMC)*, Pilsen, Czech Republic, pp. 1–6, Sep. 2024. doi:10.1109/PEMC61721.2024.10726378.

[3] K.-W. Hu, P.-H. Yi, and C.-M. Liaw, "An EV SRM drive powered by battery/supercapacitor with G2V and V2H/V2G capabilities," *IEEE Trans. Ind. Electron.*, vol. 62, no. 8, pp. 4714–4727, Aug. 2015. doi:10.1109/TIE.2015.2396873.

[4] Z. Xia and J. Bauman, "An integrated modular converter for switched reluctance motor drives in range-extended electric vehicles," in *2019 IEEE Transportation Electrification Conference and Expo (ITEC)*, Detroit, MI, USA, pp. 1–7, June 2019. doi:10.1109/ITEC.2019.8790494.

[5] Z. Yu, C. Gan, K. Ni, Y. Chen, and R. Qu, "Dual-electric-port bidirectional flux-modulated switched reluctance machine drive with multiple charging functions for electric vehicle applications," *IEEE Trans. Power Electron.*, vol. 36, no. 5, pp. 5818–5831, May 2021. doi:10.1109/TPEL.2020.3029822.

[6] G. Han and H. Chen, "Improved power converter of SRM drive for electric vehicle with self-balanced capacitor voltages," *IEEE Trans. Transp. Electrific.*, vol. 7, no. 3, pp. 1339–1348, Sep. 2021. doi:10.1109/TTE.2020.3037111.

[7] H.-C. Chen, W.-A. Wang, and B.-W. Huang, "Integrated driving/charging/discharging battery-powered four-phase switched reluctance motor drive with two current sensors," *IEEE Trans. Power Electron.*, vol. 34, no. 6, pp. 5019–5022, June 2019. doi:10.1109/TPEL.2018.2880259.

[8] T. Wu, W. Li, K. Ni, S. Song, and M. Alkahtani, "Modular tri-port converter for switched reluctance motor based hybrid electrical vehicles," *IEEE Access*, vol. 7, pp. 15989–15998, 2019. doi:10.1109/ACCESS.2019.2894818.

[9] C. Gan, N. Jin, Q. Sun, W. Kong, Y. Hu, and L. M. Tolbert, "Multiport bidirectional SRM drives

for solar-assisted hybrid electric bus powertrain with flexible driving and self-charging functions," *IEEE Trans. Power Electron.*, vol. 33, no. 10, pp. 8231–8245, Oct. 2018. doi:10.1109/TPEL.2017.2780622.

[10] Q. Sun, H. Xie, X. Liu, F. Niu, and C. Gan, "Multiport PV-assisted electric-drive-reconstructed bidirectional charger with G2V and V2G/V2L functions for SRM drive-based EV application," *IEEE J. Emerg. Sel. Topics Power Electron.*, vol. 11, no. 3, pp. 3398–3408, June 2023. doi:10.1109/JESTPE.2023.3240434.

[11] Y. Hu, C. Gan, W. Cao, Y. Fang, S. J. Finney, and J. Wu, "Solar PV-powered SRM drive for EVs with flexible energy control functions," *IEEE Trans. on Ind. Applicat.*, vol. 52, no. 4, pp. 3357–3366, July 2016. doi:10.1109/TIA.2016.2533604.

[12] A. F. Dewi and S. Riyadi, "The impact of SRM rotor speed on regenerative braking to optimize the performance," in *2019 IEEE Conference on Energy Conversion (CENCON)*, Yogyakarta, Indonesia, pp. 104–109, Oct. 2019. doi:10.1109/CENCON47160.2019.8974687.

[13] V. F. Pires, A. J. Pires, A. Cordeiro, and D. Foito, "A review of the power converter interfaces for switched reluctance machines," *Energies*, vol. 13, no. 13, p. 3490, July 2020. doi:10.3390/en13133490.

[14] X.-H. Huang and G.-Q. Liu, "Research on brake control of switched reluctance motor," in *2018 International Conference on Sensor Networks and Signal Processing (SNSP)*, Xi'an, China, pp. 361–364, Oct. 2018. doi:10.1109/SNSP.2018.00076.

[15] M. Deepak, C. Bharatiraja, S. S. Williamson, and M. Krishnamurthy, "Enhanced direct torque control of SRM based on a novel multilevel hysteresis torque band with effective voltage vectors for low torque ripple," *IEEE Transactions on Transportation Electrification*, vol. 11, no. 6, pp. 12758–12770, Dec. 2025. doi:10.1109/TTE.2025.3585500.

[16] G. D. Wahyu and S. Riyadi, "PWM control strategy of regenerative braking to maximize the charging current into the battery in SRM drive," in *2019 International Seminar on Application for Technology of Information and Communication (iSemantic)*, Semarang, Indonesia, pp. 523–527, Sep. 2019. doi:10.1109/ISEMANTIC.2019.8884342.

[17] X. Sun, L. Feng, Z. Zhu, G. Lei, K. Diao, and Y. Guo, "Optimal design of terminal sliding mode controller for direct torque control of SRMs," *IEEE Transactions on Transportation Electrification*, vol. 8, no. 1, pp. 1445–1453, Mar. 2022. doi:10.1109/TTE.2021.3111889.

[18] M. A. Gaafar, A. Abdelmaksoud, M. Orabi, H. Chen, and M. Dardeer, "Switched reluctance motor converters for electric vehicles applications: Comparative review," *IEEE Trans. Transp. Electrific.*, vol. 9, no. 3, pp. 3526–3544, Sep. 2023. doi:10.1109/TTE.2022.3192429.



Chenhe Zhang received the B.S. degree in electrical engineering and automation from Yancheng Institute Of Technology, Yancheng, Jiangsu, China, in 2024. He is currently pursuing a master degree in electrical engineering at China University of Mining and Technology, Xuzhou. His research interests include switched reluctance motor design control, electric traction, and electric vehicles.



Hao Chen (SM'08) received the B.S. and Ph.D. degrees from the Department of Automatic Control, Nanjing University of Aeronautics and Astronautics, Nanjing, China, in 1991 and 1996, respectively. In 1998, he became an Associate Professor with the School of Information and Electrical Engineering, China University of Mining and Technology, Xuzhou, where he has been a Professor since 2001. From 2002 to 2003, he was a Visiting Professor at Kyungsung University, Busan, Korea. Since 2008, he has also been an Adjunct Professor at the University of Western Australia, Perth, Australia. He is the author of one book and has also authored more than 190 papers. He is the holder of 15 US Patents, 23 Australian Patents, one Danish Patent, seven Canadian Patents, three South African Patents, 10 Russian Patents, 87 Chinese Invention Patents, and six Chinese Utility Model Patents. His current research interests include motor control, linear launcher, electric vehicles, electric traction, servo drives, and wind power generator control.

Chen was the recipient of both the Prize of Science and Technology of Chinese Youth and the Prize of the Fok Ying Tong Education Foundation for Youth Teachers in 2004. He was awarded first prize in the Science and Technology advanced of Province and Ministry once, second prize in the Science and Technology advanced of Province and Ministry seven times, and third prize in the Science and Technology advanced of Province and Ministry 14 times. He became the Chinese New Century Hundred-Thousand Ten-Thousand Talents Engineering National Talent in 2007, and won the Government Especial Allowance of People's Republic of China State Department since 2006.



Olimjon Toirov earned the degree of Doctor of Philosophy (Ph.D.) in technical sciences in the specialty "Energy Systems and Complexes" at the Institute of Energy and Automation of the Academy of Sciences of the Republic of Uzbekistan in 2012. In 2018, he defended his Doctor of Technical Science (D.Sc.) dissertation at Tashkent State Technical University (TSTU). In 2020, he was awarded the academic title of Full Professor in the specialty "Energy Systems and Complexes". Throughout his professional career, Toirov served as a research fellow at the Institute of Energy and Automation of the Academy of Sciences of the Republic of Uzbekistan from 2007 to 2016; a leading researcher and project manager at "Scientific-Technical Center", "Uzbekenergo" from 2016 to 2017. In 2017–2018, he worked as a Senior Researcher for the UNESCO/Poland Fellowship Programme in Engineering Project, AGH University of Science and Technology (Poland) and as Head of the "Electrical Machines and Drives" Department at TSTU from 2019 to 2024. Since 2024, he has been serving as the Dean of the "Electrical Engineering" Faculty at TSTU.

Toirov's research activities are focused on design and automatic electric drive, green energy, renewable energy sources, improving energy efficiency in electric power supply systems, control of asynchronous generators, and enhancing the efficiency of electromechanical systems. Under his leadership, automated control devices were developed and successfully implemented across several key industrial sectors, including the Almalyk and Navoi Mining and Metallurgical Combines, Uzbekhydroenergo, oil and gas enterprises, and automotive factories. He has participated in more than 50 industry-funded projects and over 15 fundamental and applied research projects and has won more than 12 international research grants. He is the author of over 300 scientific publications, including 32 inventions and patents, six textbooks, five teaching manuals, 16 methodological guidelines, and two monographs. More than 40 of his articles are indexed in Web of Science and Scopus databases. Toirov has supervised one Doctor of Technical Science (D.Sc.), five Doctors of Philosophy (Ph.D.), more than 50 bachelors', and over 20 master's students. He was awarded the honorary 1st place in the "Most Active Young Scientist of the Year" competition held in the Republic of Uzbekistan in 2016. In 2023, he was honored with the "Scopus Edwards Uzbekistan" award for his outstanding publication activity. He was awarded the "Shuhrat" medal by the Decree of the President of the Republic of Uzbekistan in 2024. Toirov has completed international training and research programs in countries such as China, Russia, India, South Korea, Germany, France, Azerbaijan, Belarus, Poland, Slovakia, and Belgium. He currently serves as a member of the Expert Council on energy sciences under the Higher Attestation Commission of the Republic of Uzbekistan. He is also an editorial board member of several national and international scientific journals.



Sherif Moussa is Dean of the School of Engineering, Applied Science, and Technology at the Canadian University Dubai (CUD), UAE. He earned his Ph.D. in Electrical and Computer Engineering from the University of Québec at Trois-Rivières, Canada, and his M.Sc. in Electrical and Computer Engineering from the University of Waterloo, Canada. Since joining CUD in 2007, Moussa has led the School's remarkable growth, overseeing the launch and accreditation of several engineering and computing programs, including Mechatronics Engineering, Computer Science, Cybersecurity, Software Design, Power and Renewable Energy Engineering, and the M.Sc. in Artificial Intelligence. His leadership has also advanced international collaborations, notably with Queen's University and the University of Ottawa, and strengthened CUD's engagement with industry partners in emerging technologies. Moussa's research interests span wireless communication, computer networks, machine learning, and digital systems design. He has published widely in international journals and conferences, serves on technical committees, and is the recipient of the 2015 CUD Research Excellence Award. He is also the founder of CUD's Robotics Club and a strong advocate for innovation and experiential learning in engineering education.



Habes Ali Khawaldeh (Member, IEEE) received the B.E. degree in electrical and computer engineering from The Hashemite University, Jordan, in 2009, and the M.S. degree in electrical power engineering from Yarmouk University, in 2013. In 2022, Habes received his Ph.D. degree in power electronics engineering from the Faculty of Engineering and Information Technology, University of Technology Sydney (UTS), Australia. Since 2018, he has been a Casual Academician with UTS for various power electronics subjects. Since July 2009, he has been working as an electrical engineer with different companies in Jordan. He was a part-time Faculty Member with Yarmouk University for various power electronics subjects. He was a full-time Faculty Member with Al-Hussein Bin Talal University from 2015 to

2018. His current research interests include renewable energy (RE) systems, power converter design for RE applications, battery systems, multi-port DC/DC converters, and energy conversion systems for the smart grid. He received a Grant from Al al-Bayt University for his Ph.D. degree. He is currently a reviewer for several IEEE, IET, and Elsevier journals. Currently, Habes is an assistant professor at the University of Al al-Bayt in Jordan.



Marcin Wardach was born in Poland in 1980. He graduated and received the Ph.D. degree from the Electrical Department, Szczecin University of Technology, Szczecin, Poland, in 2004 and 2009, respectively. From 2020 until now, he has been an Associate Professor with the Faculty of Electrical Engineering, West Pomeranian University of Technology in Szczecin. Since 2024, he has served as Vice-Dean for Organization and Development and Head of the Department of Electrical Machines and Drives at the Faculty of Electrical Engineering, West Pomeranian University of Technology in Szczecin. From 2019 to 2025, he worked as an electrical machine designer at mPower Sp. z o.o. company. His research interests include the design of electrical machines and drives, especially unconventional and hybrid excited. He is the author of over 100 scientific papers and post-conference publications. Since 2022, he has been the President of the Szczecin Branch of the Association of Polish Electrical Engineers (SEP). He is also a member of the Polish Society of Theoretical and Applied Electrical Engineering.



Sergei Brovanov received the engineer degree from the Industrial Electronics Department, Novosibirsk Electrotechnical Institute in 1987. In 1999, he became an Associate Professor in the Industrial Electronics Department, Novosibirsk State Technical University, where he has been a Professor since 2013. In 2004, he was a Visiting Professor at Ulsan University, South Korea. He is the author of one book and has also authored more than 150 papers. He had obtained 17 Russian patents. His current research interests include semiconductor converters, vector PWM of multilevel NPC converters, and semiconductor converters for electrical energy storage systems. In 1996–1997, he was awarded a scholarship from the Swiss Academy of Engineering Sciences. In 2023, he was awarded the State Prize of the Novosibirsk Region for the development of intelligent power electronic systems and devices. Brovanov currently is a professor in the electronics and electrical engineering Department at Novosibirsk State Technical University.



Ali Asghar Memon is professor in Electrical Engineering at Mehran University of Engineering and Technology Jamshoro, Pakistan. He holds B.E. and M.E. in Electrical Engineering from Mehran University and Ph.D. from University of Leeds, UK. Memon is head of Electrical Machine and Drives group at Mehran University. He has been member of National Curriculum Review Committee in Pakistan. Memon has served as an expert evaluator for National Research Project for Universities (NRPU), Post doc fellowship and project(s) under Technology Development Fund (TDF), under Higher Education Commission (HEC), Government of Pakistan. Memon is a keynote speaker and reviewer of prestige international research journals. Memon's interests include modeling and simulation of switched reluctance machines and inverters.



Emmanuel Karapidakis is an Electrical and Computer Engineer. He was Dean at School of Engineering from 2019 to 2025, and Director of Energy, Environment and Climate Change Institute IEECC (ieecc.hmu.gr) in Hellenic Mediterranean University HMU (hmu.gr). Since 2022, he is President of the Board in Hellenic Association of Electricity Storage Systems HAESS (www.haess.gr). His research interest focuses on energy systems, power systems operation, diverse & dispersed generation, micro-grids, renewable energy technologies, energy storage, and energy markets. He is/was scientific coordinator (PI) in 12 European financed projects, 15 National programs and several private funded projects, with more than 8 million euros in total. He has published more than 120 papers (Scopus Author ID 6506872824) in prestigious journals and scientific conferences, and four scientific book chapters. From 2011 to 2015, he was Member of the Board in Regional Council of Innovation, and from 2015 to 2017, Member of Board in Energy Planning Council at Region of Crete.



Aris Dimeas is an Assistant Professor at the School of Electrical and Computer Engineering of the National Technical University of Athens (NTUA), with more than 20 years of experience in power systems operation, smart grids, and energy system digitalization. His expertise spans distribution and transmission system operation, renewable energy integration, microgrids, flexibility markets, artificial intelligence applications, and advanced control and decision-support software. He has played a leading technical and coordination role in more than 30 EU-funded research and innovation projects (H2020 and Horizon Europe), collaborating closely with TSOs, DSOs, regulators, industry, and the European Commission. His work bridges research and real-world deployment, with demonstrated impact on system supervision, resilience, market design, and data-driven grid operation, while his scientific contributions include high-impact publications in leading IEEE and international journals.